



Etude de la relation entre la microstructure et les propriétés mécaniques d'un acier durci par précipitation intermétallique intense : le Fer-Silicium-Titane

Malika Perrier

► To cite this version:

Malika Perrier. Etude de la relation entre la microstructure et les propriétés mécaniques d'un acier durci par précipitation intermétallique intense : le Fer-Silicium-Titane. Autre. Université de Grenoble, 2011. Français. NNT : 2011GRENI007 . tel-00721729

HAL Id: tel-00721729

<https://theses.hal.science/tel-00721729>

Submitted on 30 Jul 2012

HAL is a multi-disciplinary open access archive for the deposit and dissemination of scientific research documents, whether they are published or not. The documents may come from teaching and research institutions in France or abroad, or from public or private research centers.

L'archive ouverte pluridisciplinaire **HAL**, est destinée au dépôt et à la diffusion de documents scientifiques de niveau recherche, publiés ou non, émanant des établissements d'enseignement et de recherche français ou étrangers, des laboratoires publics ou privés.

THÈSE

Pour obtenir le grade de

DOCTEUR DE L'UNIVERSITÉ DE GRENOBLE

Spécialité : **Matériaux, Mécanique, Génie Civil, Electrochimie**

Arrêté ministériel : 7 août 2006

Présentée par

Malika PERRIER

Thèse dirigée par **Yves BRECHET** et
codirigée par **Olivier BOUAZIZ** et **Alexis DESCHAMPS**

préparée au sein du Laboratoire **Sciences et Ingénierie des
Matériaux et Procédés**
dans l'**École Doctorale Ingénierie-Matériaux, Mécanique,
Environnement, Energétique, Procédés, Production**

Etude de la relation entre la microstructure et les propriétés mécaniques d'un acier durci par précipitation intermétallique intense : le Fer-Silicium-Titane

Thèse soutenue publiquement le **10 janvier 2011**,
devant le jury composé de :

Mr Philippe MAUGIS

Professeur IMP2NP Marseille, Président du jury

Mr Alain HAZOTTE

Professeur LETAM, Metz, Rapporteur

Mr Bernard VIGUIER

Professeur CIRIMAT, Toulouse, Rapporteur

Mr David EMBURY

Professeur Emerite, MacMaster University, Canada, Invité

Mr Yves BRECHET

Professeur Grenoble-INP, Directeur de thèse

Mr Olivier BOUAZIZ

Ingénieur de Recherche ArcelorMittal, co-encadrant



*An Opi, für den Stahl
ohne Kohle ein Rätsel war*

Abstract

The Iron-Silicon-Titanium alloy system is known to have an interesting hardening potential thanks to its ability to produce a fine and dense precipitation microstructure. The high yield stress obtained for steels from this system, makes them potential candidates for automotive applications. The aim of this study is to improve the understanding of the precipitation sequence and kinetics, as well as to analyze the influence of the precipitates on the mechanical properties (yield strength and strain hardening) in the objective of alloy design and process optimization.

The approach used is classical in physical metallurgy. It consists namely, of the characterization of precipitation followed by the study of the mechanical properties. The characterization of precipitation has been carried out using the combination of Small-Angle Neutron Scattering, Transmission Electron Microscopy and Atom Probe Tomography. This provides an accurate description of the precipitates in terms of crystal structure, composition, size and volume fraction. These properties have been subsequently reproduced with a precipitation model.

The mechanical tests performed on the alloy at room temperature, have revealed a large hardening potential that depends on ageing time and temperature. Physically-based models for yield strength and strain hardening rate (including the effect of isotropic and kinematic hardening) have been applied to interpret the measured stress-strain curves, and allow to reach a comprehensive understanding of the microstructure/properties relationship in the Fe-Si-Ti alloy system.

Résumé

L'amélioration des propriétés mécaniques dans les alliages du système Fer-Silicium-Titane grâce à l'introduction d'une précipitation nanométrique a été démontrée dans la littérature. La haute valeur de limite d'élasticité qui peut être atteinte dans ces aciers en fait de bons candidats pour des applications dans l'élaboration de structures automobiles. Dans ce contexte, cette étude a pour objectif de caractériser et comprendre la séquence et la cinétique de précipitation dans ces alliages, ainsi que les relations entre microstructure de précipitation et propriétés mécaniques, dans une démarche de conception d'alliages optimisée.

La démarche utilisée a tout d'abord consisté en une caractérisation multi-échelle de la précipitation par diffusion des neutrons aux petits angles, microscopie électronique en transmission et sonde atomique tomographique, qui a permis d'aboutir à une description précise de la structure, composition, taille et fraction volumique des précipités, qui ont ensuite été reproduites par modélisation.

Dans un deuxième temps, les tests mécaniques réalisés à température ambiante ont révélé un fort potentiel durcissant, qui dépend du temps et de la température de vieillissement. Des modèles à base physique pour la limite d'élasticité et le taux d'écrouissage (tenant compte des contributions isotropes et cinématiques) ont été appliqués pour décrire les courbes de traction mesurées. Ceux-ci ont permis d'aboutir à une bonne compréhension des relations entre microstructures et propriétés dans le système Fe-Si-Ti.

Table of content

RÉSUMÉ ÉTENDU	14
I. Introduction	14
II. Matériaux et techniques expérimentales	15
A. Matériaux et traitements thermiques	15
B. Techniques expérimentales	15
1) Caractérisation de la précipitation	15
2) Etude des propriétés mécaniques	16
III. Etude de la précipitation dans l'alliage Fe-Si-Ti	16
A. Diffusion de neutrons aux petits angles (SANS)	16
B. Microscopie électronique en transmission (MET)	17
C. Sonde atomique tomographique (APT)	18
D. Modélisation des cinétiques de précipitation	19
1) Modèle "DBPréci"	20
2) Modèle par classes	21
3) Comparaison des deux types de modèles	22
IV. Etude des propriétés mécaniques de l'alliage Fe-Si-Ti	23
A. Essais de dureté	24
B. Essais de traction	24
C. Essais Bauschinger	25
V. Influence de la microstructure sur le comportement mécanique : modélisation	27
A. Modélisation de la limite d'élasticité	27
B. Modélisation de l'écrouissage	28
VI. Conclusion générale	31
A. Conclusion	31
B. Perspectives	31

GENERAL CONTEXT	33
CHAPTER I : INTRODUCTION TO MATERIALS FOR AUTOMOTIVE APPLICATIONS	35
Introduction	37
I. State of the art on automotive steel solutions	37
A. Light weight materials	37
B. Steels for automotive applications	38
1) General presentation	38
2) Weight saving high strength steels	40
C. Age-hardened Iron-based systems	41
II. Structure of the manuscript	43

CHAPTER II : MATERIAL AND EXPERIMENTAL TECHNIQUES	45
I. Material	47
A. Pre-deformation conditions	47
B. Ageing treatments	49
1) Technical devices	49
2) Metallurgical route	50
C. Texture	53
II. Experimental Techniques	55
A. Mechanical properties	55
1) Vickers hardness	55
2) Tensile tests	55
3) Bauschinger tests	57
B. Precipitation characterization	58
1) Microstructure observation at an “average” level: Small Angle Neutron Scattering (SANS)	58
i. Conditions for experiments on Fe-Si-Ti system	58
ii. General description	58
iii. Extraction of Radius values	64
iv. Extraction of Volume fraction values	65
2) Local microstructure observation: Microscopy	67
i. Optical microscope	67
ii. Scanning Electron Microscope with Field Emission Gun (SEM-FEG)	67
iii. Transmission Electron Microscopy: TEM	67
iv. Sample Preparation	67
3) Microstructure at atom scale: APT	69
i. Principle	69
ii. Analysis	70

**CHAPTER III : CHARACTERIZATION OF THE YIELD STRESS IN AN FE-SI-TI
ALLOY 73**

Introduction	75
I. Bibliographic review	75
A. Strengthening methods	75
B. Solid solution hardening	76
C. Precipitation hardening	77
1) Generalities	77
i. Penetrable Particles	78
ii. Impenetrable Particles for dislocations	79
2) Influence of precipitates on Yield Stress	80
i. Particle shearing	80
ii. Particle by-passing	80
D. Mechanical behavior of Fe-Si-Ti alloys	82
1) Yield stress evolution	82
2) Deformation mechanisms	84
II. Experimental Results	84
A. Vickers Hardness	85
B. Tensile tests	86
C. Dislocation structures	87
III. Conclusion	91

CHAPTER IV : PRECIPITATION REACTIONS IN FE-SI-TI: KINETICS AND MODELING

93

Introduction	97
I. Literature review	97
A. General description of precipitation	97
B. Modeling: existing models of precipitation kinetics	98
1) Classical nucleation, growth and coarsening model	98
i. Nucleation	98
ii. Growth	100
iii. Coarsening	101
2) Model for homogeneous precipitation: nucleation, growth and coarsening as coupled phenomena	102
i. Nucleation and growth:	102
ii. Growth and coarsening:	103
3) Modeling by classes of precipitates: "Multipréci"	104
C. State of the art on precipitation in the Fe-Si-Ti alloy	105
1) Binary systems	106
i. Fe-Si	106
ii. Fe-Ti	107
iii. Si-Ti	108
2) Ternary System Fe-Si-Ti	109
i. Structure and composition	111
ii. Precipitation kinetics	113
II. Experimental characterization of precipitation in the Fe-Si-Ti system	116
A. Precipitation during heat treatments at 550°C	116
1) Mean microstructural data : SANS experiments	116
2) Imaging and Electron diffraction analysis: TEM	118
3) Quantitative microstructural analysis: APT	121
i. As-quenched sample	121
ii. Precipitation treatment at 550°C during 2 hours	122
iii. Precipitation treatment at 550°C during 3.5 hours	124
iv. Precipitation treatment at 550°C over 6 hours	127
v. Sample aged at 550°C during 20hours	129
B. Other temperatures	131
1) 450°C-500°C	131
2) 520°C and 580°C	131
C. Influence of the initial state	133

III.	Modeling of the precipitation kinetics	134
A.	Model “DBPreci”	135
B.	Class Model	138
1)	Modeling results	138
2)	Influence of the parameters on the modeling results	139
i.	550°C	140
ii.	Other temperatures	141
3)	Influence of the alloy composition on the precipitation kinetics	142
i.	Constant initial solubility product	143
ii.	Variable initial solubility product	144
C.	Comparison between DBPreci and Multipreci models	146
IV.	Conclusion	147

CHAPTER V : STUDY OF MECHANICAL PROPERTIES IN THE FE-SI-TI ALLOY. YIELD STRESS AND STRAIN HARDENING MODELING	149
Introduction	151
I. Bibliographic review	151
A. Parameters influencing strain hardening	151
1) Influence of solid solution	152
2) Influence of precipitates	152
B. Strain Hardening Models	154
1) Introduction to the Kocks-Mecking-Estrin model	155
2) Model considering kinematic strain hardening	156
i. Grain size effect	156
ii. Effect of precipitates	157
II. Experimental Results on Fe-Si-Ti	159
A. Bauschinger Tests	159
B. Modeling results	162
1) Modeling of the Yield stress evolution	162
2) Modeling strain hardening	164
III. Discussion	167
CONCLUSIONS	169
PERSPECTIVES	173
REFERENCES	175

Résumé étendu

Le manuscrit de thèse ayant été intégralement rédigé en anglais il convient de faire un résumé détaillé en français sur les objectifs atteints au cours de ces travaux.

Dans un premier temps nous présenterons le contexte général de la thèse, ainsi que les objectifs initiaux de l'étude, puis nous détaillerons les résultats obtenus tant du point de vue de l'étude de la précipitation que sur les propriétés mécaniques.

I. Introduction

Cette thèse a été réalisée dans le cadre d'une collaboration scientifique entre le centre de Recherche et Développement d'ArcelorMittal (*ArcelorMittal Research SA*), situé à Maizières-les-Metz, et le laboratoire SIMAP, à Grenoble. Elle a émané d'une volonté toujours grandissante de contribuer à l'allègement des structures en général, et des automobiles en particulier. Dans ce contexte, le développement de nouveaux alliages paraît inéluctable et c'est pourquoi un grand nombre d'études portent sur ce sujet.

L'utilisation grandissante de matériaux autres que l'acier est un moyen de répondre à cette demande, par l'introduction de pièces polymères, composites ou encore plus simplement d'alliage d'aluminium. Mais l'inconvénient de ces nouveaux éléments se situe au niveau du coût – c'est le cas de l'aluminium - ou au niveau des propriétés mécaniques. C'est pourquoi l'acier reste encore le meilleur compromis pour coupler propriétés mécaniques élevées et coût moindre. Au sein de l'industrie de l'acier, un des moyens de répondre au besoin de l'allègement de structure est l'utilisation d'aciers de très haute résistance dans les tôles automobiles, puisque celles-ci peuvent être plus fines pour des propriétés mécaniques au moins aussi élevées, et donc allègent les structures. C'est dans ce contexte que se situe cette étude sur l'alliage base Fer, le Fer-Silicium-Titane.

Des études menées dans les années 1970 ont déjà démontré les possibilités de durcissement de l'alliage Fe-Si-Ti, grâce à l'introduction de précipités par traitement thermique. L'augmentation de la limite d'élasticité ainsi obtenue peut atteindre des valeurs allant jusqu'à 1500MPa.

L'objectif de cette thèse est donc de comprendre l'influence de cette précipitation sur les propriétés mécaniques. Pour ce faire, deux démarches ont été couplées à savoir dans un premier temps l'étude de la précipitation, et plus particulièrement des cinétiques de précipitation par des méthodes classiques d'étude microstructurale, telles que le Microscope électronique en Transmission, mais aussi des méthodes moins classiques telles que la diffusion de Neutrons aux petits angles (SANS) ou encore la sonde atomique tomographique (APT), suivie par une modélisation des cinétiques de précipitation. Dans un deuxième temps, l'étude des propriétés mécaniques de l'alliage a été menée en mesurant l'évolution de la dureté avec la température et le temps, ainsi qu'avec des essais de traction, mais aussi en étudiant l'écrouissage et en distinguant l'écrouissage cinématique par des essais Bauschinger.

Pour comprendre alors l'influence de cette précipitation sur les propriétés mécaniques de l'alliage, on met en oeuvre une démarche de modélisation de la limite d'élasticité mais surtout de l'écrouissage. Pour cela, c'est un modèle tenant compte de l'influence de la précipitation sur l'écrouissage cinématique basé sur les modèles développés par G. Fribourg [FRI2009] et A. Aouafi [AOU2009] qui a été utilisé.

II. Matériaux et techniques expérimentales

A. Matériaux et traitements thermiques

L'alliage Fe-Si-Ti a été coulé en deux lingots au centre de Recherche d'Arcelormittal à Maizières-les-Metz. Les compositions exactes de ces lingots sont données dans les tableaux 1 et 2 ci-dessous.

Elément	Si	Ti	C	S	P	B
Quantité (pds%)	2.54	1.05	0.0055	0.003	0.003	0.0023

Tableau 1 : composition de l'alliage coulé en 2006

Elément	Si	Ti	C	S	Mn	P	B	N
Quantité (pds%)	2.57	1.17	0.0072	0.0008	0.005	0.003	<0.001	0.0004

Tableau 2: composition de l'alliage coulé en 2007

Ces lingots de 15kg chacun ont ensuite été laminés à chaud puis à froid afin de faciliter la recristallisation et obtenir une épaisseur finale d'environ 0.9mm.

Les traitements thermiques ont été effectués en partie dans des bains de sels et un four tubulaire, toujours suivant le même schéma, à savoir un premier traitement thermique à 900°C, afin de recristalliser la structure et mettre tous les éléments en solution solide, suivi d'un traitement thermique de précipitation à des températures comprises entre 450 et 650°C pour des temps variables.

B. Techniques expérimentales

L'étude ayant été menée sur deux aspects, d'une part l'étude de la précipitation et d'autre part celle des propriétés mécaniques, les techniques expérimentales peuvent être également divisées en deux parties.

1) Caractérisation de la précipitation

La précipitation a été observée à plusieurs échelles :

- tout d'abord locale, grâce à :

- la microscopie électronique en transmission (MET), utilisée pour avoir une vision à l'échelle des précipités et obtenir des informations sur leur structure cristallographique, employant à la fois de la diffraction d'électrons mais aussi de l'imagerie champ sombre
- la sonde atomique tomographique (APT), pour une vision à l'échelle atomique et une reconstruction 3D de la précipitation. Ces expériences ont été menées à la fois à Rouen au sein du GPM, et à Marseille au sein de l'IM2NP.
- ensuite à l'échelle moyenne du matériau grâce à :
 - la diffusion de Neutrons aux petits angles (SANS) permettant d'obtenir des données de rayons et fractions volumiques moyennes sur l'ensemble de l'échantillon. Ces expériences ont été effectuées à l'Institut Laue Langevin (ILL), sur la ligne D11.

Le couplage de ces trois techniques a permis d'obtenir des valeurs de rayons et de fractions volumiques en bonne concordance d'une technique à l'autre.

2) Etude des propriétés mécaniques

La deuxième partie de l'étude portait sur les propriétés mécaniques du matériau en fonction du traitement thermique effectué. Pour ce faire, un suivi de l'évolution de la microdureté a été effectué, et pour certains échantillons, avérés intéressants en terme de microdureté, des essais de traction ont également été faits. En parallèle, des essais Bauschinger, de cisaillement inversé, ont été effectués sur un traitement thermique en particulier, afin d'étudier l'influence des précipités sur l'écrouissage cinématique.

III. Etude de la précipitation dans l'alliage Fe-Si-Ti

Dans un premier temps, nous avons fait un compte rendu bibliographique sur les connaissances existantes sur la précipitation dans l'alliage Fe-Si-Ti. Des études menées dans les années 1970 ([HEN1968], [JAC1972]) ont montré l'apparition d'une phase métastable Fe_2SiTi , de structure L2_1 ayant un paramètre de maille de 5.7Å, sphérique et cohérente avec la matrice, dans les premiers stades de précipitation à des températures inférieures à 800°C. Cette phase est remplacée par la phase stable Fe_2Ti dès les premiers stades de précipitation à des températures supérieures à 800°C [LOE2004].

C'est sur la phase sphérique et cohérente, Fe_2SiTi , que s'est particulièrement portée notre étude. En effet, il nous est apparu que la phase Fe_2Ti est certes très durcissante, mais également fragilisante pour l'alliage. Elle ne semblait donc pas convenir à nos objectifs. Trois méthodes de caractérisation ont pu être utilisées, afin d'obtenir des données microstructurales, permettant ensuite de paramétrer des modèles de cinétiques de précipitation.

A. Diffusion de neutrons aux petits angles (SANS)

Des essais de microdureté systématiques sur des échantillons recuits à différentes températures de traitements thermiques ont montré un fort durcissement à des temps relativement courts pour des échantillons vieillis à 550°C. Par la suite, l'essentiel de l'étude a donc été mené pour des traitements thermiques à 550°C. Les résultats des expériences de

diffusion de Neutrons aux petits angles sont représentés dans la Figure 0-1 ci-dessous. Les courbes supérieures représentent les évolutions de rayons en fonction du temps, dont l'échelle est représentée à gauche, pour les signaux magnétiques et nucléaires. En effet, une des particularités du SANS est l'obtention, dans le cas d'échantillons magnétiques, de deux signaux distincts, correspondant respectivement à l'interaction entre les neutrons et le moment magnétique de l'échantillon et à l'interaction entre les neutrons et les noyaux des atomes. Les courbes inférieures montrent l'évolution de la fraction volumique en fonction du temps, dont l'échelle est représentée à droite. On note sur cette figure que la fraction volumique moyenne atteint quasiment un plateau à environ 3.5-4% déjà pour des échantillons vieillis à 3h à 550°C. En revanche, l'évolution du rayon semble moins nette puisque certaines fluctuations sont observées à environ 2h30 et 5h de traitements thermiques. Des études microstructurales plus détaillées ont donc été menées à l'aide de la microscopie électronique en transmission et de la sonde atomique tomographique.

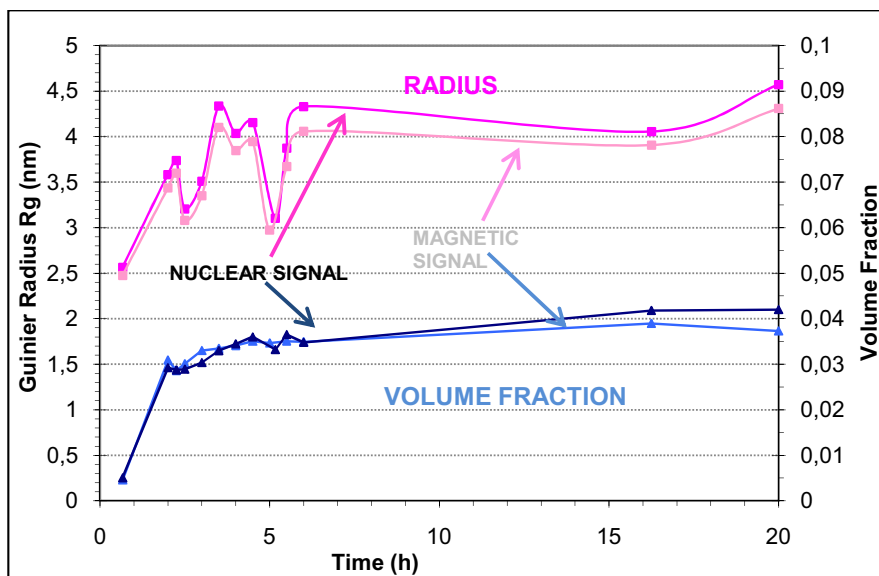


Figure 0-1: résultats des expériences de SANS: évolution du rayon et de la fraction volumique en fonction du temps pour des échantillons vieillis à 550°C

B. Microscopie électronique en transmission (MET)

Des lames minces d'échantillons vieillis à 550°C ont pu être observés au MET par champ sombre et diffraction des électrons. Dans le cas présent, des difficultés liées à la réalisation de lames minces de bonne qualité nous ont poussés à utiliser essentiellement la diffraction des électrons pour révéler la phase présente. Un cliché de diffraction représentatif est donné Figure 0-2 ci-dessous. On peut observer sur cette figure, les taches principales correspondant à la matrice dans la direction $\langle 110 \rangle$, mais également des tâches de sur-structure correspondant à la phase métastable Fe_2SiTi , de structure L2_1 . Ces clichés de diffraction peuvent être trouvés dans des échantillons vieillis à 550°C jusqu'à 15heures.

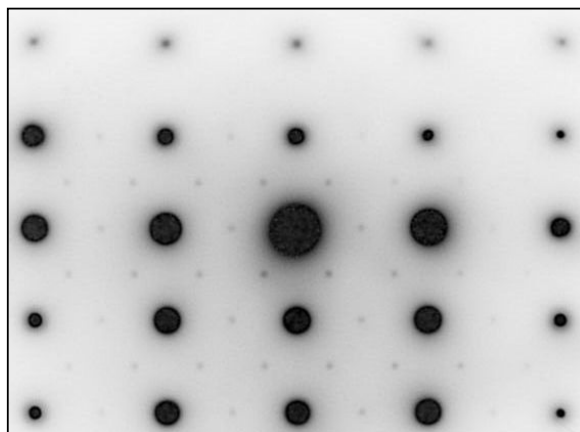


Figure 0-2: observation en diffraction des électrons d'un échantillon vieilli à 550°C°C durant 3heures suivant la direction $\langle 110 \rangle$ de la matrice

Une observation à une échelle encore plus fine que le MET a pu être faite grâce à la sonde atomique tomographique (APT) à l'échelle de l'atome.

C. Sonde atomique tomographique (APT)

Les échantillons pour la APT sont taillés en pointes pour améliorer l'évaporation des atomes sur le détecteur. Les atomes sont identifiés par leur temps de vol et leur emplacement dans l'échantillon est repéré à l'aide d'une grille, ce qui permet la reconstruction en 3D des atomes pour la pointe entière. Par une méthode automatique de classification statistique (« cluster analysis ») il est possible de séparer la matrice et les précipités pour alors obtenir les images représentées Figure 0-3 et Figure 0-4 ci-dessous (les couleurs ne représentent rien de physique, elles permettent simplement de mieux distinguer les précipités). Cinq traitements thermiques ont pu être observés : un échantillon « témoin » en solution solide, ainsi que quatre traitements thermiques différents allant de 2heures à 20heures. La séparation de la matrice et des précipités par « cluster analysis » permet de faire des analyses séparées des compositions en éléments principaux, à savoir le Fer, le Silicium et le Titane. Cela a permis de mettre en évidence qu'il s'agissait bien de la phase Fe_2SiTi , à savoir 50%Fe-25%Silicium-25%Titane dans les 4 échantillons contenant des précipités, et même jusqu'à 20heures de vieillissement. Le bilan de matière permet également d'obtenir des valeurs de fractions volumiques, qui se sont avérées être en bonne corrélation avec le SANS. De plus, il est possible d'effectuer un profil de concentration sur chaque précipité permettant alors d'obtenir des valeurs de rayons des précipités, comme le montrent les figures 5 et 6 ci-dessous. Ces histogrammes montrent respectivement des rayons moyens de 3.5 et de 5 nm pour les échantillons vieillis à 3,5heures et 6 heures, ce qui concorde bien avec les résultats SANS également.

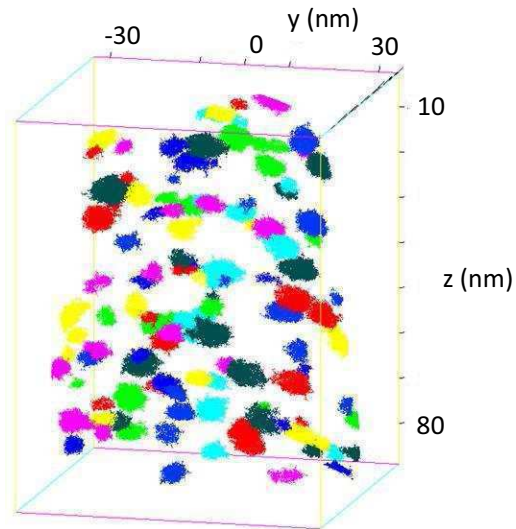


Figure 0-3: reconstruction 3D d'une pointe d'un échantillon vieilli à 550°C durant 3heures et 30 minutes

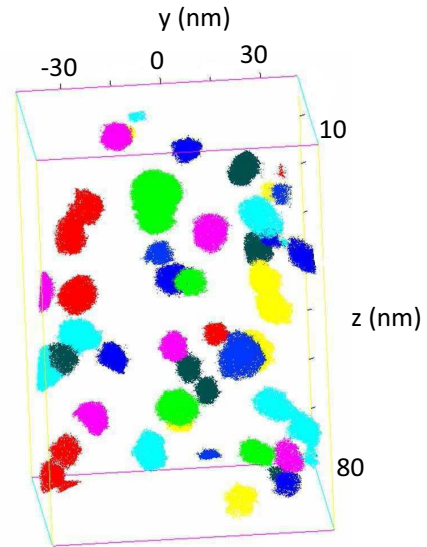


Figure 0-4: reconstruction 3D d'une pointe d'un échantillon vieilli à 550°C durant 6heures

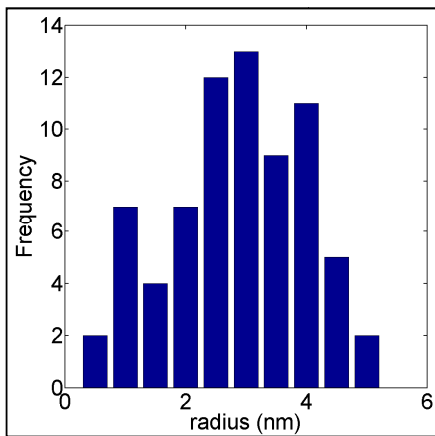


Figure 0-5: histogramme de taille de précipités obtenus sur l'échantillon vieilli durant 3 heures et demie à 550°C

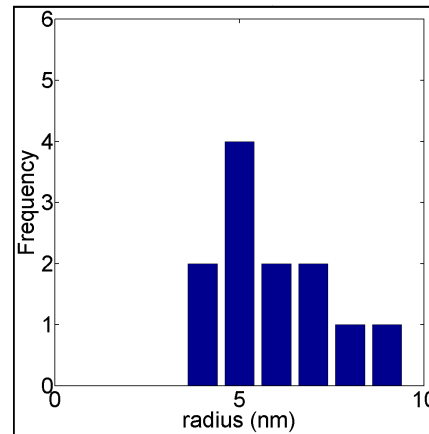


Figure 0-6: histogramme de taille de précipités obtenus sur l'échantillon vieilli durant 6 heures à 550°C

Une fois que les données de fractions volumiques et de rayons sont disponibles, il est alors possible de paramétrer des modèles déjà existants de cinétiques de précipitation pour essayer de prédire celles-ci.

D. Modélisation des cinétiques de précipitation

Les modèles utilisés pour cette modélisation des cinétiques de précipitations, basés sur la théorie classique de germination-croissance-coalescence, ont été de deux types :

- modèle « DBPréci » : considérant les étapes couplées de germination-croissance et croissance-coalescence
- modèle par classes basé sur les algorithmes de type « Multiprécipi » et « Preciso »

1) Modèle “DBPréci”

Ce modèle a été développé par A. Deschamps et Y. Bréchet [DES1999] et est basé sur les travaux de Langer et Schwartz [LAN1980] ainsi que ceux de Wagner et Kampmann [WAG1991]. Il répond aux hypothèses classiques de la théorie d'évolution par germination-croissance-coalescence, et a pour particularité de considérer les 3 étapes comme couplées en 2 étapes principales : tout d'abord la germination-croissance puis la croissance-coalescence. Les équations principales sont données par les principes suivants.

L'évolution du rayon moyen lors de la phase germination croissance peut être exprimée via une équation unique, dont le premier terme décrit la croissance des précipités déjà existants, et le second décrit la naissance du rayon de germination R' :

$$\left. \frac{dR}{dt} \right|_{Nucl-Growth} = \frac{D}{R} \frac{C_{SS} - C_i}{C_p - C_i} + \frac{1}{N} \frac{dN}{dt} (R' - R) \quad (1)$$

$$R' = R^* + \frac{1}{2} \sqrt{\frac{k_B T}{\pi \sigma}} \quad (2)$$

La transition continue de la croissance à la coalescence est exprimée par le paramètre f_{coars} qui est alors utilisé pour l'expression de l'évolution du rayon moyen et de la densité au cours de ces 2 étapes :

$$f_{coars} = \sup \left[1 - 100 \left(\frac{f_v}{f_v^{eq} - 1} \right)^2, 0 \right] \quad (3)$$

$$\frac{dR}{dt} = (1 - f_{coars}) \left. \frac{dR}{dt} \right|_{Growth} + f_{coars} \left. \frac{dR}{dt} \right|_{Coars} \quad (4)$$

$$\frac{dN}{dt} = f_{coars} \left. \frac{dN}{dt} \right|_{Coars} \quad (5)$$

La modélisation utilisant ce modèle montre un très bon accord avec les résultats expérimentaux, comme le montrent les figures 7 et 8 ci-dessous.

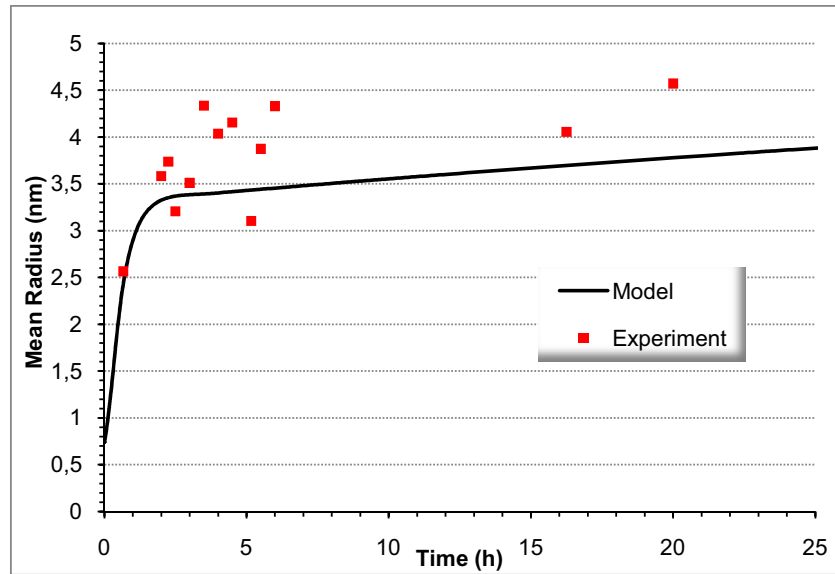


Figure 0-7 : Modélisation de l'évolution du rayon avec le temps pour des échantillons recuits à 550°C par le modèle "DBPreci"

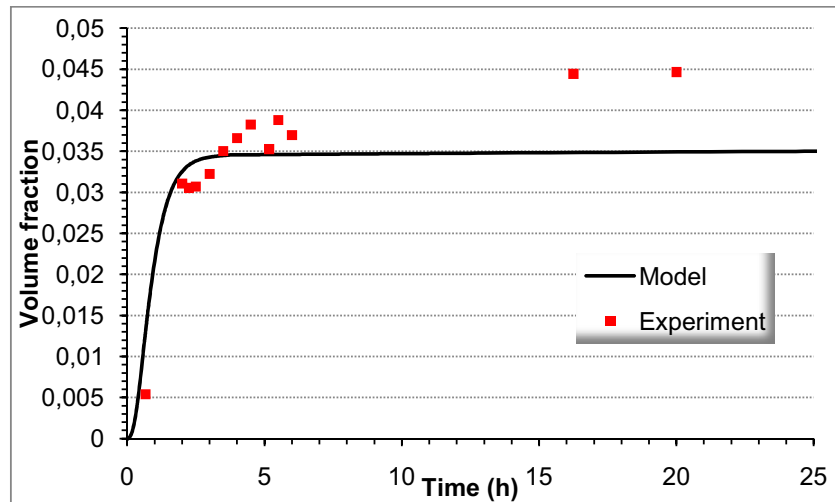


Figure 0-8 : Modélisation de l'évolution de la fraction volumique avec le temps pour des échantillons recuits à 550°C par le modèle « DBPreci »

2) Modèle par classes

Ce modèle est également basé sur les théories classiques de germination-croissance-coalescence, mais utilise une démarche différente de celle du modèle utilisé précédemment « DBPreci », à savoir la définition de « classes » de précipités. Ce modèle considère les trois étapes germination-croissance-coalescence comme liées, non pas par un coefficient introduit, mais par la résolution à chaque instant des équations de germination et croissance/dissolution en parallèle. Cela revient alors à résoudre un système d'équations différentielles indépendantes, résolues successivement en commençant par l'équation de germination, par la méthode des différences finies sur un pas de temps Δt [GEN2001].

Le modèle par classes a été implémenté au laboratoire SIMAP, utilisant un algorithme de type « Preciso » ([PER2007], [ACE2007]) et « Multipreci » ([GEN2001],

[MAU2005]). Les résultats obtenus dans notre cas ont montré une très bonne description des résultats expérimentaux, tant pour les cinétiques de précipitation à 550°C que pour celles qui ont été observées à 450°C, 500°C, 520°C et 580°C, comme le montrent les figures 9 et 10.

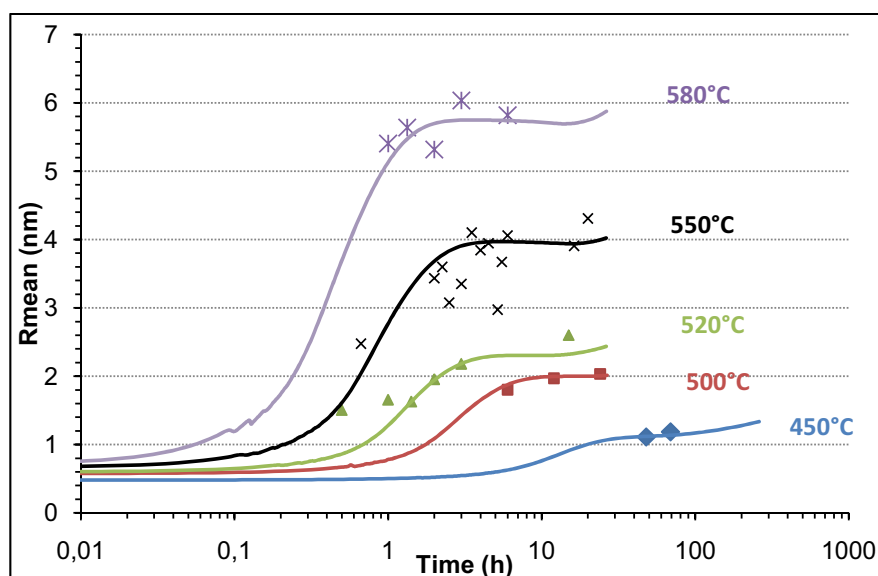


Figure 0-9: modélisation de l'évolution du rayon de précipités en fonction du temps, pour des températures de traitement thermique comprises entre 450°C et 580°C utilisant le modèle par classes de précipités

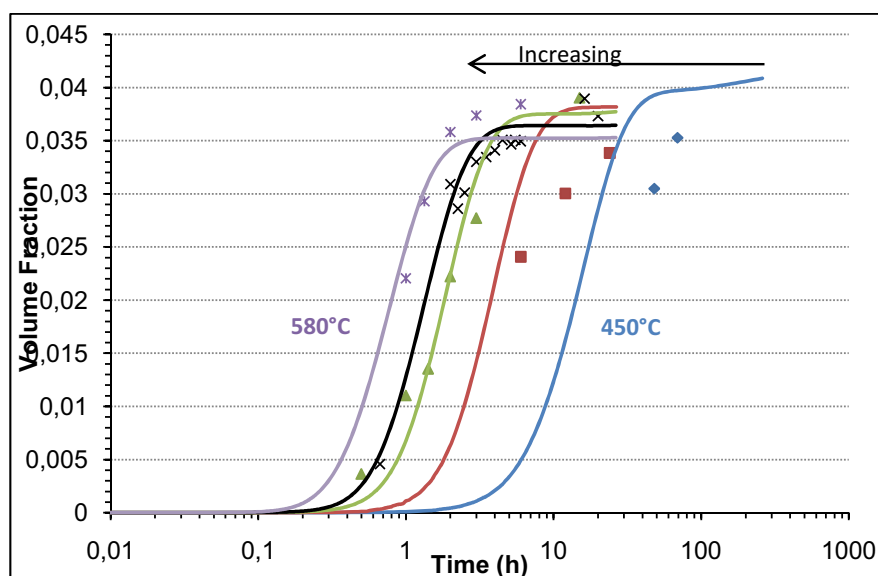


Figure 0-10: modélisation de l'évolution de la fraction volumique de précipités en fonction du temps, pour des températures de traitement thermique comprises entre 450°C et 580°C utilisant le modèle par classes de précipités

3) Comparaison des deux types de modèles

Les deux modèles étant tous les deux basés sur la théorie classique de germination-croissance-coalescence, mais utilisant des approches différentes, il paraît intéressant de comparer les résultats obtenus. La comparaison est montrée figures 11 et 12 ci-dessous. Comme dans la thèse de F. Perrard [PER2004], cette comparaison met en évidence la

capacité des deux modèles à décrire les cinétiques de précipitation convenablement, bien que le modèle « DBPréci » repose sur des hypothèses plus simplificatrices.

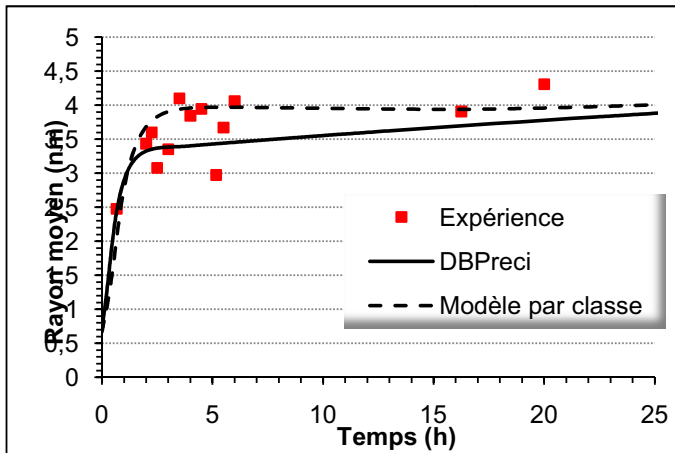


Figure 0-11: Comparaison entre les modèles "DBPréci" et par classes pour la description de l'évolution du rayon en fonction du temps pour les échantillons vieillis à 550°C

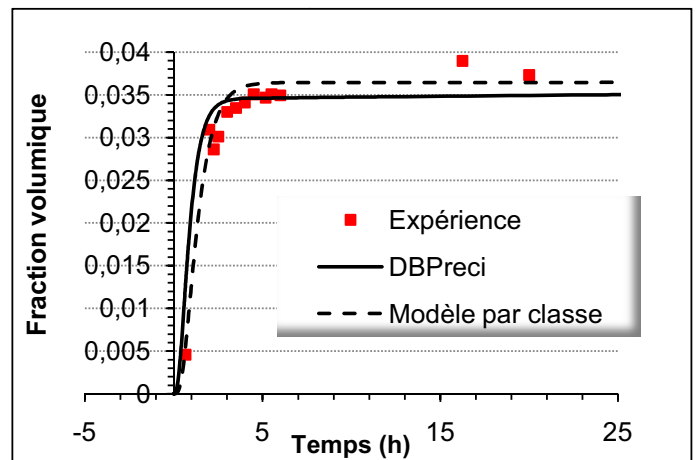


Figure 0-12 Comparaison entre les modèles "DBPréci" et par classes pour la description de l'évolution de la fraction volumique en fonction du temps pour les échantillons vieillis à 550°C

Pour conclure sur cette partie, l'étude de la précipitation a permis de mettre en évidence une précipitation fine et particulièrement dense pour un alliage base Fer allant jusqu'à une fraction volumique de 4%. Il apparaît que la phase présente à des températures comprises entre 450°C et 650°C est toujours la phase métastable Fe_2SiTi même pour des temps allant jusqu'à 20h à 550°C. Ces techniques ont également permis d'obtenir un assez grand nombre de données expérimentales de rayons et fractions volumiques nécessaires à la modélisation des cinétiques de précipitation. Cette modélisation des cinétiques de précipitation a montré une bonne corrélation avec les données expérimentales tant pour le modèle « DBPréci » que pour le modèle par classes de précipités.

Une fois que la précipitation a été caractérisée, il a semblé intéressant de comprendre son impact sur les propriétés mécaniques.

IV. Etude des propriétés mécaniques de l'alliage Fe-Si-Ti

L'étude des propriétés mécaniques dans l'alliage Fer-Silicium-Titane a été le sujet d'un certain nombre d'études dans les années 1970, telles que Hénon et al. [HEN1966] ou encore Jack et al. [JAC1975]. Ces études portaient sur l'évolution de la dureté en fonction du temps et de la température de recuit des échantillons, ainsi que sur le comportement en compression d'échantillons vieillis à des temps différents. Ces études ont montré une grande capacité de durcissement des précipités dans ces alliages, allant jusqu'à une dureté de 600Hv pour un alliage Fe-3.5pds%Si-1.5pds%Ti, et jusqu'à 1500MPa en limite d'élasticité en compression pour ce même alliage. Un rappel des différents paramètres microstructuraux influençant la limite d'élasticité et l'écrouissage a été fait, basé sur une étude bibliographique.

A. Essais de dureté

Dans un premier temps, des essais de dureté ont été effectués sur un grand nombre d'échantillons, vieillis à différentes températures pour déterminer ceux pour lesquels le durcissement semblait intéressant. Les résultats pour des échantillons vieillis à 450, 500 et 550°C sont montrés Figure 0-13 ci-dessous. On note que les valeurs de durcissement des échantillons vieillis à 550°C atteignent des valeurs relativement élevées au bout de seulement quelques heures. C'est pourquoi cette température a été étudiée plus largement.

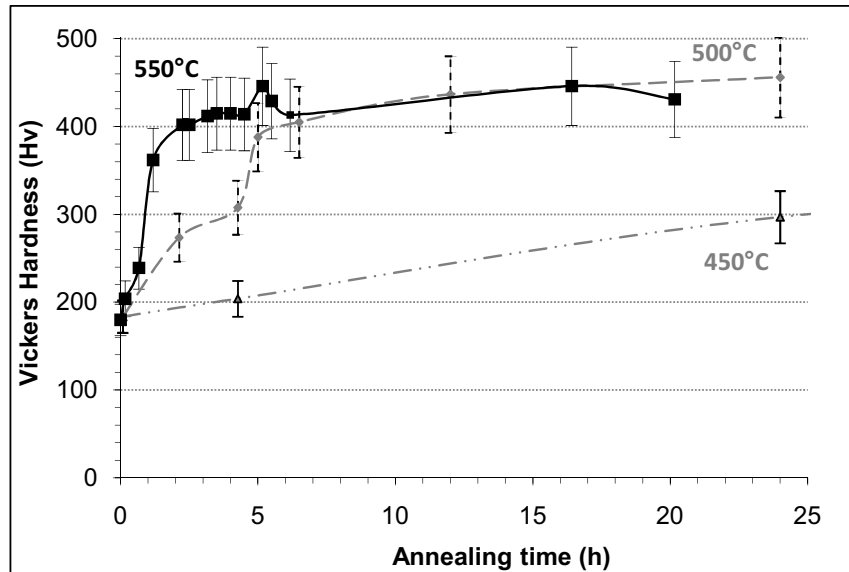


Figure 0-13: Evolution de la dureté Vickers en fonction du temps pour des échantillons vieillis à des températures différentes : 450°C, 500°C et 550°C

Afin de voir le comportement mécanique plus en détail, des essais de traction ont été effectués sur des échantillons pour différents temps de traitement à 550°C.

B. Essais de traction

Les résultats obtenus par essais de traction sont représentés Figure 0-14 ci-dessous. On note que le durcissement obtenu par les précipités est important, puisqu'il atteint 800MPa dans certains cas, quand on compare à l'échantillon en solution solide. L'allongement uniforme est autour de 7% pour la majorité des échantillons, sauf pour les échantillons à 15heures qui ont rompu subitement lors des essais.

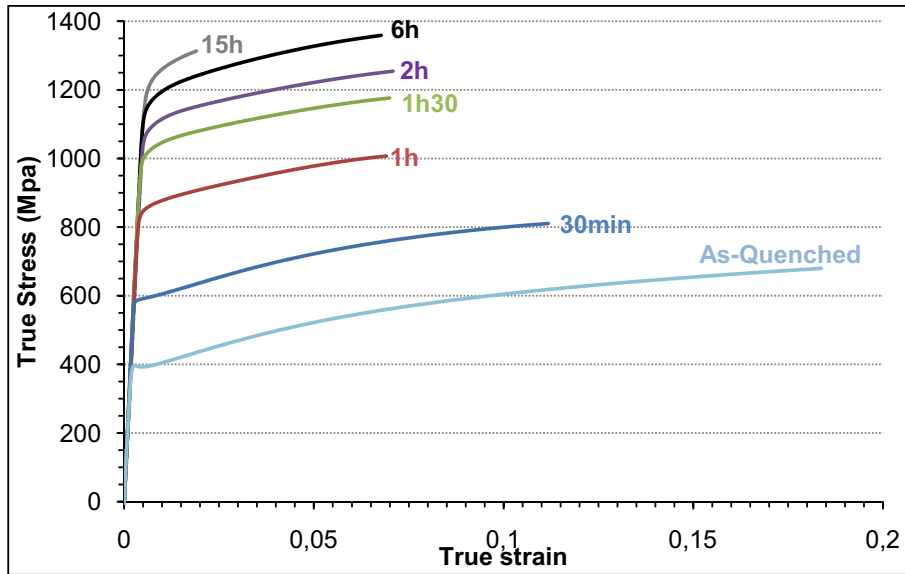


Figure 0-14 : courbes de contraintes vraies en fonction de la déformation vraie obtenues par essais de traction sur des échantillons vieillis préalablement à 550°C pour des temps variables

L'importante augmentation de limite d'élasticité obtenue grâce à l'introduction des précipités nous a amenés à vouloir voir l'effet des précipités sur l'écrouissage, et plus particulièrement sur l'écrouissage cinématique. C'est pour cela des essais Bauschinger ont été effectués.

C. Essais Bauschinger

Les essais de cisaillement inversé ont été faits sur plusieurs échantillons vieillis à 550°C durant 2h, avec des taux de pré-déformation différents. Les courbes obtenues grâce à ces essais sont représentées Figure 0-15. Lorsqu'on inverse le cisaillement, on obtient des courbes de retour telles que sur la Figure 0-16. On remarque sur cette courbe qu'il y a un léger décalage entre la courbe de cisaillement simple et la partie inverse de la courbe de l'essai Bauschinger. Cela est de « l'adoucissement permanent » (« permanent softening »), qui est un phénomène bien connu ([WIL1965], [BRO1977], [EMB1987], [RAU2007]) et qui a été attribué à la non réversibilité du glissement, qui dépend de la structure des dislocations ; on peut également noter sur cette courbe l'importante valeur de la contrainte Bauschinger, σ_B .

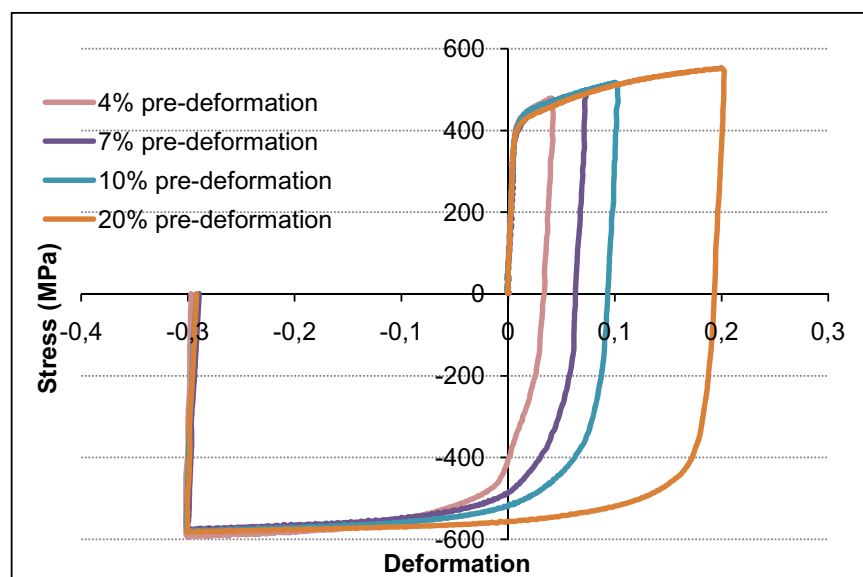


Figure 0-15: Courbes des essais Bauschinger effectués sur des échantillons vieillis à 550°C durant 2heures à des taux de pré-déformation différents

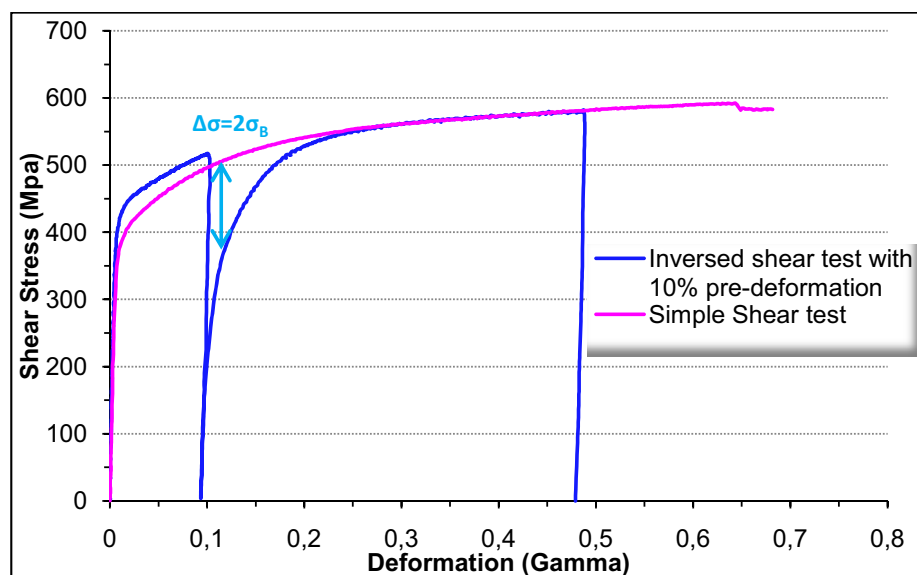


Figure 0-16 : Essai Bauschinger inversé après une pré-déformation de 10% comparé avec l'essai de cisaillement simple sur le même type d'échantillon

Pour conclure sur cette partie, il convient de rappeler qu'à la fois des essais de dureté, de traction ainsi que des essais Bauschinger ont pu être effectués sur des échantillons de l'alliage Fe-Si-Ti. Les résultats ont montré un fort pouvoir durcissant des précipités Fe_2SiTi , ainsi qu'une forte influence de ceux-ci sur l'écrouissage cinématique. Afin d'être capable de prédire et donc prévoir le comportement mécanique de ce type de matériau, il est alors utile de passer par une étape de modélisation, couplant les données microstructurales obtenues sur la précipitation, et les propriétés mécaniques du matériau.

V. Influence de la microstructure sur le comportement mécanique : modélisation

A. Modélisation de la limite d'élasticité

Les observations faites par microscopie électronique en transmission sur échantillons déformés n'ayant pas permis de trancher de manière définitive sur le mécanisme de déformation dans l'alliage, plusieurs modèles ont été envisagés pour la modélisation de la limite d'élasticité, considérant les deux mécanismes de déformation les plus classiques dans les alliages contenant des précipités, à savoir le cisaillement et le contournement des précipités. Les trois modèles classiques sont rappelés ci-dessous :

- Modèle de cisaillement des précipités (si on considère que la statistique de Friedel est applicable) :

$$\sigma = \sigma_0 + 0.7 \frac{k^{3/2} M \mu}{\sqrt{b}} \sqrt{R f_p} \simeq \sigma_0 + K \sqrt{R f_p} \quad (6)$$

avec les paramètres suivants :

- σ_0 étant le durcissement dû à la friction de réseau et à la solution solide (estimée à 400MPa)
 - M le facteur de Taylor, $M=2.77$
 - μ le module de cisaillement de la matrice (80GPa)
 - b le vecteur de Burgers des dislocations
 - k exprimant la force d'obstacle
 - R et f_p étant respectivement le rayon et la fraction volumique des précipités
- Equation d'Orowan, de contournement d'obstacles (espacés de λ_p):

$$\sigma = \sigma_0 + 0.8 \frac{M \mu b}{\lambda_p} \quad (7)$$

- Equation d'Ashby-Orowan:

$$\sigma = \sigma_0 + 0.84 \frac{1.2 M \mu b}{2\pi \lambda_p} \ln \left(\frac{R}{b} \right) \quad (8)$$

De ces trois modèles existants, le modèle d'Ashby-Orowan est le plus apte à décrire la l'évolution de la limite d'élasticité en fonction du temps pour les échantillons vieillis à 550°C. Les résultats de ce modèle sont montrés Figure 0-17 ci-dessous. Celle-ci représente l'évolution de la limite d'élasticité en fonction du temps, mesurée par essais de traction, ainsi que l'évolution de la dureté (multipliée par 3) comparées au modèle d'Ashby-Orowan.

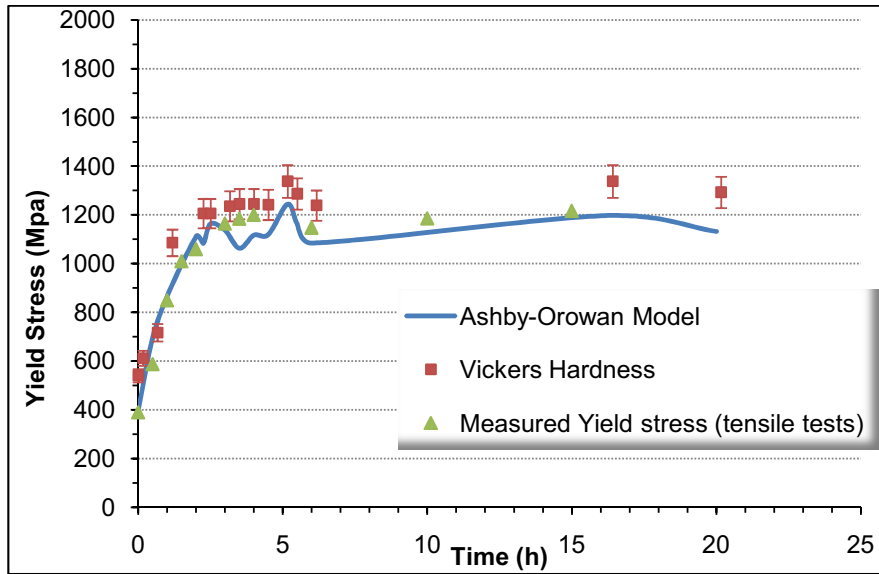


Figure 0-17: Comparaison de la modélisation Ashby-Orowan et des mesures expérimentales de dureté et de limite d'élasticité en fonction du temps sur des échantillons vieillis à 550°C

En regardant l'évolution de la limite d'élasticité, ainsi qu'en considérant les résultats des essais Bauschinger sur cet alliage, il paraît correct de supposer que la déformation se fait par contournement de type Orowan. C'est sur cette hypothèse que réside la modélisation de l'écrouissage.

B. Modélisation de l'écrouissage

Le modèle utilisé pour décrire l'évolution de l'écrouissage en fonction du temps, donc pour décrire la partie plastique des courbes de traction, est un modèle tenant compte de l'influence des précipités sur l'écrouissage cinématique. Il a été développé par A. Aouafi, dans ses travaux de thèse [AOU2009], et est basé sur des modèles développés antérieurement par Estrin et al. ([EST1996], [EST1999]) ainsi que plus récemment par Proudhon et al. [PRO2008]. Les principales équations sont données dans le Tableau 3 ci-dessous, la formule générale de l'évolution de la contrainte d'écoulement s'écrivant comme suit :

$$\sigma = \sigma_0 + (\sigma_f^m + \sigma_p^m)^{1/m} + X_D + X_p \quad (9)$$

où m est un paramètre égal à 1 ou 2 (ici nous avons pris 2, pour tenir compte de la loi puissance de l'écrouissage isotrope)

	Ecrouissage isotrope	Ecrouissage cinématique
Effet des joints de grains	$\sigma = \alpha M \mu b \sqrt{\rho}$	$X_D = n \frac{M \mu b}{d}$

Effet des précipités	$\sigma_p = 0.84 \frac{1.2M\mu b}{2\pi\lambda_p} \ln \left(\frac{d_p}{2b} \right)$	$X_p = \frac{f_p E_p b}{M d_p} n_p$
-----------------------------	---	-------------------------------------

Tableau 3 : équations utilisées pour la modélisation de l'écrouissage tenant compte de l'effet de l'écrouissage cinématique

avec les paramètres suivants :

- α étant une constante numérique introduite dans le terme de durcissement par forêt de dislocations
- ρ la densité de dislocations
- d la taille de grains
- d_p le diamètre des précipités
- E_p le module d'élasticité des précipités
- n étant le nombre de dislocations s'accumulant aux joints de grains par bande de glissement, exprimé ainsi : $n = n_0 \left[1 - \exp \left(-\frac{\lambda}{bn_0} \varepsilon \right) \right]$ où λ est l'espacement moyen entre deux bandes de glissement et n_0 un paramètre tenant compte de la saturation du nombre de dislocations aux joints de grains [BOU2006]
- n_p étant le nombre de dislocations s'accumulant aux précipités exprimé par : $n_p = n_{0p} \left[1 - \exp \left(\frac{-Md_p}{bn_{0p}} \varepsilon \right) \right]$ où n_{0p} tient compte de la saturation du nombre de dislocations due à la relaxation [AOU2009]

Tous les paramètres ont été adaptés des résultats de [AOU2009], étude basée sur les aciers IF, sauf pour E_p et n_{0p} qui ont été déterminés afin de correspondre aux données expérimentales. La valeur de σ_0 a été déterminée à partir de la courbe de l'échantillon en solution solide, c'est-à-dire évaluée à 400MPa, mais afin de tenir compte de la diminution des éléments en solution solide lors de l'apparition des précipités ; σ_0 a été modifiée à 300MPa pour les autres temps de traitement thermique. Les résultats obtenus sont donnés Figure 0-18 ci-dessous, où on voit que le modèle décrit de façon satisfaisante les données expérimentales. Le seul échantillon pour lequel le modèle n'arrive pas bien à décrire le comportement est celui qui a été traité à 550°C durant 30minutes, où sans doute la solution solide est encore importante et influe donc plus sur l'écrouissage que ne le considère le modèle.

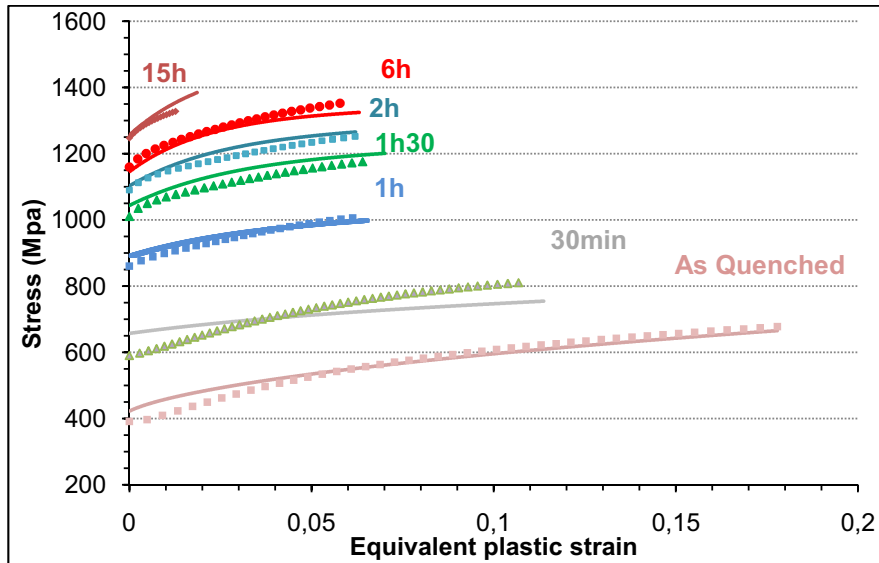


Figure 0-18: Comparaison entre résultats expérimentaux et de la modélisation de la partie plastique des courbes de tractions pour des échantillons traités à 550°C pour différents temps

Une autre façon de vérifier les paramètres utilisés est la confrontation entre les résultats expérimentaux de mesures des contraintes internes dans le matériau et la modélisation. En effet, les essais Bauschinger ont permis d'obtenir une valeur de la contrainte interne qui correspond aux composantes cinématiques de l'écrouissage, à savoir X_D et X_p . Les résultats sont donnés Figure 0-19 ci-dessous, et l'on peut constater que l'effet des joints de grains sur l'écrouissage cinématique est négligeable comparé à l'effet des précipités (faible valeur de X_D). On remarque également que la contrainte interne est sous-estimée pour des petites pré-déformations. Ceci a été noté dans un certain nombre d'études auparavant ([FRI2009], [AOU2009], [BOU2010]), où les auteurs attribuent ce phénomène à une irréversibilité du glissement due à la présence de boucles de dislocations (cf. chapitre V).

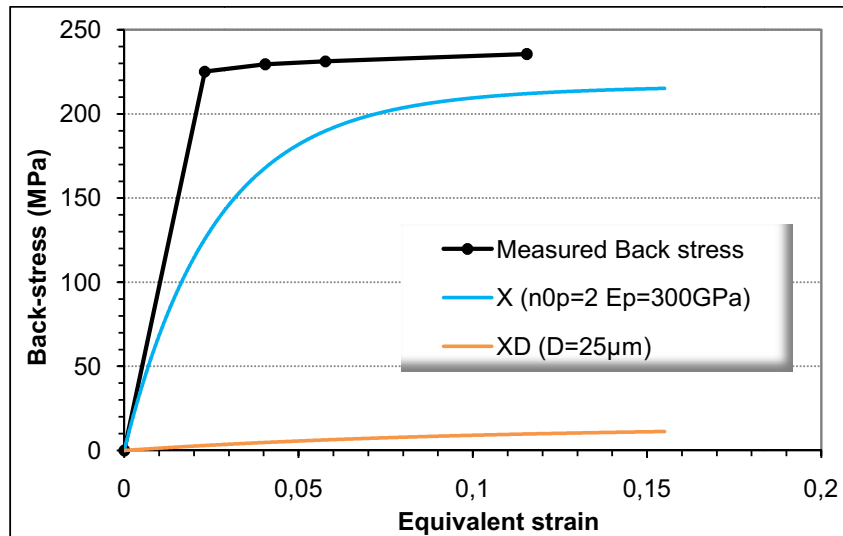


Figure 0-19: modélisation de la contrainte interne dans le matériau, à partir des composantes cinématiques de l'écrouissage

Pour conclure sur cette dernière partie, nous pouvons dire que la limite d'élasticité et l'écrouissage sont relativement bien décrits par des modèles existants, qui considèrent que le mécanisme de déformation se fait par contournement d'Orowan des précipités. Aucune preuve expérimentale n'étant disponible pour infirmer cette hypothèse, c'est celle-ci qui a été retenue.

VI. Conclusion générale

A. Conclusion

Dans ces travaux de thèse portant sur les relations entre la microstructure et les propriétés mécaniques d'un acier, le Fer-Silicium-titane, deux aspects ont été abordés. Tout d'abord concernant l'étude de la précipitation, des expériences intéressantes de diffusion de neutrons aux petits angles (SANS) ont permis d'avoir des données quantitatives sur les précipités, à savoir l'évolution de leur taille et de leur fraction volumique en fonction du temps. Les expériences SANS couplées à des mesures par sonde atomique (APT) et MET, ont permis d'avoir une analyse très détaillée de la précipitation pour les échantillons vieillis à 550°C. Les études antérieures sur le Fe-Si-Ti avaient démontré que, pour des traitements thermiques à des températures inférieures à 800°C, la phase présente était la phase métastable, dite d'Heusler, Fe_2SiTi . Cela a pu être confirmé expérimentalement à des temps allant jusqu'à 20 heures à 550°C. Les données quantitatives ont permis de paramétrer des modèles de cinétique de précipitation basés sur la théorie classique de germination-croissance-coalescence. Deux modèles ont alors été comparés : le modèle « DBPréci » et le modèle par classes basés sur l'algorithme « Multiprési ». Ces deux modèles ont montré une bonne capacité à décrire les cinétiques de précipitation dans l'alliage Fe-Si-Ti, ce qui ouvre des perspectives de prédiction des cinétiques dans une volonté d'optimisation de la microstructure.

Dans un deuxième temps, cette étude portait sur les propriétés mécaniques du matériau. Pour ce faire, des essais de dureté, de traction, mais aussi des essais Bauschinger ont pu être effectués sur cet alliage. Ceux-ci ont permis de mettre en évidence une très forte contrainte interne dans le matériau essentiellement induite par les précipités. Un modèle d'écrouissage tenant compte de l'écrouissage cinématique dû aux précipités a alors été utilisé, paramétré sur les données expérimentales, montrant un très bon accord avec celles-ci. La limite d'élasticité a, elle, pu être décrite par une loi d'Ashby-Orowan classique, laissant présumer que les précipités sont contournés lors de la déformation, malgré leur petite taille.

B. Perspectives

Précipitation

L'étude de la précipitation durant ces travaux ayant essentiellement porté sur la phase métastable Fe_2SiTi à des températures comprises entre 450°C et 580°C, et pour des temps relativement courts (allant jusqu'à 20 heures à 550°C), il semblerait intéressant d'étudier la transition à des temps plus longs de la phase métastable à la phase stable. Pour cela des expériences in-situ de SANS ou de SAXS pourraient être envisagées.

Écrouissage

La modélisation de l'écrouissage a permis de décrire très convenablement les courbes de traction, mais elle a également montré une certaine faiblesse dans la description de la contrainte interne dans les premiers stades de pré-déformation. Une amélioration tenant compte de l'irréversibilité du glissement dans le sens inverse de la déformation pourrait sans doute améliorer la description du modèle.

Mécanisme de rupture

Dans cette étude, des observations de faciès de rupture ont montré que le mécanisme de rupture n'est pas seulement influencé par l'état de précipitation dans l'alliage, mais semble également présenter un aspect aléatoire, n'en permettant pas la prédiction. La présence d'inclusions dans les lingots de coulées, de type TiC ou TiN, est sans doute en partie responsable de certaines ruptures par clivage observées. Mais certaines études antérieures concernant l'alliage binaire Fe-Si ont également démontré une forte fragilisation par la présence de Silicium, puisque celui-ci favorise le glissement planaire en augmentant l'énergie de défaut d'empilement. Une étude précise et rigoureuse de la rupture dans l'alliage Fe-Si-Ti serait donc nécessaire pour comprendre l'influence de ces différents paramètres sur celle-ci.

Compréhension générale

L'alliage Fe-Si-Ti, dans les compositions étudiées ici, présente une matrice ferritique ne comportant pas de changement de phase dans le domaine du solide, dû au caractère alpha-gène des deux éléments d'alliage. Les grains présents sont de tailles relativement importantes et n'induisent aucun durcissement. Cela pourrait être sans doute amélioré en permettant un changement de phase de la matrice, comme c'est le cas pour les aciers maraging, par exemple, où la précipitation se fait dans le domaine martensitique. Dans un contexte d'alloy-design, on pourrait donc envisager l'addition d'un élément γ -gène qui n'interfère pas sur le Titane et le Silicium de façon trop importante.

General Context

The present work is the result of a collaboration between the R&D Auto Research Center (part of ArcelorMittal) in Maizières-Les-Metz, and the SIMAP Laboratory in Grenoble. The leadership of ArcelorMittal in the Steel Industry is well-known and its products have main applications in the automotive, construction, household appliances and packaging fields. The SIMAP laboratory (Sciences et Ingénierie des Matériaux et Procédés) is composed of researchers working in different fields of physical metallurgy, mechanics of materials, or chemical properties of materials.

The numerous requirements in terms of energy and weight savings, which are the main threads of the industrial world nowadays, demand more and more innovative solutions from the steel industries. We can quote for instance the prohibition of some alloying elements in steels for automotive applications such as Lead, Cadmium, Chromium VI and Mercury to enable their full recyclability. Another important step was the definition of the Life Cycle Analysis leading to the will of ArcelorMittal to reach the target figure of 85% materials recycling in a vehicle by 2015. In the context of global warming prevention, the European Union has decided to reduce the emission of greenhouse gases, such as CO₂, which can be achieved in part by reducing the weight of cars. The ways to limit this weight while keeping steels in the composition of the cars' structure are not numerous: either the thickness of steel sheets must be reduced or lighter alloying elements must be integrated. Since the final mechanical properties of these materials must not be degraded due to the weight reduction and costs cannot be increased drastically, new steel solutions have to be developed.

In this context, the Fe-Si-Ti alloy investigated in this study presents some advantages. It enables a decrease in weight on the order of three to five percent thanks to the addition of Silicon and Titanium, for a relatively reasonable increase in cost of 200€ to 300€ per ton (compared to a classical Interstitial Free Steel (IF)). In this context, it has become of interest for car makers to check whether the mechanical properties of this alloy comply to the required standards. From their perspective, mechanical properties of a material are important for two main reasons: they affect the formability and they are responsible for the component's behavior in service conditions. Thus, the global aim of the present work is the study of the relation between microstructure and mechanical properties.

The first objective of the present work is to analyze the global context of the study, namely the automotive steel industry, in order to understand the interests and requirements of the car makers in terms of mechanical properties. The second objective is to quantify the mechanical properties of the alloy in terms of yield stress and elongation capacities, which are the most relevant features of steels in automotive field of application. This implies the characterization of the precipitate microstructure, which mainly controls these mechanical properties. The last objective is to quantify the strain hardening evolution, for which specific requirements exist in terms of formability and chock absorption capability.

Chapter I : Introduction to Materials for automotive applications

In this chapter, we will present the different metallic alloys existing in the automotive industry and responding to the safety and cost requirements, namely light alloys in general and in particular age-hardened alloys. In this context, the case of the Fe-Si-Ti alloy will be developed, and its main interesting features will be presented. The last part of this chapter will present the global structure of the manuscript.

INTRODUCTION 37

I. STATE OF THE ART ON AUTOMOTIVE STEEL SOLUTIONS 37

A. Light weight materials 37

B. Steels for automotive applications 38

1) General presentation 38

2) Weight saving high strength steels 40

C. Age-hardened Iron-based systems41

II. STRUCTURE OF THE MANUSCRIPT 43

Introduction

As for the aerospace industry, the main requirements influencing the choice of materials are primarily governed by the passenger safety, especially in case of a crash. It also calls for significant weight savings in the current economic and ecological context. While the aerospace industry deals with the airlines, which are able to endorse important investigation costs, the automotive industry is designed for private customers, which means that costs have to remain within a reasonable range. Therefore the main challenge for new materials developments for automotive applications is to find the best compromise between service properties, weight and costs.

In the following part various recently elaborated solutions used in the automotive industry will be presented, which make use of steels. Then a description of the specific example of High Strength Steels will be provided. In a second part the interests of Precipitation-hardened alloys will be analyzed with the case of the Fe-Si-Ti alloy. The last part will describe the structure of the manuscript.

I. State of the art on automotive steel solutions

A. Light weight materials

Today, weight saving is a challenging objective in very diverse industries, such as sportive equipment, aerospace industry, structural design, automotive industry and much more. Each field has its reasons for aiming to this need. While the sportsman will have the ambition to surpass his own performances, the aerospace industry will have the aim to fly longer and further using the same energy input, the architect will be able to create even more innovative shapes and the automotive industry will be able to improve the comfort of the passengers while reducing the car's body weight and decreasing CO₂ emissions. All these fields have in common the need to rely completely on materials that are essentially designed for the sake of safety. In the last decades, new materials have been developed with this objective, such as for instance composite materials with polymer matrix and fiber reinforcement in aerospace, but still, metallic materials often offer the best compromise between high mechanical characteristics and cost.

The most common light metallic materials are presented in Table I-1, extracted from the list of light-materials for structural applications proposed by Ashby et al. [ASH1986]. Table I-1 compares the characteristics of Aluminum, Magnesium and Titanium alloys, with steels. The former three alloys are also potential candidates for automotive applications, but since Magnesium and Titanium alloys are still expensive, the only reasonable candidates are Aluminum alloys and steels. Table I-1 shows that steels have the highest yield stress and Young's modulus. Their properties remain, although steel's density is much more important than for other alloys, one of the main attractive arguments in the choice of steels.

Alloy	Density ρ (Mg m ⁻³)	Young's Modulus E (GPa)	Yield Strength σ_y (MPa)	E/ ρ	E ^{1/2} / ρ	E ^{1/3} / ρ	σ_y / ρ	Creep Temperature (°C)
Al alloys	2.7	71	25-600	26	2.1	1.5	9-220	150-250
Mg alloys	1.7	45	70-270	25	4.0	2.1	41-160	150-250
Ti alloys	4.5	120	170-1280	27	2.4	1.1	38-280	400-600
Steels	7.9	210	220-1600	27	1.8	0.75	28-200	400-600

Table I-1: Mechanical properties of structural light alloys [ASH1986]

One can also mention the use of more and more polymers and composite materials for a large number of components, even in automotive applications. However, they rarely concern safety equipments. In fact, a large number of alternative solutions to steels are proposed, and in the last decade some parts of a vehicle, which used to be made of steel, have been replaced by other materials, such as aluminum alloys or plastics or even glass. However, most parts that deal with the safety of passengers or pedestrians are still made of steel due to their high mechanical properties and competing cost.

B. Steels for automotive applications

1) General presentation

Generally speaking the framework of a car is made of a chassis, which corresponds to the base of the vehicle, on which the body of the car is attached. This body consists of the engine and passenger compartment as well as the trunk. 55wt.% of the completely assembled car is made of steel, namely up to 40 types of steels. The chassis and the body can be made of one single piece or of two pieces bolted together, and are essentially composed of steels as shown Figure I-1. The parts in dark blue (see arrows) are the crash-critical areas [SAE2010]. Thus, depending on the part of the vehicle, the steel will have to satisfy different characteristics.

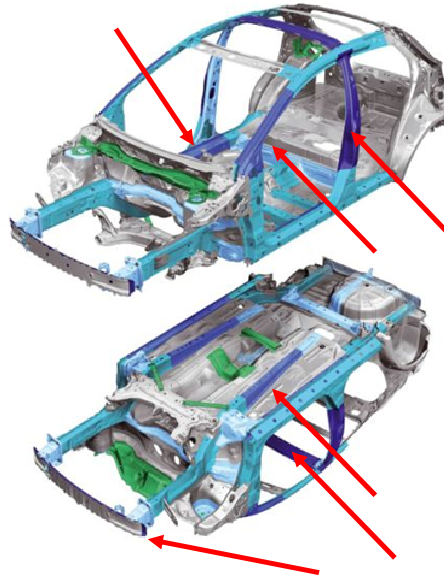


Figure I-1: Example of the body in white of a car made of steel (source [SAE2010])

The main features expected from the different types of steels are as follows:

- Energy absorption. This is one of the most important characteristics in case of a crash. Elements such as the front bumper need to have a strong energy absorption capability. The concept underlying the design of such a material is its ability to increase its strength during the impact, in other words its capability of having an important strain-hardening.
- Stiffness. It is related to the Young's modulus of the material; steels with high stiffness can support very high stresses with very little deformation. Thus, these materials are used for parts such as the center pillar, which are designed to protect the passenger compartment.
- Static or Fatigue Strengths. They define the capability of a material to undergo either unique or cyclic loading. These properties are important to consider in long time durability.
- Resistance to exceptional loads.
- Corrosion resistance. It is essential in order to preserve the lifetime of a material, since corrosion can be destructive. Materials of a vehicle will be confronted to different environments such as rain, cold, heat, marine air, which can be very corrosive. Today, the main method to protect automotive materials of corrosion is the use of Zinc coatings.
- Temperature resistance.
- Dent and Blistering resistance.
- Sound and Vibration dampening.

Another argument in favor of one or another material is also the question of esthetics. This is more and more a key issue in a saturated market in which fashion plays a major role. Parts which are visible to the customer need to have a perfect surface and receptivity to coatings.

Two types of steels are used in the automotive industry:

- Conventional steels: with Yield Stress less than 500 MPa. Most of them are multiphase using the strength of martensite, bainite, etc, to improve their mechanical properties
- High Strength Steels (HSS) and Ultra High Strength Steels (UHSS) with Yield Stress over 800 MPa. In order to improve their mechanical properties, more a Carbon is currently added. However, the Carbon has the drawback to induce weldability problems, weaknesses in process robustness, etc. Therefore, the development of “carbon-free” steels, meaning “steels with almost no Carbon”, can be of great interest.

Regarding the former requirements and characteristics of steels, the development of new alloys seems necessary.

2) Weight saving high strength steels

In the automotive industry the use of high strength steels (HSS) is increasing, since they enable to reduce the quantity of material while keeping the same mechanical strength for the component, inducing a reduction in weight. These HSS steels also enable to increase the safety potential since their mechanical properties are far beyond the ones of conventional steels. The graph of Figure I-2 shows two key-mechanical properties of the different solutions existing today in the automotive industry, namely the elongation capacity as a function of the tensile strength. One can see that the conventional steels (blue on Figure I-2) have Tensile strength ranging approximately from 200 to 600MPa while the HSS range from 500 to 1500MPa. The well-known “banana” formed by these properties of steels is observed. It illustrates the commonly accepted inverse correlation between Elongation and Tensile Strength: if one of these properties increases, the second decreases, and vice-versa. Objectives in the development of materials for automotive applications would be to reach the region called “Current area of Research” in Figure I-2. This region corresponds to a compromise between Ultra high strength austenitic based steels and HSS.

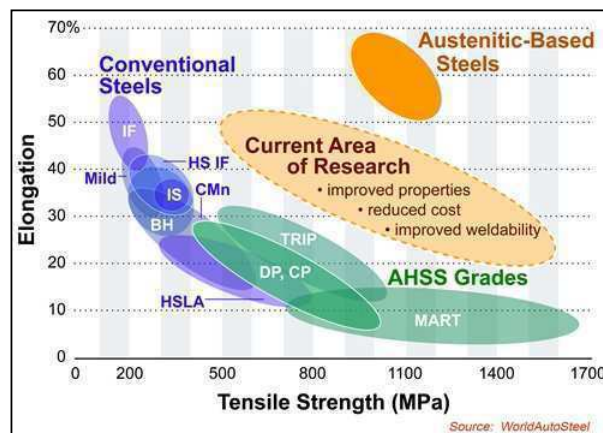


Figure I-2: state of the art of automotive steels (source Worldautosteel [WOR2010])

Among the materials having mechanical properties that meet the requirements, the following analysis can be made (Figure I-3). For very high strength a feasible solution could

be the use of Maraging steels (e.g. Maraging steels with 17wt%Ni) that are composed of Nickel, which is an expensive alloying element.

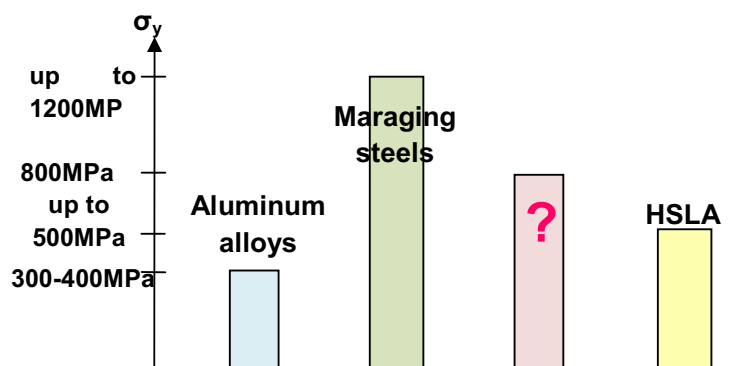


Figure I-3: simplified scheme of the state of the art for materials used in automotive applications today

To sum up, in the general context of research in innovative Steel solutions, the challenge is to combine important yield stress and reasonable elongation, with low cost and low carbon content. In this objective the age-hardened materials present interesting features since they combine the use of other alloying elements than Carbon, with various and interesting mechanical properties.

C. Age-hardened Iron-based systems

In aluminum alloys, for example, the use of precipitation to enhance mechanical properties is very common. This is less the case for Iron-based alloys or steels which can reach very high mechanical properties by creating a multiphase microstructure. However still a certain number of precipitation-hardened steels are known today and are subject of studies. The best known age-hardening phase in steels is the carbide Fe_3C , also called cementite, formed in binary Fe-C alloys. Some other well-known binary systems are able to generate a fine particulate microstructure such as Iron-Copper (Fe-Cu) alloys, which have the particularity to contain pure Copper particles (e.g. [GOU2004], [PER2004]). Another well-known alloy is the Maraging steel, consisting of the precipitation of particles in a martensitic matrix [NIOC1971], conferring very high mechanical properties, as mentioned above. A certain number of ternary alloys such as Fe-Nb-C ([PER2004]), Fe-C-Ni or even quaternary alloys such as Fe-Ni-Cr-Ti, Fe-Ni-Al-Ti, Fe-Cr-Ni-Al [PIN1982a and b] have been proven to contain strengthening particles.

In a study by Hobbs et al. [HOB1968] the comparison between the hardness increments of certain precipitation-hardened alloys can be found. One can see on Figure I-4, 5, and 6 the curves of the Vickers hardness evolution as a function of time for three alloys: Fe-Cu-Al, Fe-W-Co and Fe-Cr-Si. All hardness values range from 150 to 350Hv for temperatures comprised between 400°C and 750°C. If one compares these values to the hardness tests done by Henon et al. in [HEN1966] on an Fe-Si-Ti alloy (Figure I-7), where the hardness values range from 200 to 600Hv for temperatures comprised between 500°C and 800°C, the very interesting hardening capacity of the Fe-Si-Ti alloys becomes obvious.

The presence of Silicon and Titanium in the alloy, which are both α -stabilizers, leads to a matrix which stays ferritic for any temperature in the solid state. This can be seen as drawback since the range of different matrix microstructures is limited (25 μ m ferritic grains). However, it is also an advantage when studying the precipitation evolution, since the precipitate microstructure is then the only variable likely to change the microstructure. Furthermore, the precipitates formed in the first stages of precipitation at low temperatures are spherical, which is an advantage in terms of modeling.

Now that the general expectations in steel research have been presented, one can understand the study's main objectives, which is the relation between microstructure and mechanical properties in Fe-Si-Ti alloys. Since the matrix is ferritic the number of microstructural parameters permitting to change mechanical properties of this alloy is reduced to the radius and volume fraction of precipitates. The aim would be to find a satisfying compromise between this precipitate microstructure and the obtained mechanical properties by varying the radius and volume fraction. This is not the only challenge of the research concerning the development of new materials, since the ideal objective would be the ability to predict the mechanical properties of a material, in the purpose of "alloy design". Meaning for a given alloy composition to find the optimal heat treatment for the best mechanical properties.

In summary, the advantages of the Fe-Si-Ti are the low-carbon content, the high hardening capacity of the spherical precipitates and the ferritic matrix.

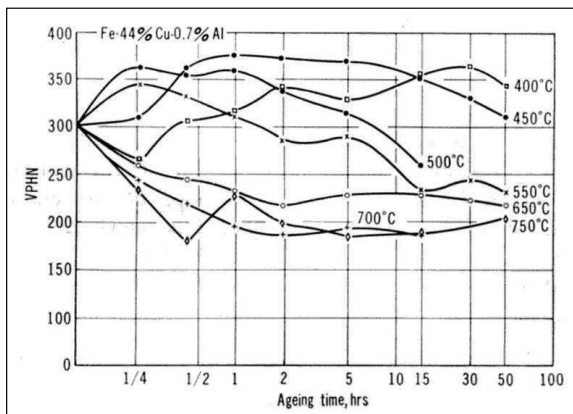


Figure I-4: hardness evolution of Fe-4.4%Cu-0.7%Al alloy [HOB1968]

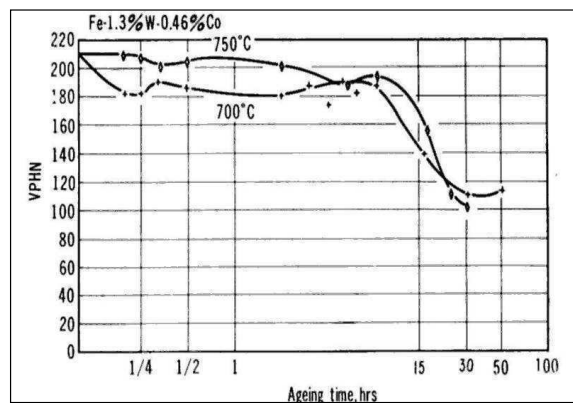


Figure I-5: hardness evolution of Fe-1.3%W-0.46%Co alloy [HOB1968]

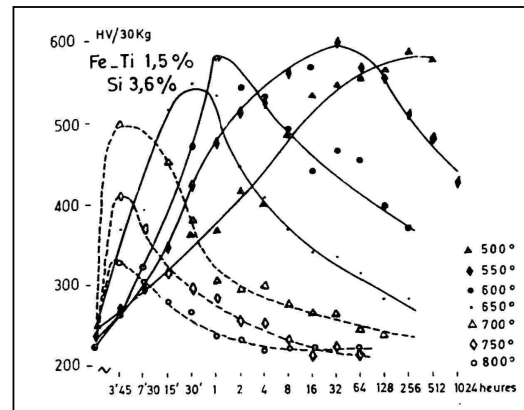
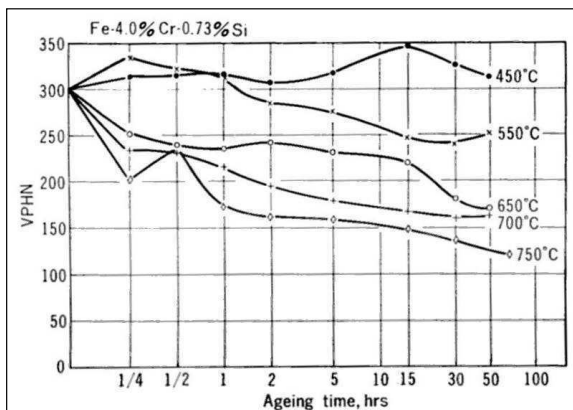


Figure I-6: hardness evolution of Fe-4%Cr-0.73%Si alloy [HOB1968]

Figure I-7: Hardness evolution with time of Fe-3.6%Si-1.5%Ti alloy [HEN1966]

II. Structure of the manuscript

In the former chapter we have presented the global context of research in steels for automotive applications. The remaining part of the manuscript is composed of four chapters, which will be the presentation of the material and experimental methods, followed by the study of the yield stress evolution of the Fe-Si-Ti alloys as well as some modeling attempts, since in the context of the study the knowledge of the strength evolution is essential. The particularity of the present alloy is the formation of precipitated particles which will control the mechanical properties' evolution. Thus, we will present the microstructural analysis of the alloy and try to understand how these influence the mechanical properties. The industrial context involves the study of the feasibility of certain industrial processes such as formability. An analysis of work hardening behavior which contributes to this formability issue will be given in the last chapter. The conclusions will provide a first glance into fracture modes as an introduction to further studies required.

Chapter II : Material and experimental Techniques

In this Chapter, we will describe the material used during the study, the heating route which it has followed, as well as its main characteristics such as texture and XRD measurements. In a second part, we will list the experimental techniques used and their relevant characteristics.

I. MATERIAL.....	47
A. Pre-deformation conditions	47
B. Ageing treatments.....	49
1) Technical devices	49
2) Metallurgical route	50
C. Texture.....	53
II. EXPERIMENTAL TECHNIQUES.....	55
A. Mechanical properties	55
1) Vickers hardness	55
2) Tensile tests	55
3) Bauschinger tests	57
B. Precipitation characterization	58
1) Microstructure observation at an “average” level: Small Angle Neutron Scattering (SANS)	58
i. Conditions for experiments on Fe-Si-Ti system	58
ii. General description	58
iii. Extraction of Radius values	64
iv. Extraction of Volume fraction values	65
2) Local microstructure observation: Microscopy	67
i. Optical microscope	67
ii. Scanning Electron Microscope with Field Emission Gun (SEM-FEG)	67
iii. Transmission Electron Microscopy: TEM	67
iv. Sample Preparation.....	67
3) Microstructure at atom scale: APT	69
i. Principle.....	69
ii. Analysis.....	70

I. Material

During the study of the Fe-Si-Ti alloy, ingots of different composition were cast at ArcelorMittal Research S.A. laboratory. Essentially one was found out to be particularly of interest and it was therefore investigated more thoroughly: Fe-2.5wt%Si-1wt%Ti. In fact, this alloy composition corresponds to the minimum content of Titanium and Silicon enabling to obtain precipitation for reasonable ageing times and low temperatures (under 600°C). Two castings of this composition were molten in 2006 and 2007, for which the chemical analyses are slightly different in Titanium content, as shown Table II-1 and 2.

Element	Si	Ti	C	S	P	B
Amount (wt%)	2.54	1.05	0.0055	0.003	0.003	0.0023

Table II-1: Chemical analysis of casting performed in 2006

Element	Si	Ti	C	S	Mn	P	B	N
Amount (wt%)	2.57	1.17	0.0072	0.0008	0.005	0.003	<0.001	0.0004

Table II-2: Chemical analysis of casting performed in 2007

The presence of a very small quantity of carbon can be observed. It was noticed that this little amount was sufficient to trigger the formation of titanium carbides (TiC) which are detrimental to mechanical properties.

In the present study, the two castings were used. In a first time the casting dating from 2006 (Table II-1) was used for all preliminary experiments. Since the alloy was shown to have interesting properties, a new one was casted (Table II-2) with a very similar composition but not exactly the same. Since a difference in kinetics was observed between the two castings, only the second was used for all experimental results such as SANS, APT, and mechanical testings. However, it is important to notice that the Bauschinger tests were performed before the second casting was done, and thus a difference can be observed between the equivalent elastic stress of the shearing test and the elastic stress of the tensile test performed afterwards. This is due to the difference in composition of the alloys. Thus, the Backstress measured is probably different as well from one casting to the other, but the order of magnitude stays correct. To be very accurate one would need to perform Bauschinger tests on the second casting as well.

The final microstructural state is obtained after hot rolling and cold rolling with end thickness around 0.9mm. The process to obtain the final microstructure is detailed below.

A. Pre-deformation conditions

The 15kg ingots were cut into pieces (see Figure II-1) and hot rolled using specific conditions (Figure II-2). As shown Figure II-2, the temperature at which hot rolling starts is around 1230°C and the fifth and last pass is carried out at 980°C followed by water quench.

These conditions have been chosen to favor recrystallization, namely by minimizing the time between each pass.

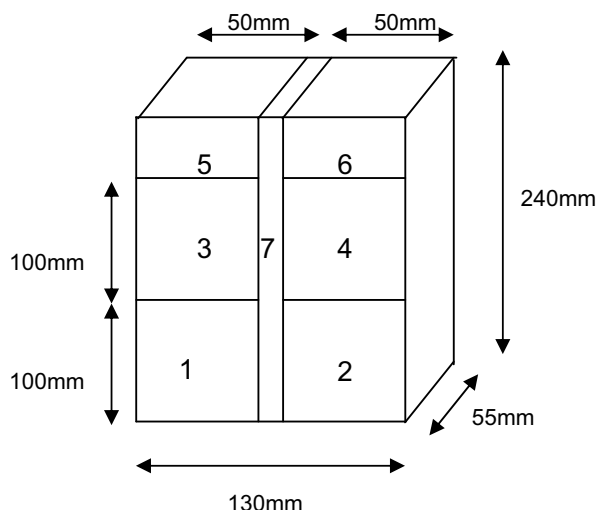


Figure II-1: Cutting method of the ingots

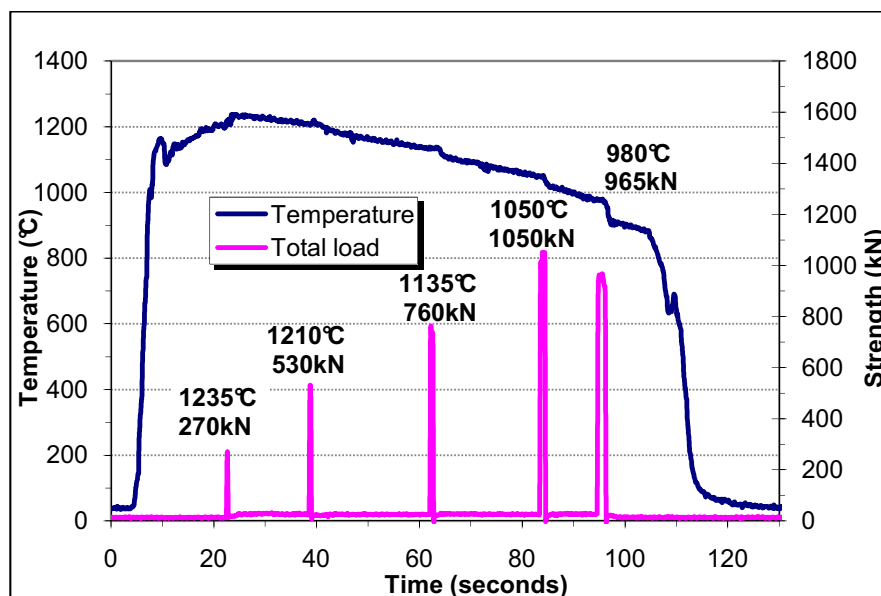


Figure II-2: schematic of hot rolling conditions for Fe-2.54wt%Si-1.05wt%Ti (June 2007) showing the evolution of temperature of the ingot with time and the strength exerted on the rolling cylinders at the successive passes

After hot rolling, bars are honed in order to suppress the oxide layer and calamine. Irregular borders are cut off and cold rolling is performed to reach a final thickness around 1mm. An example of cold rolling conditions is shown Table II-3, giving the different loads exerted on each cylinder corresponding to the different passes. It has been shown that the higher the load of the first pass, the smaller are the final grains (due to higher strain hardening induced). The schedule of cold rolling was determined with that goal in mind.

Initial thickness (mm)	Tensile stress (daN)	Passes	Weight on cylinder 1 (tons)	Weight on cylinder 2 (tons)	Final thickness	ΔE (thickness reduction)
3.12	550/500	1	44.9	47.9	2.47	0.65
		2	50.0	53.5	1.92	0.55
		3	50.2	54.3	1.49	0.43
		4	50.2	52.9	1.05	0.44
0.895		5	39.9	41.7	0.82	0.23

Table II-3: cold rolling conditions

After the forming processes the samples undergo heating treatments to obtain the desired microstructure, meaning a fine and abundant precipitation.

B. Ageing treatments

1) Technical devices

For preliminary studies small bars of 10*4*1mm were heat-treated in a plasto-dilatometer Bähr followed by microscopic observations and/or hardness tests. Once these preliminary hardness tests revealed interesting and outstanding hardness values, further investigation was carried out, such as TEM or mechanical tests on larger samples (~100x80mm), such as tensile tests. For these, annealing treatments were performed using three types of heating systems: a halogen lamp furnace (AET), a tube furnace (Nabertherm) or salt bathes of different temperature ranges. Samples were cooled by direct water quench except for the halogen furnace where a helium quench system was more appropriate.

Hardness of samples was systematically tested on samples before any further experimentation in order to check reproducibility of the heating treatments and the homogeneity within a metal sheet. In fact, since for different experiments the heating devices were not systematically the same (salt bath, halogen or tube furnace), the reproducibility needed to be checked. These tests revealed that both tube furnace and salt bathes were very reproducible devices since hardness curves overlapped reasonably well from one experiment to the other. But heating treatments performed using the Halogen lamp furnace had quite different outcomes from one experiment to the other. This observation can be explained by the surface of homogeneity which is different from one technical device to another. In fact, as shown in Figure II-3 and 4, for both devices of the tube furnace and the salt bathes, volumes with homogeneous temperature are larger than the sample. Samples used in the tube furnace for SANS experiments were of 10x10x1mm for a homogeneous zone of over 80cm and a radius of 10cm. This size covers largely the samples, as for the

ones heat treated in salt bathes for tensile tests, of 100x80x1mm. This was not the case of the halogen lamp furnace, where the surface of homogeneous temperature is smaller than the width of the sheets as shown in Figure II-5. Thus, the tensile test bars were cut at the border of the homogeneous temperature zone, which could possibly explain the difference observed depending on the heating device used.

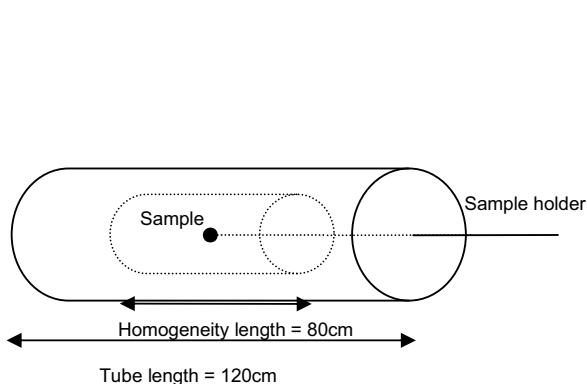


Figure II-3: schematic of the tube furnace device

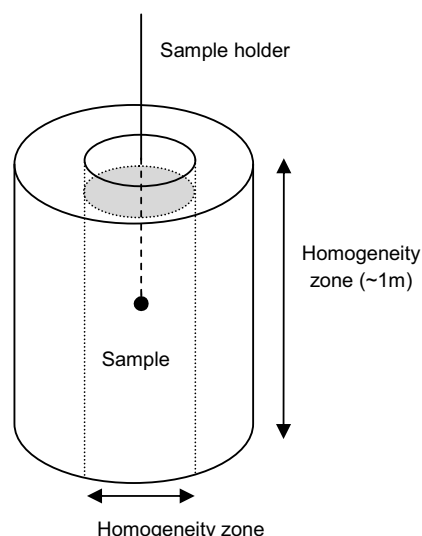


Figure II-4: schematic of the salt bath device

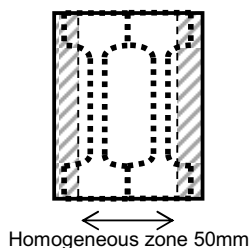


Figure II-5: Schematic of a sheet heat-treated in AET halogen furnace showing the small homogeneity zone

2) Metallurgical route

Ageing treatments were performed for SANS experiments and tensile tests. Electron microscopy (TEM) and Atom Probe (APT) observations were done on the same samples as the ones used for SANS. All the heating cycles were of same type, namely a first step for recrystallization and solutionizing at 900°C for five minutes, followed by precipitation ageing at temperatures ranging from 450 to 700°C for various times (see figure 6, 7 and 8 below). These annealing treatments were performed on both types of samples of 100x80x1mm and 10x4x1mm. But in order to study the influence of the initial state on the precipitation kinetics, we compared three different initial conditions.

- The complete heating treatment in salt bathes using two salt bathes at different temperatures and passing the sample from one bath to the other:

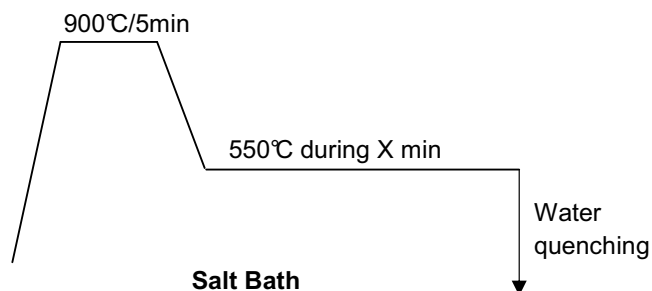


Figure II-6: Schematic of heating route when passing the sample from a salt bath to the other

- As quenched samples: solution treated at 900°C during five minutes in order to dissolve and recrystallize the matrix in salt bath followed by water quenching. These samples were then precipitation treated in the tube furnace for the desired time:

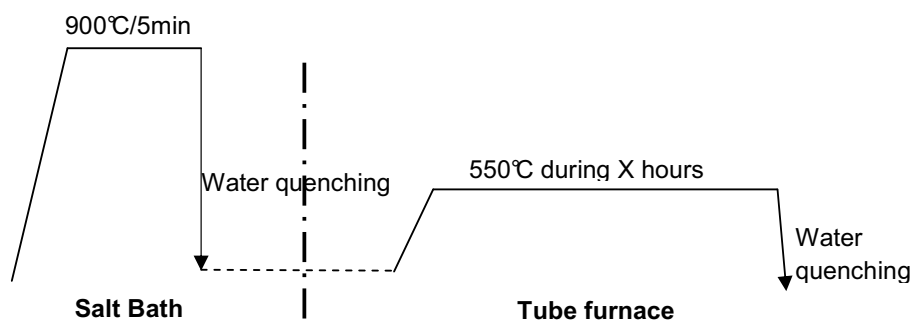


Figure II-7: Heating route with sample passing through room temperature before the precipitation treatment

- Samples in solid solution followed by a pre-precipitation treatment at various temperatures (ranging from 450 to 650°C) in salt bathes in order to “pre-precipitate” the samples, followed by water quenching. The complete precipitation treatment is then achieved in the tube furnace for the desired time.

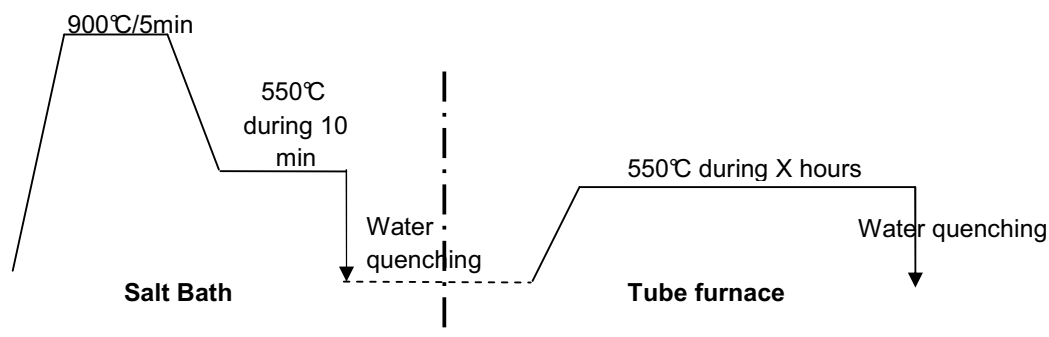


Figure II-8: Heating treatment with pre-precipitation treatment

The purpose of the recrystallization treatment is to obtain the same granular microstructure for all samples, meaning a 100 percent ferritic matrix of grains around 25 μ m. No α/γ phase transformation in the matrix is known to happen in these alloys in the solid state since Titanium and Silicon are two α -stabilizers elements. Thus, before precipitation heating treatments, samples are always in the same state, namely recrystallized and with all elements in solid solution. Therefore, in this manuscript, the samples will be denominated with a shortcut indicating only their precipitation treatment (such as 550 $^{\circ}$ C during 2 hours).

The heating and cooling rates to pass from room temperature to 900 $^{\circ}$ C and from 900 $^{\circ}$ C to 550 $^{\circ}$ C were measured experimentally. The curves are given in Figure II-9 for the salt bath device in the sample heated at 900 $^{\circ}$ C during five minutes and aged at 550 $^{\circ}$ C during 30 minutes.

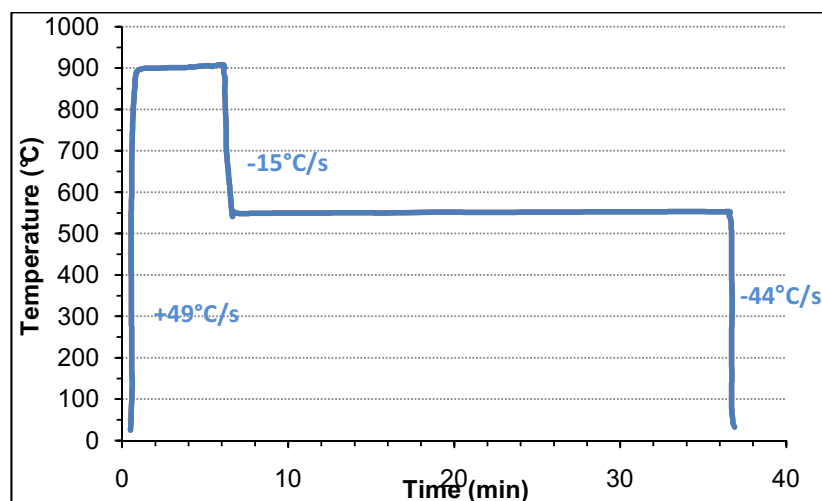


Figure II-9: schematics of a heating treatment with salt bath passing from salt bath at 900 $^{\circ}$ C to one at 550 $^{\circ}$ C with corresponding heating and cooling rates.

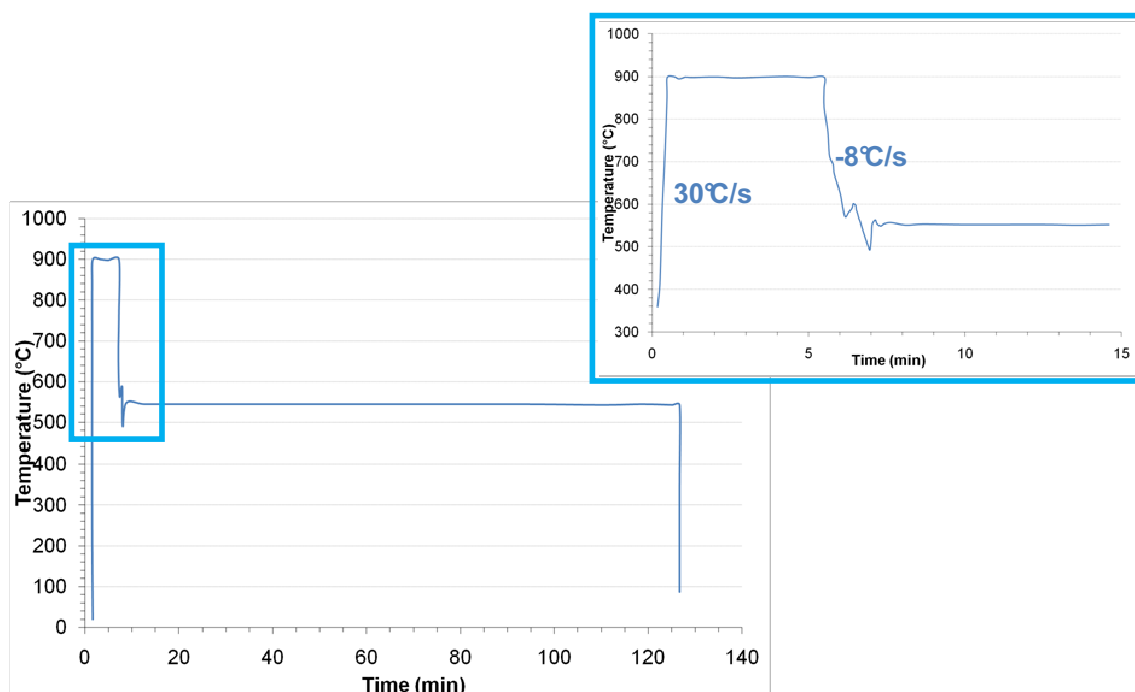


Figure II-10: schematic of a heating treatment using halogen furnace (AET) with corresponding heating and cooling rates.

C. Texture

As mentioned previously, the matrix of the samples is 100 percent ferritic with grains around 25 μ m but a pronounced texture was observed in XRD experiments, and was therefore quantified by EBSD observations.

EBSD experiments

The EBSD experiments were performed at the Consortium des Moyens Technologiques Communs (CMTC), thanks to the help of Florence Robaut, using OIM software for analysis. The samples were polished mechanically up to 1 micron diamond paste. The analyzed surface is of 1x1 mm². The cartography obtained corresponds to the orientation of the grains with the direction perpendicular to the sample as a reference. The rolling direction is given in Figure II-12 below by "RD". The results are depicted in Figure II-11 and 12 showing a predominant orientation in $\langle 111 \rangle$ and $\langle 211 \rangle$ directions. The corresponding pole figures are represented in Figure II-13 below. No Goss-texture was revealed, which is otherwise often observed in Fe-Si alloys [MAG1994] & [MIS1984].

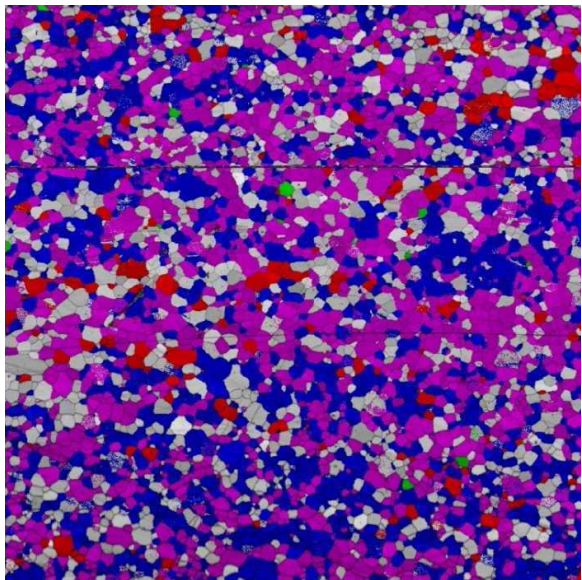


Figure II-11: EBSD map performed on as-quenched sample (900°C during 5minutes) (image size 1x1mm)

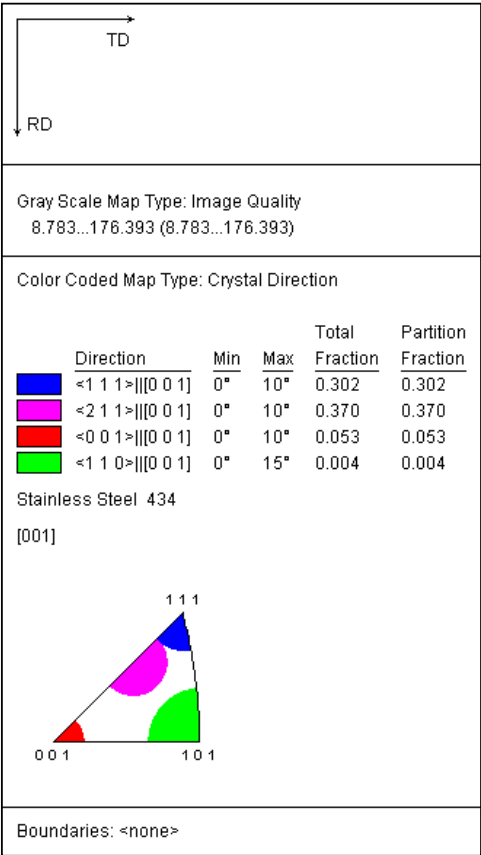


Figure II-12: orientation of grains with the direction perpendicular to the sample as a reference (corresponding to Figure II-11)

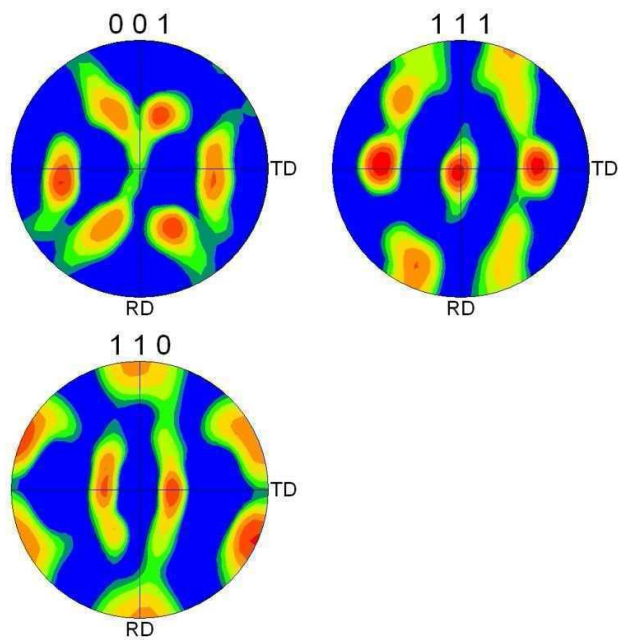


Figure II-13: Pole figures obtained by EBSD observations on as-quenched sample

II. Experimental Techniques

Two topics were investigated in the present study: mechanical properties and precipitation characterization. Mechanical tests consisted of Vickers hardness tests, simple tensile tests at room temperature and Bauschinger tests. Concerning microstructural observations two kinds of tools were used: those for global microstructural study such as Small Angle Neutron Scattering (SANS) or Atom Probe Tomography (APT) and those for local investigation such as Electron microscopy (TEM).

A. Mechanical properties

1) Vickers hardness

The use of hardness measurements can be interesting to rapidly compare samples in terms of mechanical properties. It can also give information on local variations of hardness for example in the presence of large inclusions or second phases in general.

Hardness tests were performed on samples polished down to 1 μ m with diamond paste, and slight etching (Nital 2%) to see where the indentation takes place (grain boundaries, inclusions, ...). On each sample ten indentations were usually performed, separated each by a distance equivalent to two indentation prints, and the final value taken as a mean. The difference between the individual values would generally not exceed 20Hv.

The definition of Vickers Hardness is:

$$H_v = \frac{\text{Indentation Load (kg)}}{\text{Indentation area (mm}^2\text{)}} \quad (\text{II-1})$$

2) Tensile tests

Tensile tests are useful to accurately determine mechanical properties of a material. The values of interest in our case were the Yield stress (YS), the Young's modulus, Strain (or elongation) and stress at fracture (σ_f and ϵ_f (or e_f)), as well as the maximal stress before necking (Ultimate Tensile Stress UTS) (see Figure II-14).

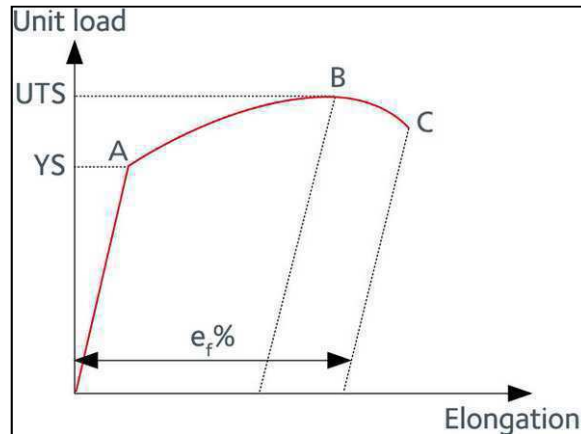


Figure II-14: classical stress-strain curve in steels

The dimension of tensile test bars was chosen using the format machined in the laboratory at ArcelorMittal Research, Maizières-Les-Metz, with code TCP6-46F (Figure II-15) with sheets having 0.9mm thickness cut in the direction transverse to the rolling direction (RD).

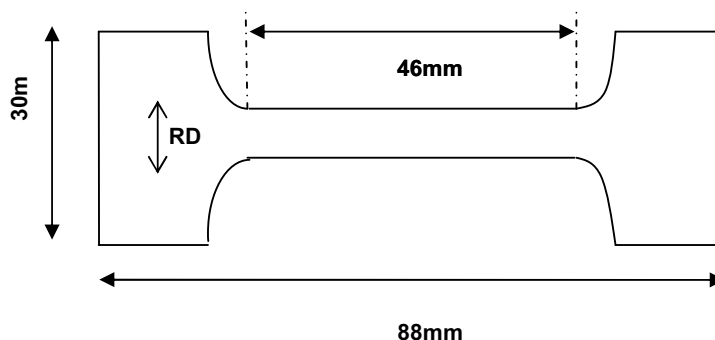


Figure II-15: schematic of TCP6-46F tensile test bars

The tensile tests were performed on a Zwick machine of 50kN capacity (Figure II-16) and were performed at room temperature with constant crosshead velocity of 7.5mm/min, which corresponds to a macroscopic strain rate of $3 \cdot 10^{-3} \text{s}^{-1}$. A mechanical extensometer of 20mm stroke was used, which means that for tensile test bars of 46mm useful length, there exists a significant chance for the tensile test bar to break out of the measurement zone. This can induce some errors on the final elongation measured. For each heating treatment two tensile test specimens were successively tested in order to make sure that these treatments are reproducible.



Figure II-16: Zwick Roell tensile test machine

3) Bauschinger tests

The Bauschinger tests were performed in the context of the PhD work by A. Aouafi [AOU2009] using an inverse shear device at the LMPTM laboratory (Paris). The use of shear tests, rather than tensile-compression was done to avoid necking or buckling and it is particularly well adapted to samples with small thickness (here around 0.9mm). The samples were prepared using an electroerosion device and were cut into rectangles of 30x18mm² with an effective zone of 30x2mm² (see figure ii-17) in order to have an homogeneous deformation and to reduce edge effects [AOU2009]. The shear direction was defined so as to follow the rolling direction of the initial sheet. Tests were done at constant deformation rate of $\dot{\gamma} = \sqrt{3} * 10^{-3} s^{-1}$ as controlled by an optical extensometer. Therefore the samples were previously painted in white with a black line in the shear direction. The angle θ between the initial line and the final line was then followed by a CCD camera in order to define the shear stress $\gamma = \tan\theta$ (see figure ii-17) [AOU2009].

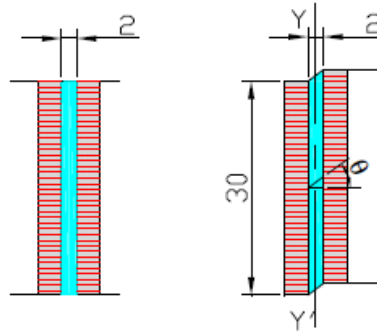


Figure II-17: Schematic of the shear test experiment used for inverse shear tests [AOU2009]

Determination of the offset of plastic deformation

Former studies have shown the importance the value of offset for plastic deformation after reversal in the value of Bauschinger tests. [FRI2009] and [AOU2009] compared the orders of magnitude for the Bauschinger stress for offset values ranging from 0.1% to 2%, showing that the higher the value of the offset, the lower the value of the Bauschinger stress. In the present case, the offset has been taken at 0.3% which corresponds to the value taken at ArcelorMittal Research, used by Aouafi [AOU2009]. It was shown to give reasonable values of Bauschinger stress.

B. Precipitation characterization

1) **Microstructure observation at an “average” level: Small Angle Neutron Scattering (SANS)**

i. Conditions for experiments on Fe-Si-Ti system

The SANS measurements were made at the Institut Laue Langevin (ILL), in Grenoble on the beamline D11 (Figure II-18). The experimental device under magnetic field does not allow any heating possibility, thus all the samples were observed ex-situ.

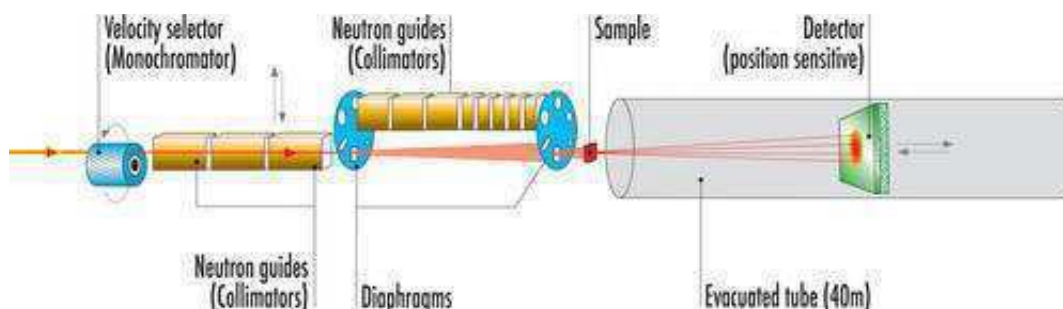


Figure II-18: Scheme of the ILL beamline D11 (www.ill.eu)

Sample preparation

The samples prepared were prepared from sheets of 1mm thickness with a square surface of 10x10mm². The sample thickness, e , is calculated in order to have a transmission coefficient around 37%, which is the optimum, in order to avoid neutron absorption by the sample while keeping enough material to have a good signal. The transmission of a sample is defined as $Tr = \frac{I_{diffused}}{I_{incident}} = \exp(-\mu e)$, where μ is the linear absorption coefficient. In the present case, the wave length of the experiment was $\lambda = 6\text{\AA}$. The iron has $\mu=0.693\text{cm}^{-1}$. In our case the maximum thickness was calculated around 1.4cm. The first tests were carried out using a superimposition of two samples of ~0.9 mm, meaning an effective thickness of ~1.8mm. In fact one sample of 0.9mm was shown to be sufficient to get enough signal.

Samples were mechanically polished with up to 1 μm diamond paste on both sides to avoid undesired scratches.

ii. General description

Small Angle Scattering, either by X-rays (SAXS) or by Neutrons (SANS), is a technique used to characterize quantitatively the average microstructure of a material. The basics of SANS technique will be given here for a better understanding of the study. For further information one can be referred to the books by G.E. Bacon [BAC1955] or Feigin et al. [FEI1987].

The presence of precipitates of different composition and structure than the matrix will cause the scattering of the beam in a way which is specific to its shape, size, volume fraction and composition. Hence, the analysis of such signals gives important information on the precipitation state. In the case of Fe-Si-Ti alloys, the use of SANS was found out to be more appropriate than SAXS for several reasons. Firstly, the preparation of samples for Neutron beams is less demanding, since the wavelength in the case of SAXS is much lower ($\lambda=1.74\text{\AA}$). The transmission of 37% can only be reached with samples having a thickness around $25\mu\text{m}$. Another advantage of SANS experiments is the possibility to use wavelengths which avoid the occurrence of parasitic effects due to the matrix diffraction [PER2004]. The drawbacks of SANS are, however, that no in-situ experiments can be performed under magnetic field; the higher wavelength in case of SANS leads to a lower q -range available, and the detector needs consequently to be moved back and forth during the experiment.

The aim of SANS is to send a monochromatic beam on a sample in order to reveal the precipitates by the scattering of a neutron beam. From the scattering signals a variation of the intensity as a function of the scattering angle 2θ is obtained. These signals are then corrected and analyzed, and give information on radius and volume fractions.

Like any other scattering process, SANS is characterized by a reciprocity law which gives an inverse relationship between particle size and scattering angle. Since the precipitates observed are usually large (a few nm) compared to the neutron wavelength (here 6\AA), the observed scattering angles are therefore small.

In the case of small angle scattering the incoherent scattering can be neglected. The coherency of the waves implies that the amplitudes are added and the intensity is given by the square of the resulting amplitude. The resulting amplitude is the sum of the responses of all neutrons included in the investigated volume:

$$F(q) = \iiint \rho(r) e^{-iqr} dV \quad (\text{II-2})$$

Where $\rho(r)$ is the density of scattering

With q the scattering vector defined as:

$$q = \frac{4\pi \sin\theta}{\lambda} \quad (\text{II-3})$$

Where λ is the wavelength of the source and θ the scattering semi-angle

In the case of a spherical particle of radius R , volume $V(R)$ and density ρ_p included in a matrix of neutron density ρ_m , the scattered amplitude can be calculated:

$$F(q, R) = (\rho_p - \rho_m) \cdot V(R) \cdot 3 \cdot \left(\frac{\sin(qR) - qR \cos(qR)}{(qR)^3} \right) \quad (\text{II-4})$$

Since the intensity is given by the absolute square of the resulting amplitude, one can define:

$$I(q, R) = \Delta\rho^2 V(R)^2 3 \left(\frac{\sin(qR) - qR \cos(qR)}{(qR)^3} \right)^2 \quad (\text{II-5})$$

In the case of a dilute distribution of particles –where one can consider that the particles are distant enough so that they do not interact with each other (interparticle distance $\lambda_p \gg R$)- the total scattering intensity is the sum of the intensity scattered by each particle:

$$I(q) = \int_0^\infty f(R) I(q, R) dR \quad (\text{II-6})$$

With $f(R)$ the distribution function of particles of different sizes

Interactions between neutron and matter are of two kinds:

- The magnetic interaction takes place between the magnetic moment of the neutrons and the atoms (if they have one). In our case the matrix is magnetic while the precipitates are not. Therefore the samples are placed under magnetic field in order to saturate all spins from the ferritic matrix and distinguish the contrast between magnetic matrix and non-magnetic precipitates.
- The interaction between neutrons and the nucleus of the atoms: This is the nuclear interaction. It is dependent on the nature of the atoms and thus the composition of the precipitates.

Magnetic contrast:

The magnetic contrast is defined as:

$$\Delta\rho_{MAG} = \frac{b_{MAG}^m}{V_{at}^m} - \frac{b_{MAG}^p}{V_{at}^p} \quad (\text{II-7})$$

with b_{MAG}^m and b_{MAG}^p the magnetic scattering lengths from the ferrite and the precipitates respectively and V_{at}^m and V_{at}^p the atomic volumes.

However, since the precipitates are non-magnetic, their magnetic scattering length is equal to zero and therefore the magnetic contrast is reduced to:

$$(\Delta\rho_{MAG})^2 = \left(\frac{b_{MAG}^m}{V_{at}^m} \right)^2 = 2.57 \times 10^{-11} \text{Å}^{-4} \text{ for a ferritic matrix [PER2004]}$$

A scattering signal obtained with Fe-Si-Ti precipitated samples is shown Figure II-20 a. Since Fe-Si-Ti has a magnetic matrix, the signal is anisotropic compared to an isotropic signal for the austenitic Fe-Mn-C-V alloy which is non magnetic (Figure II-20 b).

This anisotropy is due to the fact that the interaction between the magnetic moments of the neutron and the atoms depends on the angle with the scattering vector α . Saturating the atoms magnetically permits then to set α , and therefore separate the magnetic and the

3) Bauschinger tests

The Bauschinger tests were performed in the context of the PhD work by A. Aouafi [AOU2009] using an inverse shear device at the LMPTM laboratory (Paris). The use of shear tests, rather than tensile-compression was done to avoid necking or buckling and it is particularly well adapted to samples with small thickness (here around 0.9mm). The samples were prepared using an electroerosion device and were cut into rectangles of 30x18mm² with an effective zone of 30x2mm² (see figure ii-17) in order to have an homogeneous deformation and to reduce edge effects [AOU2009]. The shear direction was defined so as to follow the rolling direction of the initial sheet. Tests were done at constant deformation rate of $\dot{\gamma} = \sqrt{3} * 10^{-3} s^{-1}$ as controlled by an optical extensometer. Therefore the samples were previously painted in white with a black line in the shear direction. The angle θ between the initial line and the final line was then followed by a CCD camera in order to define the shear stress $\gamma = \tan\theta$ (see figure ii-17) [AOU2009].

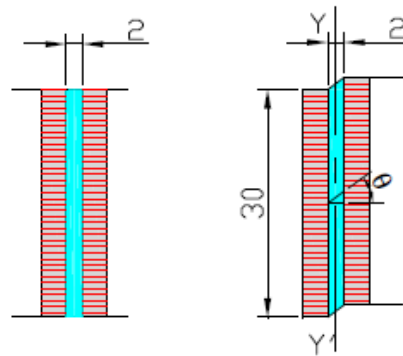


Figure II-17: Schematic of the shear test experiment used for inverse shear tests [AOU2009]

Determination of the offset of plastic deformation

Former studies have shown the importance the value of offset for plastic deformation after reversal in the value of Bauschinger tests. [FRI2009] and [AOU2009] compared the orders of magnitude for the Bauschinger stress for offset values ranging from 0.1% to 2%, showing that the higher the value of the offset, the lower the value of the Bauschinger stress. In the present case, the offset has been taken at 0.3% which corresponds to the value taken at ArcelorMittal Research, used by Aouafi [AOU2009]. It was shown to give reasonable values of Bauschinger stress.

B. Precipitation characterization

1) Microstructure observation at an “average” level: Small Angle Neutron Scattering (SANS)

i. Conditions for experiments on Fe-Si-Ti system

The SANS measurements were made at the Institut Laue Langevin (ILL), in Grenoble on the beamline D11 (Figure II-18). The experimental device under magnetic field does not allow any heating possibility, thus all the samples were observed ex-situ.

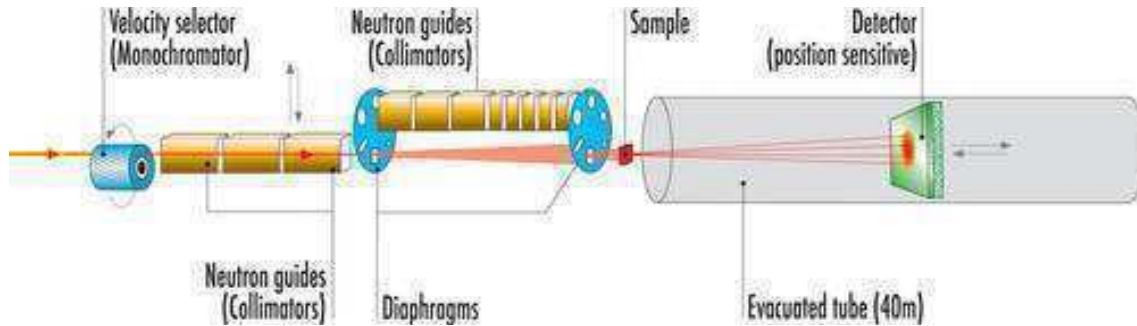


Figure II-18: Scheme of the ILL beamline D11 (www.ill.eu)

Sample preparation

The samples prepared were prepared from sheets of 1mm thickness with a square surface of 10x10mm². The sample thickness, e , is calculated in order to have a transmission coefficient around 37%, which is the optimum, in order to avoid neutron absorption by the sample while keeping enough material to have a good signal. The transmission of a sample is defined as $Tr = \frac{I_{diffused}}{I_{incident}} = \exp(-\mu e)$, where μ is the linear absorption coefficient. In the present case, the wave length of the experiment was $\lambda = 6\text{\AA}$. The iron has $\mu=0.693\text{cm}^{-1}$. In our case the maximum thickness was calculated around 1.4cm. The first tests were carried out using a superimposition of two samples of ~0.9 mm, meaning an effective thickness of ~1.8mm. In fact one sample of 0.9mm was shown to be sufficient to get enough signal.

Samples were mechanically polished with up to 1 μm diamond paste on both sides to avoid undesired scratches.

ii. General description

Small Angle Scattering, either by X-rays (SAXS) or by Neutrons (SANS), is a technique used to characterize quantitatively the average microstructure of a material. The basics of SANS technique will be given here for a better understanding of the study. For further information one can be referred to the books by G.E. Bacon [BAC1955] or Feigin et al. [FEI1987].

The presence of precipitates of different composition and structure than the matrix will cause the scattering of the beam in a way which is specific to its shape, size, volume fraction and composition. Hence, the analysis of such signals gives important information on the precipitation state. In the case of Fe-Si-Ti alloys, the use of SANS was found out to be more appropriate than SAXS for several reasons. Firstly, the preparation of samples for Neutron beams is less demanding, since the wavelength in the case of SAXS is much lower ($\lambda=1.74\text{\AA}$). The transmission of 37% can only be reached with samples having a thickness around $25\mu\text{m}$. Another advantage of SANS experiments is the possibility to use wavelengths which avoid the occurrence of parasitic effects due to the matrix diffraction [PER2004]. The drawbacks of SANS are, however, that no in-situ experiments can be performed under magnetic field; the higher wavelength in case of SANS leads to a lower q-range available, and the detector needs consequently to be moved back and forth during the experiment.

The aim of SANS is to send a monochromatic beam on a sample in order to reveal the precipitates by the scattering of a neutron beam. From the scattering signals a variation of the intensity as a function of the scattering angle 2θ is obtained. These signals are then corrected and analyzed, and give information on radius and volume fractions.

Like any other scattering process, SANS is characterized by a reciprocity law which gives an inverse relationship between particle size and scattering angle. Since the precipitates observed are usually large (a few nm) compared to the neutron wavelength (here 6\AA), the observed scattering angles are therefore small.

In the case of small angle scattering the incoherent scattering can be neglected. The coherency of the waves implies that the amplitudes are added and the intensity is given by the square of the resulting amplitude. The resulting amplitude is the sum of the responses of all neutrons included in the investigated volume:

$$F(q) = \iiint \rho(r) e^{-iqr} dV \quad (\text{II-2})$$

Where $\rho(r)$ is the density of scattering

With q the scattering vector defined as:

$$q = \frac{4\pi \sin\theta}{\lambda} \quad (\text{II-3})$$

Where λ is the wavelength of the source and θ the scattering semi-angle

In the case of a spherical particle of radius R , volume $V(R)$ and density ρ_p included in a matrix of neutron density ρ_m , the scattered amplitude can be calculated:

$$F(q, R) = (\rho_p - \rho_m) \cdot V(R) \cdot 3 \cdot \left(\frac{\sin(qR) - qR \cos(qR)}{(qR)^3} \right) \quad (\text{II-4})$$

Since the intensity is given by the absolute square of the resulting amplitude, one can define:

$$I(q, R) = \Delta\rho^2 V(R)^2 3 \left(\frac{\sin(qR) - qR \cos(qR)}{(qR)^3} \right)^2 \quad (\text{II-5})$$

In the case of a dilute distribution of particles –where one can consider that the particles are distant enough so that they do not interact with each other (interparticle distance $\lambda_p \gg R$)- the total scattering intensity is the sum of the intensity scattered by each particle:

$$I(q) = \int_0^\infty f(R) I(q, R) dR \quad (\text{II-6})$$

With $f(R)$ the distribution function of particles of different sizes

Interactions between neutron and matter are of two kinds:

- The magnetic interaction takes place between the magnetic moment of the neutrons and the atoms (if they have one). In our case the matrix is magnetic while the precipitates are not. Therefore the samples are placed under magnetic field in order to saturate all spins from the ferritic matrix and distinguish the contrast between magnetic matrix and non-magnetic precipitates.
- The interaction between neutrons and the nucleus of the atoms: This is the nuclear interaction. It is dependent on the nature of the atoms and thus the composition of the precipitates.

Magnetic contrast:

The magnetic contrast is defined as:

$$\Delta\rho_{MAG} = \frac{b_{MAG}^m}{V_{at}^m} - \frac{b_{MAG}^p}{V_{at}^p} \quad (\text{II-7})$$

with b_{MAG}^m and b_{MAG}^p the magnetic scattering lengths from the ferrite and the precipitates respectively and V_{at}^m and V_{at}^p the atomic volumes.

However, since the precipitates are non-magnetic, their magnetic scattering length is equal to zero and therefore the magnetic contrast is reduced to:

$$(\Delta\rho_{MAG})^2 = \left(\frac{b_{MAG}^m}{V_{at}^m} \right)^2 = 2.57 \times 10^{-11} \text{Å}^{-4} \text{ for a ferritic matrix [PER2004]}$$

A scattering signal obtained with Fe-Si-Ti precipitated samples is shown Figure II-20 a. Since Fe-Si-Ti has a magnetic matrix, the signal is anisotropic compared to an isotropic signal for the austenitic Fe-Mn-C-V alloy which is non magnetic (Figure II-20 b).

This anisotropy is due to the fact that the interaction between the magnetic moments of the neutron and the atoms depends on the angle with the scattering vector α . Saturating the atoms magnetically permits then to set α , and therefore separate the magnetic and the

nuclear components. The total scattering intensity is given by the sum of the amplitudes of the nuclear and the magnetic scattering: $\Delta\rho^2 = (\Delta\rho_{NUC})^2 + (\Delta\rho_{MAG})^2 * \sin^2\alpha$ (Figure II-19).

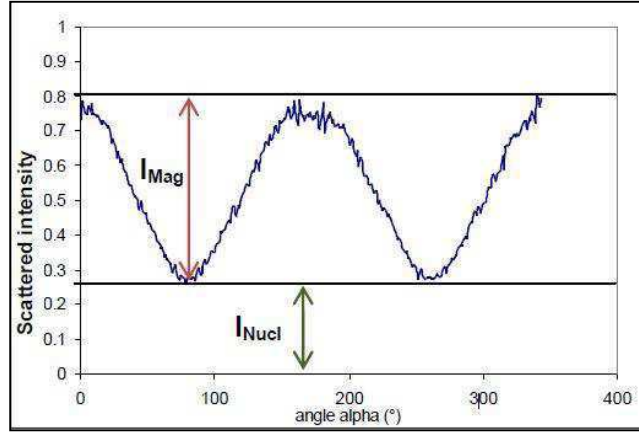


Figure II-19 relation between magnetic and nuclear scattering intensities, showing the non isotropic evolution of I_{Mag} with α

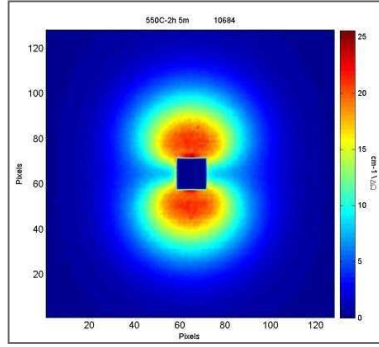


Figure II-20 a)

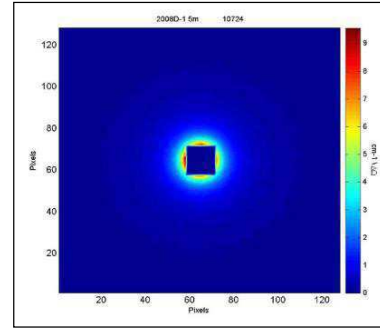


Figure II-20 b)

Figure II-20 : Comparison between the scattering signals of a) Fe-Si-Ti and b) Fe-Mn-C-V showing the difference between the case of a magnetic matrix (a) with anisotropic intensity evolution and a non-magnetic material (b) with isotropic intensity evolution with scattering angle.

Nuclear contrast:

The nuclear contrast is defined as:

$$\Delta\rho_{NUC} = \frac{b_{NUC}^m}{V_{at}^m} - \frac{b_{NUC}^p}{V_{at}^p} \quad (II-8)$$

With b_{NUC}^m and b_{NUC}^p being the nuclear lengths of the matrix and the precipitates respectively (values taken from: <http://www.ncnr.nist.gov/resources/n-lengths/>).

$$b_{Ti} = -3.438 \cdot 10^{-5} \text{Å}, b_{Si} = 4.1491 \cdot 10^{-5} \text{Å}, b_{Fe} = 9.45 \cdot 10^{-5} \text{Å}.$$

For a cubic cell the atomic volume is defined by: $V_{at} = \frac{a^3}{nb \text{ of atoms per cell}}$

Where a is the lattice parameter:

- $a = 2,85\text{\AA}$ for ferrite with bcc structure containing 2 atoms per unit cell.
Meaning $V_{at}^m = 11.73 \text{ \AA}^3$
- $a = 5,709\text{\AA}$ for Fe_2SiTi
Meaning $V_{at}^p = 11.62 \text{ \AA}^3$
- b_{NUC}^p is calculated using : $\frac{1}{2} b_{\text{Fe}} + \frac{1}{4} b_{\text{Ti}} + \frac{1}{4} b_{\text{Si}} = 9.31 \cdot 10^{-5} \text{ \AA}$ which corresponds to the case where the composition is Fe_2SiTi
- b_{NUC}^m is calculated using: $0.96 b_{\text{Fe}} + 0.025 b_{\text{Si}} + 0.01 b_{\text{T}} = 4.90 \cdot 10^{-5} \text{ \AA}$, corresponding to the matrix composition.

Thus, the nuclear contrast depends on the composition of the precipitates, meaning that it is necessary to identify the present phase. Once the signal is obtained, it has to be corrected by several elements. All these corrections are done by the software *Grasp*, developed by C. Dewhurst from ILL (available on the ILL website <http://www.ill.eu>). These corrections are detailed as:

- Determination of the beam center: use of the direct beam image
- Subtraction of the detector defects: a quartz cell containing water is used. In fact, water scatters in a totally isotropic way and permits to correct the signal with the detector's efficiency (called "flat"). The water cell is also a mean to calibrate the global scattering intensity.
- Due to the several distances (2, 5.5 and 16.5 m) used for the detector, there exist differences in the solid angle of detection and some collimation errors can be introduced. In order to normalize the data, we use a sample full of water and thanks to the signal obtained at 4 meters distance one can calibrate all other distances. Thanks to these, the data curves (Figure II-21) can then also be unified in a single one (Figure II-22).

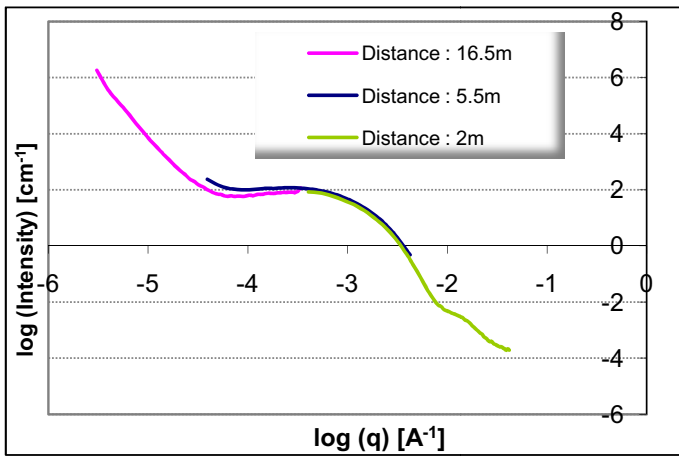


Figure II-21: Curve of the intensity as a function of the scattering vector q for 3 distances from the detector: 2, 5.5 and 16.5m.

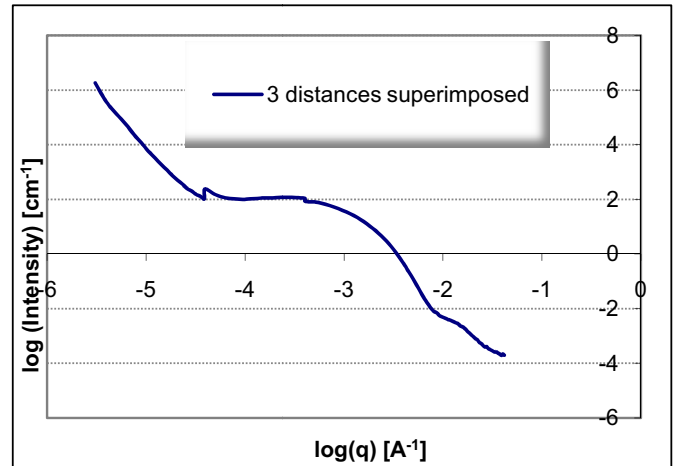


Figure II-22 : Merged curve for the three distances from the detector taken from Figure II-21

- **Background noise subtraction:** it is measured by using a sample of pure cadmium in the sample holder, which stops the neutron beam (Figure II-23). Hence the neutrons passing around the sample holder can be measured and then subtracted from the scattering signal.

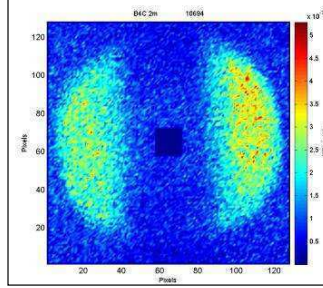


Figure II-23: Scattering signal of Cadmium sample used to subtract background noise and defaults due to the scattering of the sample holder

Once all these corrections are made, the scattering signals have to undergo a last correction: the subtraction of the scattering of the solid solution and of the incoherent signal, so called Laue intensity, in order to keep only the scattering coming from the precipitates. The Laue intensity is defined as:

$$I_{Laue} = I(q) - \frac{K}{q^4} \quad (II-9)$$

where $K = \frac{Q_0 S}{\pi V}$, S and V being the surface and the volume of the precipitates respectively.

The Porod's Law shows that for high q-values the intensity has an asymptotic behavior. Thus, by plotting Iq^4 versus q^4 , the Laue intensity is given by the slope (Figure II-24). Thus, the new corrected intensity is $I_{corrected} = I - I_{Laue}$, as shown Figure II-25.

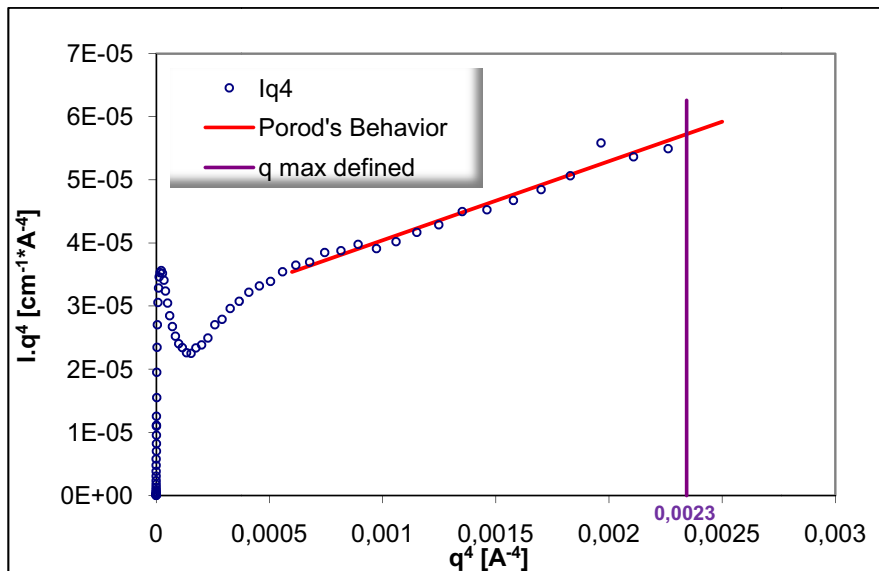


Figure II-24: Asymptotic behavior of the curve of Iq^4 as a function of q^4 . Enables the determination of Laue Intensity which corresponds to the slope of the asymptote

After this last step, the data obtained is a table of intensity values as a function of the scattering vector q , enabling to plot $Iq^2 = f(q)$ the curve (blue spots on Figure II-25) which is then modeled by a log-normal approximation (plain curve). The analysis of these signals gives us two main values, namely the radius and volume fraction of precipitates present in the matrix, which are proportional respectively to the q -value of the intensity peak and to the area under the Iq^2 curve. The precise steps for their determination are described briefly in what follows.

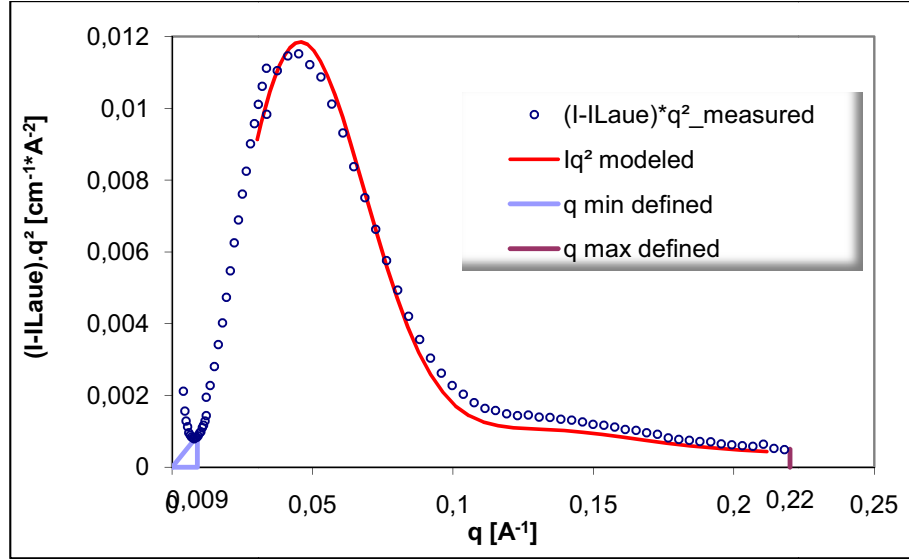


Figure II-25: Complete corrected curve of the evolution of $(I-I_{Laue})q^2$ as a function of q , for an Fe-Si-Ti sample

iii. Extraction of Radius values

An important approximation in small angle scattering is the Guinier approximation, valid for small q values. Guinier showed that for any particle morphology one can consider that:

$$I(q) = (\rho_p - \rho_m)^2 \cdot V^2 \cdot \exp\left(\frac{-q^2 R_g^2}{3}\right) \quad (II-10)$$

Where R_g is the Guinier radius or radius of gyration.

R_g is defined as the mean square distance from each point of the particle to its center of gravity. In the case of monodispersed spherical precipitation, R_g is related to the mean radius, R_m , by a geometrical factor:

$$R_g = \sqrt{\frac{3}{5}} R_m \quad (II-11)$$

In the case of polydispersed particles, which is assumed to be the case in our study since the observations showed an important size distribution, the R_g radius is closer to R_m , as shown by M. Nicolas in [NIC2002]. In the calculation for the determination of the mean radius we thus have supposed that Guinier Radius and mean Radius are the same. This assumption probably induces an error close to 5% in the final radius value.

Experimentally, the Guinier radius is determined in practice after several calculation steps:

1. The plot Iq^2 versus q (Figure II-25) shows a peak at a q -value called q_{max} which is proportional to R_g :

$$R_{g1} = \frac{\sqrt{3}}{q_{max}} \quad (II-12)$$

2. The first value of R_g , R_{g1} is then used to determine a q -range $[1.2 R_{g1}; 2.8 R_{g1}]$ for a new estimation of the Guinier radius, R_{g2} , thanks to a linear regression of the plot $\ln(I)$ versus q^2 (Figure II-26).

Both steps are then iterated until convergence is reached.

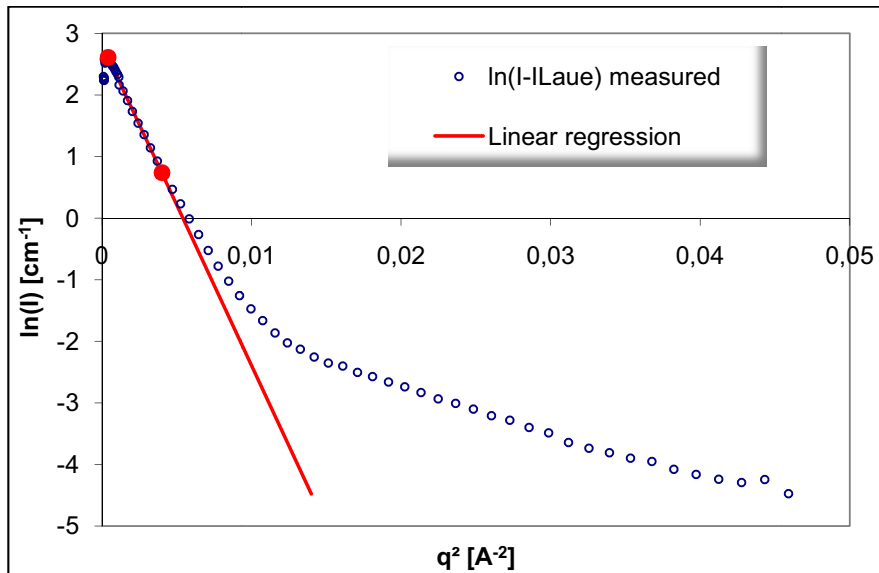


Figure II-26: Evolution of $\ln(I)$ as a function of q^2 . The beginning of the curve is taken as linear, using its slope for determining R_g

iv. Extraction of Volume fraction values

It has been shown by Bacon [BAC1955] that the integrated intensity, Q_0 , is independent of the morphological parameters of the material, and is thus a constant, such as:

$$Q_0 = \int_0^{\infty} I(q) q^2 dq \quad (II-13)$$

In the case of a material containing a precipitated second phase, this integrated intensity is directly related to the volume fraction, f_v , by the following formula:

$$Q_0 = 2\pi^2 \Delta\rho^2 f_v (1 - f_v) \quad (II-14)$$

$\Delta\rho$ being the difference in contrast between matrix and precipitates.

Experimentally Q_0 corresponds to the area under the curve Iq^2 versus q in the q range $[0; +\infty]$. In reality the experimental curve is limited in q -values by $[q_0; q_\infty]$. Thus Q_0 is evaluated by considering three contributions (see Figure II-27):

$$Q_0 = \int_0^{q_0} I(q) q^2 dq + \int_{q_0}^{q_\infty} I(q) q^2 dq + \int_{q_\infty}^{+\infty} I(q) q^2 dq \quad (II-15)$$

The first term covers the area from 0 to the beginning of the experimental acquisition, q_0 . It is approximated by a triangle of base and height respectively q_0 and $I(q_0)q_0^2$. The second term is the area under the experimental spectrum. The third term corresponds to the behaviour at high q -values, hence, following the Porod's law as shown previously.

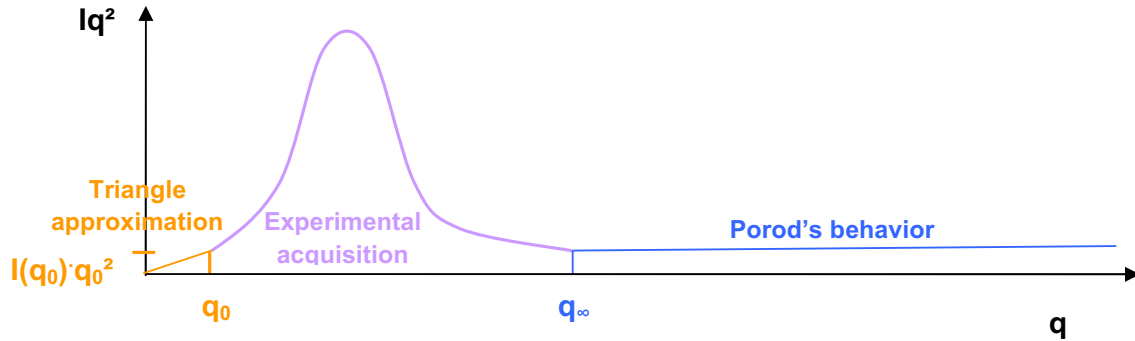


Figure II-27: Schematic of the evolution of Iq^2 as a function of q showing the 3 terms used for the calculation of the integrated intensity Q_0

Finally, the total integrated intensity can be written as:

$$Q_0 = \frac{I(q_0)q_0^3}{2} + Q_{0Mes} + \frac{K}{q_\infty} \quad (II-16)$$

In fact, in SANS, since there are two origins for the contrast, the values must be calculated for each component:

$$\Delta\rho_{TOT}^2 = \Delta\rho_{NUC}^2 + \Delta\rho_{MAG}^2 \quad (II-17)$$

For the magnetic signal we use

$$\frac{Q_0}{2\pi^2\Delta\rho_{MAG}^2} - f_v + f_v^2 = 0 \quad (II-18)$$

For the nuclear signal we use

$$\frac{Q_0}{2\pi^2\Delta\rho_{NUC}^2} - f_v + f_v^2 = 0 \quad (II-19)$$

The volume fraction values are then calculated using one of these two equations (equation (II-18) or (II-19)).

2) Local microstructure observation: Microscopy

i. Optical microscope

This is a very classical tool but it remains useful when macroscopic data is needed. The optical microscope was used in the present study for observations of grain size and distribution. Mechanical polishing up to 1µm diamond paste was performed. The samples having a 100%-ferritic matrix a simple etching by 2%-Nital (Nitric Acid dissolved in ethanol) was sufficient to reveal grain boundaries as well as microstructural defects (such as inclusions). Some image analysis was then performed in order to determine mean grain size using up to 400 grains intercept.

ii. Scanning Electron Microscope with Field Emission Gun (SEM-FEG)

Due to the very small precipitate size (a few nm), SEM-FEG could only be useful for observations at larger scales such as global view of the grains (depletion zones, grain boundary precipitation ...), fractography observations and chemical analysis of inclusions.

iii. Transmission Electron Microscopy: TEM

In the present study, TEM was used with two types of methods: dark field imaging and electron diffraction for the observation of precipitation. For more details on the TEM technique generally speaking one could refer to the volumes by Williams & Carter [WIL1996].

Sample Preparation

The samples are prepared in a classical way. First, mechanical polishing permits to reach a thickness around 80-100µm, followed by punching to obtain 3mm chips, which are then electropolished between 16 and 18°C using either a solution of acetic acid and perchloric acid (90%-10%) or a solution of ethylene glycol monobutyl ether and perchloric acid (90%-10%). Results were more satisfying with the second solution, but these methods needed additional ion cleaning by PIPS (3keV, 5°).

Observation were carried out on a Jeol 3010 microscope operating at 300keV.

- Electron Diffraction mode

Electron Diffraction uses the polycrystalline characteristic of a material. Interaction between the electron beam and the matter will create several diffracted beams (Bragg's law) which are then condensed by the objective lens to give a diffraction pattern. This pattern gives information concerning the orientation of the sample since it depends on the crystallography. These patterns are commonly used in metallurgical research for the study phase and defect identification. In the presence of another phase the diffraction pattern will be the superimposition of both (if they are different). Thus, in the present study the diffraction patterns were especially used to determine the structure of the precipitates.

- Imaging mode

Imaging mode is more visual but not less complex. In fact, one has to be very careful on the image interpretation which can be easily influenced by what we "want to see". The technique consists in orientating the sample in the wanted direction and selecting either the direct beam (Bright Field, see Figure II-28) or a diffracted beam (Dark Field, see Figure II-29). In Bright Field images a lot of different contrasts (precipitates, dislocations, thickness contrasts, polishing artifacts...) can appear making the conclusion difficult to draw. In Dark Field Imaging, the selection of a diffracted beam will reveal only one sort of orientation. In the presence of precipitates, if one selects the extra-spot related to them, these will appear in bright on a dark matrix. In Figure II-29 the schematized dark field imaging technique introduces additional astigmatism, which can be limited by using "centered dark field" technique. In the latter, the beam is tilted to align the diffracted beam with the incident direction.

In our case the use of dark field imaging was found to be more appropriate since some artifacts appeared on bright field images, probably due either to dynamic diffraction or even to electropolishing, and was therefore used to observe the precipitates and determine their size. Once the diffracted beam is selected, the beam is slightly tilted in order to center the selected beam in the optical axis: this is called centered dark field technique (see schematic below Figure II-29).

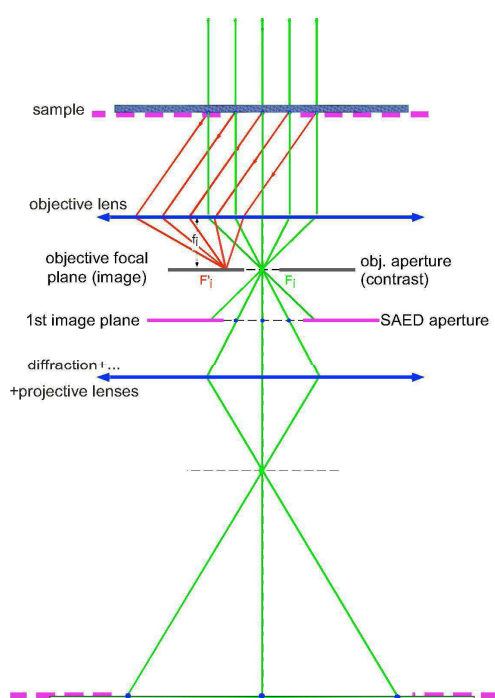


Figure II-28: Bright field imaging technique

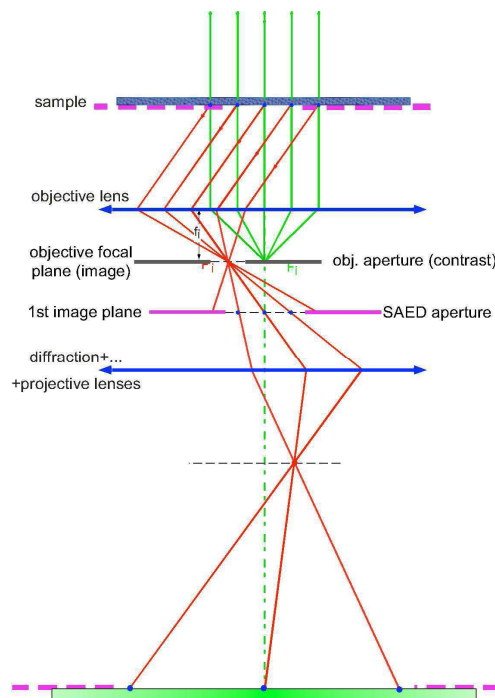


Figure II-29: Dark field imaging technique

3) Microstructure at atom scale: APT

Thanks to collaboration with the Université de Rouen and especially Frédéric Danoix, but also with the Université Paul Cezanne in Marseille with Khalid Hoummada and Dominique Mangelinck, Atom Probe Tomography experiments have been performed and analyzed. Three different atom probes were used all enabling to send electric impulses on the sample: the Ecotap in Rouen, the wide angle Probe in Austria (which results from collaboration with Frédéric Danoix) and the wide angle LEAP in Marseille. The aim of these measurements was to quantify the composition of the precipitates and the matrix at some relevant ageing times.

i. Principle

Atom Probe Tomography (APT) is a quite recent characterization technique developed in the 1980's by M. Miller [MIL1986] based on works by Müller et al. [MUE1968] and on the global knowledge of Field Ion Microscopy. It has been further improved until today.

The principle of an atom probe is to combine Time-of-Flight mass spectrometry and field ion microscopy to characterize the different atoms and allow their 3D reconstruction in space. Therefore, a rectangular sample with a square surface of $300 \times 300 \mu\text{m}^2$ and a length of 2 cm is transformed into a tip (Figure II-30) by electroerosion using a combined solution of Acetic acid and perchloric acid. The tip is placed into ultra high vacuum at low temperature (here 80K) where the atoms on its surface can be ionized either by a positive pulsed voltage

or a laser. In the case of the present experiments an electric APT was used since the samples are conductive.

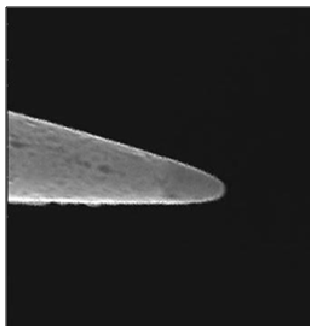


Figure II-30: Sharp tip used for atom probe observation; tip radius < 50 nm

ii. Analysis

Once the x million atoms on the surface are ionized (with efficiency around 60%) and the software has done a 3D reconstruction of the volume, which needs to be analyzed. In our case the objective is to separate the matrix from the precipitates in order to quantify their composition individually. One of the possible methods is called “Cluster analysis”, which is the one used with the software IVAS (belonging to IMAGO). The general concept is to define two parameters: N , the minimal number of atoms which can define a cluster and d_{\max} , the maximum distance between two atoms in a cluster. These two parameters are determined roughly by analyzing atom per atom and considering its next neighbor. One can decide to analyze one solute atom or the other or all solute atoms together. In the present case, analysis was done on one side for Titanium atoms and Silicon atoms separately and on the other side for Silicon and Titanium atoms together. The distance between an analyzed atom and its neighbor is calculated and this is done for each atom. The result is a curve showing the number of clusters existing as a function of distance d_{\max} as shown in Figure II-31, where the red curve is the randomized curve. This randomized curve corresponds to a simulation of a solid solution and the black curve is the data obtained. One then chooses a d_{\max} corresponding to a constant number of clusters, as shown Figure II-31. This will enable us to calculate the number of clusters for each number of atoms, N , considered, as shown in Figure II-32. Similar to Figure II-31 the red curve represents the randomized values, as for a solid solution, and the black curve corresponds to the data. The number N is thus evaluated as the minimum number of atoms for which the signal is different from solid solution, as shown in Figure II-32 for $N \sim 8$ atoms.

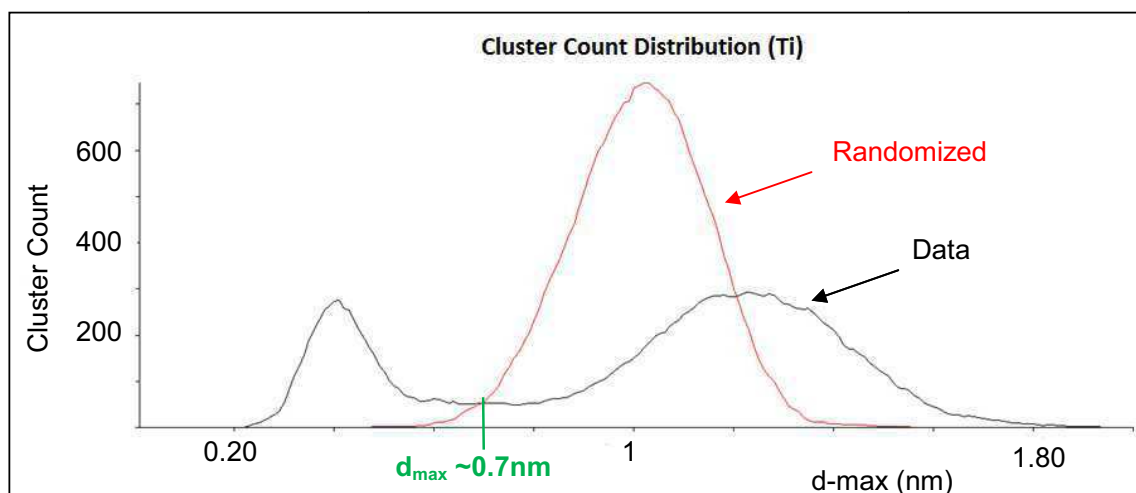


Figure II-31: Example of determination of d_{\max} , the minimum distance between two Ti atoms to form a cluster

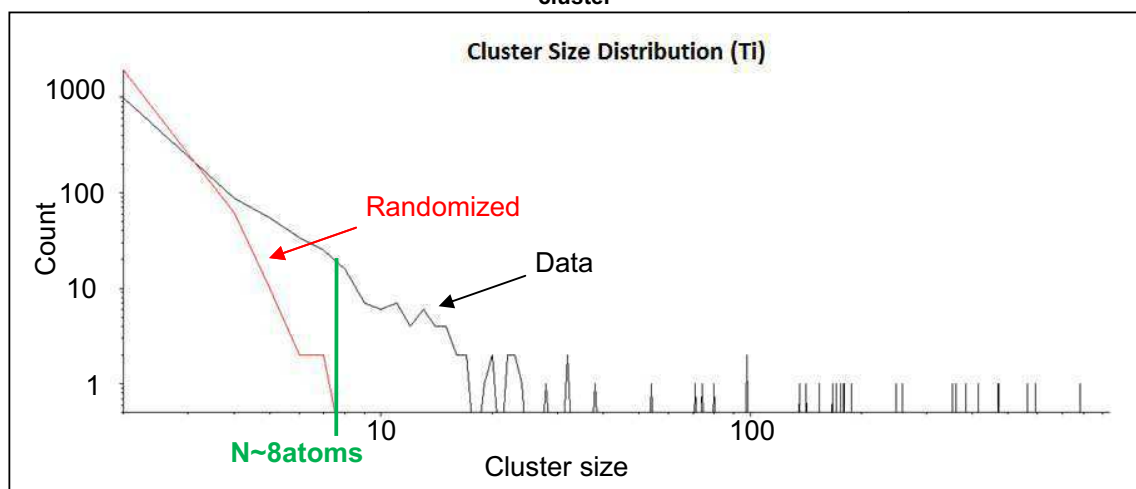


Figure II-32: Example of determination of N , the minimum number of Ti atoms forming a cluster

The determination of d_{\max} and N is thus the way to define a cluster. Once these are calibrated for each sample, the software can now separate the matrix from the precipitates as illustrated Figure II-33 versus Figure II-34 and 35. This also defines a sort of external contour of each cluster, corresponding to its radius.

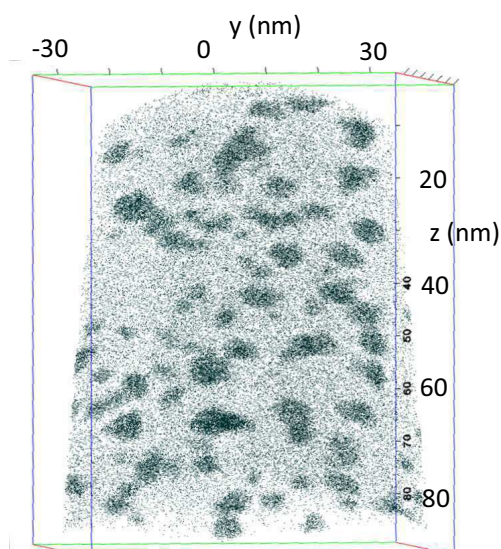


Figure II-33: Initial 3D reconstruction of the tip reproducing the Titanium atoms in the matrix and the precipitates

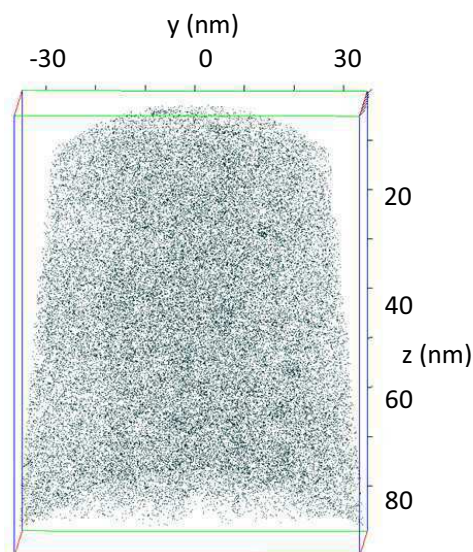


Figure II-34: 3D reconstruction of the Titanium atoms present in the matrix without precipitates

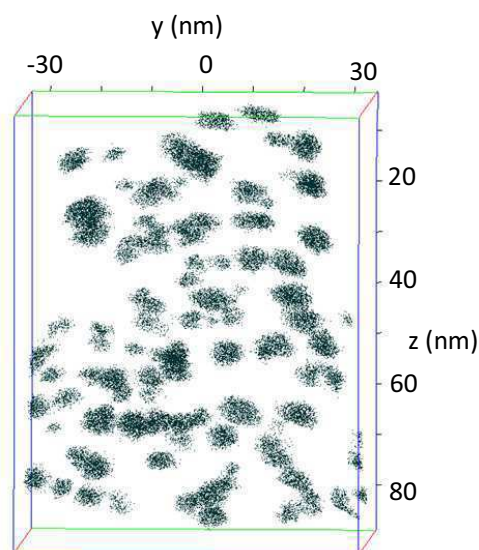


Figure II-35: 3D reconstruction of the Titanium atoms present in the clusters isolated from the matrix

This separation enables the independent analysis of the matrix and the precipitates, and allows on the one hand side the determination of the composition of the solid solution after precipitation, and on the other hand the composition of the precipitates. Since the clusters are defined by the search for the closest neighbor among the atoms, one needs to be very careful with the value since it depends on the parameters used to define the clusters. If one changes N or d_{\max} the cluster size will be different. Thus, the radius value can only be used as an order of magnitude.

Chapter III : Characterization of the Yield Stress in an Fe-Si-Ti alloy

INTRODUCTION	79
I. BIBLIOGRAPHIC REVIEW	79
A. Strengthening methods.....	79
B. Solid solution hardening.....	80
C. Precipitation hardening.....	81
1) Generalities.....	81
i. Penetrable Particles.....	82
ii. Impenetrable Particles for dislocations.....	83
2) Influence of precipitates on Yield Stress.....	84
i. Particle shearing	84
ii. Particle by-passing.....	84
D. Mechanical behavior of Fe-Si-Ti alloys	86
1) Yield stress evolution	86
2) Deformation mechanisms.....	88
II. EXPERIMENTAL RESULTS	88
A. Vickers Hardness	89
B. Tensile tests	90
C. Dislocation structures.....	91
III. CONCLUSION	95

Introduction

In research and development within the steel industry the major interest is to combine a reasonable cost and good mechanical properties. Several kinds of mechanical properties are of interest in this case: one will have to optimize the combination between yield stress and ductility. As mentioned in introduction of Chapter I, a high yield stress often comes together with a reduction in ductility.

In the following chapter we will make a brief introduction to the current level of knowledge concerning different microstructural parameters influencing the yield stress of a material, followed by the presentation of experimental results, those of tensile tests, on the Fe-Si-Ti alloy.

I. Bibliographic review

A. Strengthening methods

Hardening methods in materials have been a center of interest since many decades. The definition of the hardening of a material is an increase in yield stress, $\Delta\sigma$, due to the creation of obstacles to the dislocation motion. The most common methods to strengthen a material are:

- 1) Grain size refinement. As predicted by the Hall-Petch equation, the yield stress of a material is inversely proportional to the square root of the grain size:

$$\Delta\sigma = \sigma_0 + \frac{k}{\sqrt{D}} \quad (\text{III-1})$$

Where σ_0 is the friction stress, k a constant and D the mean grain size. Hence, a way to harden a material is to decrease the grain size.

- 2) Dispersion strengthening. It is used in composite materials by adding for example ceramic or oxide particles in a metallic matrix to create a non-deformable region surrounded by a plastically deforming matrix. In contrast to precipitation, dispersion often refers to non-metallic particles, produced (for example) by internal oxidation of a component dissolved in a less oxidizable matrix or by powder metallurgy.
- 3) Work hardening describes the hardening by plastic strain. This will be the object of Chapter V.
- 4) Solid solution strengthening, which provides both weak obstacles and additional viscosity opposing dislocation motion.
- 5) Precipitation strengthening, in which precipitates create obstacles to dislocation motion.

In most cases the hardness increase is due to the combination of several contributions, such as phase transformation, solid solution, or precipitation hardening, and it is difficult to separate the contribution of each factor.

In the following parts, solid solution and precipitation hardening will be described in more detail, as the most relevant to our system.

B. Solid solution hardening

Solid solution strengthening consists in the addition of alloying elements into a pure metal matrix in order to use the solute atoms as obstacles to dislocation motion. There exist two types of solid solution: one based on interstitial elements the second on substitutional elements. Figure III-1 shows the effect of some alloying elements when added into a material [MEY1999]. The dashed line corresponds to the addition of Carbon or Nitrogen, which are two interstitial solute elements, while the full lines correspond to elements which will be substituted to the solvent atoms. We notice the very important contribution of Carbon and Nitrogen compared to the other alloying elements, showing that interstitial solid solution has an important hardening effect. This graph enables to determine the hardening potential of Silicon, which is estimated to be of 80MPa per wt%.

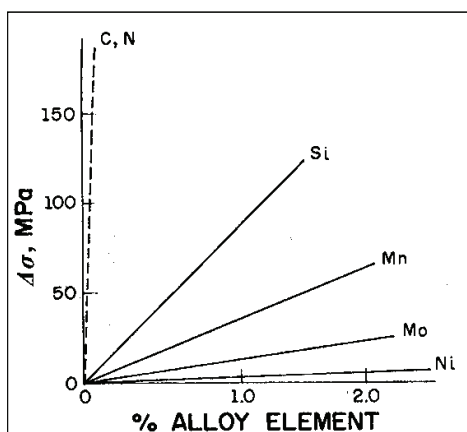


Figure III-1: Increase in yield stress of steel as a function of the percentage of alloying elements [MEY1999]

The hardening potential of Titanium in solid solution has already been shown by Wasmuht et al. [WAS1931], but the Fe-Ti phase diagram predicts a pronounced hardness only from 4wt% Titanium. Such alloys are extremely brittle and very difficult to manufacture due to the great affinity of Titanium to Carbon and Nitrogen leading to high inclusion content. The authors showed that the supplement addition of certain alloying elements, such as Silicon or Nickel, could reduce the amount of Titanium necessary to harden a material [LEN1957].

A large number of studies have found interest in investigating the influence of solid solution on mechanical properties, and the various parameters contributing to it. For example H. Suzuki in [CON1971], P. Haasen in [CAH1996], and much earlier Cottrell [COT1954] and J.C. Fisher [FIS1954].

The hardening effect due to the addition of alloying elements can be explained in terms of energy interactions between dislocations and the atoms. In fact, a dislocation has a stress field associated with it, which can interact with the stress fields around the solute

atom. One type of interactions is the so-called elastic misfit interaction, which is due to the difference in size between the solute atom and the host atom in the matrix [MEY1999]. But other types of interactions exist such as the ones due to the difference in modulus between the solute and the solvent, chemical interactions or electrical interactions, which all have the effect to hinder the movement of dislocations.

Another hardening mechanism which will be of interest in the present study is the precipitation hardening. The following part will describe it briefly.

C. Precipitation hardening

1) Generalities

Precipitation hardening consists in the creation of a new phase by heat treatments (quench and annealing) of a supersaturated solid solution. It has been proven to be of great interest for the hardening of metallic alloys. In Aluminum alloys for example the low yield stress values reached when using only solid solution strengthening can be greatly increased by the presence of a second dense, hard phase at a nanometric scale. Reviews on this subject are numerous, as for example V. Gerold in [GER1979], J-L. Lena in [LEN1957], Nicholson et al. in [CON1971] or A. Reppich in [REP1993].

Precipitation strengthening is one of many methods to harden a material. Within this concept, several mechanisms of interactions between dislocation and precipitates have to be considered, such as the ones listed in ([GER1979], [REP1993]):

- Surface energy hardening is also commonly called chemical strengthening because it is governed by the chemical bonding between matrix and precipitates.
- Modulus mismatch strengthening is due to the fact that the elastic energy of the crystal is changed locally around the precipitate. A force corresponding to the gradient of this energy appears on the dislocation.
- Coherency-strengthening is induced by the difference in lattice parameters of the precipitate and the matrix. This difference enhances a strain field around the precipitate by which it will interact with dislocations.
- Stacking-fault strengthening occurs when a strong interaction exists between the dislocation and a precipitate in which the stacking fault energy (γ_{SF}^P) is substantially different from that of the matrix (γ_{SF}^M).
- Atomic order strengthening. When a matrix dislocation shears a coherent ordered particle, it creates a disorder in the form of an antiphase boundary (APB) on the slip plane within the precipitate phase. The second trailing dislocation, on the other hand, removes the antiphase boundary. The APB thus causes pair-coupling. Therefore, in alloys containing ordered particles, dislocations often travel in pairs.

The prevailing mechanism will depend on the properties of the mismatch between the matrix and the precipitates. The different types of interphases between matrix and precipitates are well illustrated in Meyers et al. [MEY1999] as shown in Figure III-2.

Depending on the alloy studied, the strengthening mechanism involved can also be a combination of all these types.

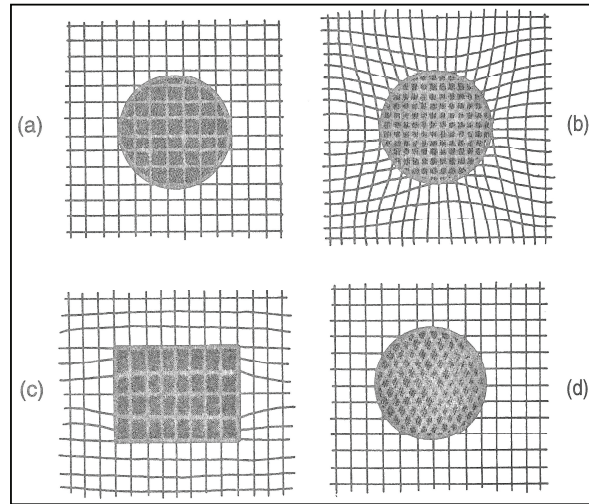


Figure III-2: Different types of matrix-precipitate interface a) coherent; b) coherent with mismatch strains; c) semi-coherent; d) incoherent (after [MEY1999])

For the understanding of the interaction between particles and dislocations, it is relatively unimportant how the particles have been produced. Hardening methods in the presence of precipitates are either based on the interaction between dislocations and defects, or on the interaction between dislocation and long range incompatibility stresses (*).

Precipitates or second-phase particles commonly act as geometric barriers to dislocation glide. Two limiting cases are possible, depending mainly on the size of the particles:

i. Penetrable Particles

In this case, particles are sheared (Figure III-3), but only if the interface between the matrix and the precipitates is coherent, meaning if there is no geometrical discontinuity in the atomic arrangement. Only a small change in the atomic distances is observed, which gives rise to an elastic coherency strain field around the particles.

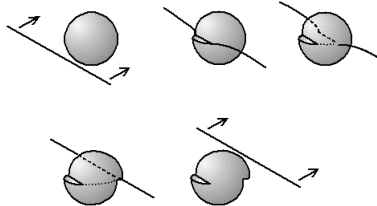


Figure III-3: Schematic of precipitate shearing by a dislocation

If a particle is ordered as well as coherent, a dislocation passing through it will create an antiphase boundary [JAC1972]. This implies that in systems containing coherent ordered precipitates the dislocations will tend to move in pairs. Hence, the strengthening by antiphase boundary is easily distinguishable when observing the dislocation structure. Furthermore, in

(*) The situation is different for “composite” reinforcement which may depend on the thermal history due to thermal dilation mismatch between the matrix and the reinforcement, giving rise to internal stresses.

the case of antiphase boundary hardening, the distance between two dislocations of a same pair allows calculating the antiphase boundary energy.

ii. Impenetrable Particles for dislocations

In this case Orowan loops are created as shown schematically in Figure III-4. In addition to the direct effect that particles have on flow stress (stress required for a dislocation to circumvent particles) through Orowan mechanism, they also enhance dislocation storage and thus increase the strain hardening rate. Orowan mechanism is usually expected for incoherent strong particles. If these particles are small and very closely spaced, the line tension of the dislocation may even be able to break the particle.

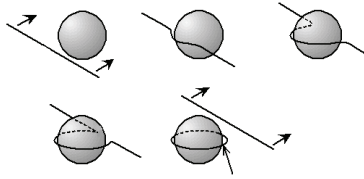
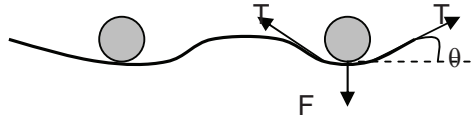


Figure III-4: Orowan looping mechanism

The bending of dislocation is provoked by the pinning of the dislocation at the particles. The pinning force F exerted by each particle being: $F = 2T \sin \theta$ (see Scheme III-1). T being the line tension given by $T = \frac{\mu b^2}{2}$.



Scheme III-1 : bending of dislocations around precipitates [GLA1997]

There exists a maximum force, F_m , which a particle can sustain. If this maximum force is reached before the bending angle θ becomes 90° , the particles will be cut by the dislocation. However, if the bending angle becomes 90° before F_m is reached, the dislocation by-passes the particle by the Orowan mechanism.

General expression of the increase of flow stress due to the presence of precipitates also depends on the inter-particle distance λ_p and is thus given by:

$$\tau = \frac{\mu b}{\lambda_p} \sin \theta \quad (\text{III-2})$$

2) Influence of precipitates on Yield Stress

The influence of precipitated particles on the yield stress of a material depends on their way to interact with dislocations. As mentioned previously there exist two main types of particle-dislocation interactions: the shearing by dislocations and the creation of loops.

i. Particle shearing

Shearing of particles needs less energy and thus is a less hardening method than the bending of dislocations around precipitates. Nevertheless, particles can contribute to the increase of the force necessary to shear the precipitates because, for example, of the more difficult dislocation gliding in the particle, the interaction between dislocation and the matrix-particle interface, or because of elastic interactions between matrix and precipitates. This force is proportional to the precipitate radius R and the strength of the obstacle following:

$$F = k\mu bR \quad (\text{III-3})$$

Where k is a constant expressing the strength of the obstacle

In the case where the Friedel statistics can be applied, namely in the case of shearing precipitates with low obstacle strength [FRI1964], the increase in yield stress due to the presence of precipitates can be written as:

$$\Delta\sigma = 0.7 \frac{k^{3/2} M \mu}{\sqrt{b}} \sqrt{R f_v} \simeq K \sqrt{R f_v} \quad (\text{III-4})$$

K being a constant depending on the material and the obstacle strength.

also written as $\Delta\sigma = M \sqrt{\frac{3 f_v}{2 \pi \mu} \frac{F_c^{3/2}}{R b^2}}$ with $F_c = \left(\frac{2 \pi b^4 \mu R^2}{3 f_v M^2} \Delta\sigma^2 \right)^{1/3}$ where F_c is the obstacle strength (III-5)

ii. Particle by-passing

As described in equation (III-2) the increase in flow stress is inversely proportional to the inter-particle distance, λ_p , which, in the case of spherical particles, can be expressed by the precipitate radius, R , and volume fraction, f_p .

In fact, the definition of the volume fraction is:

$$f_p V = N V_p \quad (\text{III-6})$$

with V being the volume considered, N the number of particles per unit volume and V_p the particle volume. If one considers a volume of thickness $2R$ and length λ_p one will obtain:

$$f_p = N \frac{\frac{4}{3} \pi R^3}{2 R \lambda_p^2} \quad (\text{III-7})$$

Thus, if one takes N equal to 1 we have:

$$\lambda_p = \sqrt{\frac{2\pi}{3f_p}} R \quad (\text{III-8})$$

In the case of non-shearable precipitates we have seen that the bending angle reaches a maximum of 90° giving $\sin \theta = 1$. Thus, $\tau = \frac{\mu b}{\lambda_p} \sin \theta$ becomes:

$$\tau = \frac{\mu b}{\lambda_p} \quad (\text{III-9})$$

which is the classical Orowan equation [ORO1948].

In the case of a polycrystalline material, one needs to consider the Taylor factor, M, to obtain the increase in yield stress due to the presence of non-shearable particles, from the expression of the critical resolved shear stress:

$$\Delta\sigma = \frac{M\mu b}{\lambda_p} \quad (\text{III-10})$$

This Orowan equation supposes that particles which have an important distance to their next neighbors have very little effect on hardening. It was thus modified by A.J.E. Foreman et al. and U.F. Kocks ([FOR1966] and [KOC1966]) into equation (III-11), where the effective distance inter-particles was reevaluated to $1.25\lambda_p$, giving [MAR1980]:

$$\Delta\sigma = 0.8 \frac{M\mu b}{\lambda_p} \quad (\text{III-11})$$

This equation was then modified by M.F. Ashby [ASH1968] taking the distance between particles not as a center-to-center distance but from surface-to-surface. This modification of the classical Orowan equation gives:

$$\Delta\sigma = 0.84 \frac{1.2M\mu b}{2\pi\lambda_p} \ln \left(\frac{d_p}{2b} \right) \quad (\text{III-12})$$

Where d_p is the particle diameter.

The difference observed between the classical Orowan (equation (III-9)) and the Ashby-Orowan equation (equation (III-12)) is shown in Figure III-5. It shows that the Orowan equation tends to overestimate the increase in Yield stress due to precipitates and that this influence is more important in the case of small particles (e.g. 5nm)

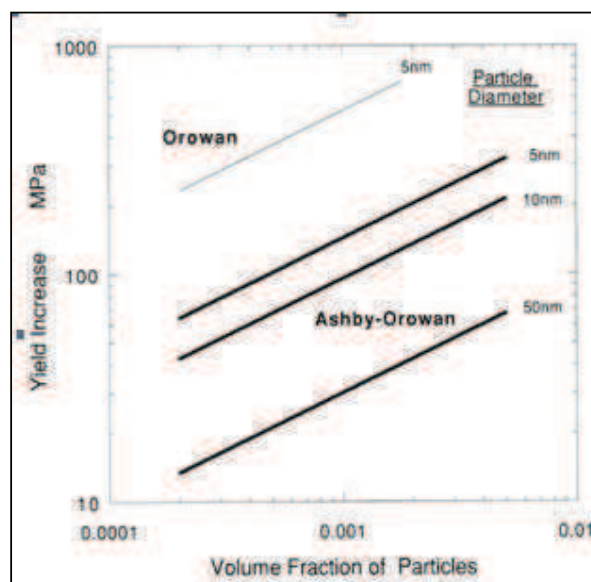


Figure III-5: Graph showing the effect of second-phase particles on the yield stress of materials. Comparison between the Orowan and Ashby-Orowan approach [GLA1997]

D. Mechanical behavior of Fe-Si-Ti alloys

Studies of the Fe-Si-Ti system in the literature concern essentially the precipitation characterization. There exist very few results relating to mechanical properties in the literature. Hardness tests have been performed by Hénon et al. [HEN1966], compression tests have been done by Jack et al. [JAC1975], and more recently Loeffler [LOE2004] measured the hardness of some Fe-Si-Ti alloys aged at high temperatures. Two studies concerning the deformation mechanisms at dislocation scale have been done by Papaleo & Whiteman in [CON1971] and [PAP1970].

1) Yield stress evolution

Figure III-6 shows the hardness curves for an Fe-3.6wt%Si-1.5wt%Ti alloy at different temperatures. One can notice that the highest hardness is obtained at relatively low temperature, 500°C, after close to 300 hours ageing while samples aged at 800°C reach peak hardness in a few minutes.

Compression tests performed on the same alloy are shown in Figure III-7 [JAC1975]. On these curves one can see the contribution of Titanium in solid solution to the increase in yield stress compared to the binary Fe-Si system. Another point of interest is the difference in work-hardening observed between the sample at peak hardness (600°C/1 hour) and the over-aged sample (600°C/125 hours). Usually an increase in work-hardening is associated with a change in deformation mechanism from shearing to by-passing of particles [PAP1971] but it can also be the signature of an important increase in precipitates density. Thus, this would imply that the increase in yield stress for samples aged at 600°C during 1hour (upper Figure III-7) would be due only to solid solution strengthening and shearable particles. The only way to explain a considerable increase of yield stress produced by small volume fractions of shearable particles is that the antiphase boundary energy of the particles is very

high [PAP1971]. In that context, the authors R. Papaleo & Whiteman [PAP1971] tried to observe the evolution of deformation mechanisms in order to explain this increase.

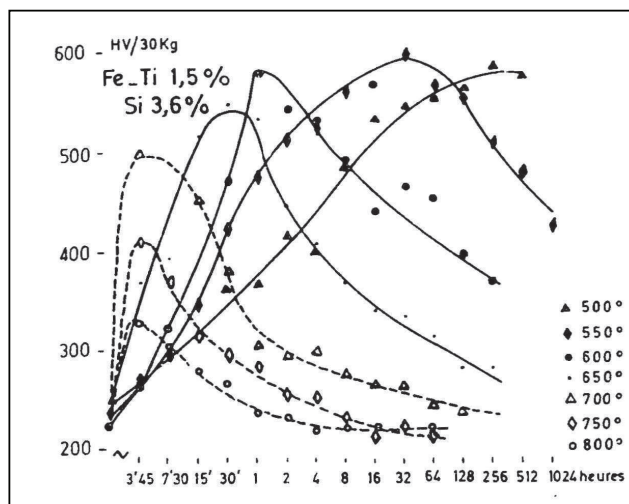


Figure III-6: Hardness evolution with time (log scale) for Fe-3.6wt%Si-1.5wt%Ti samples aged at temperatures ranging from 500°C to 800°C [HEN1966]

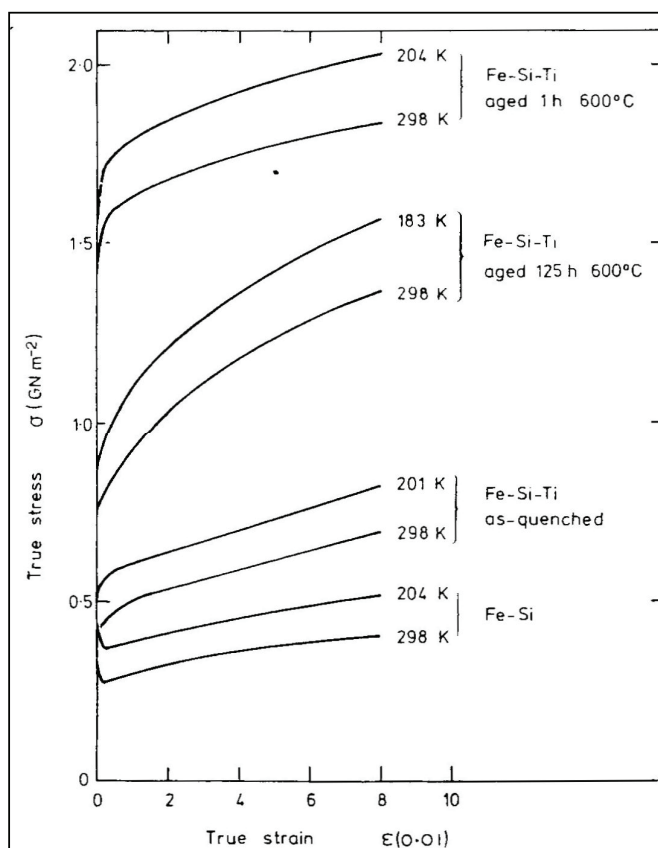


Figure III-7: True stress-true strain curves obtained by compression tests on Fe-Si-Ti samples for three different aging conditions compared with the binary Fe-Si as-quenched sample [JAC1975]

2) Deformation mechanisms

Observation of the dislocation structure can reveal some interesting information concerning the deformation mechanism. In fact, during deformation the dislocations can be stored in different ways such as pile-ups, cells or dislocation pairs (also called superdislocations) or dislocation loops around precipitates. The presence of pile-ups tends to show that the dislocations do not cross-slip easily and accumulate on the same gliding plane.

The structure of deformed samples in the Fe-Si-Ti alloys has been studied extensively by Papaleo & Whiteman ([PAP1970] & [PAP1971]). They observed dislocation structures by TEM thin foils of two alloys at different deformation states: Fe-2.5wt%Si-1.4wt%Ti and Fe-3.5wt%Si-1.4wt%Ti. For as-quenched samples at 1100°C at low deformation ranges, the dislocations are more or less distributed homogeneously within the grains. Some loops are present, probably produced by the pinching-off of dipoles [PAP1971], and the global dislocation structure is similar to the ones observed in binary Fe-Si alloys [GRI1966].

After 13% deformation dislocation cells are formed like those observed in pure iron. For samples containing precipitates, after ageing at 600°C for 20 minutes and very low deformation rates, the dislocation structure looks similar to as-quenched samples. But for samples aged at 600°C during 45 minutes and 1% deformation the authors observed narrow bands of very dense dislocations. A similar dislocation structure was observed for the same heat treatment temperature after 5 hours ageing, but with the addition of some dislocation pairs. For samples aged at 600°C during 100 hours no more superdislocations are observed and the dislocation structure is formed of randomly distributed dislocation loops. This is consistent with observations done by Jack et al. [JAC1972], which report that for specimens aged at 600°C for times longer than 3.3 hours the deformation structure is characterized by strongly bowed single dislocations and loops around precipitate particles. As well as single loops there are loops enclosing several particles, which suggests that they are formed by a classical Orowan mechanism. The slip line behaviour of Fe-Ti-Si alloys at all stages of ageing is similar to that for Fe-Si. Slip is initiated at a limited number of sources, forming pronounced slip bands which broaden by dislocation cross slip as the deformation proceeds. Slip is largely confined to {110} and {112} planes and the dislocations are predominately in screw orientations parallel to $\langle 111 \rangle$ directions.

To summarize, it was observed that in as-quenched samples or in samples after short aging times the dislocations are distributed randomly within the matrix, while the samples containing more precipitates present dislocation arrangements in bands of very dense dislocations. These bands are thought to be due to the more difficult cross-slip enhanced by the presence of Silicon in the matrix. But the peak strength in these alloys is not clearly associated with a transition in the deformation mechanism passing for example from shearing to by-passing of precipitates.

II. Experimental Results

As mentioned in Chapter II, the alloy studied in the present study contains less Silicon than the ones mostly mentioned in literature in order to reduce costs. In fact, Titanium is a

relatively expensive alloying element and the composition of the alloy was chosen so as to contain the minimum of Titanium required in order to harden by precipitation. Studies of the evolution of hardening as a function of the Titanium content have shown an interesting potential of the alloy Fe-2.5wt%Si-1wt%Ti.

A. Vickers Hardness

Hardness tests were performed on samples aged between 450°C and 900°C. Samples aged above 600°C did not show any interesting hardening capacities and therefore the investigations were emphasized on lower temperatures between 450°C and 550°C. Results of hardness measurements are shown in Figure III-8 below. One can see that a hardness of around 400Hv is reached already after a few hours for the samples aged at 550°C. We notice that the hardness already reaches a plateau around 1.5 hours ageing; after that the hardness increases very slowly, even up to 20 hours ageing.

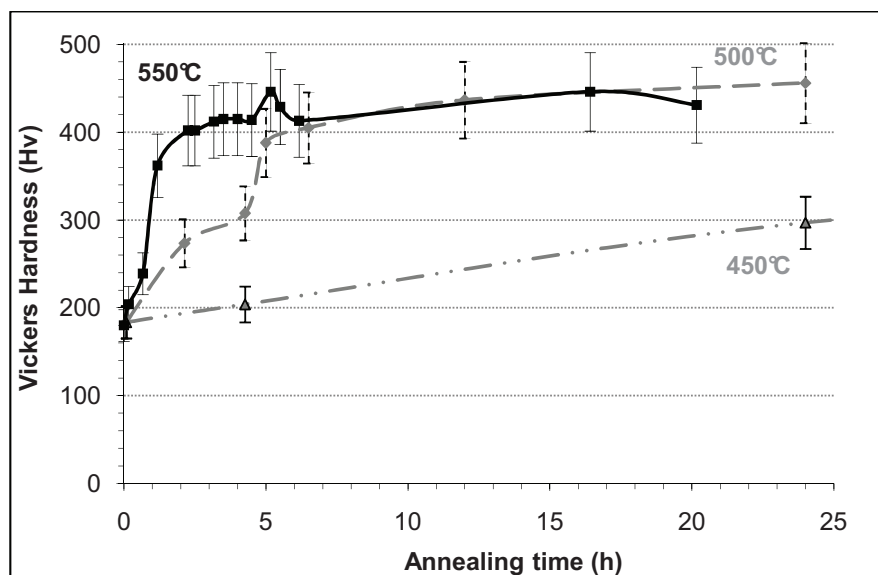


Figure III-8: Vickers Hardness evolution as a function of time for Fe-Si-Ti samples aged at 450°C, 500°C and 550°C

The constant value of the Vickers hardness observed at 550°C shows that the precipitate structure does not evolve in a classical way, namely with the presence of a hardness peak implying the change from shearable precipitates to Orowan loops. This seems consistent with the results found in the literature (Figure III-9) showing that the hardness peak is only reached after more than 64 hours ageing at 550°C, for a sample containing slightly more Silicon and Titanium; thus the hardness peak would probably be reached after even longer ageing times, which was though not checked in the present study.

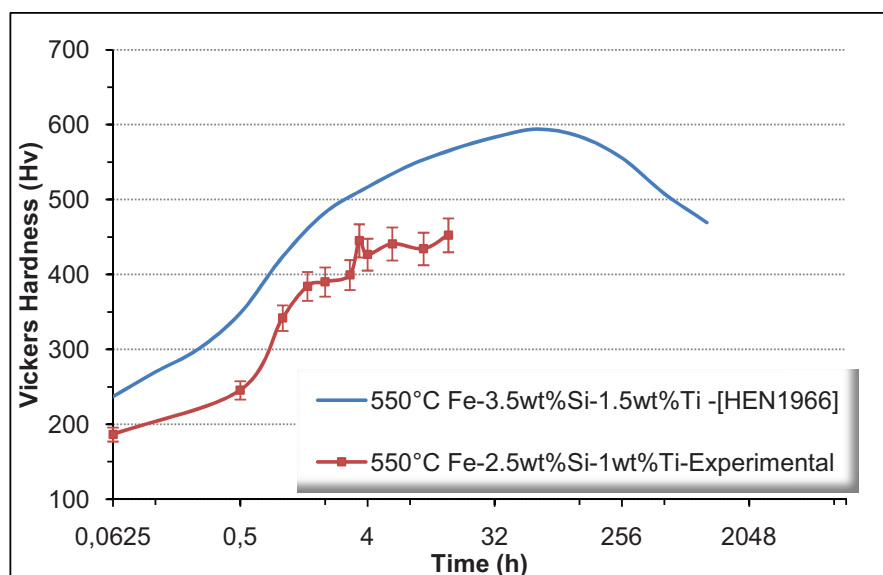


Figure III-9: Comparison between hardness evolution with time from literature [HEN1966] and our experimental data

B. Tensile tests

A much more precise way to measure the yield stress is the tensile test. The complete tensile test curves are reported in Figure III-10 for different durations of precipitation treatments. These were performed on 0.9mm thick sheets of metal (see details in Chapter II). The values of yield stress deduced from the tensile tests were plotted in the graph in Figure III-11. Here we confirm again the observations done with the Vickers hardness tests, showing a slow increase in yield stress after two hours of ageing, before beginning a progressive “re-hardening”.

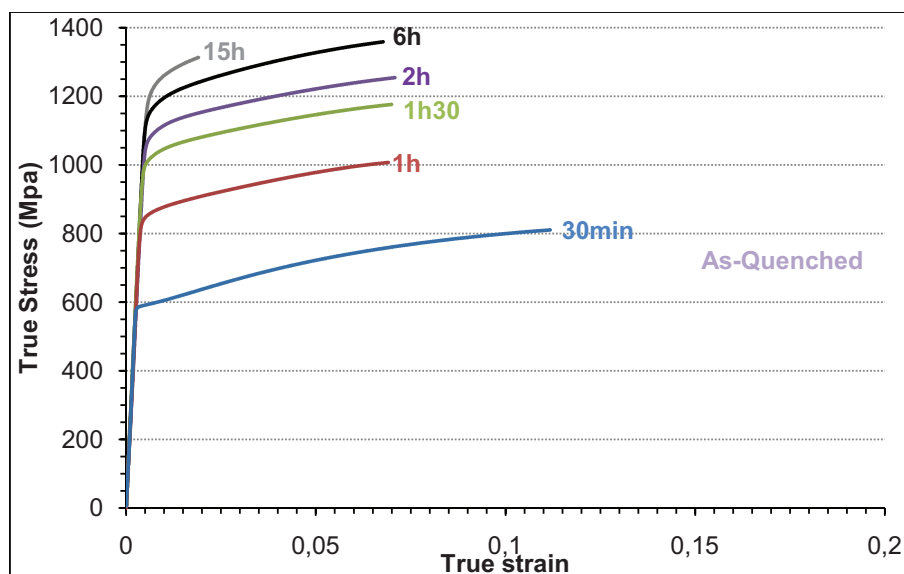


Figure III-10: tensile test curves performed at room temperature on samples aged at 550°C. Evolution of the true stress as a function of the true strain for samples aged for different times.

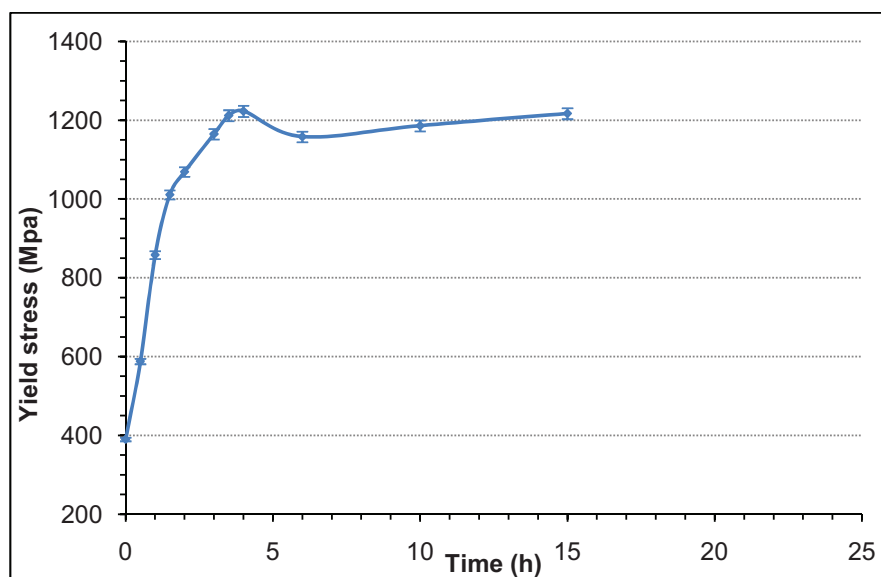


Figure III-11: Yield stress obtained from tensile tests on samples aged at 550°C

In order to check the reproducibility of the yield stress measurements, comparisons between Hardness tests and Yield stress were done. Figure III-12 shows the relatively good correlation between the yield stress measured using the tensile tests and the hardness tests performed on samples used for SANS experiments and those performed on the bars used for tensile tests. This is quite encouraging for the reproducibility of the heat treatments.

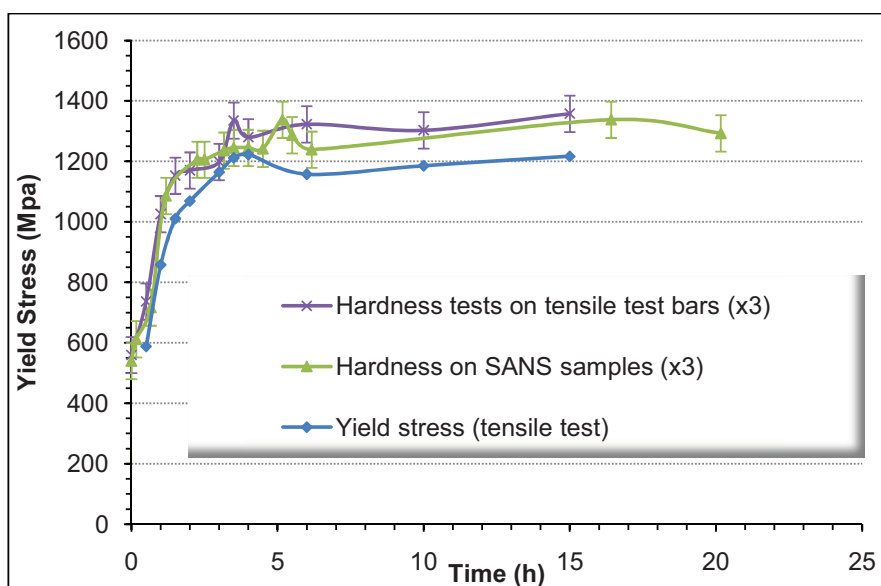


Figure III-12: Comparison between the Yield stress measured by tensile tests, hardness tests performed on same samples and hardness tests performed on samples for SANS experiments

C. Dislocation structures

TEM observation of samples after deformation can give information on the deformation mechanisms involved. Thus, two samples were observed after deformation, thanks to collaboration with X. Wang from the MacMaster University, in order to compare

their dislocation structure: an as-quenched sample (900°C during five minutes) and a sample aged at 550°C during two hours, containing precipitates around 7nm diameter.

Figure III-13, 14 and 15 below show the images of the as-quenched sample after 7% deformation. Deformation was obtained by skin-passing in order to control the deformation rate precisely. In Figure III-13 one can see quite uniformly distributed dislocations, which is consistent with dislocation structure observation found in the literature by Papaleo et al. [PAP1971]. Figure III-14 is a magnified part of the dislocation structure which reveals the presence of loops, although no precipitates are inside the matrix. Thus, these loops are probably simply dislocation pins due to quenching. But the dislocation structure is not homogeneous from one grain to another since some grains present a band structure, as shown Figure III-15. A band structure is often a signature of a relatively planar deformation mechanism.

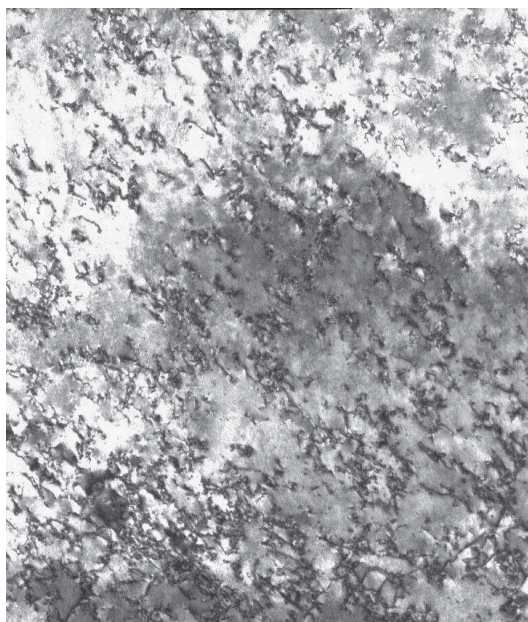


Figure III-13: TEM observation of as-quenched sample after 7% deformation (magnification 35'000x) showing homogeneous dislocation structure

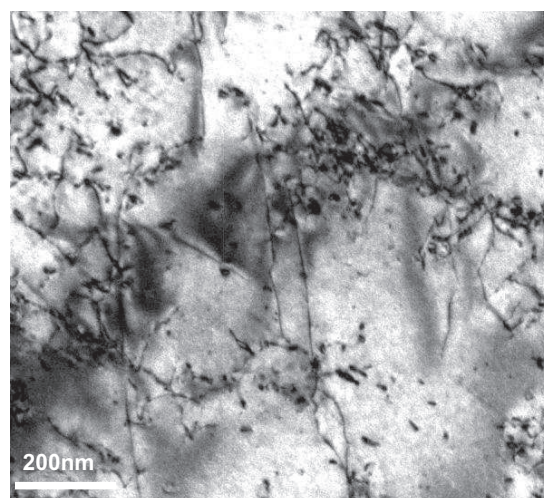


Figure III-14: TEM observation of as-quenched sample after 7% deformation

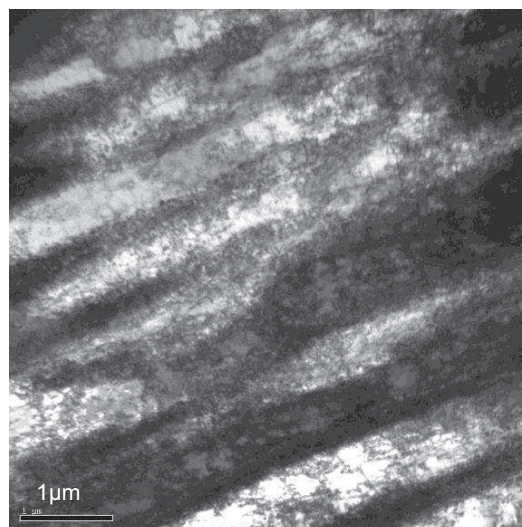


Figure III-15: TEM observation of as-quenched sample after 7% deformation showing well developed cell-walls aligned in certain direction

Observation of the dislocation structure of a sample containing precipitates, aged at 550°C during two hours is shown in figures 16, 17 and 18. Figure III-16 shows the global dislocation structure of the sample aged at 550°C during 2hours and reveals a structure in bands, just as Figure III-17, indicating a planar glide of the dislocations. In fact, it has been often mentioned in the literature that ferrous alloys containing Silicon had a planar dislocation structure ([GRI1966], [WIT2008]). Magnification of a band wall in Figure III-18 shows tangled dislocations and the presence of some dislocation loops, which are probably induced by quenching. The nanometric scale of the precipitates is not visible here.

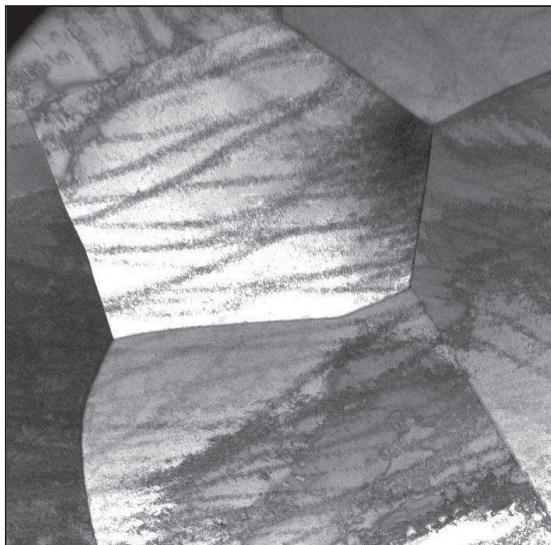


Figure III-16: TEM image at grain scale of sample aged at 550°C during two hours after 5% deformation (grain size ~25μm)

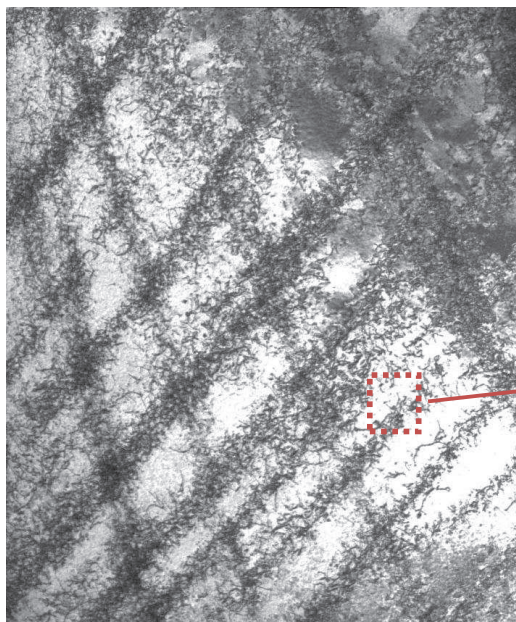


Figure III-17: TEM image of sample aged at 550°C during two hours after 5% deformation (magnification 10'000X)

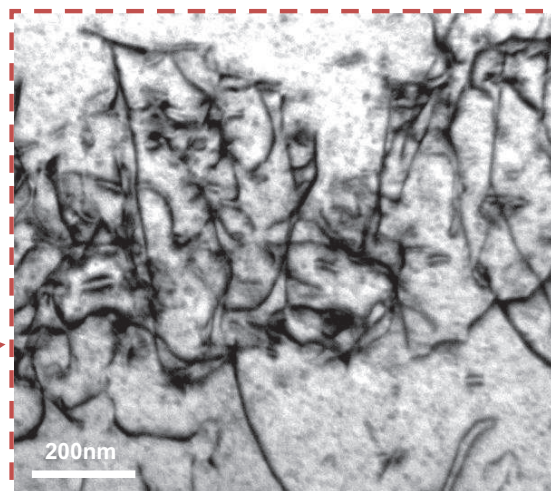


Figure III-18: magnified dislocation cell wall. TEM image of sample aged at 550°C during two hours after 5% deformation

The observation of deformed samples thus did not permit to unambiguously distinguish the deformation mechanism around particles, namely shearing or by-passing of particles, but they confirmed the rather planar slip, that often goes with the presence of Silicon.

III. Conclusion

In the present chapter we have seen the different parameters influencing the yield stress and particularly the presence of precipitates. Experimental results of hardness tests and tensile tests have been presented showing a very interesting hardening potential of the Fe-Si-Ti alloy. In fact, the yield stress measured reached values of up to 1300MPa for samples aged at 550°C, indicating the presence of an important density of precipitates. Thus, in order to understand the influence of the precipitates on the mechanical behavior of the Fe-Si-Ti alloy, the precipitation needs to be characterized, which is the objective of the next chapter.

Chapter IV : Precipitation reactions in Fe-Si-Ti: kinetics and modeling

In the following chapter, we will present the general aspects of precipitation namely the different steps of nucleation, growth and coarsening by the description of existing models. Then, we will review the state of the art concerning precipitation kinetics and structure in the Fe-Si-Ti system. Finally, the experimental results of precipitation characterization obtained by SANS and APT will be presented and briefly compared with theoretical modeling.

INTRODUCTION	101
I. LITERATURE REVIEW	101
A. General description of precipitation.....	101
B. Modeling: existing models of precipitation kinetics	102
1) Classical nucleation, growth and coarsening model	102
i. Nucleation	102
ii. Growth.....	104
iii. Coarsening.....	105
2) Model for homogeneous precipitation: nucleation, growth and coarsening as coupled phenomena	106
i. Nucleation and growth:	106
ii. Growth and coarsening:	107
3) Modeling by classes of precipitates: "Multiprécipité"	108
C. State of the art on precipitation in the Fe-Si-Ti alloy	109
1) Binary systems	110
i. Fe-Si	110
ii. Fe-Ti	111
iii. Si-Ti.....	112
2) Ternary System Fe-Si-Ti.....	113
i. Structure and composition	115
ii. Precipitation kinetics	117
II. EXPERIMENTAL CHARACTERIZATION OF PRECIPITATION IN THE FE-SI-TI SYSTEM	120
A. Precipitation during heat treatments at 550°C	120
1) Mean microstructural data : SANS experiments.....	120
2) Imaging and Electron diffraction analysis: TEM	122
3) Quantitative microstructural analysis: APT.....	125
i. As-quenched sample	125
ii. Precipitation treatment at 550°C during 2 hours	126
iii. Precipitation treatment at 550°C during 3.5 hours.....	128
iv. Precipitation treatment at 550°C over 6 hours.....	131
v. Sample aged at 550°C during 20hours	133
B. Other temperatures	135
1) 450°C-500°C	135
2) 520°C and 580°C	135
C. Influence of the initial state	137
III. MODELING OF THE PRECIPITATION KINETICS	138

A.	Model “DBPreci”	139
B.	Class Model	142
1)	Modeling results	142
2)	Influence of the parameters on the modeling results	143
i.	550°C	144
ii.	Other temperatures.....	145
3)	Influence of the alloy composition on the precipitation kinetics	146
i.	Constant initial solubility product	147
ii.	Variable initial solubility product.....	148
C.	Comparison between DBPreci and Multipreci models.....	150
IV.	CONCLUSION.....	151

USED SYMBOLS

c_m^e = Composition of matrix at equilibrium [at%]

c_p^e = Composition of precipitate at equilibrium [at%]

a_M = Lattice parameter of the matrix [m]

a_P = Lattice parameter of the precipitate [m]

c_0 = Composition of solid solution [at%]

D = Volume diffusion coefficient [m^2/s]

D_0 = Frequency factor

F_{ch} = Chemical free energy due to the change in local chemical composition [J/mol]

F_{el} = Strain free energy due to the change in structure [J/mol]

k = Boltzmann constant = $1,38 \cdot 10^{-23}$ [J/K]

N = Number density of precipitates

N_0 = Number of potential nucleation sites

R = Radius of particles [m]

R^* = Critical radius [m]

T = Temperature [K°C]

V_p = Molar Volume of precipitate [m^3/mol]

Z = Zeldovich factor

μ = Shear modulus

δ = Misfit between matrix and precipitates

ΔG = Change in total free energy [J/mol]

ΔG^* = Maximum value of total free energy [J/mol]

ν = Possion's ratio

σ = Interfacial energy [J/m²]

τ = Incubation period [s]

Introduction

The study of precipitation phenomena is nowadays one of the fundamental tools for new research of new alloy design since metals containing precipitation have been proven to be interesting in terms of mechanical properties, corrosion resistance, and weldability. In the following chapter, we will provide a general description of precipitation phenomena; it will then be applied to the present example, the Fe-Si-Ti alloy. Finally, modeling of precipitation kinetics will be presented and applied to the present system.

I. Literature review

A. General description of precipitation

Decomposition of supersaturated solid solution can take place by two main mechanisms: nucleation and growth or spinodal decomposition. The distinction between the two processes, although clearly defined from a theoretical viewpoint, is difficult to make on an experimental basis. Most metallic alloys seem to undergo the classical nucleation and growth mechanism, or rapidly evolve toward this situation. Hence, it will be the only process described in the following.

The nucleation, growth and coarsening theory differentiates 3 steps in isothermal precipitation (see Figure IV-1), corresponding to a progressive decrease in the driving force for precipitation. First the birth of nuclei in the matrix leading to an increase of the volume fraction at roughly constant precipitate radius; followed by the growth, meaning an increase in the radius of precipitates while the number density stays constant. And finally coarsening, leading to a saturation of volume fraction but an increase in radius. These three “idealized” steps are in fact continuously evolving one into another.

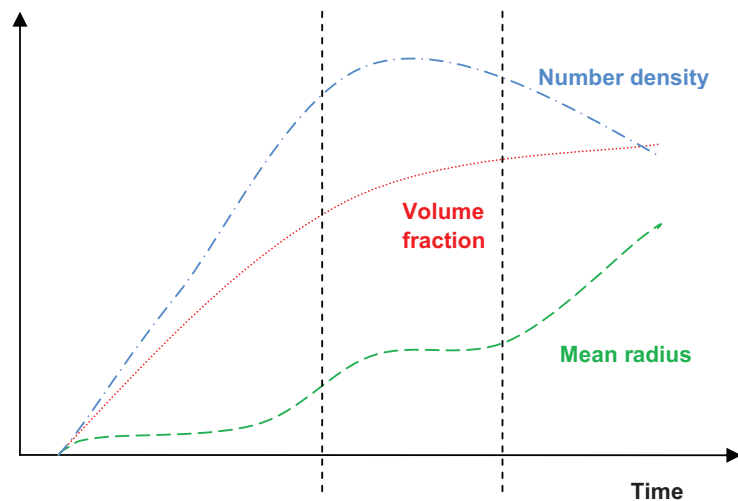


Figure IV-1: scheme of the evolution of Radius, Volume Fraction and number density with time

A great number of studies attempted to describe completely these different stages in precipitation by modeling tools.

B. Modeling: existing models of precipitation kinetics

The modeling of precipitation kinetics is a classic issue in material science and therefore a great number of models already exist and have been tested successfully. They can be physically-based or phenomenological. In the following part, the classical approach of nucleation-growth-coarsening approach will be described, as well as some more recent models considering the nucleation-growth-coarsening together in a simultaneous description.

1) Classical nucleation, growth and coarsening model

This approach is based essentially on the early works of Becker and Döring [BEC1935]. Classical nucleation-growth-coarsening models take the three steps as separated from each other. All three will be presented in detail, inspired by the PhD Thesis of M. Nicolas [NIC2002] and F. Perrard [PER2004].

During nucleation the supersaturation of the solid solution leads to an increase of the number of precipitates. Once the driving force for nucleation is too low, the precipitates start to grow, while the number density stays constant (see Figure IV-1). Once the supersaturation of the solid solution is close to zero the only driving force for the evolution of the system is the reduction in surface energy, which leads to the coarsening step, meaning a growth of the large particles and dissolution of the small ones. The number density during coarsening starts to decrease [PER2004].

i. Nucleation

Precipitation from solid solution appears after appropriate annealing treatments. The driving force for this precipitation is the decrease in global free energy of the system.

There exists a competition between two components of the free energy which are the chemical free energy and the elastic free energy.

The decrease of chemical free energy is due to the change in local chemical composition given by equation (IV-1)) in the case of a supersaturated matrix and a binary system (in the case of ideal-dilute-solution approximation) [WAG1991].

$$\Delta F_{ch} = -\frac{k_B T}{V_p} \left[c_p^e \ln \left(\frac{c_0}{c_m^e} \right) + (1 - c_p^e) \ln \frac{1 - c_0}{1 - c_m^e} \right] \quad (\text{IV-1})$$

- k_B being the molar gas constant
- T the given temperature
- V_p the molar volume of the precipitate
- c_0 the composition of the solid solution [at%]
- c_p^e and c_m^e the composition of precipitate and matrix at equilibrium [at%]

The reduction of free energy induced by the change in chemical composition is decreased by the elastic strain energy due to the change in structure, inducing new strains at

the precipitate-matrix interface, essentially due to the difference in atomic radii. The elastic strain energy is given by:

$$\Delta F_{el} = 2\mu \left(\frac{1+\nu}{1-\nu} \right) \delta^2 \quad (IV-2)$$

- μ being the shear modulus
- δ is the misfit between matrix and precipitate: $\delta = 2 \frac{a_m - a_p}{a_m + a_p}$ with a_m and a_p being respectively the lattice parameter of the matrix and the precipitate

The cluster dynamics approach images the formation of precipitates as droplets embedded in a supersaturated matrix with a sharp interface between the two phases. Hence another term needs to be added to the change in energy due to the nucleation of a new phase, the interfacial energy σ .

Thus, the change in free energy associated with the formation of a coherent cluster with radius R is expressed as:

$$\Delta G(R) = (\Delta F_{ch} + \Delta F_{el}) \frac{4\pi}{3} R^3 + 4\pi R^2 \sigma \quad (IV-3)$$

This explains the formation of metastable phases in the early stages of nucleation, which are often coherent, reducing the interface energy, and with a small misfit with the matrix.

The first term is negative since it represents the gain of free energy due to the formation of the cluster. The second term is positive since it stands for the formation of a new interface which requires energy. The dependence on the radius of the cluster leads to the idea that there exists a critical radius for the formation of a stable nucleus. Clusters of radius R^* are in unstable equilibrium with the solid solution. Therefore only clusters with radii exceeding the radius R^* of the critical nucleus are predicted to grow. This critical radius, R^* , leading to the maximum $\Delta G(R^*) = \Delta G^*$ of the free energy is expressed as:

$$R^* = \frac{-2\sigma}{(\Delta F_{ch} + \Delta F_{el})} \quad (IV-4)$$

and

$$\Delta G^* = \frac{16\pi}{3} \frac{\sigma^3}{(\Delta F_{ch} + \Delta F_{el})} \quad (IV-5)$$

A difficult step in the description of the nucleation phenomenon is to calculate the probability for a nucleus to have this critical size and to grow above it. Several studies [VOL1925], [BEC1935] & [ZEL1949] permitted to express the nucleation rate: the density of over-critical nuclei (number of over-critical nuclei appearing per unit time and volume). This parameter was given, in the case of a steady-state, as:

$$\left. \frac{dN}{dt} \right|_s = Z\beta^* N_0 \exp\left(\frac{-\Delta G^*}{k_B T}\right) \quad (\text{IV-6})$$

- N_0 being the number of potential nucleation sites
- Z is the Zeldovich factor, expressing the fluctuation of the particle radius around the critical radius value R^* .

$$Z = \left(\frac{V_p}{2\pi R^{*2}} \right) \sqrt{\frac{\sigma}{k_B T}} \quad (\text{IV-7})$$

- β^* is the atomic impingement rate:

$$\beta^* = \frac{4\pi R^{*2} D C_0}{a^4} \quad (\text{IV-8})$$

a being the cluster lattice parameter

The steady-state is not reached immediately; hence a time factor is added to introduce a transitory nucleation rate (equation (IV-9)) the incubation period τ (equation (IV-10)).

$$\frac{dN}{dt} = \left. \frac{dN}{dt} \right|_s \left(1 - \exp\left(\frac{-t}{\tau}\right) \right) \quad (\text{IV-9})$$

$$\tau = \frac{1}{2Z\beta^*} \quad (\text{IV-10})$$

ii. Growth

After nucleation one can consider the growth of precipitates. The growth rate is proportional either to the rate at which atoms are supplied to the matrix/particle interface by diffusion (long range scale) or by the rate at which they cross the interface, meaning the interface mobility (short-range scale). When the particles are still small, the diffusion distances are short and the interface reaction is usually the rate controlling step. Though, when the particles start to grow, this is associated with a lower supersaturation of the matrix, reducing the driving force and making diffusion slower. Hence, diffusion becomes the rate controlling step at this point, and it is assumed to be true during the whole growth process [WAG1991]. Under this assumption it is considered that local thermodynamical equilibrium is reached at the particle-matrix interface at all times.

The growth of a spherical particle with radius R and concentration c_p surrounded by a matrix is expressed as equation (IV-11) below, under the assumption of a same atomic volume inside the precipitates and in the matrix.

$$\frac{dR}{dt} = \left(\frac{\bar{c}(t) - c_{M/P}}{c_p - c_{M/P}} \right) \frac{D}{R} \quad (\text{IV-11})$$

- D is the diffusion coefficient of the matrix $D = D_0 \exp \left(\frac{-Q_{diff}}{k_B T} \right)$
- $c_{M/P}$ the composition at the matrix/precipitate interface
- $\bar{c}(t)$ the mean concentration of the matrix

The concentration at the interface is proportional to the concentration of the matrix at equilibrium, c_m^e , via a corrective term that accounts for the Gibbs-Thomson effect:

$$c_{M/P}(R) = c_m^e \exp \left(\frac{2\sigma V_p}{k_B T R} \right) \quad (IV-12)$$

- σ is the interfacial energy
- V_p the molar volume of precipitates

iii. Coarsening

Classically, while precipitation proceeds, and decreases the available driving force, the system is described as going from a nucleation regime (increasing number of precipitates) to a growth regime (constant number of precipitates) to a coarsening stage (decreasing number of precipitates). Thus, the coarsening process is usually considered to be confined to the latest stage of a precipitation reaction. However, coarsening may accompany the growth process or may even start while the system is still in its nucleation period, depending on the initial supersaturation of the solid solution [WAG1991].

Once the driving force for growth by diffusion has sufficiently decreased, the particles will coarsen in order to reduce the surface energy. The Gibbs-Thomson equation (equation (IV-12)) predicts the lower solubility of larger particles, meaning that small particles will dissolve while larger will grow. The critical radius between growth and dissolution, R^* is expressed as [NIC2002]:

$$R^* = \frac{2\sigma V_p}{k_B T C_p} \frac{1}{\ln \left(\frac{\bar{c}}{c_i^\infty} \right)} \quad (IV-13)$$

In the case of an infinitely diluted matrix, one can apply the radius evolution after the Lifshitz-Slyozov-Wagner equation (LSW) ([LIF1961] & [WAG1961]), when $R=R^*$, one can write the evolution of mean radius as:

$$R^3 - R_0^3 = K t \quad (IV-14)$$

Where

$$K = \frac{8\sigma D c_m^e V_p^2}{9k_B T} \quad (IV-15)$$

- D being the diffusion coefficient of the solute in the matrix at temperature T

- c_m^e is the equilibrium molar concentration of solute in the matrix
- V_p is the molar volume of solute in the particle
- k_B is the Boltzmann constant

If the coarsening rate is considered to be controlled by the diffusivity of one type of atom alone, it is reasonable to expect that this will be the solute for which the diffusive flux is lowest.

2) Model for homogeneous precipitation: nucleation, growth and coarsening as coupled phenomena

The model described in this part has been developed by A. Deschamps and Y. Bréchet in [DES1999]. It is principally based on works by Langer and Schwartz [LAN1980] and later modified by Wagner and Kampmann [WAG1991] and was developed in the case of an Aluminum alloy (Al-Zn-Mg). The system is considered to be quasi-binary, meaning that the diffusion of solute atoms can be described by an equivalent diffusion coefficient.

This model considers nucleation, growth and coarsening as coupled phenomena. In fact they are divided in two main steps: the nucleation-growth and the growth-coarsening. Passing from one step to another is described by a simple criterion.

The assumptions are as follows:

- Ternary system
- Only one type of precipitates
- Precipitates are spherical and stoichiometric in a homogeneous matrix
- The growth is diffusion controlled at a large distance from the limiting element
- The interfacial energy is considered as being isotropic
- The equilibrium at the matrix-particle interface is kept, with a Gibbs-Thompson correction

General thermodynamics of the model are the same as for the classical nucleation, growth and coarsening model described previously. Hence, expressions of the driving force are still applicable here. The differences are in the coupling of nucleation and growth and growth and coarsening.

i. Nucleation and growth:

In the first steps of precipitation, the variation of the precipitate density is given by the nucleation rate:

$$\left. \frac{dN}{dt} \right|_{\text{Nucleation}} = Z\beta^* N_0 \exp\left(\frac{-\Delta G^*}{k_B T}\right) \left(1 - \exp\left(\frac{-t}{\tau}\right)\right) \quad (\text{IV-16})$$

The growth rate is given below, with reference the slowest diffusing element:

$$\left. \frac{dR}{dt} \right|_{\text{Growth}} = \frac{\bar{C}(t) - C_i}{C_p - C_i} \frac{D}{R} \quad (\text{IV-17})$$

Coupling the two phenomena (nucleation and growth) enables to simplify the equations. The final expression of the radius evolution is composed of two terms, namely the growth of precipitates already existing and the appearance of new precipitates at the nucleation radius R' . This is expressed as:

$$\left. \frac{dR}{dt} \right|_{\text{Nucl-Growth}} = \frac{D}{R} \frac{C_{SS} - C_i}{C_p - C_i} + \frac{1}{N} \frac{dN}{dt} (R' - R) \quad (\text{IV-18})$$

Where C_{SS} is the composition of the solid solution and R' is the modified nucleation radius of precipitates, above which their probability of growing is close to 1. It is slightly larger than R^* , expressed by:

$$R' = R^* + \frac{1}{2} \sqrt{\frac{k_B T}{\pi \sigma}} \quad (\text{IV-19})$$

Transition from the nucleation-growth to the growth-coarsening stages is progressive. One can define a simple criterion for passing from one to another, which is when the diminution of the precipitates density by coarsening is larger than the increase of the precipitates density by nucleation:

$$\left| \frac{dN}{dt} \right|_{\text{Growth-coars}} > \left| \frac{dN}{dt} \right|_{\text{Nucleation}} \quad (\text{IV-20})$$

ii. Growth and coarsening:

In later stages of precipitation, if the mean particle radius, \bar{R} , is much larger than the critical radius R^* ($\bar{R} \gg R^*$), meaning that all particles are growing whatever their size, the pure growth equations can be applied:

$$\left\{ \begin{array}{l} \left. \frac{dR}{dt} \right|_{\text{Growth}} = \frac{C_{SS} - C_i}{C_p - C_i} \frac{D}{R} \\ \frac{dN}{dt} = 0 \end{array} \right. \quad (\text{IV-21})$$

$$(\text{IV-22})$$

The other limiting case is when $\bar{R} = R^*$, which defines the conditions where the Lifshitz-Slyosov-Wagner (LSW) theory applies, and therefore ([LIF1961] & [WAG1961]):

$$\left\{ \begin{array}{l} \frac{dR}{dt} \Big|_{Coars} = \frac{4}{27} \frac{C_e}{1 - C_e} \frac{2\sigma V_p D}{k_B T R^2} \end{array} \right. \quad (IV-23)$$

$$\left\{ \begin{array}{l} \frac{dN}{dt} \Big|_{Coars} = \frac{4}{27} \frac{C_e}{1 - C_e} \frac{2\sigma V_p D}{k_B T R^3} \left[\frac{2\sigma V_p}{k_B T R} \frac{C}{1 - C} \left(\frac{3}{4\pi R^3} - N \right) - 3N \right] \end{array} \right. \quad (IV-24)$$

Where $\frac{dN}{dt} \Big|_{Coars}$ is determined from the mass conservation.

The transition between growth and coarsening is determined by a criterion, the coarsening fraction, f_{coars} . It varies between 0 and 1 and makes the transition continuous.

$$f_{coars} = \sup \left[1 - 100 \left(\frac{f_v}{f_v^{eq} - 1} \right)^2, 0 \right] \quad (IV-25)$$

- f_v is the precipitated volume fraction
- f_v^{eq} the equilibrium volume fraction of precipitates of radius R

This transition parameter is then used to determine the radius evolution and precipitate density evolution.

$$\left\{ \begin{array}{l} \frac{dR}{dt} = (1 - f_{coars}) \frac{dR}{dt} \Big|_{Growth} + f_{coars} \frac{dR}{dt} \Big|_{Coars} \end{array} \right. \quad (IV-26)$$

$$\left\{ \begin{array}{l} \frac{dN}{dt} = f_{coars} \frac{dN}{dt} \Big|_{Coars} \end{array} \right. \quad (IV-27)$$

3) Modeling by classes of precipitates

The precipitation models described previously consist either in separating the three precipitation steps (classical model) or by considering them correlated and introducing an artificial criteria to pass from one to another.

The model by classes of precipitates is another approach where the different precipitation steps are always correlated and “classes” of precipitates sizes are defined [ACE2007]. For each time step equations of nucleation, growth and coarsening are resolved simultaneously. The model cited here uses the same mathematical tools as presented in “Multipréci”, which was developed by D. Gendt and P. Maugis in the case of NbC precipitates in ferrite [GEN2001] and applied also to the Nb(C,N) in ferrite by P. Maugis and M. Gouné in [MAU2003] and [MAU2005].

The equations used for nucleation and growth are the same as before, namely equations (IV-16) and (IV-17). To describe the coarsening process, the Gibbs-Thomson effect is taken into account in the growth equation, and does not need any new equation.

The following description concerns only the global idea of the model, for further details one can refer to [GEN2001].

Two main steps are permanently correlated in this model: the definition of a new class and the disappearance of another.

Definition of a new class:

Nucleation implies to consider a new class of precipitate size when ΔN is larger than a certain fraction of the total density of precipitates (10^{-7} - 10^{-8}), N being the density of precipitates. This new class will contain precipitates with a radius slightly larger than the critical radius so that they will grow. When ΔN is too low, we can consider that the nucleation process is over, meaning supersaturation is depleted.

Phase dissolution:

During coarsening, it is important to take into account not only the growing precipitates (over critical radius) but also the ones that dissolve (sub critical). Hence it is necessary to introduce a parameter for the dissolution of the precipitates, meaning the loss of a class. This will enable to suppress a class of precipitate. The criterion chosen is that all precipitates having a size lower than 1/10 of the critical radius, are considered to dissolve into solid solution.

The time step is taken so as to fit the particle size histogram. Hence, it will be short for the nucleation process and will grow afterwards. This model can also be used in the case of dissolution of particles like has been done for the heat-affected zone of a welded material by M. Nicolas [NIC2002] in the case of Al-Zn-Mg.

The precipitation models concern especially Aluminum alloys, for which the knowledge is very much advanced today. No results of modeling of the precipitation in the Fe-Si-Ti alloys can be found in literature, but numerous works concern the precipitation characterization, which will be described in the following part.

C. State of the art on precipitation in the Fe-Si-Ti alloy

The addition of the alloying elements Silicon and Titanium in steels is common today in all sorts of applications. Silicon is for example known to increase corrosion resistance and strain-hardening of steels. So does the addition of Titanium and it can produce a precipitation reaction leading to stable Fe_2Ti particles.

The capacity of Titanium and Silicon to form intermetallic precipitation in iron-based alloys as well as their hardening potential was first noticed in the 1930's by Wasmuht [WAS1931]. The Fe-Si-Ti system was the subject of many other research projects later in the 1970's ([ABS1968]; [BOW1968]; [BRA1968]; [HEN1966]; [JAC1970]; [JAC1972]; [JAC1975];

[PAP1970]; [SCH1969]; [WAL1976]). The observation methods used in the studies found in literature for precipitation are mainly FIM (Field Ion Microscope) and TEM (Transmission Electron Microscope); each of them give different information concerning their structure, their composition or their size and volume fraction.

In the following part the main results found in these papers are summarized. First we will describe briefly the binary systems Fe-Si, Fe-Ti and Si-Ti, then we will present the different potential precipitate phases present in the ternary system and give a description of the structure and composition of the alloys, followed by the precipitation kinetics.

1) Binary systems

i. Fe-Si

Binary Fe-Si system has been studied by several authors, as for example Massalski in [MAS1990], especially with high Silicon concentrations. The Fe-rich part of the binary phase diagram was especially investigated in terms of its well-known Goss-texture ([MIS1984] & [MAG1994]).

The phase diagram of the binary Fe-Si system is shown Figure IV-2. It appears that in the composition intervals which will be of interest in this study, meaning between 0 and 4wt% Silicon, appear the BCC α -Fe phase of Pearson symbol cI2 and phase group $Im\bar{3}m$ or the BCC-B2 Fe_3Si phase with Pearson symbol cF16 phase group $Fm\bar{3}m$ and DO3 structure (shown as α_1 on Figure IV-3).

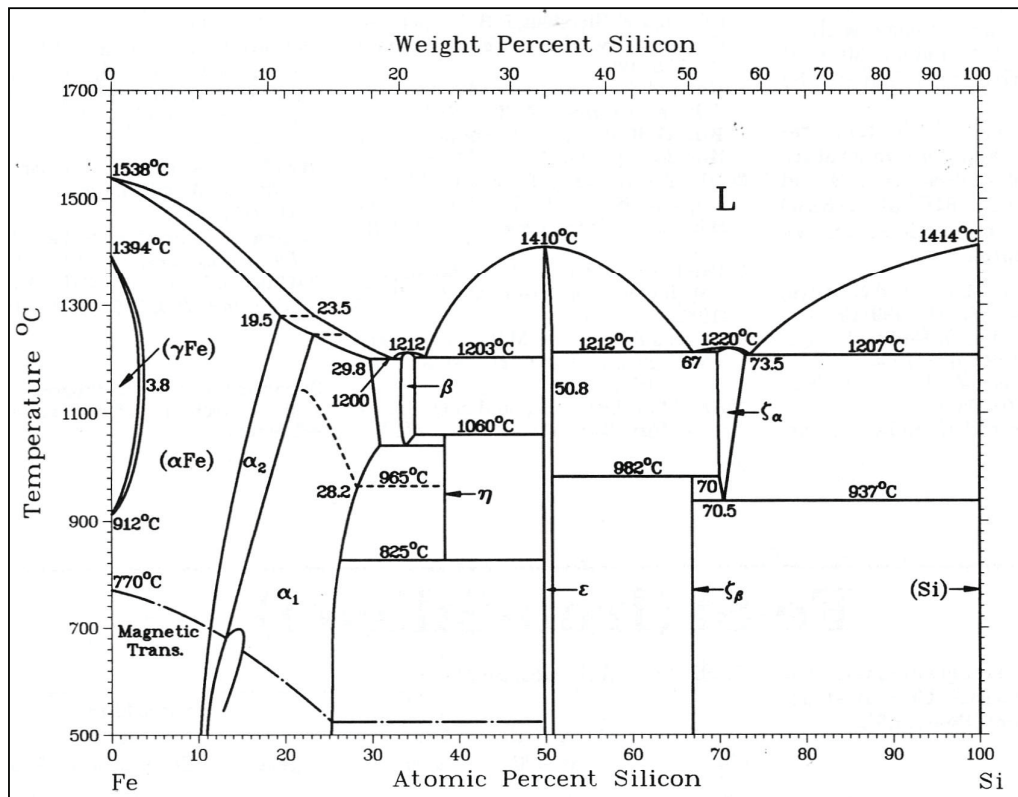


Figure IV-2: phase diagram of binary system Fe-Si [MAS1990]

Fe-Si Crystal Structure Data					
Phase	Composition, at.% Si	Pearson symbol	Space group	Struktur- bericht designation	Prototype
(α Fe).....	0 to 3.19	<i>cI2</i>	<i>Im\bar{3}m</i>	A2	W
(γ Fe).....	0 to 19.5	<i>cF4</i>	<i>Fm\bar{3}m</i>	A1	Cu
α_2	-10 to 22	<i>cP2</i>	<i>Pm\bar{3}m</i>	B2	CsCl
α_1	-10 to 30	<i>cF16</i>	<i>Fm\bar{3}m</i>	D0 ₃	BiF ₃
Fe ₂ Si.....	~ 33.3	<i>hP6</i>	<i>P\bar{3}m1</i>
Fe ₅ Si ₃	37.5	<i>hP16</i>	<i>P6₃/mcm</i>	D8 ₈	Mn ₅ Si ₃
FeSi.....	~50	<i>cP8</i>	<i>P2₁3</i>	B20	FeSi
α FeSi ₂	66.7	<i>oC48</i>	<i>Cmca</i>
β FeSi ₂	69.5 to 73.5	<i>tP3</i>	<i>P4/mmm</i>
(Si).....	100	<i>cF8</i>	<i>Fd\bar{3}m</i>	A4	C(diamond)

Figure IV-3: details of the FeSi phase diagram [MAS1990]

ii. Fe-Ti

The binary Fe-Ti alloy is used essentially today in the case of Ferrotitanium alloys using from 10 to 40wt% Titanium. They are known for their high corrosion resistance and interesting strength with very long lifetimes.

The phase diagram of the binary Fe-Ti system is given Figure IV-4 where we see that in the Fe-rich part the precipitation of the Fe₂Ti precipitates in the α -phase is very stable up to 1293°C. Another phase in this binary Fe-Ti diagram is the FeTi phase which is found in alloys containing high amounts of Titanium (around 50%).

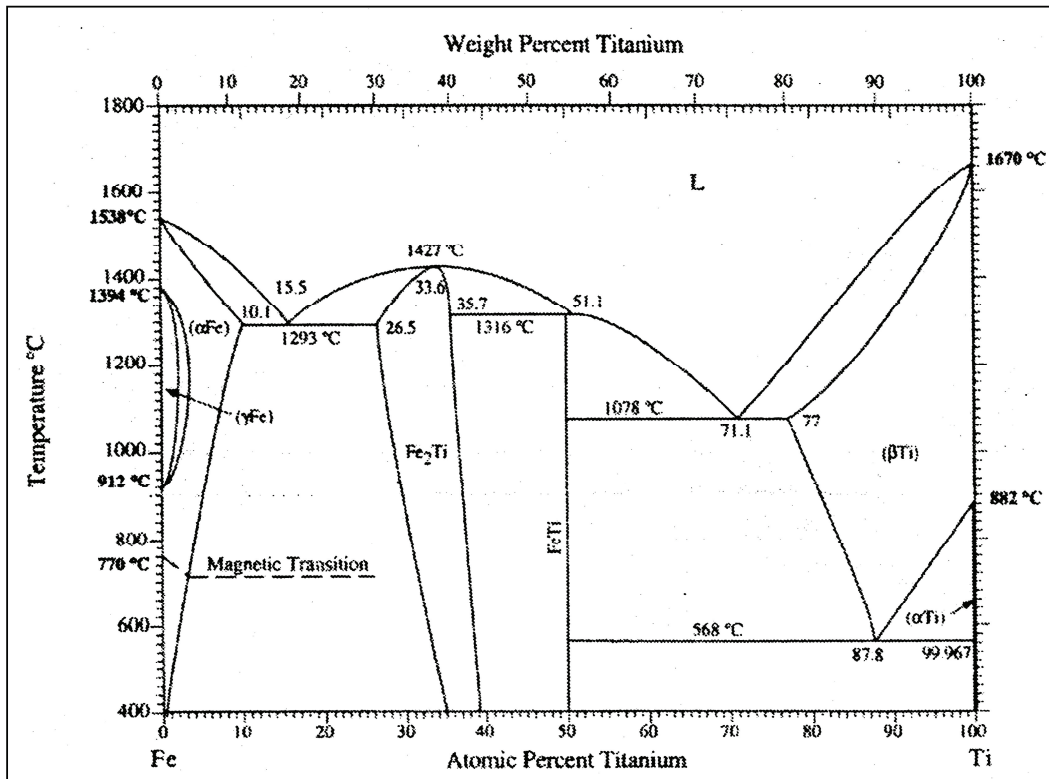


Figure IV-4: phase diagram of binary Fe-Ti system [LOE2003]

iii. Si-Ti

Binary phase diagram of Si-Ti system based on work of Massalski [MAS1990] is given Figure IV-5 below. Five phases are known in this binary system: TiSi_2 , TiSi , Ti_5Si_4 , Ti_5Si_3 and Ti_3Si . It appears that for compositions with same Ti/Si proportions as studied hereby, meaning approximately 1 to 5, the phases at equilibrium could be TiSi or TiSi_2 .

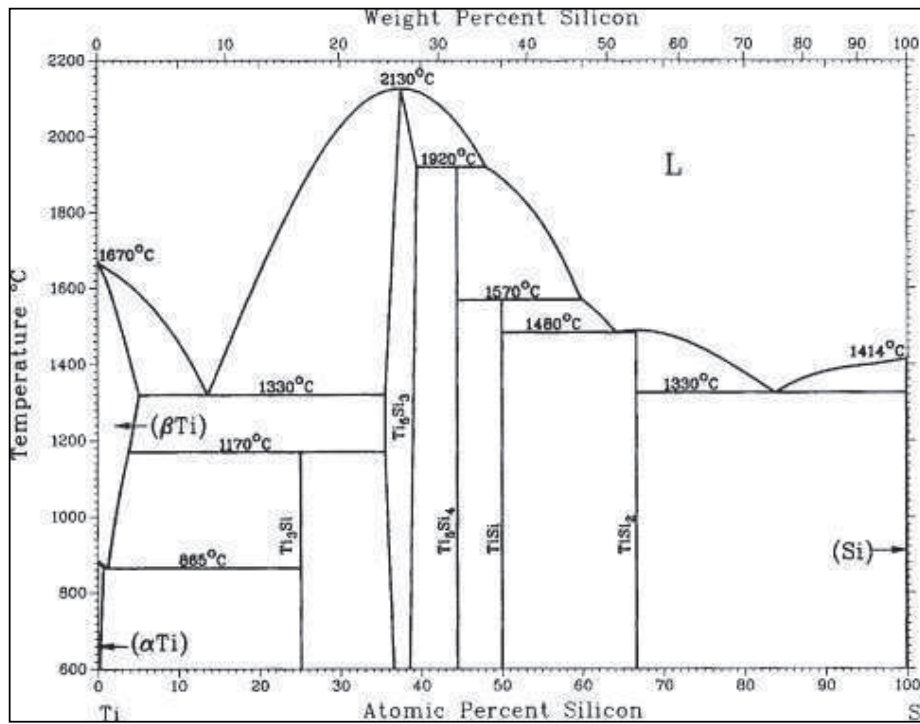


Figure IV-5: phase diagram of binary Si-Ti system [MAS1990]

2) Ternary System Fe-Si-Ti

The very first mention of this ternary system was found in works by R. Vogel [VOG1909] followed years later by Wasmuth [WAS1931]. The first study concerning the ternary phase diagram was done by R. Vogel in [VOG1938] and later V. Raghavan investigated it very accurately in [RAG1987] and [RAG2009], as shown figure iv-6.

A summary of all ternary phases present in the Fe-Si-Ti system is given Table IV-1 containing 6 stable phases and 4 metastable phases. For temperatures over 800°C, the precipitated phase is the binary Fe₂Ti, as has been reported in several studies ([HEN1963], [LOE2003]). It is a stable phase which resists to high temperatures but which is known to embrittle the alloy.

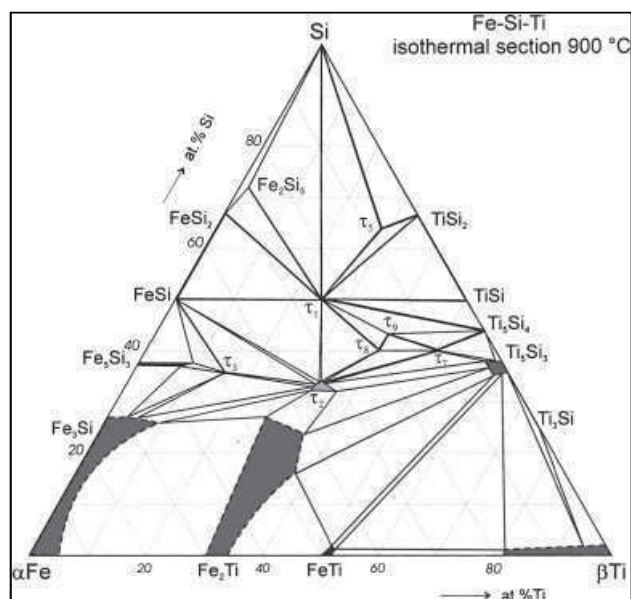


Figure IV-6: isothermal section at 900°C of ternary phase diagram of Fe-Si-Ti alloy [RAG1987]

Phase	Composition Range (at%)	Space Group	Pearson Symbol	Prototype	Lattice Parameter
FeSi ₂ Ti (τ_1)	49-50 Si 24-25 Ti	Pbam	oP48	MnSi ₂ Ti	a=8.6115 Å b=9.5427 Å c=7.6313 Å
FeSiTi (τ_2)	33-35 Si 33-35 Ti	Ima2	oI36		a=6.997 Å b=10.830 Å c=6.287 Å
Fe ₄ Si ₃ Ti (τ_3)		P6/mmm	hP168	Pd ₄₀ Sn ₃₁ Y ₁₃	a=17.206 Å c=7.981 Å
Fe ₇ Si ₂ Ti (τ_4)	20 Si 11 Ti	I $\bar{4}$ 3m	cI58		a=8.837 Å
Fe ₁₀ Si ₄₄ Ti ₄₆ (τ_5)					
Fe ₁₅ Si ₄₀ Ti ₄₅ (τ_6)					
Fe ₂ SiTi (<u>metastable</u>)		Fm $\bar{3}$ m		MnCu ₂ Al	a=5.709 Å

$\text{Fe}_{1-x}\text{Si}_x\text{Ti}$ (metastable)		$\text{Pm}\bar{3}\text{m}$	cP2		$a=2.98 \text{ \AA}$ $c=26.82 \text{ \AA}$
$\text{Fe}_{26}\text{Si}_6\text{Ti}_{68}$ (metastable)					
$\text{Fe}_{28}\text{Si}_4\text{Ti}_{68}$ (metastable)					$a=11.3 \text{ \AA}$

Table IV-1: Phases crystal structure and lattice parameter data for Fe-Si-Ti system [XIO2009]

i. Structure and composition

An extensive list of all important studies concerning the Fe-Si-Ti alloy is found in [XIO2009]. The most studied structure of precipitates in the Fe-Si-Ti system is Fe_2Ti , a Laves phase with hexagonal structure of MgZn_2 type which nucleates preferentially on defects, grain-boundaries or inclusions, which is also a phase in the binary Fe-Ti system ([HEN1963] and [LOE2003]) and can be found essentially for ageing temperatures above 800°C . The authors explain the presence of this binary phase in the ternary system by a lower solubility of Silicon compared to Titanium, at these higher temperatures [LOE2003]. The Fe_2Ti phase is known to increase the hardness of the alloys but also to lead to a brittle fracture mechanism.

Often the precipitation of a stable phase is preceded by the formation of a metastable coherent intermetallic phase, which has lower solute concentration than the equilibrium phase. Often, they have large associated coherency strains but small interfacial energy $\sigma_{\alpha\beta}$ [WAG1991]. This is the case in the Fe-Si-Ti alloy, in the Fe-rich part of the phase diagram. In fact, in the early stages of precipitation, a population of fine dispersed particles have ordered L_{21} crystal structure (of the so called Heusler alloys (see Figure IV-7)) and a composition close to Fe_2SiTi ([JAC1970] & [JAC1972]). The face centered cubic unit cell with 16 metal-atom sites can be considered as 8 B.C.C pseudo-units in which 2 sets of 4 atoms, Titanium and Silicon, respectively, are ordered to form a superlattice with a unit-cell edge-length approximately twice that of the pseudo-cell.

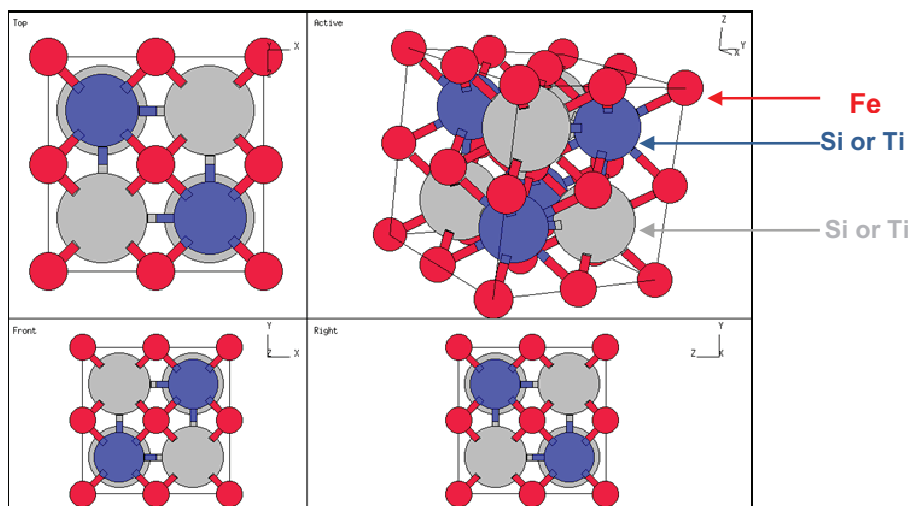


Figure IV-7: Heusler crystal structure of $L2_1$ type as for example the metastable Fe_2SiTi phase

The lattice parameter of the metastable precipitate is very nearly twice that of the matrix, with the result that particles of 1500\AA in diameter still exhibit coherency strain field contrast in electron micrographs, although at radii greater than 650\AA some particles are observed to lose coherency [JAC1972]. Investigation of precipitation steps has been done by several authors ([ABS1968], [HEN1966]). All observations were done on compositions close to Fe-3.5wt%Si-1.5%Ti. The conditions are also quite the same from one study to another: quenching after solution treatment at 1150°C or 1200°C during 2h followed by heating at different temperatures. The peak hardness of these alloys is observed for 1 hour at 600°C . They have observed that the precipitates formed in an Fe-3.5wt%Si-1.5%Ti are spherical, coherent with the matrix, ordered and with face cubic centered structure. Their lattice parameter, 5.70\AA , is slightly less than twice that of the matrix.

Not all authors agree on the precipitation sequence. Abson, Brown & Whiteman [ABS1968] believe that the precipitates have a DO_3 structure (for instance Fe_3Si) and change with time. They give as a proof the observed increment in lattice parameter during ageing, from 5.67\AA to 5.72\AA . According to their version, this increase would be due to the incorporation of Ti in the precipitate, namely a transition from the pre-precipitation phase Fe_3Si to the metastable Heusler ($L2_1$) phase Fe_2SiTi .

Another possible scenario, proposed by D.H. Jack & R.W.K Honeycombe [JAC1972], is a change in composition with temperature. Between 800°C and 1000°C , the phase present is assumed to be Fe_2Ti which nucleates preferentially on grain boundaries and dislocations, whereas below 800°C the Fe_2SiTi phase does not nucleate on any visible defects.

A slightly different version, suggested by D.H. Jack & F. Guiu [JAC1975], is that the Fe_2SiTi precipitates lose coherency when the diameter is larger than 15nm and are eventually replaced by Fe_2Ti after long ageing times.

Later studies, such as that of F. Löffler et al. in [LOF2004], assume that both processes are involved, meaning that the metastable phase Fe_2SiTi is present in early stages of precipitation at temperature lower than 800°C . It is replaced by the Laves Phase Fe_2Ti after long annealing treatments or by increasing temperature.

ii. Precipitation kinetics

There exist very little data on the thermodynamics of the Fe-Si-Ti system in the literature. The study done by D.H. Jack et al. in [JAC1972] consists of the compared kinetics of different compositions of Fe-Si-Ti alloys and tries to find an existence domain of the metastable Fe_2SiTi phase (Figure IV-8).

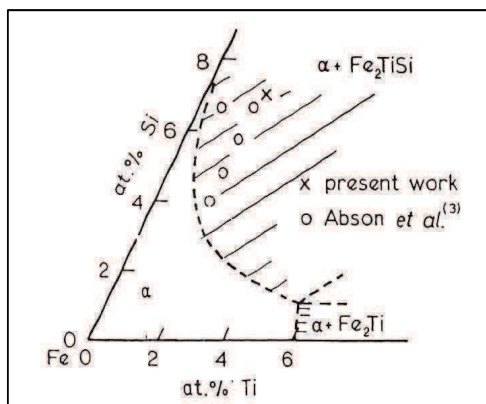


Figure IV-8: isothermal section at 600°C of the metastable Fe-Ti-Si phase diagram based on experiments by D.J Abson et al. [ABS1968] and D.H. Jack et al. [JAC1972]

In the case of the Fe-Si-Ti system, Titanium has a lower diffusivity in iron than Silicon, and a lower concentration in equilibrium with Fe_2SiTi . The experimental results are consistent with the hypothesis that the growth rate is determined by the flux of titanium in the matrix. This is also consistent with qualitative observations by D.J. Abson et al. [ABS1968] that precipitates in lower silicon alloys have faster growth rate whereas lower titanium contents hardly affect the rate. This was explained by [JAC1972], regarding Figure IV-8, by the fact that the alloys with lower Silicon contents have larger atomic fractions of Ti in equilibrium with Fe_2SiTi and the coarsening rate is faster.

The lack of data concerning the precipitation kinetics in literature could be due to the difficulty to measure the density of small particles. In fact, the use of TEM to measure the volume fractions can be subject to large uncertainties. The uses of thin foils as well as carbon replicas have both drawbacks. In fact, TEM pictures from thin foil are very much depending on the thickness of the foil, and the projection in 2 dimensions can give the impression of very large densities of precipitates. The drawback of carbon replicas is that, in the pre-peak conditions, the precipitates are very small and therefore difficult to extract, meaning that the volume fraction measured is not very accurate. However, several approximations have been made on the volume fraction for instance concerning the Fe-3.65wt%Si-1.55wt%Ti [JAC1972]. For a sample annealed 27 hours at 600°C a volume fraction of $6 \pm 1\%$ was measured and for a sample annealed 40 hours at 700°C the measurements give $4.5 \pm 1\%$. These two values concern the equilibrium volume fraction, since the conditions are far beyond peak strength, corresponding to 1 hour ageing for 600°C and 4 minutes at 700°C.

Estimations done during internal studies also with TEM at *Arcelor Research* [URI2006] have shown a volume fraction around $5 \pm 1\%$ for a Fe-2.35wt%Si-1.22wt%Ti annealed for 2 hours at 600°C, which is quite consistent with the previous findings.

Regarding the evolution of volume fraction with time, it appears that it will grow until reaching a plateau. This was confirmed by the results of Schwartz and Ralph [SCH1969] given in Figure IV-9. We notice that the volume fraction levels off just after peak strength is reached (600°C/1hour). This is due to the fact, that the peak strength is related to the beginning of coarsening of the precipitates, according to the theory confirmed by Hutchinson et al. [HUT2007].

Compared to volume fractions found in usual precipitation hardened steels, as for instance NbC or VC, these values are relatively important, since the carbides are rarely found at volume fractions larger than a few 0.1%.

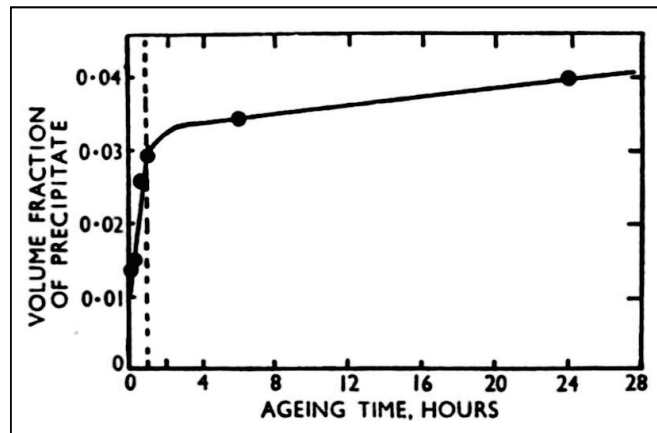


Figure IV-9: Volume fraction evolution with time for an alloy with composition Fe-3.4wt%Si-1.4wt%Ti and aged at 600°C; results by Schwartz et al. [SCH1969]

Concerning the radius evolution of precipitates, numerous measures have been provided in several studies. The first measurements of radius found in literature is the comparison between the evolution with time at 650°C and 700°C for the Fe-3.6wt%Si-1.5wt%Ti by Hénon et al. [HEN1966] (Figure IV-10) and a close composition by Schwartz et al. [SCH1969]. Figure IV-11 shows radii comprised between 1 and 10nm for samples aged at 600°C. In Figure IV-10 both curves are linear in power law representation, which was showed to be true only in the later stages, as can be seen on the results given in a later study, by Jack and Honeycombe [JAC1972] plotting R^3 as a function of time, linear as well (Figure IV-12). To model this evolution, the authors assumed that it followed the Lifshitz-Wagner kinetic (Figure IV-12).

However, it appears that there is a variation between the theoretical kinetics given by Lifshitz-Wagner, and the kinetics measured at short ageing times at 600°C [SCH1969]. Figure IV-12 clearly shows the non-linear kinetics in the first two hours of ageing. This difference is probably due to the fact that the Ostwald ripening has not started at this stage. Thus, this model is not sufficient and it shows the importance to consider the nucleation and growth steps as well.

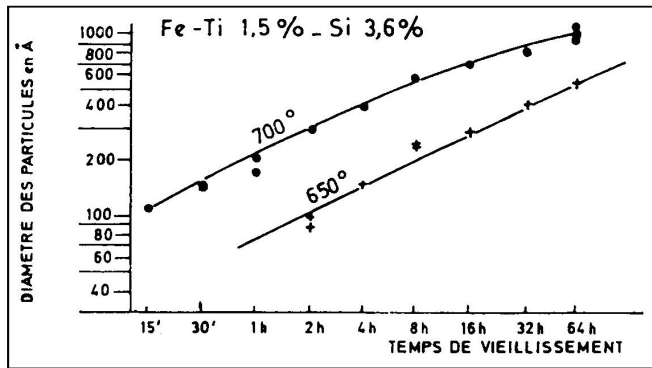


Figure IV-10: Radius evolution with time for ageing temperature of 650°C and 700°C. for an alloy composition of Fe-3.64wt%Si-1.52wt%Ti [HEN1966]

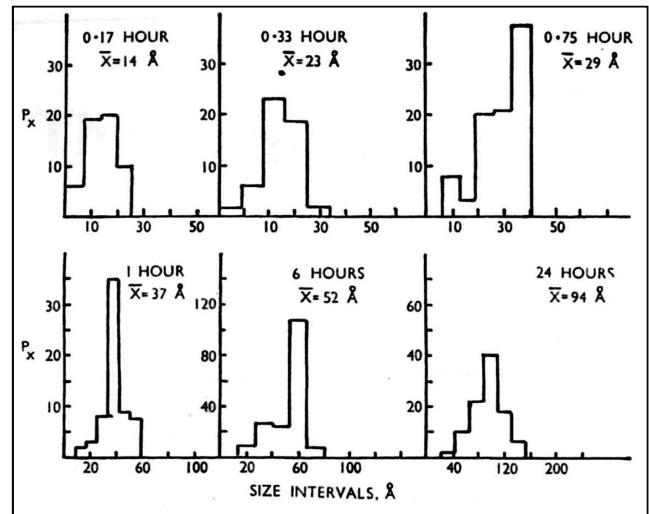


Figure IV-11: Histogram of radius values at different ageing times at 600°C for the alloy Fe-3.4wt%Si-1.4wt%Ti [SC H1969]

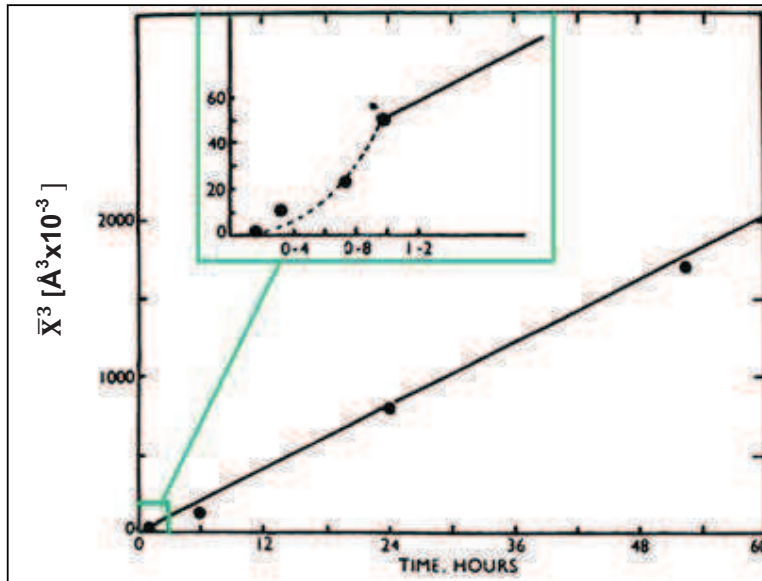


Figure IV-12: variation of the cube mean particle size with ageing time at 600°C Fe-3.65wt%Si-1.55wt%Ti [SCH1969]

One can see that the Fe-Si-Ti system was the object of an important number of studies which were essentially performed in the years 1970's. These essentially concern the structure of the precipitates and thermodynamics in alloys containing more Titanium and Silicon than in the present study. Furthermore, probably the limit of observation and characterization tools at this time did not permit to image more the particles themselves.

The following part will present the experimental results obtained concerning the precipitation characterization in terms of kinetics and structure. The evolution of precipitation was especially studied at precipitation temperature of 550°C and was then compared to other ageing temperatures.

II. Experimental characterization of precipitation in the Fe-Si-Ti system

Preliminary results of the study of Fe-Si-Ti alloys [URI2006] have shown that very interesting mechanical properties are obtained for alloys aged at 550°C, which was confirmed in the present study, as mentioned in Chapter III. Thus, systematic observation of precipitate microstructure was performed for this temperature, in order to understand its influence on the mechanical properties. The following section will first expose results of precipitation characterization at 550°C in particular and then compare with the results at other ageing temperatures.

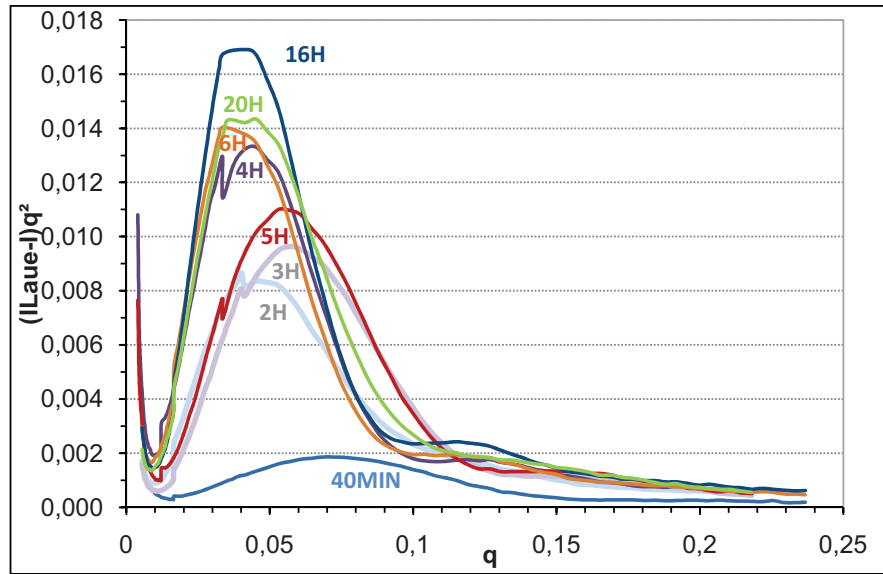
A. Precipitation during heat treatments at 550°C

1) Mean microstructural data : SANS experiments

The understanding and modeling of mechanical properties, as well as precipitation kinetics needs two essential data measurements: volume fraction and radius evolution. A very accurate method for the determination of volume fraction and radius was used: Small Angle Neutron Scattering (SANS). Principle of SANS experiment is to send a neutron beam on a sample of 10x10x1 mm which will scatter the incident beam if it contains a microstructural fluctuation such as precipitates. Analysis of this scattering signal will give quantitative averaged information on microstructure of the sample. In fact matrix and precipitates in SANS have a contrast which is two folds: magnetic and nuclear. More details concerning this method have been explained in Chapter II Part II.B.1.

The evolution of the Iq^2 curve as a function of the scattering vector is one of the main tools for the analysis of SANS experiments. We have seen that the area under the curve is proportional to the volume fraction of the precipitates and the value of q corresponding to the peak is inversely proportional to the precipitate radius.

Figure IV-13 shows the evolution of the Iq^2 curves between 40 minutes and 20 hours ageing. We notice that at the early stages of precipitation, namely between 40 minutes and 2 hours, the evolution of the curves is logical since we have a decrease in the q_{max} value corresponding to an increase in the mean radius. In this time range we also have an increase of the integrated intensity meaning an increase of volume fraction. But once arriving at a state of 3 hours ageing the curve changes shape: it is much wider and shifts again into larger q -values which means a decrease in the mean radius. This phenomenon is also observed between 4 and 5 hours ageing. Another interesting observation on the evolution of these curves is the change in curve shape between 16 and 20 hours ageing where the q_{max} stays constant but the curve becomes somewhat wider indicating possibly a wider size distribution.


 Figure IV-13: Comparison of Iq^2 curves at 550°C for different ageing times

Once we have had a global look on the evolution of the Iq^2 curves we can look at the results obtained after analysis of these scattering signals. The evolutions of mean radius and volume fraction are shown Figure IV-14 below. We can directly notice that the unusual change in the shape of the curves observed on Figure IV-13 around 3 and 5 hours ageing are confirmed. It does not follow a classical evolution since the radius value goes up and down. The decrease after 3 and 5 hours ageing is of respectively 0.5 and 1 nm while radius should either increase or stay constant at this point. No uncertainties in the experimental device could explain this unusual evolution. Experiments were repeated to understand its existence. Hence, a microstructural change could be responsible for this evolution.

We notice that during the whole time the volume fraction is globally constant reaching a plateau around 3.5-4% already after 2 or 3 hours which should indicate that the precipitates have reached the coarsening stage.

Another point which can be discussed regarding these curves (Figure IV-14) is the comparison between nuclear and magnetic signal. As mentioned previously, the origin of the contrast with a neutron source is of two types. Hence two signals have to be interpreted which both give a volume fraction and a radius value. Comparing both signals can be interesting for two reasons: concerning the magnetic signal to see whether the approximation concerning the non-magnetic nature of the precipitates is true and concerning the nuclear signal, to make sure that the composition approximation is consistent with the results obtained. In fact, the calculation of volume fraction is done with the use of equation (IV-28) below (see Chapter II).

$$Q_0 = 2\pi^2 \Delta\rho^2 f_v (1 - f_v) \quad (IV-28)$$

It shows its dependence to $\Delta\rho^2$ the contrast between matrix and precipitate which can be either nuclear or magnetic. Precipitates being considered as non-magnetic, the magnetic contrast term between matrix and precipitates is calculated with magnetic lengths of the matrix. The nuclear contrast is calculated using the composition of the precipitates.

For all samples studied in the present work, comparison between magnetic and nuclear signals showed good consistency (see Figure IV-14), which means that both the hypothesis of non-magnetic precipitates and their composition seem to be plausible.

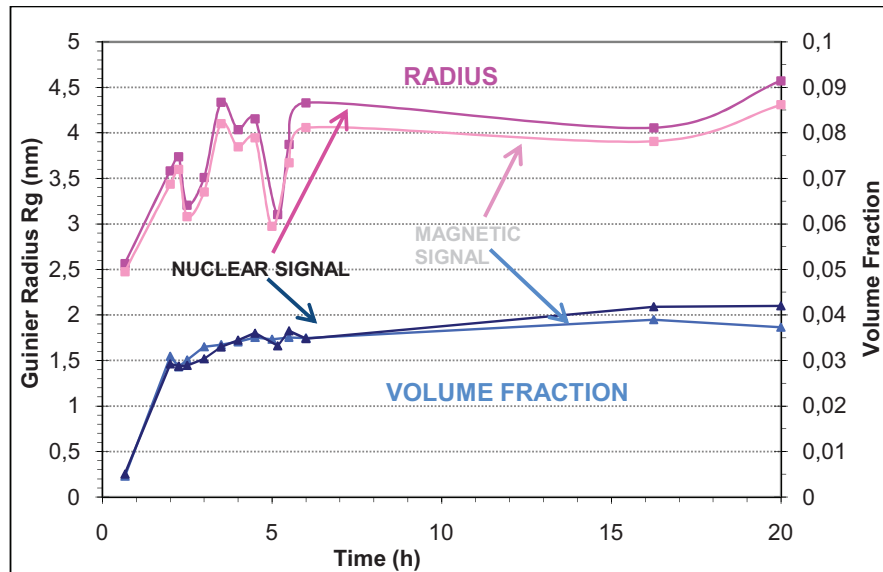


Figure IV-14: samples aged at 550°C. Comparison between nuclear and magnetic signal

Regarding the results obtained by SANS a more direct microstructural investigation seems necessary in order to obtain information on the precipitate structure. Thus, systematic TEM was performed on the samples used for SANS experiments.

2) Imaging and Electron diffraction analysis: TEM

The precipitates in the Fe-Si-Ti are difficult to image satisfactorily with TEM in thin foils. These difficulties arise probably from several aspects: the very low mismatch between particle and matrix, which leads to negligible strain fields around the precipitates and makes them less visible; or the surface oxide formation on Iron-containing thin foils [KEO1966] which often creates either surface roughness or even extra layer opaque to electrons; the very small size of the precipitates. Though, structural study was done essentially by TEM and later confirmed by APT. TEM observations were done either using Dark Field imaging technique or Electron Diffraction (for more details refer to Chapter II).

Simulations of Electron Diffraction Patterns were made using CaRIne software for the metastable phase Fe_2SiTi . Results are shown Figure IV-15 and 16. They show the presence of extra spots in the $\langle 110 \rangle$ and $\langle 100 \rangle$ zone axis, as shown Figure IV-15 and 16 below. These extra spots were confirmed by experimental observations done by [JAC1970] in the $\langle 110 \rangle$ direction.

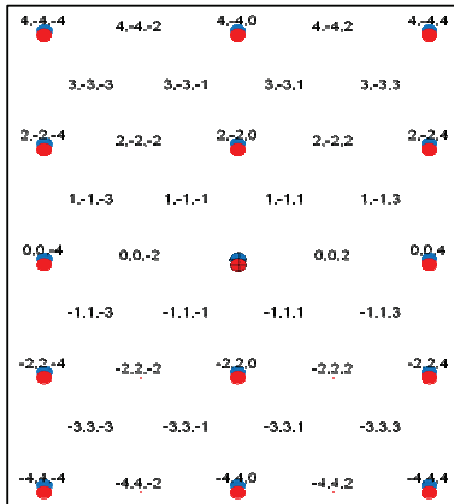


Figure IV-15: simulation of electron diffraction pattern of ferritic matrix (blue) in $\langle 110 \rangle$ direction and Fe_2SiTi extra spots (red)

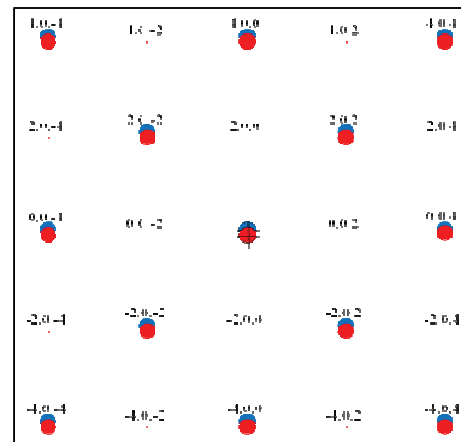


Figure IV-16: simulation of electron diffraction pattern of ferritic matrix (blue) in $\langle 100 \rangle$ direction and Fe_2SiTi extra spots (red)

Two main techniques of observations were used: electron diffraction pattern and dark field imaging (see section Chapter II Part II.1 for more details). In the early stages of precipitation the very small size of the precipitates does not allow good image analysis. Thus, in these early stages electron diffraction was mainly used. Once the precipitates have grown to more observable sizes at longer ageing times, both electron diffraction and imaging can be used.

In the first stages of precipitation, namely before reaching the volume fraction equilibrium the size of the precipitates reaches up to 3.5nm radius as predicted by SANS experiments meaning a diameter of 7 nm. Around these sizes usually TEM imaging technique is sufficient to observe the particles, but in our case no particles could be very well distinguished, probably because of the important density and size distribution. Thus, essentially electron diffraction patterns were used to identify the presence of precipitates. Images were therefore only used to confirm the expected results.

Electron diffraction patterns of sample aged during 2 hours were observed for the $\langle 100 \rangle$ and $\langle 110 \rangle$ matrix directions and revealed the expected extra spots for the Heusler phase. Bright field (Figure IV-17) and dark field (Figure IV-18) images were performed on samples aged during 2 hours. These confirmed the spherical shape and size around 7nm of the precipitates. However, an important distribution size was observed with radius measurements varying approximately from 1.5 to 3.5 nm. It is probably this important distribution size and the high density which makes it difficult to see the precipitates in these early stages of ageing.

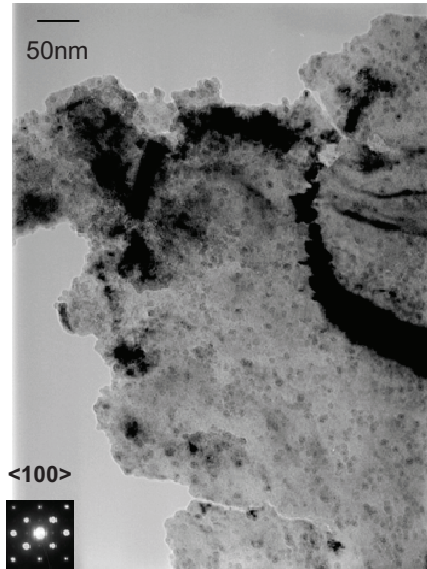


Figure IV-17: bright field image of sample aged during 2 hours

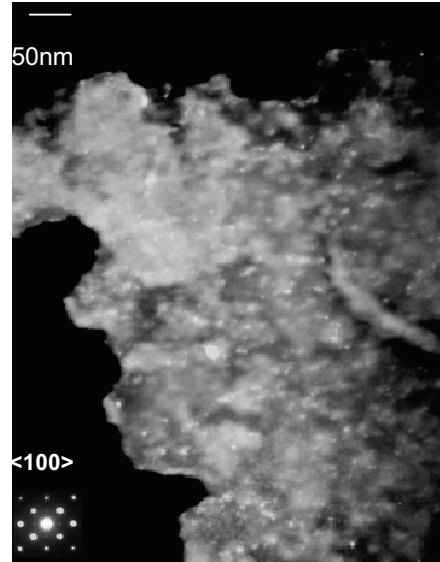


Figure IV-18: dark field image of sample aged during 2 hours

For sample aged during 3 hours, observation of electron diffraction patterns reveals as well the presence of Fe_2SiTi . On Figure IV-19 and 20 one can see extra spots in $\langle 100 \rangle$ and $\langle 110 \rangle$ directions, as predicted by the simulations. Figure IV-21 shows no extra-spots in $\langle 111 \rangle$ direction, which is consistent with the presence of Fe_2SiTi precipitates as well, since precipitates and matrix spots overlap in this direction.

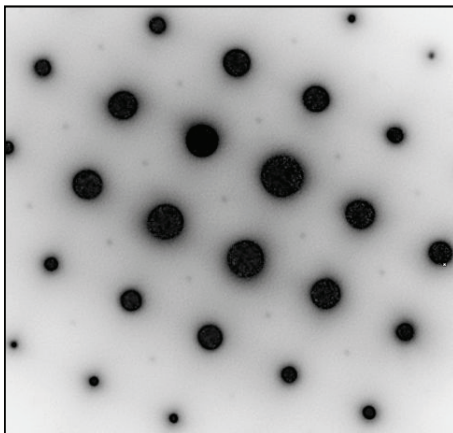


Figure IV-19: Electron diffraction pattern in $\langle 100 \rangle$ matrix direction for sample aged during 3 hours

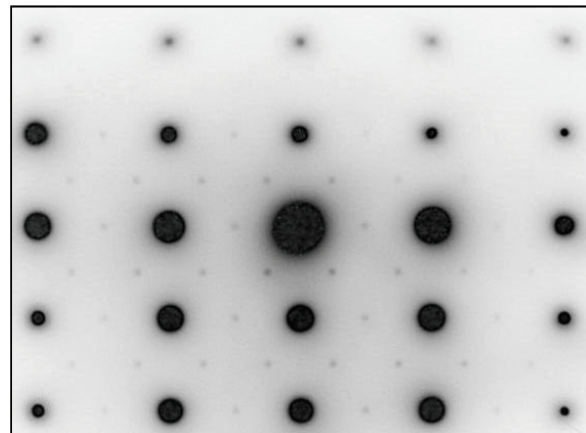


Figure IV-20: Electron diffraction pattern in $\langle 110 \rangle$ matrix direction for sample aged during 3 hours

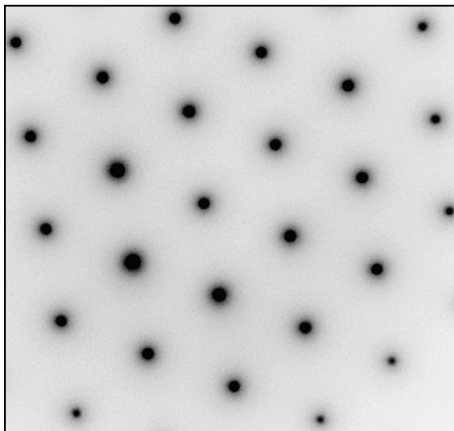


Figure IV-21: Electron diffraction pattern in $\langle 111 \rangle$ matrix direction for sample aged during 3 hours

To summarize, TEM observations strongly suggest that the precipitation sequence is dominated by the Fe_2SiTi phase. The observed precipitate sizes are compatible with SANS measurements; however, due to the difficulty to obtain images of high quality, a complete comparison is difficult. Thus, another method was used to provide additional insight, namely Atom Probe Tomography.

3) Quantitative microstructural analysis: APT

Atom Probe Tomography (APT) was used to identify the compositions of the precipitates and the matrix. This method enables the 3D reconstruction atom per atom of a sample using time of flight spectrometry. The experiments were performed in Rouen, Marseille and Austria thanks to collaboration in particular with Frédéric Danoix (GPM Rouen). The detailed principle of this technique has been explained Chap II.

Fives samples were analyzed: an as-quenched sample, a sample containing precipitates aged at 550°C during 2 hours, one after 3.5 hours treatment, one after 6 hours ageing at 550°C and the last after 20 hours ageing. These heating treatments were chosen so as to be relevant for the precipitation states, namely one as-quenched sample as a test sample and the others to have a complete panel of the precipitation state up to 20 hours ageing.

i. As-quenched sample

Analysis of a sample in solid solution gave the composition shown Table IV-2. We find globally the expected averages found by chemical analysis (see Chapter II): Titanium is given 1.15at% while one expected 1.22at% (1.05wt.%); Silicon is given 4.95at.% while the analysis of the ingot gave 5.05at% (2.54wt.%). We can also notice that there is a little bit of Aluminum found in these samples and that the tip contains no Carbon atoms.

Total number of atoms : 72156.000000		
Element	% of atoms	Number of atoms
C	0	0
Si	4.95	3574
Ti	1.15	831
Fe	93.79	67673
Al	0.11	78

Table IV-2 : global composition of solid solution sample

ii. Precipitation treatment at 550°C during 2 hours

On Figure IV-22, 23 and 24 we can see the 3D reconstructions of the tip observed by APT on a sample aged at 550°C during 2 hours. We notice the low concentration of Titanium in the matrix compared to Silicon. Another interesting point is to see that there is no noticeable depletion zone either in Silicon or in Titanium around the precipitates (**Erreur ! Source du renvoi introuvable.**).



Figure IV-22: Iron atoms in the matrix with 2 precipitates (box size : $7 \times 7 \times 53 \text{ nm}^3$)



Figure IV-23: Titanium atoms in the matrix with 2 precipitates (box size : $7 \times 7 \times 53 \text{ nm}^3$)



Figure IV-24: Silicon atoms in the matrix with 2 precipitates (box size : $7 \times 7 \times 53 \text{ nm}^3$)

Analysis of the precipitated sample gave the global composition in Table IV-3. We notice that there is a slightly smaller amount of Titanium and Silicon measured in this sample as compared to the one in solid solution. When comparing the global composition of the sample with the one found in the matrix (Table IV-4), we can calculate the amounts of element which precipitated. It was found that approximately 6% of the Silicon ($4.39/4.66$) and 30% of the Titanium was consumed for precipitation ($0.74/1.06$).

Total number of atoms : 521106.000000		
Element	% of atoms	Number of atoms
C	0	0

Si	4.66	24290
Ti	1.06	5529
Fe	94.13	490506
Al	0.15	781

Table IV-3: global composition of sample aged at 550°C during 2 hours

Total number of atoms : 130210.000000		
Element	% of atoms	Number of atoms
C	0	0
Si	4.39	5721
Ti	0.74	962
Fe	94.73	123349
Al	0.14	178

Table IV-4: composition of matrix for sample aged at 550°C during 2 hours

As mentioned previously, the precipitates are believed to be the Fe_2SiTi with L2_1 structure which has been confirmed by TEM. APT experiments confirm a composition very close to 25% Titanium, 25% Silicon and 50% Iron (Table IV-5).

Total number of atoms: 1756		
Element	% of atoms	Number of atoms
C	0.06	1
Si	22.1	388
Ti	25	439
Fe	52.62	924
Al	0.17	3

Table IV-5: composition of a precipitate in sample aged at 550°C for 2 hours

The same samples have also been observed by a wide angle APT (Austria), enabling to see a more important number of precipitates since the volume analyzed is larger, thus increasing the probability to encounter a precipitate (Figure IV-25): $50 \times 50 \times 50 \text{ nm}^3$ compared to $7 \times 7 \times 415 \text{ nm}^3$. One can then analyze the precipitates as shown Figure IV-26 using a concentration profile.

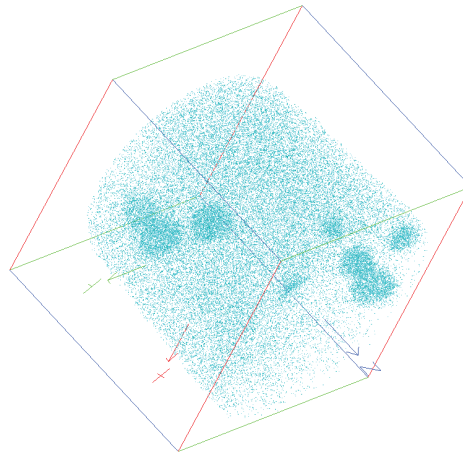


Figure IV-25: Sample aged at 550°C during 2 hours analyzed using Wide Angle APT (Volume = 50x50x50 nm³)

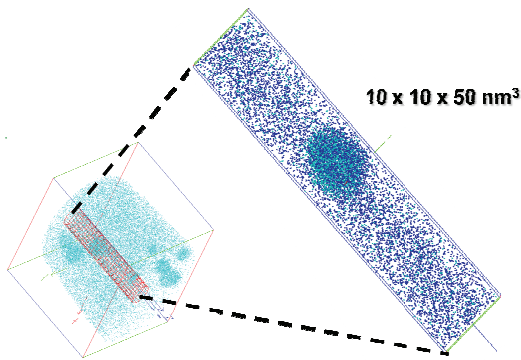


Figure IV-26: selection of one precipitate for composition analysis

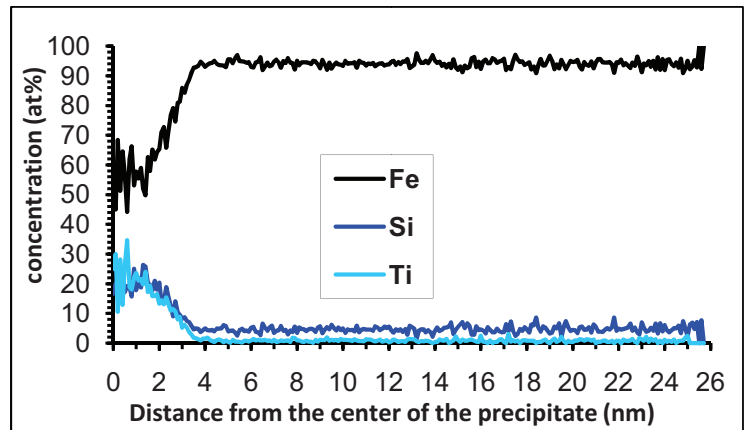


Figure IV-27: Concentration profile of one precipitate in the sample aged at 550°C during 2 hours

The composition profile (Figure IV-27) confirms a size of the precipitate of around 3nm radius (6-7nm diameter), which is consistent with the results obtained with SANS and TEM and their composition is close to Fe₂SiTi, namely around 20% Ti, 20%Si and 55%Fe.

Some more APT observations of samples in later stages of precipitation have been observed using the wide angle APT in Marseille.

iii. Precipitation treatment at 550°C during 3.5 hours

The volume analyzed contained 10 millions atoms for a volume of 90x70x70 nm³. Its global composition is given Figure IV-26 showing a slightly more important Silicon content 5.42at.% than expected (5.05at%). The difference in Silicon and Titanium amounts from one sample to another is probably due to a slight tendency of these elements to segregate.

Ion type	Counts	Ranged (%)
Si	421157	5.42
Fe	7252318	93.34
Ti	96572	1.24

Table IV-6: global composition of the tip

The software used for analysis (IVAS) permits to do an automatic “cluster analysis” in order to separate the clusters from the matrix (see details in Chapter II). The results are shown Figure IV-28 and Figure IV-29 where 119 clusters were defined. Separate composition analysis can thus be done between matrix and precipitates.

Table IV-7 gives the composition of the matrix after having done the cluster analysis indicating 0.56% Titanium and 4.19% Silicon, meaning that the precipitation consumed respectively around 50% of Titanium, 15% of Silicon and 2% Iron.

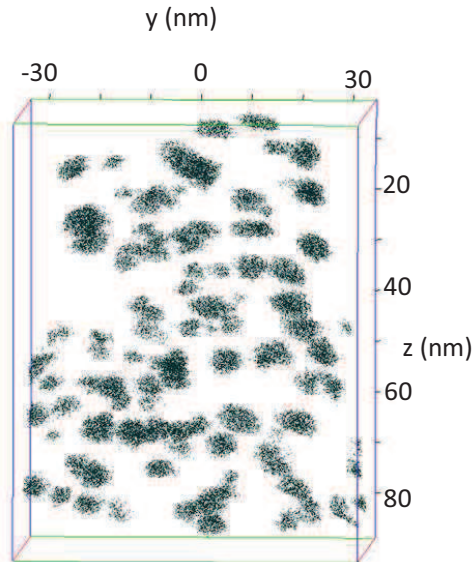


Figure IV-28: tip reconstruction with clusters separated from the matrix (Ti atoms)

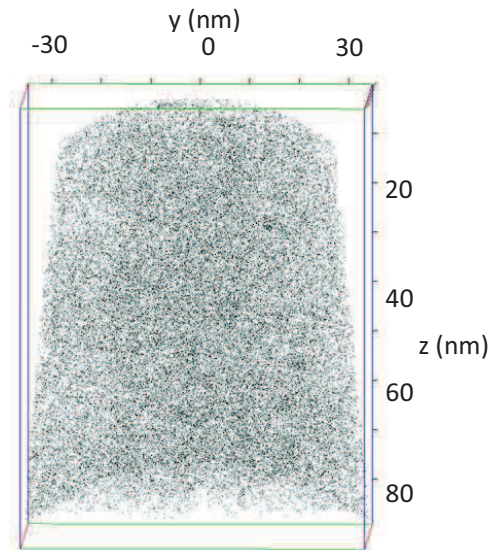


Figure IV-29: tip reconstruction with only matrix Ti atoms represented

Ion type	Counts	Ranged (%)
Si	360506	4.81%
Fe	7081166	94.54%
Ti	48642	0.65%

Table IV-7: Matrix composition after Cluster analysis

Once this Cluster analysis is done, the composition of each cluster can be measured individually, showing that they all have same compositions very close to Fe_2SiTi as shown Figure IV-30. In fact, Figure IV-30 shows the amount of elements (Fe, Si or Ti) in each of the 119 clusters analyzed, where we see that these amounts of Silicon and Titanium are close to

20% while Iron is found around 60%. The higher amount of Iron than expected is not surprising this it depends on the parameters used to define a cluster (see Chapter II).

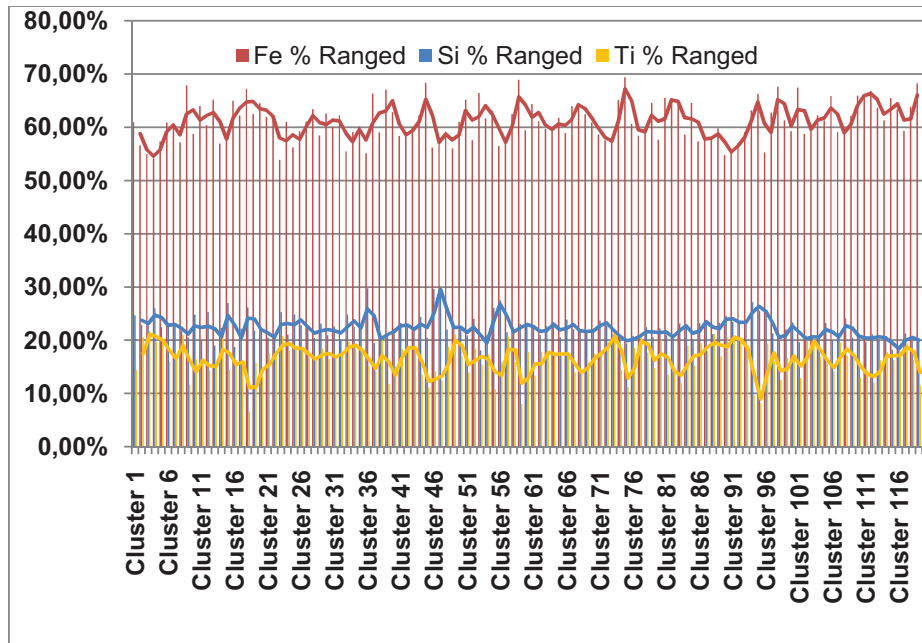


Figure IV-30: Amount of each element for the defined clusters on sample aged 3.5hours

The data concerning the composition of matrix and precipitates can be converted into a volume fraction by using the equation: $f_v = \frac{C_0 - C_m}{C_p - C_m}$

- C_0 is the initial content of the element in the sample
- C_m the element content in the matrix
- C_p the element content inside the precipitate

The calculation of the volume fraction using Silicon or Titanium atoms gives a volume fraction of 3.6 and 3.4% when taking C_p as 22 and 17% respectively (as given Figure IV-30), which is in good agreement with the experimental SANS results (3.5%). Values of radius can also be determined by APT observations using the concentration profile, as mentioned above. The concentration profile of each cluster (example Figure IV-31) enables to plot an histogram of the radius within the sample (Figure IV-32). The mean radius value for the sample aged during 3.5 hours were measured around 3.5nm, which is very consistent with the radii measured by SANS experiments which were of 4.3nm.

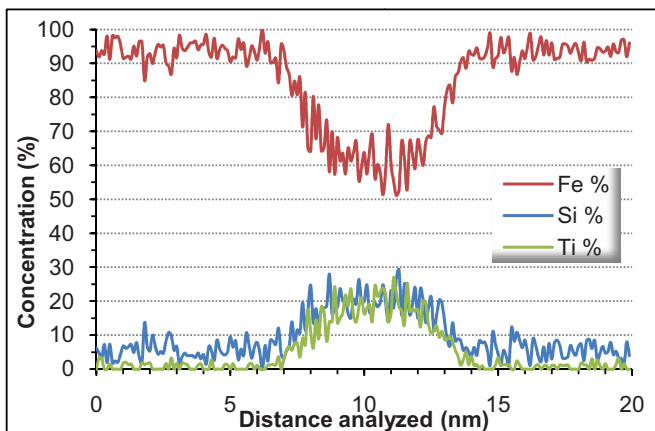


Figure IV-31: example of a concentration profile of one cluster in the sample aged 3.5 hours at 550°C

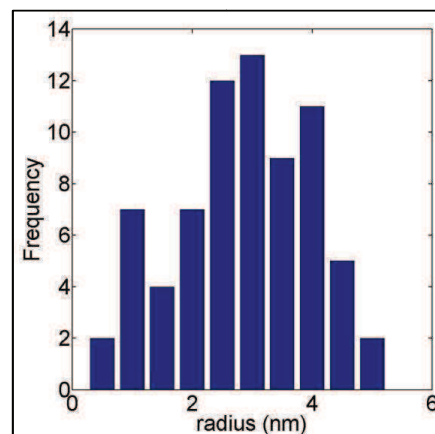


Figure IV-32: histogram of cluster Radius obtained using the concentration profiles for each cluster

iv. Precipitation treatment at 550°C over 6 hours

The global composition of the matrix (given Table IV-8) corresponds exactly to the one expected by chemical analysis on the ingot. Cluster analysis defined 43 clusters and the matrix composition after Cluster analysis (Table IV-9) shows that precipitation already consumed 85% of the Titanium, around 20% of the Silicon and around 3% of the total Iron.

Ion type	Counts	Ranged (%)
Si	306172	5.08
Fe	5650837	93.7
Ti	72152	1.2

Table IV-8: Global composition of samples aged during 6 hours

Ion type	Counts	Ranged (%)
Si	245279	4.25%
Fe	5500402	95.31%
Ti	25188	0.43%

Table IV-9: Matrix composition found after Cluster analysis on sample aged 6 hours

These values correspond to a volume fraction around 4.6% which is more than expected by comparison with SANS experiments (3.7%). This small difference is again probably due to the conditions of definition of a cluster using the automatic cluster analysis. In fact, if the conditions defined (number of atoms per cluster and minimum radius of cluster) are not restrictive enough, some of the atoms in the matrix can be considered part of a cluster. In fact, to obtain a volume of 3.7% one would need to have a matrix composition of 0.6at%Ti and 4.7at% Si, which is not very far from what we have obtained with our analysis. The composition of the clusters is again close to Fe₂SiTi as shown on the graph in Figure IV-33 below.

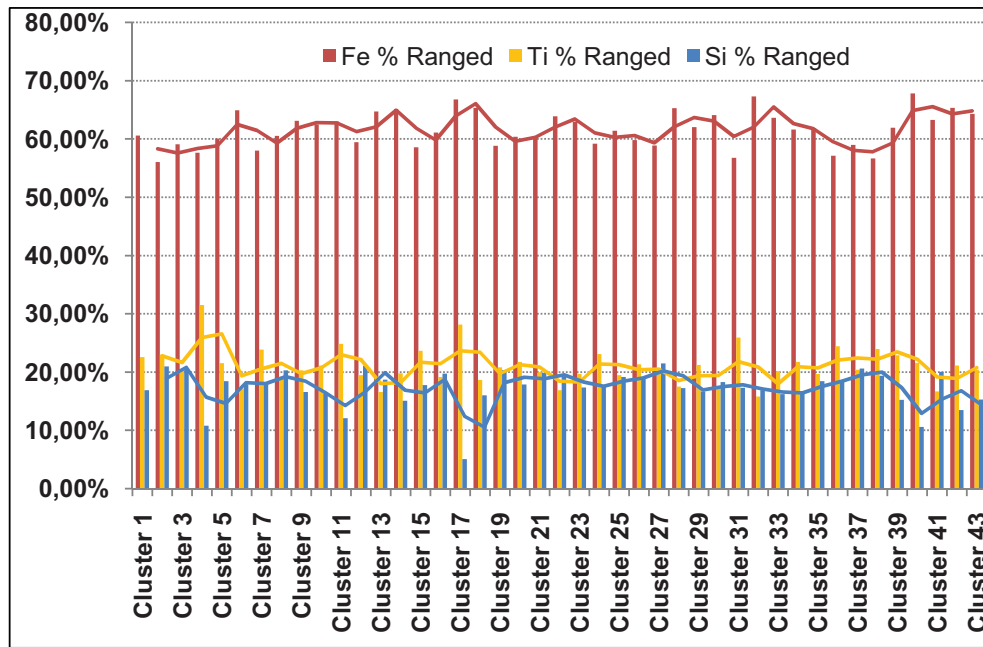


Figure IV-33: Amount of each element for the defined cluster on sample aged 6 hours

Figure IV-34 and 35 show the 3D reconstruction of the complete volume after cluster analysis of the samples aged during 3.5 and 6 hours respectively (the colors are only there to distinguish the clusters from each other). One can see the important size distribution with small and large precipitates in the sample aged 3.5 hours, which is much less the case in the sample aged during 6 hours. The sample aged during 6 hours shows that the coarsening process has started making the interparticle distance and the size of the precipitates increase while the volume fraction stays constant.

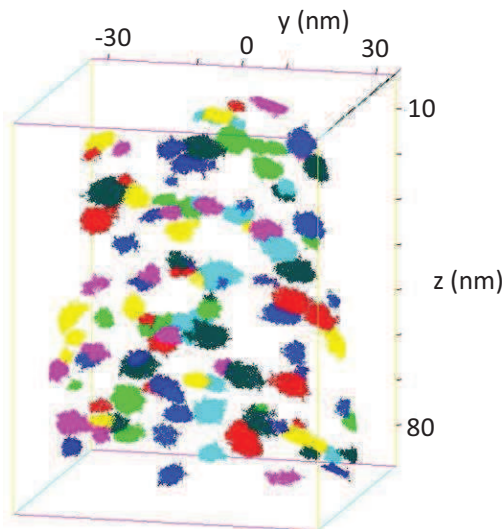


Figure IV-34: 3D reconstruction of the clusters in the tip on sample aged 3.5 hours at 550°C

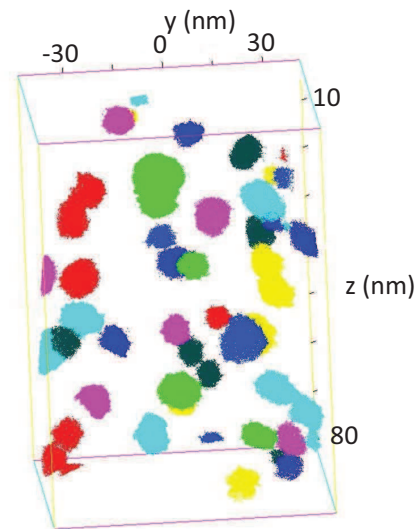


Figure IV-35: 3D reconstruction of the clusters in the tip on sample aged 6 hours at 550°C

The evolution of the cluster radius has been quantified using, as mentioned before, the concentration profile of each cluster (Figure IV-36). The histogram of radius values obtained is given Figure IV-37 indicating a mean radius around 5nm, which is in good correlation with SANS results where we obtained 4.3nm. The slight difference in sizes observed would be explained by the fact that, as we can see on Figure IV-35, some of the clusters could not be analyzed since they are on the side of the tip and are not complete, thus reducing the amount of data considered in the statistics.

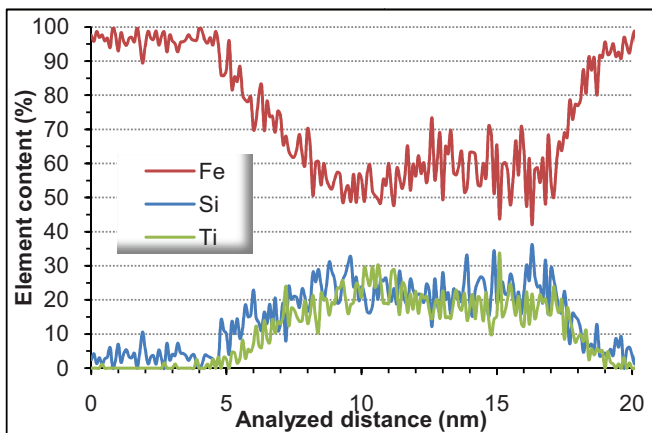


Figure IV-36: example of a concentration profile of one cluster in the sample aged 6 hours at 550°C

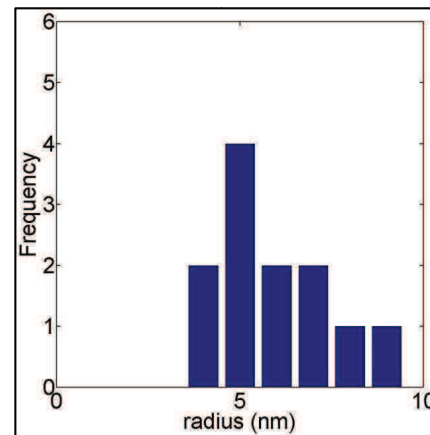


Figure IV-37: Histogram of Radius values obtained using concentration profiles for each cluster in the sample aged 6 hours at 550°C

v. Sample aged at 550°C during 20hours

Comparison between the precipitation state of samples aged during 6 hours and 20 hours does not reveal any visible difference, when comparing Figure IV-38 and Figure IV-39. The mean composition of clusters is also close to Fe_2SiTi as shown by the composition profile given Figure IV-40.

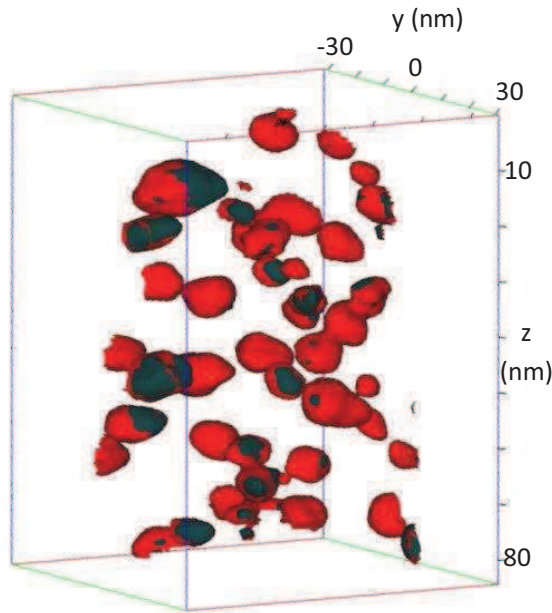


Figure IV-38: clusters in sample aged during 6 hours

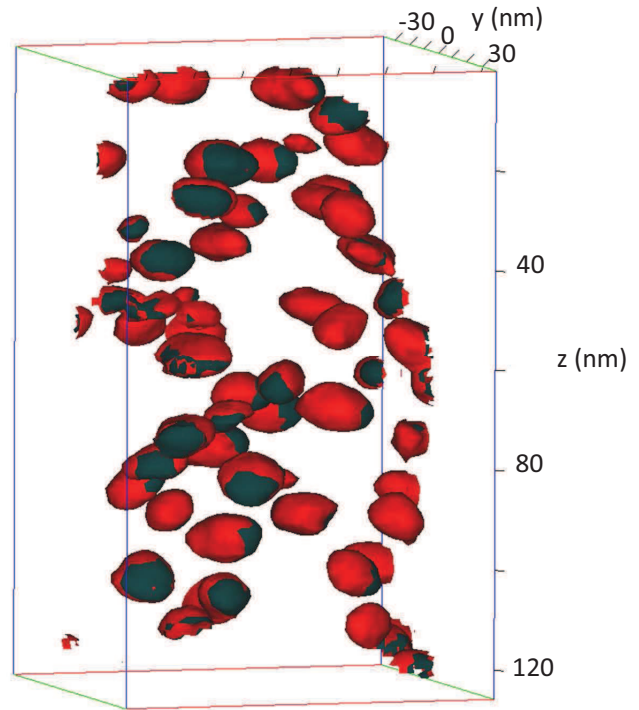


Figure IV-39: clusters in sample aged during 20 hours

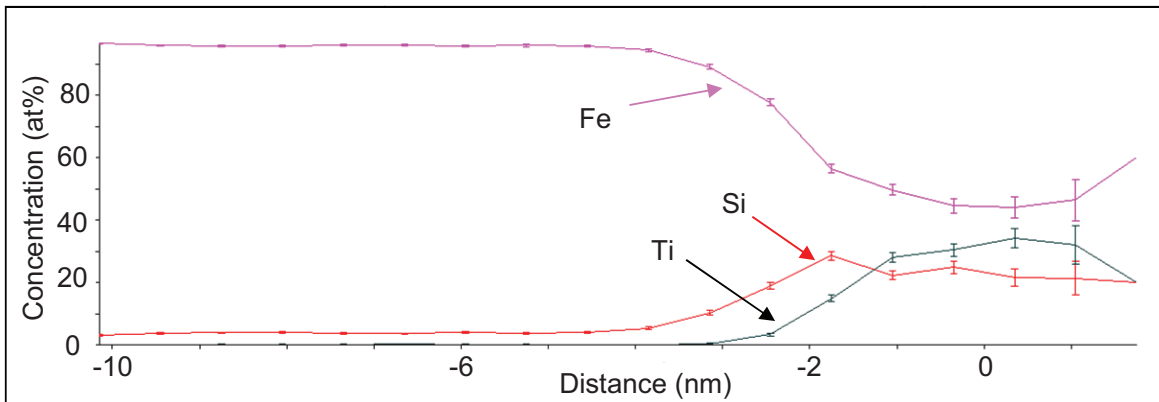


Figure IV-40: Typical Concentration profile of a cluster in sample aged during 20 hours

Thus, to conclude on the APT observations, the results show the presence of the metastable Heusler phase Fe_2SiTi up to 20 hours ageing. It seems that the size distribution of the precipitates is stable after 6 hours ageing and beyond.

The fluctuation of radius values observed by SANS at around 5 hours ageing at 550°C could not be explained in terms of microstructural evolution, neither by TEM nor by APT observations. Since the decrease in radius goes with an increase in hardness (as seen Chapter III), the probable explanation for this slight fluctuation is a change in the experimental conditions leading to a modification of the temperature for this sample.

After accurate characterization of the precipitation for samples aged at 550°C, which provided the most interesting mechanical properties, it seems interesting to study the evolution of precipitation for samples aged at other temperatures.

B. Other temperatures

1) 450°C-500°C

At lower temperatures the kinetics of precipitation are slower and hence for same ageing times one expects smaller precipitates. This is already shown Part III with the evolution of hardening as a function of the temperature, where samples aged at 500°C are much harder than those at 550°C indicating a difference in precipitated state. This seems logical when considering that small very dense coherent particles make a more important obstacle to dislocation motion [NEW1954]. SANS measurements of the size and volume fractions of precipitates at these states are shown Figure IV-41 and 42 respectively. They confirm the smaller precipitates mean radius for these low ageing temperatures, but a volume fraction of same order of magnitude leading to a higher density as shown Figure IV-43.

Microscopic observations of samples aged between 450°C and 500°C are quite difficult since precipitate density is so important that the particles are difficult to distinguish from one another. Thus, essentially electron diffraction patterns were used to identify the presence of Fe₂SiTi precipitates. They show for both temperatures the presence of an extra-spot in <100> matrix direction and for sample aged at 500°C during 6h30 the presence of extra spots in <110> matrix direction, both confirming the presence of Fe₂SiTi.

2) 520°C and 580°C

Samples aged at 520°C and 580°C were observed by SANS technique for having quantitative measurements of radius, volume fraction and density (see Figure IV-41, 42 and 43) obtained from the magnetic component of SANS experiments. But no microscopic observations were carried out. On the curves Figure IV-41, 42 and 43, it can be noticed that there is no important difference in kinetics since samples aged at 580°C have precipitates around 6 nm from 0 to 6 hours ageing which does not evolve faster than for samples aged at lower temperatures.

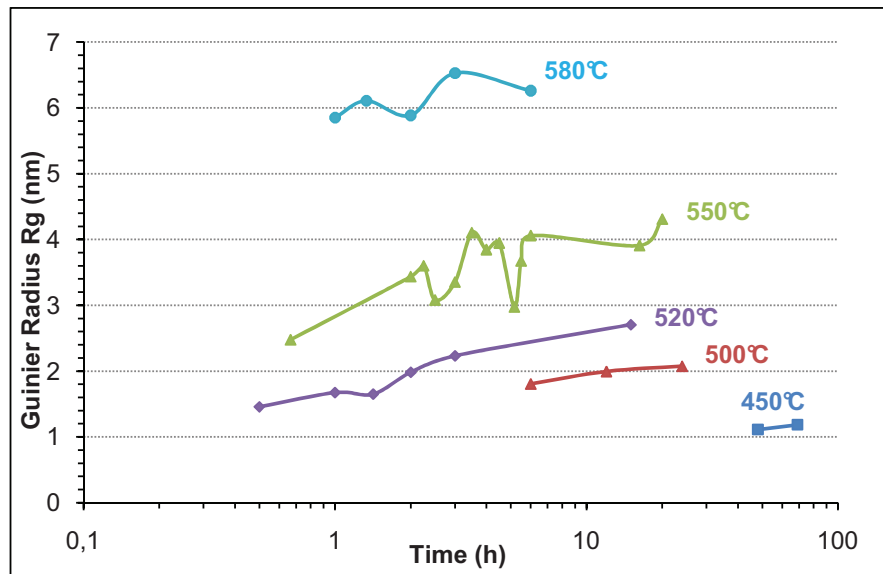


Figure IV-41: Evolution of Precipitate Radius with time for samples aged at temperatures ranging from 450 and 580°C

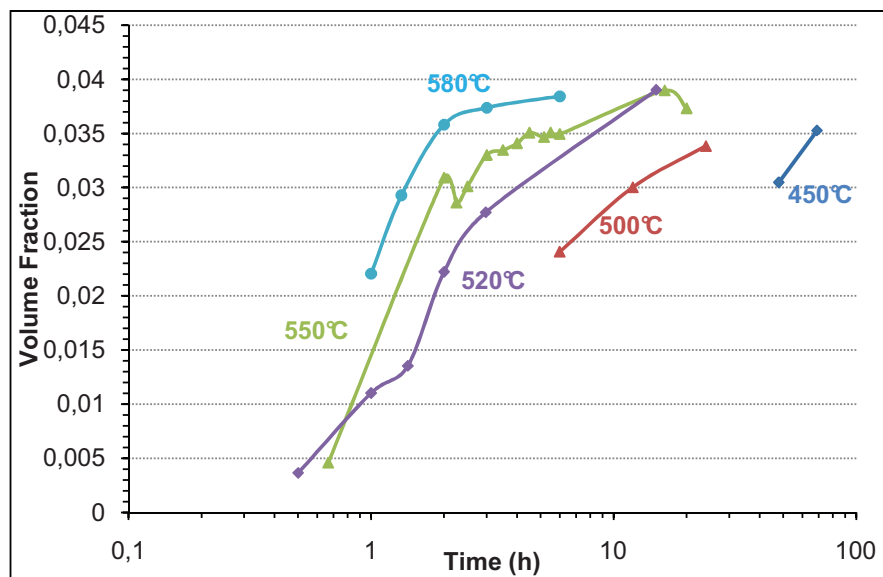


Figure IV-42: Evolution of Volume Fraction with time for samples aged at temperatures ranging from 450 and 580°C

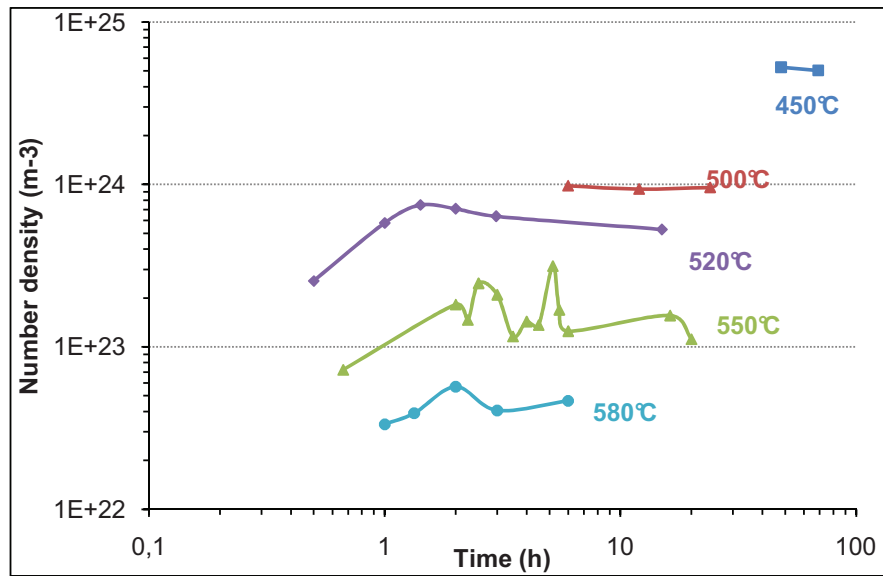


Figure IV-43: Number density evolution with time for samples aged at temperatures ranging from 450°C to 580°C

C. Influence of the initial state

Different initial conditions were compared in order to see their influence on the precipitation kinetics. Figure IV-44 shows the nuclear curves of samples aged at 550°C for four different states prior to the final heat treatment: as-quenched, pre-precipitated in salt bath during 10 minutes and during 30 minutes and pre-precipitated in halogen furnace (AET). These curves show that at least for short ageing times the use of a halogen furnace or salt bath does not make any difference, neither does the time of pre-precipitation, since 10 or 30 minutes ageing time seem to generate the same behavior.

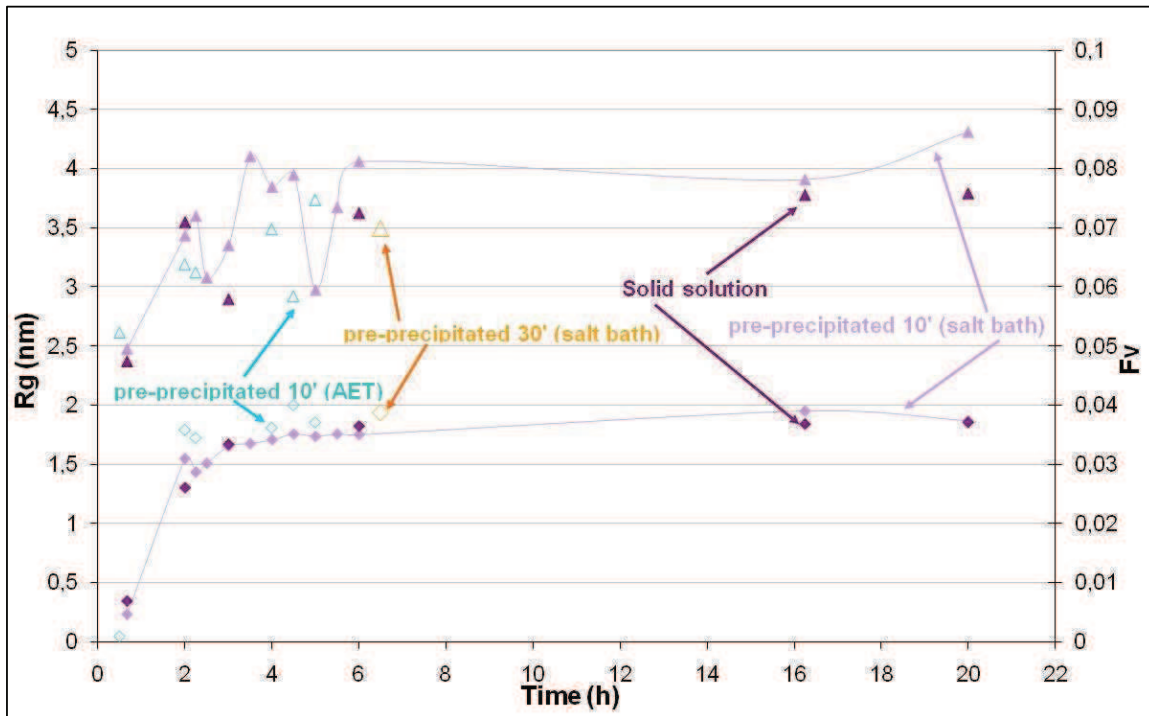


Figure IV-44: SANS results for samples aged at 550°C with different initial conditions

III. Modeling of the precipitation kinetics

The aim of modeling the precipitation kinetics is to be able to predict the evolution of sizes and volume fraction at any temperature and any ageing time. Afterwards the ideal objective is to perform what is called “alloy design” meaning finding the best compromise between microstructure and mechanical properties.

The models used in the present study are the ones presented previously, namely DBPreci and a model per classes, which are both based on the classical nucleation, growth and coarsening theory, considering these three steps as correlated. The DBPreci model was implemented by P.Maugis at the IM2NP University in Marseille. The model per classes was implemented at the SIMAP laboratory and based on the algorithms “Multipreci” ([GEN2001], [MAU2005]) and “Preciso” developed by Perez et al. ([PER2007], [ACE2007]). A certain number of parameters are necessary to use the model, which are summarized in Table IV-10 below. These are considered constant during the whole precipitation and were taken from literature. The two varying parameters are the solubility product and the interfacial energy, which were both fitted for each model used.

Atomic weights of [g/mol]		
Iron	55.85	
Titanium	47.88	
Silicon	28.09	
Molar Volumes [cm³/mol]		

Iron Fe ₂ SiTi	7.11 28.01	Calculated using the lattice parameter of Fe ₂ SiTi: a = 5.709 Å
Atomic Volumes [Å³/atom] Iron Fe ₂ SiTi	11.8 11.63	Calculated using the lattice parameter of Fe ₂ SiTi: a = 5.709 Å and a(Fe)=2.87 Å
Frequency factor of Titanium (D₀) [cm²/s] Activation energy barrier (Q_{diff}) of Titanium [J/mol]	3.15 248000	Values obtained by T. Gladman in [GLA1997] for the diffusion of Titanium in Iron
Frequency factor of Silicon (D₀) [cm²/s] Activation energy barrier (Q_{diff}) of Silicon [J/mol]	0.92 200880	Values from Batz et al. [BAT1953]
Atomic composition of the initial matrix in Titanium Silicon	0.0119 0.0492	The initial composition of the matrix being 2.54wt%Si and 1.05wt%Ti
Temperature of the precipitation treatment	550°C	Experimental condition

Table IV-10: Parameters used for the modeling of precipitation kinetics

A. Model “DBPreci”

The DBPreci model can be applied in the case of a homogeneous precipitation, which is the case here since it has been observed that the precipitation did not nucleate preferentially on grain boundaries or dislocations. The experimental data was taken from the SANS experiments, giving the evolution with time of volume fraction and radius.

The parameters introduced in the DBPreci model are given Table IV-10 above. Concerning the interfacial energy, the only value available in the literature is in [JAC1972] by D.H. Jack et al. who found 0.2 J/m²; but in the present modeling this value did not fit and this parameter was thus reevaluated to 0.13 J/m². It is a very low value in comparison with other systems as for example 0.4J/m² in the NbC system in [PER2005], but it does not seem absurd regarding the very coherent interface between the Fe₂SiTi precipitates and the fact that it contains over 50% Fe, which is the principal matrix element. Concerning the solubility factor, which is in normal cases taken from the phase diagram using the solubility curve of a phase, it could not be estimated experimentally since the Fe₂SiTi is a metastable phase, not existing on the phase diagram. This factor was therefore fitted using the definition below:

$$\Delta G = RT \ln(a_{Fe}^2 a_{Si} a_{Ti}) = RT \ln(K_s)$$

In the assumption of a dilute solution, one can consider that the activity of a minor element is equal to its concentration (in this case the atomic concentration). Thus, the activity of the solute element equals to 1.

$$\Delta G = RT \ln(X_{Fe}^2 X_{Si} X_{Ti}) = RT \ln(K_s) \quad (IV-29)$$

$$\text{At equilibrium we thus have: } \ln(X_{Fe}^2 X_{Si} X_{Ti}) = \ln(K_s) \quad (IV-30)$$

$$\text{also written as: } \ln(K_s(\text{at\%})) = \frac{\Delta S^\circ}{R} - \frac{\Delta H^\circ}{RT} = -\frac{A}{T} + B \quad (IV-31)$$

where the two parameters A and B are respectively the enthalpy and entropy of the formation of precipitates

N.B.: A and B are defined so as to fit the solubility curve when it is defined as a hyperbol. To simplify the problem, since we consider here only one temperature, we take A=0 and thus have to fit only one parameter B=K_s which was found to be equal to -0.4, which is quite low regarding the modeling experiments done on other steels as for example on NbC alloys in [PER2005].

Interfacial energy [J/m²]	0.13	Unknown parameter which was fitted. Though it is not taken by coincidence, since the Fe ₂ SiTi precipitates are known to be coherent with a lattice parameter of twice the matrix and thus have a very small misfit (0.125%).
Solubility product		When describing the solubility curve as an hyperbole with formula: $\log(K_s) = \frac{-A}{T} + B$
A	0	Since we consider here only one temperature (550°C), the problem was simplified using A = 0 in order to have B = log(K _s) which was then fitted on experimental results.
B	-0.4	

Table IV-11: Fitted parameters for the modelling of precipitation kinetics by DBPreci model

Results of modeling of Volume fraction and Radius evolution with time are shown respectively Figure IV-45 and 46.

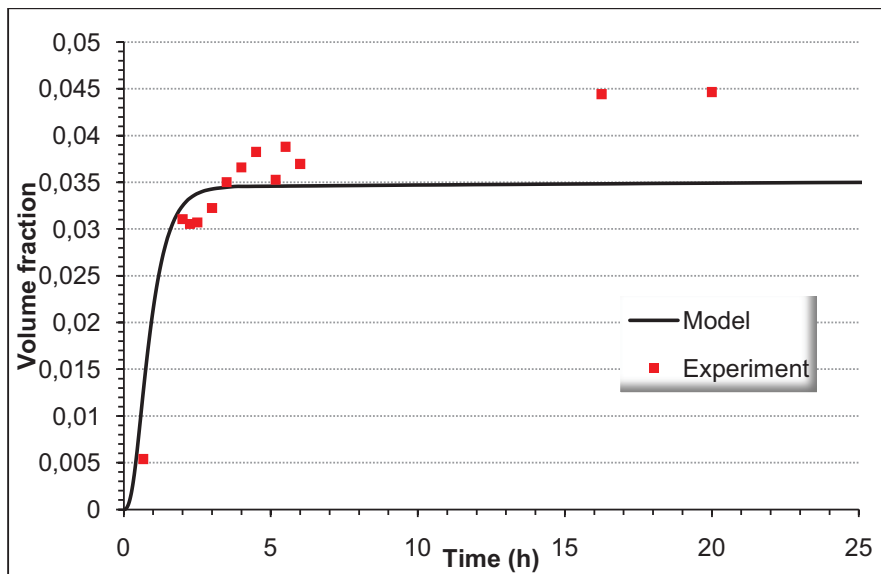


Figure IV-45: Modeling of the volume fraction evolution with time using DBPreci model compared with experimental data obtained by SANS

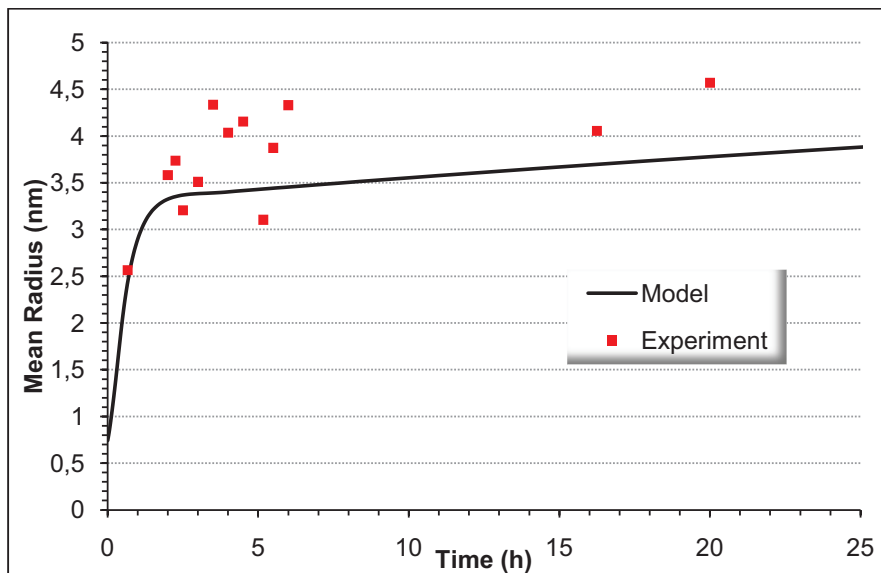


Figure IV-46: Modeling of the radius evolution with time using DBPreci model compared with experimental results by SANS

These results show a good capacity of the model to predict the volume fraction evolution in the first stages of precipitation. The radius evolution is less good predicted especially in the time ranges from 2 to 6 hours ageing where the radius measurements taken from SANS experiments go up and down.

B. Class Model

Comparison between modeling by DBPreci, using the classical nucleation, growth and coarsening theory, and the model per classes, was already done in [PER2004], showing a very good correlation.

Since the values of the parameters are not available for the metastable Fe₂SiTi phase, these were, again, adapted in order to fit the experimental data. The parameters necessary for the modeling, are the same as for DBPreci, namely the interfacial energy γ and the solubility product, K_s . The interfacial energy had been adapted already in the use of DBPreci model, at $\gamma=0.13$ J/m², thus, the value was kept in the case of “Multipreci” modeling. The solubility product was calculated using the equations below in the case of Fe₂SiTi precipitates:

$$\Delta G = RT \ln(X_{Fe}^{0.5} X_{Si}^{0.25} X_{Ti}^{0.25}) = RT \ln(K_s) \quad (IV-32)$$

$$\text{At equilibrium we thus have: } \ln(X_{Fe}^{0.5} X_{Si}^{0.25} X_{Ti}^{0.25}) = \ln(K_s) \quad (IV-33)$$

$$\text{also written as: } \ln(K_s(\text{at}\%)) = \frac{\Delta S^\circ}{R} - \frac{\Delta H^\circ}{RT} = -\frac{A}{T} + B \quad (IV-34)$$

which gives $K_s=0.098$, taken as a reference in the precipitation kinetics at 550°C, and fitted for other temperatures.

1) Modeling results

The results obtained are presented in Figure IV-47, 48 and 49 below, showing good agreement with experimental results, in particular concerning the radius evolution with time (see Figure IV-47). The volume fraction evolution (Figure IV-48) is satisfying for higher temperatures but the model does not describe very well the kinetics for smaller temperatures, namely 450 and 500°C, predicting faster kinetics than they are experimentally observed.

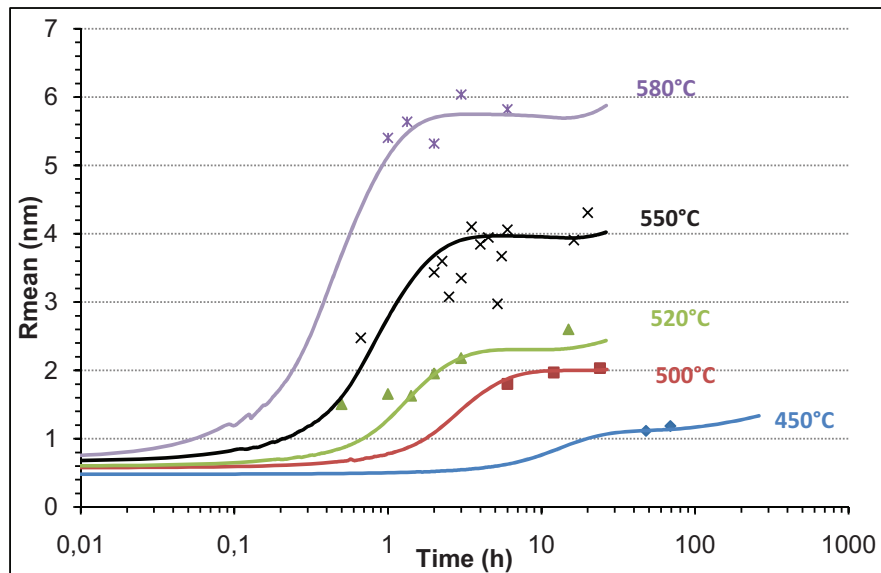


Figure IV-47: Modeling results (solid line) of Mean Radius evolution with time for temperatures ranging from 450°C to 580°C compared with experimental results (dots)

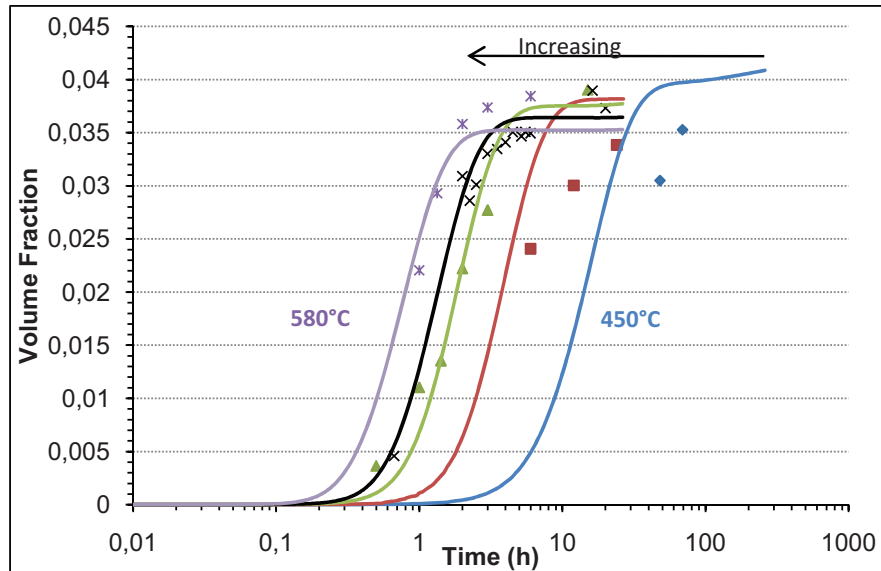


Figure IV-48: Modeling results (solid line) of Volume Fraction evolution with time for temperatures ranging from 450°C to 580°C compared with experimental results (dots)

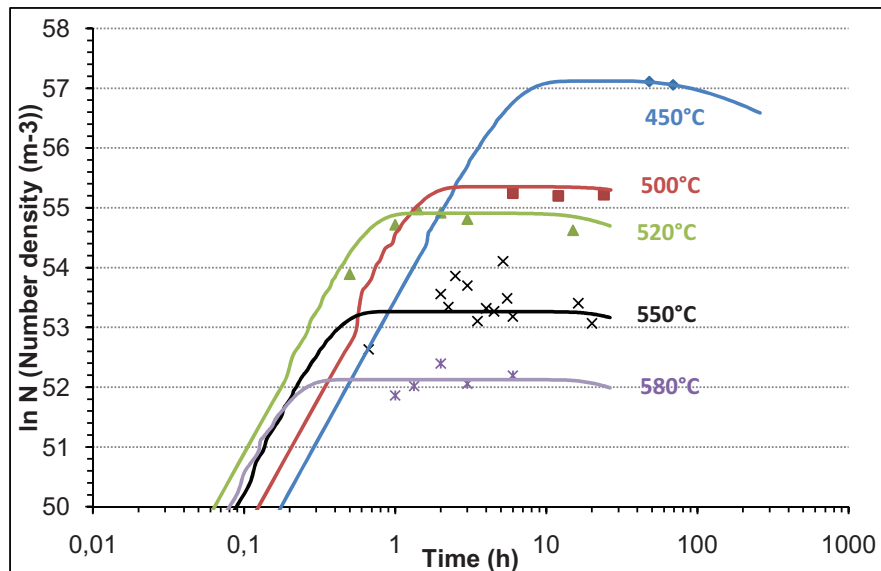


Figure IV-49: Modeling results (solid line) of Number Density evolution with time for temperatures ranging from 450°C to 580°C compared with experimental results (dots)

2) Influence of the parameters on the modeling results

Since the solubility product and the interfacial energy were not experimentally measured, but were adjusted on experimental data, it seems interesting to evaluate the influence of each of these two parameters on the precipitation kinetics. In [PER2004], the author showed the important influence of the value of interfacial energy on the precipitation kinetics compared to the solubility product.

The influence of the fitted parameters on the evolution of precipitation kinetics was analyzed on the kinetics for samples aged at 550°C and then compared with other temperatures.

i. 550°CInfluence of the interfacial energy on the precipitation kinetics.

The influence of the value of interfacial energy of the precipitates on the precipitation kinetics has been investigated as shown on Figure IV-50, 51 and 52 below. To do so, the solubility product, K_s , is kept constant at a value of 0.098. One can see the important influence of γ on the evolution of the mean radius Figure IV-50. The value of $\gamma=0.13 \text{ J/m}^2$ seems to predict well the evolution of Radius, Volume Fraction and Number density.

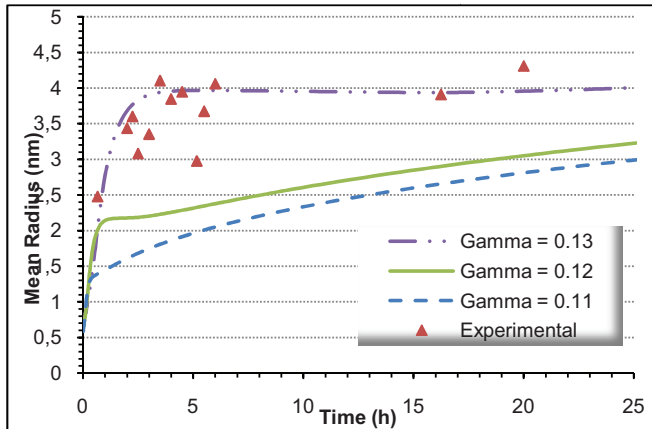


Figure IV-50: Influence of the change in interfacial energy on the evolution of Radius as a function of time for precipitation kinetics at 550°C

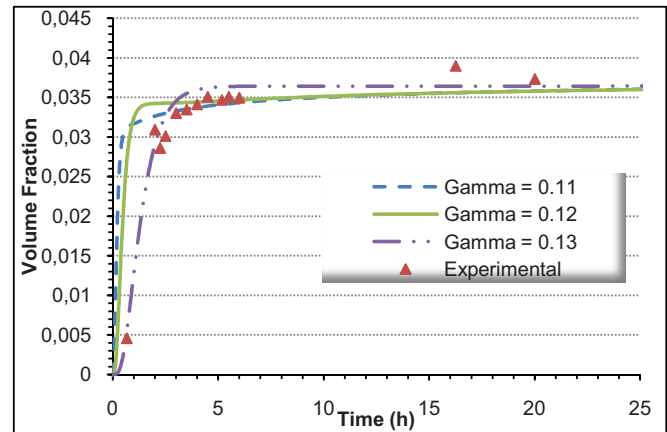


Figure IV-51: Influence of the change in interfacial energy on the evolution of Volume fraction as a function of time for precipitation kinetics at 550°C

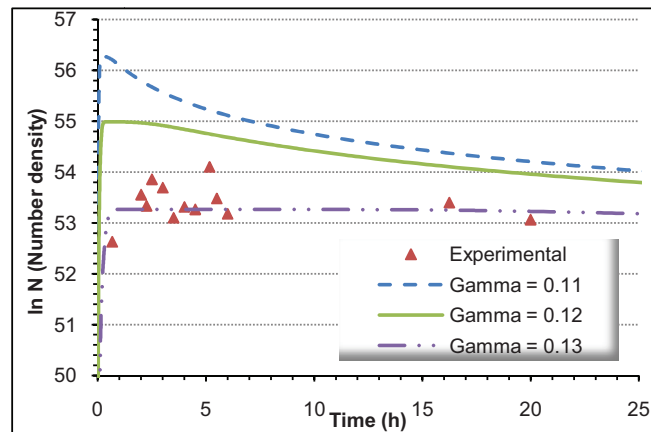


Figure IV-52: Influence of the change in interfacial energy on the evolution of Number density as a function of time for precipitation kinetics at 550°C

Influence of the change in solubility product on the precipitation kinetics

The influence of the value of the solubility product was evaluated using a constant interfacial energy, γ , at a value of 0.13 J/m^2 . The results are shown on Figure IV-53, 54 and 55, showing best prediction of the experimental results using $K_s=0.0098$, which is consistent with the calculated value.

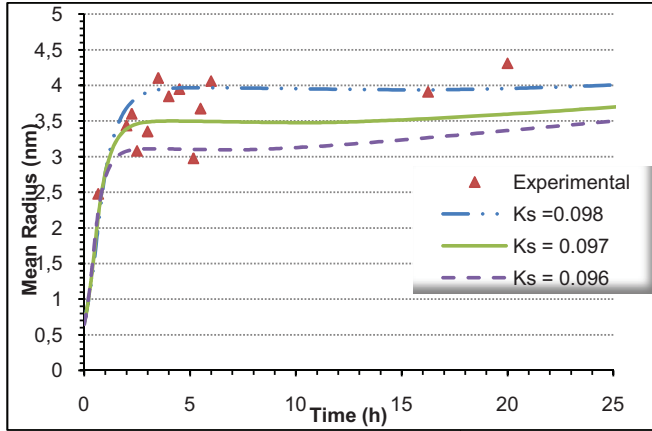


Figure IV-53: Influence of the change in solubility product on the evolution of Radius as a function of time for precipitation kinetics at 550°C

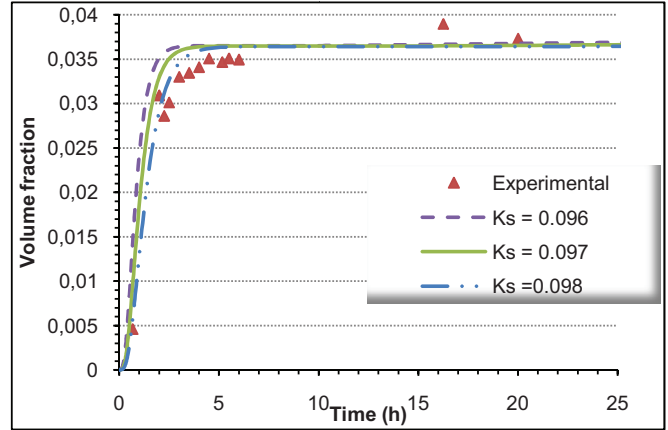


Figure IV-54: Influence of the change in solubility product on the evolution of Volume fraction as a function of time for precipitation kinetics at 550°C

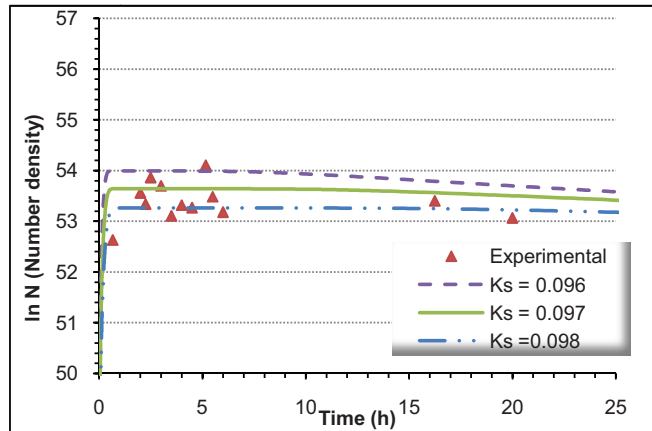


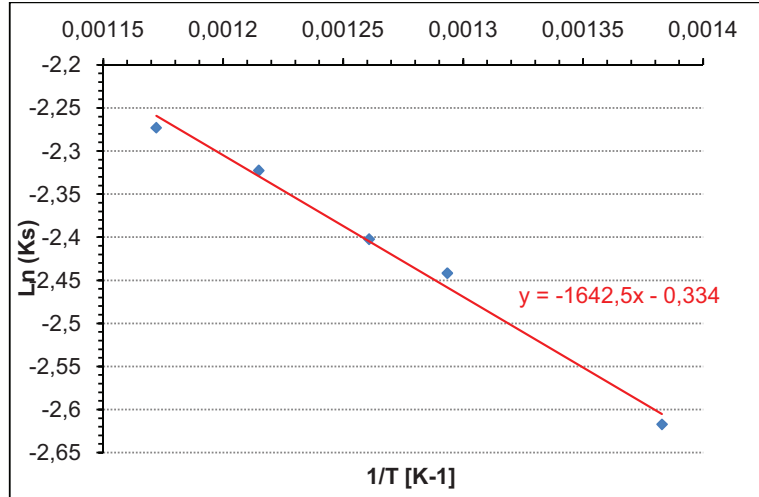
Figure IV-55: Influence of the change in solubility product on the evolution of Number density as a function of time for precipitation kinetics at 550°C

ii. Other temperatures

Study of the influence of K_s and γ on the precipitation kinetics was also done on other temperatures for which radius and volume fractions data were available, namely 450, 500, 520 and 580°C. Since the precipitates are known to be a coherent and ordered phase, the interfacial energy was estimated to stay constant with the temperature, thus only the solubility product was modified with temperature. The values found at the different temperatures are summarized in Table IV-12 below. The evolution of $\ln(K_s)$ with time as a function of $1/T$ was plotted Figure IV-56, showing a linear evolution. This is compatible with the approximation of $-\frac{A}{T} + B = \ln(K_s(at\%))$ which is consistent with the Arrhenius law of $K_s = K_0 \exp\left(\frac{-Q}{k_B T}\right)$.

Temperature [°C]	Temperature [K]	1/T	K_s	$\ln(K_s)$	Gamma [J/m ²]
450	723.15	0.00138284	0.073	-2.61729584	0.13
500	773.15	0.00129341	0.087	-2.44184716	0.13

520	793.15	0.0012608	0.0905	-2.40240543	0.13
550	823.15	0.00121485	0.098	-2.3227878	0.13
580	853.15	0.00117213	0.103	-2.27302629	0.13

Table IV-12 : Values of K_s and γ found for modeling using Multipreci modelFigure IV-56: evolution of $\ln(K_s)$ as a function of $1/T$

3) Influence of the alloy composition on the precipitation kinetics

In the context of alloy design it seems particularly interesting to study the influence of alloy composition on the precipitation kinetics in order to optimize it. Since the alloy composition in the present study was influenced by former works in the literature and chosen to have the minimum amount of Silicon and Titanium to have significant precipitation hardening, there is probably room for optimization of alloy composition with respect to the microstructure/properties relationships. The influence of alloy composition was studied using a class for precipitation, by

- Keeping the same initial solubility product, namely the same product $X_{Si} \cdot X_{Ti}$, in order to evaluate the effect of Si:Ti ratio
- Changing the solubility product at constant Si/Ti ratio to evaluate the influence of supersaturation $X_{Si} \cdot X_{Ti}$.

Since the model was calibrated on the Fe_2SiTi precipitation, these results presuppose that the precipitate structure stays the same even when changing the alloy composition, which is not necessarily the case. This is the main limitation of the following evaluation.

i. Constant initial solubility product

In the case of a constant initial solubility product, only the ratio Si(at%)/Ti(at%) changes from one alloy composition to the other. Five different ratios were tested and are summarized in Table IV-13 below. One can notice that alloys 1 to 4 contain more Silicon than Titanium contrary to alloy 5. The evolutions of Radius and Volume fractions with time, as obtained by the model, are given Figure IV-57 and 58 respectively. In each figure, the experimental results as well as the fitted model are represented. The variation of the kinetics in term of Si/Ti ratio, according to the model, are also drawn.

Figure IV-57 shows a relatively small influence of the Si/Ti ratio on the Radius evolution. Only the alloy containing more Titanium than Silicon seems to have markedly a different evolution of radius with time. This could be due to the fact that the Titanium is the diffusion-controlling element, and thus controls the kinetics. Figure IV-58 shows an important increase in Volume fraction with increasing Titanium content. This is consistent with the experimental observations made by Abson et al. [ABS1968], but only in the case where the Silicon is in stoichiometrical excess. Furthermore, one can see on Figure IV-58, that the volume fraction seems to reach its maximum for a composition close to the Si/Ti ratio of precipitates, namely Si/Ti=1, since alloys 4 and 5 have the largest volume fraction and since these fractions are very similar.

initial Ks constant			
Alloy	Si	Ti	Si/Ti
1	0.117	0.005	23.42
2	0.059	0.01	5.85
<i>REF</i>	<i>0.0492</i>	<i>0.0119</i>	<i>4.13</i>
3	0.039	0.015	2.60
4	0.029	0.02	1.46
5	0.02	0.029	0.68

Table IV-13: atomic content of Titanium and Silicon for the five different Si/Ti ratios tested keeping a constant initial Ks

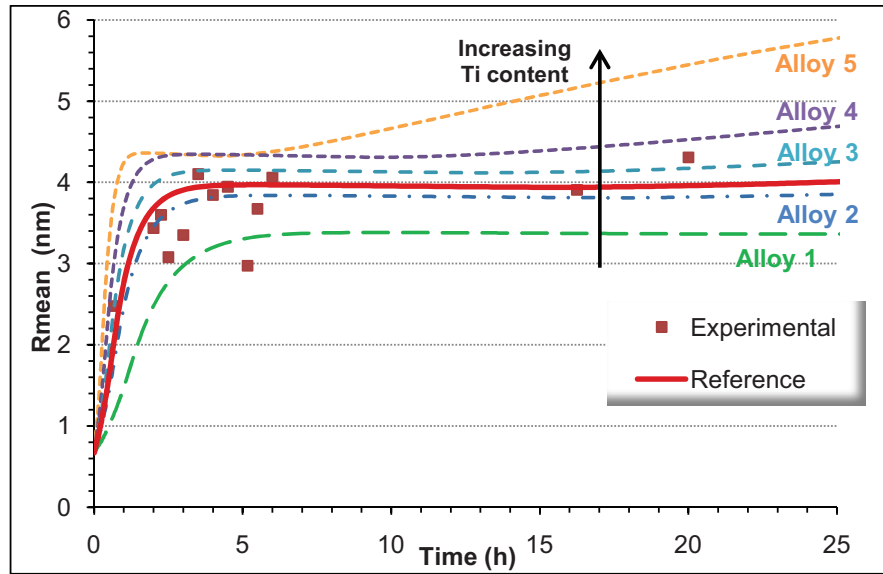


Figure IV-57: Influence of the alloy composition on the evolution of Radius with time, for a solubility product of $5.85 \cdot 10^{-4}$, and varying Si/Ti ratio

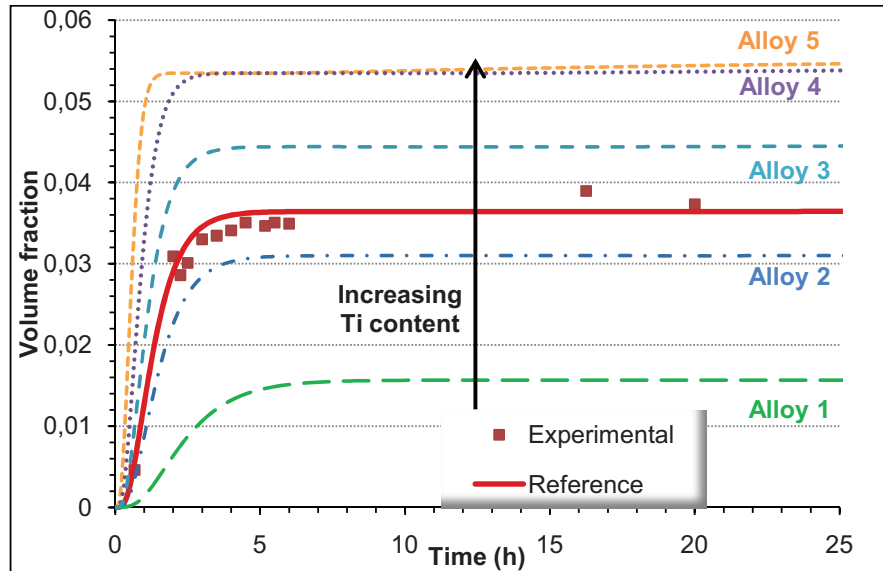


Figure IV-58: Influence of the alloy composition on the evolution of Volume Fraction with time, for a solubility product of $5.85 \cdot 10^{-4}$, and varying Si/Ti ratio

ii. Variable initial solubility product

Since the equilibrium solubility product stays the same for a given temperature, whatever the alloy composition, we have tried to vary the initial solubility product, namely $X_{Si}X_{Ti}$, to evaluate the influence of supersaturation on the precipitation kinetics. Six hypothetical alloy compositions have been tested, as shown Table IV-14 below, by investigating two cases: an initial solubility product 1.5 (Alloys 1 to 3) and 2 (alloys A to C) times greater than the reference K_s (being $K_s = 0.098$). For each case, 3 compositions have been tested: the first (1 and A) by keeping the same Si/Ti ratio (4.13), the second by keeping the same initial Silicon concentration (0.0492) and the third by keeping the same initial Titanium concentration (0.0119). The results are plotted on Figure IV-59 and 60 below. These

results show that the ratio Si/Ti does not influence much the precipitation kinetics, while the Titanium content does. In fact, when comparing alloy A2 and B2, which have the same Silicon composition, one can see that the volume fraction increases by almost 1% for the higher Titanium content (not surprising given the alloy has excess Si). However, the Silicon content does not seem to influence drastically either the radius or the volume fraction, as can be seen when comparing Alloy A3 and B3, which have the same Titanium content but a difference in Silicon of almost 2%. These observations are also in agreement with the conclusions drawn by Abson et al. [ABS1968], where the authors noticed that an increase in Titanium increased the observed volume fraction of precipitates.

Ks = Ksref*1.5				
Alloy	Si	Ti	Si*Ti	Si/Ti
REF	0.0492	0.0119	0.00059	4.13
A1	0.060	0.0146	0.00088	4.13
A2	0.0492	0.01785	0.00088	2.76
A3	0.0738	0.0119	0.00088	6.20
Ks = Ksref*2				
Alloy	Si	Ti	Si*Ti	Si/Ti
REF	0.0492	0.0119	0.00059	4.13
B1	0.07	0.0168	0.0012	4.13
B2	0.0492	0.0238	0.0012	2.07
B3	0.0984	0.0119	0.0012	8.27

Table IV-14: Compositions in Titanium and Silicon for the tested alloy compositions by taking an initial solubility product respectively 1.5 and 2 times greater than the reference initial solubility product

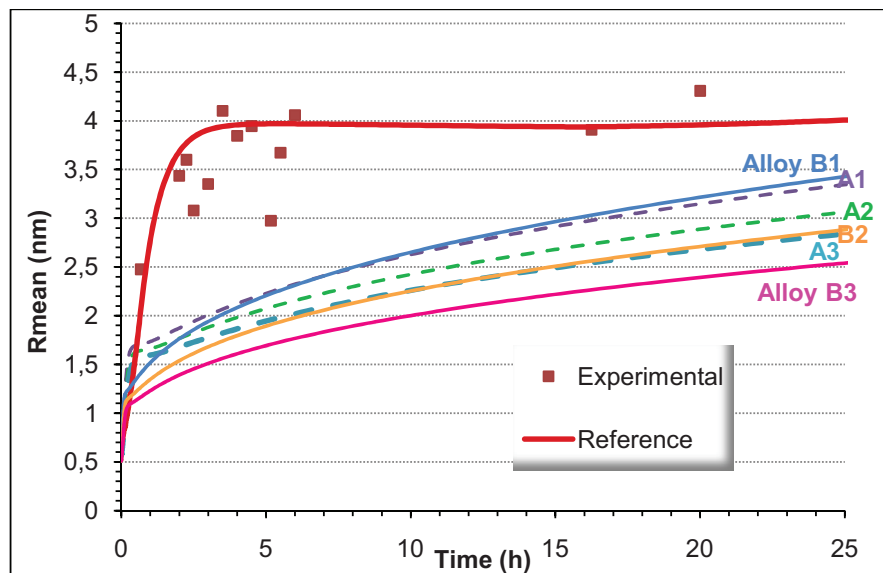


Figure IV-59: Influence of the change in initial solubility product on the evolution of Radius with ageing time

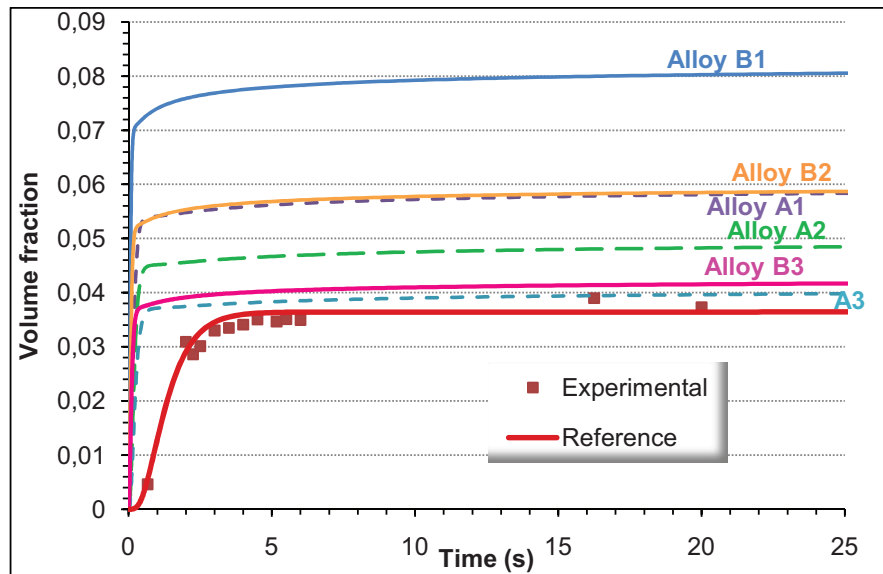


Figure IV-60: Influence of the change in initial solubility product on the evolution of Volume Fraction with ageing time

To summarize, these results from the class model have to be interpreted with caution, since they have been obtained with the assumption that the structure of the precipitates is Fe_2SiTi , whatever the alloy composition (which is obviously not the case when considering the results of [LOE2004]). However, in a general manner, it seems that Titanium content has a major influence on the volume fraction of precipitates, which is consistent with the results obtained by Abson et al. [ABS1968]. Thus, regarding these results, one can conclude that the Titanium content has an influence on the precipitation kinetics while the Silicon content is known to influence the mechanical properties of the iron matrix [JAC1975]. The optimized alloy composition in terms of relation between microstructure and mechanical properties can thus only be found by taking into account the influences of both alloying elements.

C. Comparison between DBPreci and Multipreci models

The comparison between both models is shown on Figure IV-61, 62 and 63 below for the radius, volume fraction and density evolution with time respectively. One can see that both give relatively satisfying results. The radius evolution is described with slightly faster kinetics in the case of the Multipreci model, but the volume fraction is very similar in both cases.

Thus, one can conclude that both models are able to describe the precipitation kinetics in the FeSiTi system although they induce the use of simplifying assumptions, especially in the case of the DBPreci model.

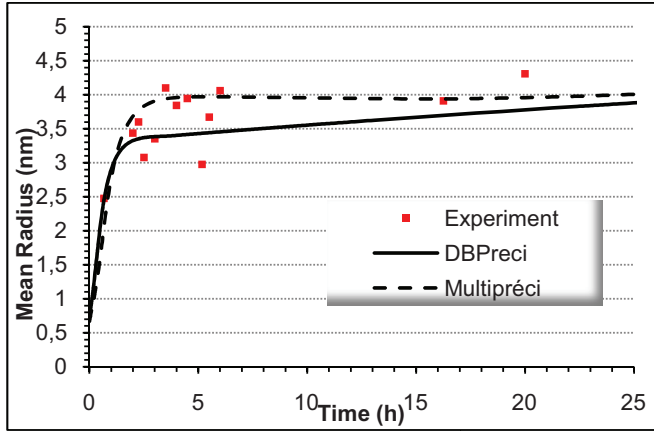


Figure IV-61: Comparison between DBPreci model and Multipreci model on the evolution of Radius with ageing time for samples aged at 550°C

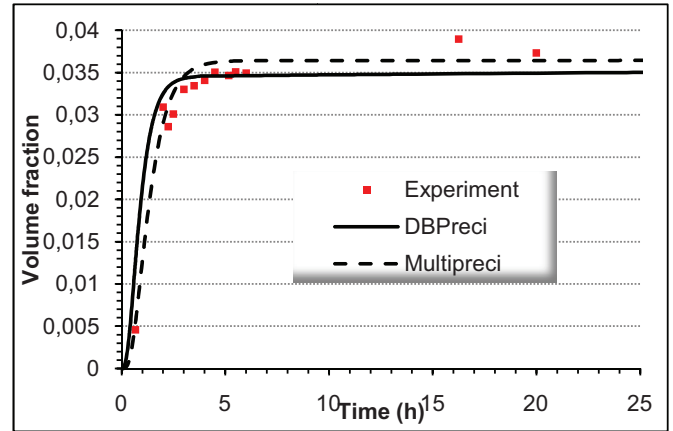


Figure IV-62: Comparison between DBPreci model and Multipreci model on the evolution of Volume fraction with ageing time for samples aged at 550°C

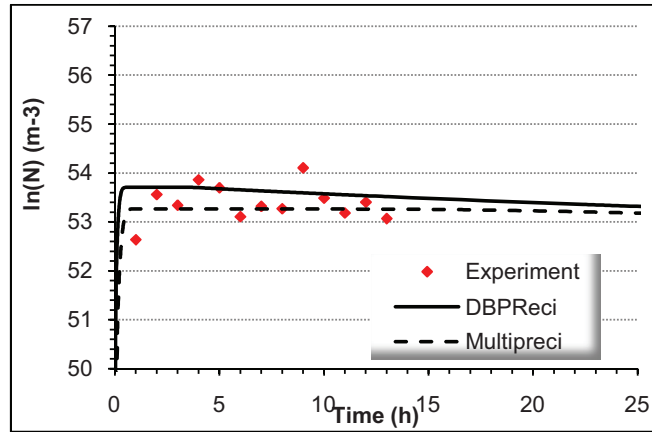


Figure IV-63: Comparison between DBPreci model and Multipreci model on the evolution of Number density with ageing time for samples aged at 550°C

IV. Conclusion

In this chapter, we have presented the general aspects of precipitation, namely the nucleation, growth and coarsening steps, followed by the outline of models describing homogeneous precipitation. Literature review on the precipitation in the Fe-Si-Ti system reveals the formation of a metastable phase Fe_2SiTi at low temperatures and for alloy composition containing small amounts of Titanium and Silicon (under 1.5 and 3.6wt% respectively) [JAC1970]. This is not the case for alloys containing larger amounts of titanium and aged at higher temperatures, over 800°C, where the stable phase Fe_2Ti forms directly [LOE2003]. Generally speaking, the studies concerning Fe-Si-Ti alloys essentially focus on higher temperatures, above 600°C.

In the present study, the precipitation in Fe-Si-Ti system have been studied experimentally for temperatures comprised between 450 and 580°C, thus containing the metastable Fe_2SiTi precipitates. Accurate characterization by Small Angle Neutron Scattering (SANS), Transmission Electron Microscopy (TEM), as well as Atom Probe Tomography (APT) has been performed in order to quantify the evolution of radius, volume fraction, size

distribution as well as their structure. A conclusion of this analysis is that the metastable phase Fe_2SiTi can be found up to long aging times, as for example after 20 hours ageing at 550°C . Furthermore, the evolution of the radius with ageing time is unusual since it stays almost constant from 2 hours ageing on. The results obtained have then permitted to fit the parameters missing for the complete description of the precipitation models. Two different models of the precipitation kinetics were applied in the present case, one describing the precipitation thanks to a classical nucleation, growth coarsening law, “DBPreci”, and the second considering the precipitation evolution by the description of classes of precipitates. The models were tested on several temperatures ranging from 450°C to 580°C , showing a good match between experimental and modeling results. Both precipitation models are in agreement with each other, meaning that both are sufficient to describe the precipitation kinetics of the metastable Fe_2SiTi precipitate phase.

Chapter V : Study of mechanical properties in the Fe-Si-Ti alloy. Yield Stress and Strain hardening modeling

In this chapter, a bibliographic review concerning strain hardening was done, considering the different aspects influencing it. The difference between isotropic and kinematic strain hardening will be presented using the description of existing models. In a second part, experimental results of tensile tests and Bauschinger tests will be reported and used to verify the validity of already existing yield stress and strain hardening models.

INTRODUCTION	155
I. BIBLIOGRAPHIC REVIEW	155
A. Parameters influencing strain hardening.....	155
1) Influence of solid solution.....	156
2) Influence of precipitates	156
B. Strain Hardening Models.....	158
1) Introduction to the Kocks-Mecking-Estrin model	159
2) Model considering kinematic strain hardening	160
i. Grain size effect	160
ii. Effect of precipitates	161
II. EXPERIMENTAL RESULTS ON FE-SI-TI	163
A. Bauschinger Tests.....	163
B. Modeling results.....	166
1) Modeling of the Yield stress evolution	166
2) Modeling strain hardening.....	168
III. DISCUSSION.....	171

Introduction

In a previous chapter (Chapter III) we have mentioned the important influence of precipitates on the yield stress. In the present chapter we will be interested in studying the influence of precipitates on the plastic behavior of the material and more precisely, on work-hardening. During plastic deformation mobile dislocations will also interact with other dislocations, which will contribute to the increase in mechanical properties. This is strain hardening, which will be the topic of the following chapter, followed by the presentation of the models describing this phenomenon.

I. Bibliographic review

A. Parameters influencing strain hardening

There exists a large number of microstructural parameters influencing strain hardening. The crystallographic structure of the material, as for example body centered cubic (bcc) or face centered cubic (fcc), has a great influence on the strain hardening of materials since it influences the glide plane of the material and generally the dislocation motion. It is well known that the strain hardening of fcc single crystal materials is divided in three steps, with increasing flow stress:

- a. the dislocation density increases with applied strain when the yield stress is reached on a slip system
- b. the dislocations start to pile-up and entangle, making the deformation more difficult and increasing the hardness of the material at least until the stress applied or the temperature is sufficient to activate cross-slip
- c. Cross-slip of dislocations is sufficiently important to start dynamic recovery of dislocations that decreases the net strain hardening rate

In the case of fcc materials the dislocations will have a tendency to dissociate into two “Shockley partials” in order to minimize the elastic energy, thus creating a stacking fault ribbon between these two partial dislocations [VAN1979]. These are not necessarily in the same glide plane and need to recombine in one dislocation (at least over a certain length) in order to cross-slip. This recombination of the two Shockley partials is easier when the stacking fault zone is small, thus the stacking fault energy is important [VER1975]. Hence, the lower the stacking fault boundary energy the more difficult the cross-slip and the less the material will be able to undergo efficient dynamic recovery.

In the case of bcc materials, such as for example the Fe-Si-Ti alloy, the dislocation dissociation is not as easy as in a fcc material, since the screw dislocations have a three dimensional core distributed over several planes ([LOU1979], [VAN 1979]), making them more or less sessile. Furthermore, the first step (a) of strain-hardening is not as noticeable as in a fcc material, it is often as though we would directly have step c [SES1979].

Strain hardening also can be influenced by microstructural features in a polycrystalline material (solid solution, grain boundaries, precipitates, interphases ...). Two of them will be described here, the solid solution and the precipitates.

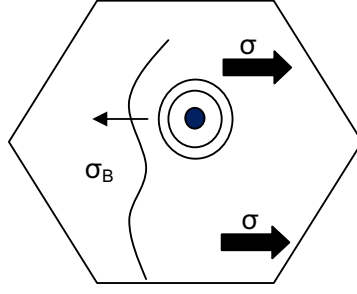
1) Influence of solid solution

The increase of the necessary stress to deform a material plastically can be due to the presence of solute atoms in the matrix. As mentioned by P. Haasen in [CAH1996] the main reason for hardening by solid solution is the change in work-hardening mechanism meaning a change in dislocation arrangement. Most of the change in dislocation arrangement can be explained by a decrease in stacking-fault energy due to alloying elements. This decrease leads to a more difficult cross-slip, which is for example the case for additions of Silicon. The effect of Silicon on the mechanical properties of ferrous alloys has been studied by numerous authors as for example Griffiths et al. [GRI1966]. It has been found that it decreases the stacking fault energy, favors dislocation dissociation and thus reduces the cross-slip probability. These alloys exhibit often a high strain hardening as well as planar dislocation glide.

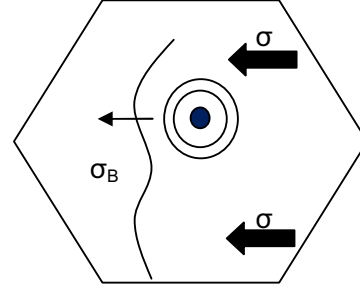
2) Influence of precipitates

In the presence of non-shearable precipitates where Orowan loops are formed during deformation, the loops will be an important obstacle to the movement of mobile dislocations. The accumulation of loops will also produce a back stress which acts to repel other dislocations. Both effects will contribute to work hardening.

Understanding the overall influence of the presence of precipitates on the strain hardening is relatively complex and needs to take into account their influence not only on the storage of dislocation but also on the recovery process of the material [BRO1971]. In fact, one other very important effect of particles on the plastic behavior of materials is the creation of internal stresses which will have an influence on the kinematic strain hardening of the material. Contrary to the isotropic strain hardening, the kinematic strain hardening is strain path dependent [BRO1977]. An easy way to describe, though somewhat simplistic, this strain path dependence is given by Figure V-1 using the fact that when dislocation loops accumulate around precipitates they make the movement of other dislocations more difficult, as if applying a stress, σ_b , in the direction opposite to the global applied stress, σ . When now the global applied stress is inversed, σ (e.g. passing from tensile to compression stress) the backstress, σ_b , will be in the direction of the applied stress thus decreasing the necessary stress to reach plastic deformation. This is called the Bauschinger effect.



a) Backstress in the opposite direction to the applied stress



b) Backstress in the same direction as the applied stress

Figure V-1: Scheme of the kinematic strain hardening: a) the Orowan loops around the precipitate make the movement of dislocations harder and b) the Orowan loops around the precipitate create a “permanent softening” in the inverse applied stress

A way to quantify this backstress is the so called Bauschinger test. The best-known Bauschinger test is the tensile-compression test but one can also perform a reverse shear test to discriminate the internal stresses. Figure V-2 shows the way to determine the Backstress experimentally, as done by Proudhon et al. [PRO2008], namely the difference between the monotonic behavior of a material and its reverse response in a tensile-compression test. The value of σ_b is then defined as shown Figure V-2 as:

$$\sigma_b = \frac{\sigma_1 - \sigma_2}{2} \quad (V-1)$$

General description of this backstress is given as:

- in the forward deformation direction the flow stress is expressed as: $\sigma = \sigma_0 + \sigma_f + \sigma_b$
- in backward direction one will have: $\sigma = \sigma_0 + \sigma_f - \sigma_b$

This backstress σ_b is also called X and can be expressed as $\frac{\Delta\sigma_B}{2}$ where $\Delta\sigma_B$ is defined in Figure V-3.

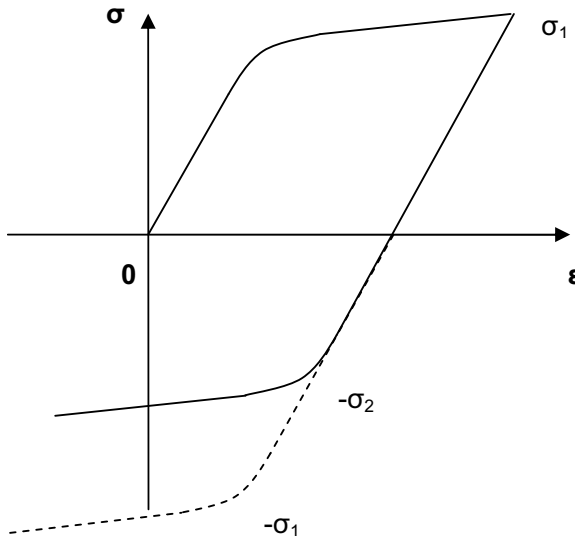


Figure V-2: scheme of the Bauschinger effect

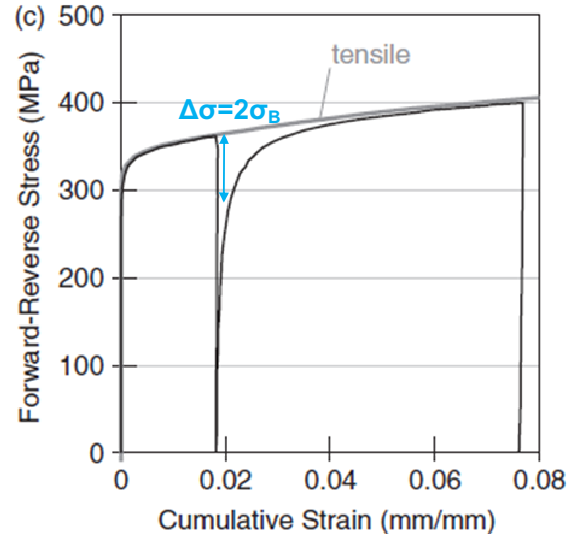


Figure V-3: stress-strain curve of a forward and reverse tensile-compression test compared with the monotonic behavior [PRO2008]

Since the Bauschinger effect is a signature of the kinematic hardening, the Bauschinger test enables in principle to differentiate the kinematic from the isotropic hardening. Since the global applied stress will be decreased by internal stresses which are polarized, the idea is to make mechanical tests in one direction and reverse.

The origin of this backstress is the internal stresses created by the obstacles inside the material such as precipitates. The detailed description of the phenomena intervening in the strain-hardening of a material by modeling either taking into account the kinematic strain hardening or not, is the objective of the next section.

B. Strain Hardening Models

Two main classes of models exist in order to describe and predict plastic deformation in polycrystalline materials: the physically based and the phenomenological models [DUN2005]. The former considers the different contributions of microstructure to the macroscopic behavior, while the latter are only descriptive and based on global behavior using internal variables, sometimes with a possible physical interpretation, but with purely phenomenological evolution.

In a pure material, the flow stress $\tilde{\sigma}$ is related to the spacing Λ of obstacles to dislocation glide:

$$\tilde{\sigma} \propto \frac{\mu b}{\Lambda} \quad (V-2)$$

If one assumes that the strength of the material depends entirely on dislocation-dislocation interactions, then the average obstacle spacing is related to the average dislocation density ρ . This is shown in the forest hardening law developed in the case of a pure material:

$$\sigma = \alpha M \mu b \sqrt{\rho} \quad (V-3)$$

- M being the average Taylor factor
- α a numerical constant
- μ the shear modulus
- b the dislocation Burgers vector

The evolution of the forest density depends on two competing processes: dislocation storage and dislocation annihilation or dynamic recovery. Obstacles to dislocation motion will stop and store mobile dislocations so increasing the density of dislocations forest. Obstacles can include the dislocation forest itself, grain or phase boundaries and second phase precipitates.

1) Introduction to the Kocks-Mecking-Estrin model

The Kocks-Mecking-Estrin model ([KOC1976], [MEC1981]) is a physically based model for the plastic deformation in FCC and BCC metals. It is based on the assumption that the properties of a material depend entirely on its current metallurgical structure [DUN2005].

Plastic deformation is controlled by dislocation motion [COT1953]. Therefore the dislocation density is the parameter used to describe the plastic behavior and thus also the strain-hardening of materials. In fact, as mentioned above, in the domain of plastic deformation the dislocations will change their arrangement in the material, meaning they will increase their number, move, annihilate, pile-up, and thus this is considered as the main element describing plastic deformation. During strain hardening of a material two main phenomena will be competing, the storage and the annihilation of dislocations. This was expressed by Lücke & Mecking in [LUE1973] by the following expression:

$$\frac{d\rho_{tot}}{d\varepsilon} = \frac{d\rho^+}{d\varepsilon} - \frac{d\rho^-}{d\varepsilon} \quad (V-4)$$

where $\frac{d\rho^-}{d\varepsilon}$ expresses the density of annihilating dislocations and $\frac{d\rho^+}{d\varepsilon}$ the ones which will store, accumulate.

The first term can be described as:

$$\frac{d\rho^+}{d\varepsilon} = k_1 \sqrt{\rho} \quad (V-5)$$

Where k_1 is an efficiency coefficient and $\sqrt{\rho}$ expresses the evolution of forest dislocations. This expression results from the assumption that the mean free path of dislocations scales as $\frac{1}{\sqrt{\rho}}$.

The second term stands for dislocation annihilation, which occurs in the case of dynamic recovery, meaning when two dislocations with opposite Burgers vector come closer by attractive forces which can lead to cross-slip and eventually annihilation. It can be written as:

$$\frac{d\rho^-}{d\varepsilon} = k_2\rho \quad (V-6)$$

Where k_2 , contrary to k_1 , is dependent on strain rate and temperature as given by ([EST1984], [EST1996], [KOC1976]):

$$k_2 = k_{20} \left(\frac{\dot{\varepsilon}}{\dot{\varepsilon}_0} \right)^{-1/n} \quad (V-7)$$

In a material, second phase particles will limit the dislocation mean free path. The main hardening mechanism is given by the Orowan stress. In the KME model, this stress is neglected compared to the hardening associated with dislocation storage but another term stands for their effect on hardening, expressed with the inter-particle distance L , using:

$$\left. \frac{d\rho}{d\varepsilon} \right|_{\text{precipitates}} = \frac{1}{bL} \quad (V-8)$$

In the case of a polycrystalline material containing hardening precipitates, the complete evolution of dislocation density can be expressed as the sum of the above given equations, by:

$$\left. \frac{d\rho}{d\varepsilon} \right|_{\text{Tot}} = M \left(\frac{1}{bL} + k_1\sqrt{\rho} - k_2\rho \right) \quad (V-9)$$

2) Model considering kinematic strain hardening

Strain hardening can be divided into two components: the isotropic and kinematic strain hardening. Isotropic strain hardening has been described previously and concerns the increase in obstacles density during deformation. The kinematic strain hardening will involve the presence of internal stresses in the material, which are long range and polarized [FRI2009].

i. Grain size effect

As in the KME model, the determinant parameter is the dislocation density, since strain hardening is a phenomenon induced by dislocation accumulation and movement. The forest dislocations are considered to be sessile and have an effect on the movement of

mobile dislocations which are generated by Frank-read sources. The effect of forest dislocations on the flow stress is expressed in equation (V-3)) given above. But the evolution of dislocation density has been modified by Sinclair et al. in [SIN2006], taking into account a saturation term, n_0 , for the number of cumulated dislocations loops at grain boundaries:

$$\left. \frac{d\rho}{d\varepsilon} \right|_{tot} = M \left(\frac{1}{bL} \left(1 - \frac{n}{n_0} \right) + k_1 \sqrt{\rho} - k_2 \rho \right) \quad (V-10)$$

While a polycrystalline material is deformed, the mobile dislocations will store at grain boundaries thus having an effect on the kinematic strain hardening. The smaller the grains the more these accumulating dislocations will interact with each other and the more they will influence on the backstress. The value of the backstress induced by the grain boundaries is expressed as:

$$X_D = n \frac{M\mu b}{d} \quad (V-11)$$

which is inspired from the equation of Bouaziz et al. in [BOU2006] expressing the backstress exerted by a pile of n dislocations on an active source at distance d . Here d is the grain size and n is a variable expressing the mean effect of grain boundaries on the backstress, namely by giving the evolution of the flux of dislocations arriving at a grain boundary per slip band as:

$$\frac{dn}{d\varepsilon} = \frac{\lambda}{b} \left(1 - \frac{n}{n_0} \right) \quad (V-12)$$

which gives $n = n_0 \left[1 - \exp \left(-\frac{\lambda}{bn_0} \varepsilon \right) \right]$ when integrating from 0 to ε .

λ is the mean spacing between slip bands at a grain boundary; it is defined by the number $\frac{\lambda}{b}$ being the number of dislocations per slip bands geometrically necessary to provide the deformation.

ii. Effect of precipitates

The first mention of the creation of internal stresses by the presence of precipitates is found in works by Orowan in 1959 [ORO1959]. The author explained their origin by the formation of dislocation pile-ups at the precipitates, which become strong obstacles to dislocation motion. A great number of studies then tried to explain those internal stresses in details, such as Wilson et al. [WIL1965], Brown [BRO1977], Embury [EMB1987] but also very recently Proudhon et al. [PRO2008]. In the case of shearable precipitates the internal stresses produced are small and the increase in flow stress is essentially attributed to the forest dislocations. In the presence of non-shearable precipitates, the presence of Orowan loops creates important internal stresses, which influence on the strain hardening cannot be neglected. These were interpreted by long-range elastic stresses produced by dislocation loops stored around the precipitates.

The following model is based on the PhD works of A. Aouafi [AOU2009] and G. Fribourg [FR2009] concerning ferritic micro-alloyed steels and Aluminum 7xxx series respectively. They are in turn essentially based on works by Estrin et al. and Proudhon et al. ([EST1996], [EST1999] and [PRO2008]).

The effect of precipitates on the flow stress has already been discussed in Chapter III concerning the evolution of the yield stress. We use the Ashby equation:

$$\sigma_p = 0.84 \frac{1.2M\mu b}{2\pi\lambda_p} \ln\left(\frac{d_p}{2b}\right) \quad (V-13)$$

where λ_p is the mean inter-particle distance

The kinematic strain hardening due to precipitates depends on their volume fraction f_p and on their Young's modulus E_p is expressed by Proudhon et al. [PRO2008] as:

$$X_p = f_p E_p \varepsilon_p^* \quad (V-14)$$

with ε_p^* being the unrelaxed strain around precipitates, which is expressed as:

$$\varepsilon_p^* = \frac{bn_p}{d_p} \text{ and modified by Aouafi [AOU2009] by } \varepsilon_p^* = \frac{bn_p}{Md_p}$$

The complete backstress due to the presence of precipitates can thus be expressed as:

$$X_p = \frac{f_p E_p b}{Md_p} n_p \quad (V-15)$$

The internal variable, n_p , is expressed as follows, modified by a factor $1 - \frac{n_p}{n_{0p}}$ taking into account the saturation of loops due to relaxation at a value n_{0p} :

$$\frac{dn_p}{d\varepsilon} = \frac{Md_p}{b} \left(1 - \frac{n_p}{n_{0p}}\right) \quad (V-16)$$

which gives $n_p = n_{0p} \left[1 - \exp\left(\frac{-Md_p}{bn_{0p}} \varepsilon\right)\right]$ when integrating from 0 to ε .

To summarize the previously described elements contributing to the increase in strain hardening, one can express the total flow stress as the sum of the isotropic strain hardening contributions and the kinematic strain hardening by equation (V-17) below.

$$\sigma = \sigma_0 + (\sigma_f^m + \sigma_p^m)^{1/m} + X_D + X_p \quad (V-17)$$

where:

- σ_0 is the stress due to friction and solid solution strengthening. In fact, solid solution hardening has an effect on strain hardening depending on the alloying

elements. It is commonly assumed that these alloying elements have different hardening capacities depending on their composition X_i . In the ArcelorMittal Research center, for example, the hardening capacity of Manganese is considered to be of 40Mpa per wt%, Copper 80MPa, Nickel 45MPa and for Titanium and Silicon both are assumed to harden 80MPa per wt%. Thus, in the present case the solid solution hardening can be calculated by:

$$\sigma_{SS} = 2.54 * 80 + 1.05 * 80 = 215\text{Mpa}$$

Since the composition of the alloy is Fe-2.54wt%Si-1.05wt%Ti. The complete σ_0 was evaluated at 400MPa, which seems reasonable when comparing it to the yield stress of the as-quenched sample

- σ_f is the stress related to the forest dislocations
- σ_p the stress due to the formation of Orowan loops
- X_D is the internal stress related to the grain boundaries effect
- X_p is the internal stress related to the presence of precipitate particles
- m equal to 1 or 2

In the next section we will show the experimental results and compare them with the theoretical predictions.

II. Experimental Results on Fe-Si-Ti

A. Bauschinger Tests

In collaboration with A. Aouafi, Bauschinger tests have been performed on the Fe-Si-Ti alloy by reverse shear tests (see Chapter II for details on the experimental setup). Four different deformation rates have been tested (4, 7, 10 and 20%) on samples with precipitation ageing at 550°C during 2 hours, containing precipitates around 7nm diameter as measured by SANS experiments. This enabled us to determine the value of the Backstress due to the precipitates. The offset of plastic deformation used for the definition of the backstress was taken at 0.3%. In [AOU2009] and [FRI2009], the authors have shown the very important influence of the offset on the order of magnitude of the Backstress. Thus, 0.3% was taken since it is the value used at ArcelorMittal Research, and it corresponds to a reasonable value of the backstress X . Figure V-4 shows the complete curves resulting from the Bauschinger tests.

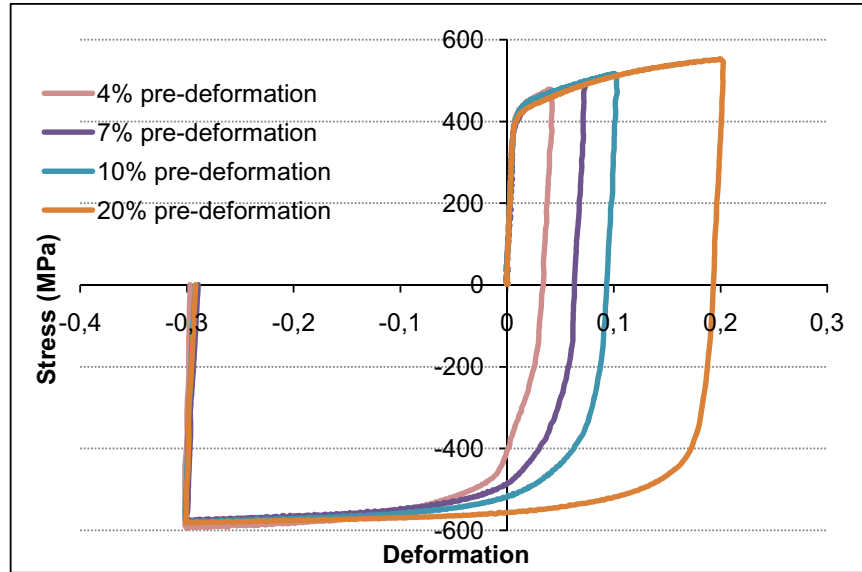


Figure V-4: Stress-strain curves of Bauschinger tests performed on samples aged at 550°C during 2 hours for various pre-deformation rates

The Backstress was calculated comparing the simple shear test curve and the one after reverse shear test. Three examples of these reverse shear tests are presented Figure V-5, 6 and 7 with respectively 7, 10 and 20% pre-deformation. We notice the permanent softening in the three cases leading to a slightly smaller stress in the reverse mode. This is a well known phenomenon ([WIL1965], [BRO1977], [EMB1987] or [RAU2007]), which is due to the fact that the deformation is not completely reversible and depends on the dislocation structure. The authors have shown that the presence of small, dense precipitation increased this phenomenon. Another interesting remark concerns the shape of the reverse loading curve. One can notice that in the first stages of the reverse curve the strain hardening is very important and slows down with increasing strain. Proudhon et al. [PRO2008] already mentioned that phenomenon and clearly distinguished two regions in the reverse curve: a transient curve with steep slope, and a steady state one. In our case, again, one can notice these two regions in the reverse loading curve as seen on Figure V-5, 6 and 7. The transient region usually increases with pre-deformation [AOU2009], which is also the case here.

Figure V-8 shows the evolution of the backstress measured as a function of the equivalent forward strain. The shear stress was converted into an equivalent tensile stress by multiplying it by: $\sigma = \sqrt{3} \cdot \tau$, while the equivalent strain was calculated using $\varepsilon = \frac{\gamma}{\sqrt{3}}$. One can see that the backstress reaches a plateau at 230MPa after 2% equivalent deformation. This is a quite important value compared to classical IF Steels, for which a common backstress is measured at around 90MPa. Figure V-8 compares the measured backstress with the theoretical Bauschinger stress, σ_B , of a material that would not be able to relax at all, namely: $\sigma_B = f_p E_p \varepsilon_p$ [PRO2008], where f_p is the volume fraction of precipitates, E_p the Young's modulus of the precipitates and ε_p the deformation of the precipitates (taken as the equivalent deformation). We can thus notice that the material already relaxes after 2% deformation. Furthermore, this unrelaxed curve enables to evaluate the Young's modulus of the precipitates at a value around 300GPa

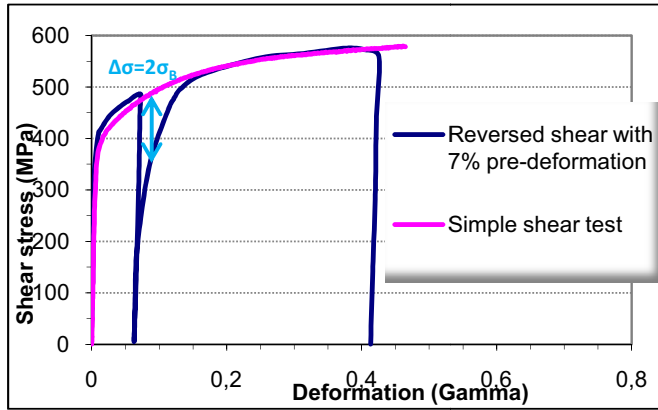


Figure V-5: Bauschinger test on sample aged at 550°C during 2 hours after 7% deformation

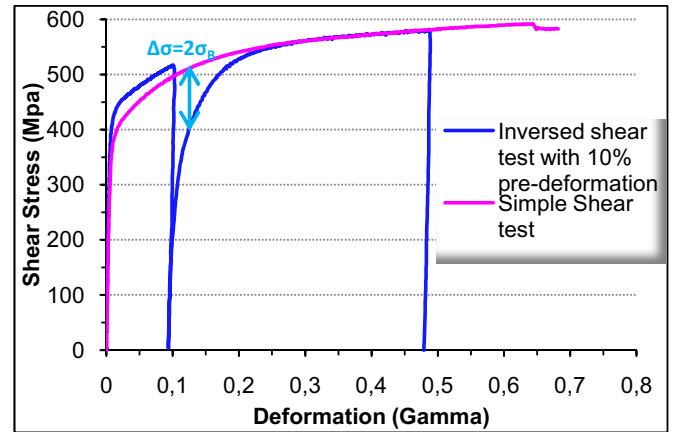


Figure V-6: Bauschinger test on sample aged at 550°C during 2 hours after 10% deformation

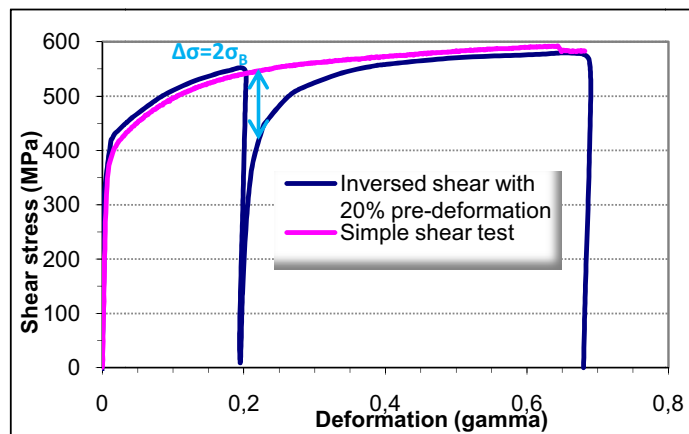


Figure V-7: Bauschinger test on sample aged at 550°C during 2 hours after 20% deformation

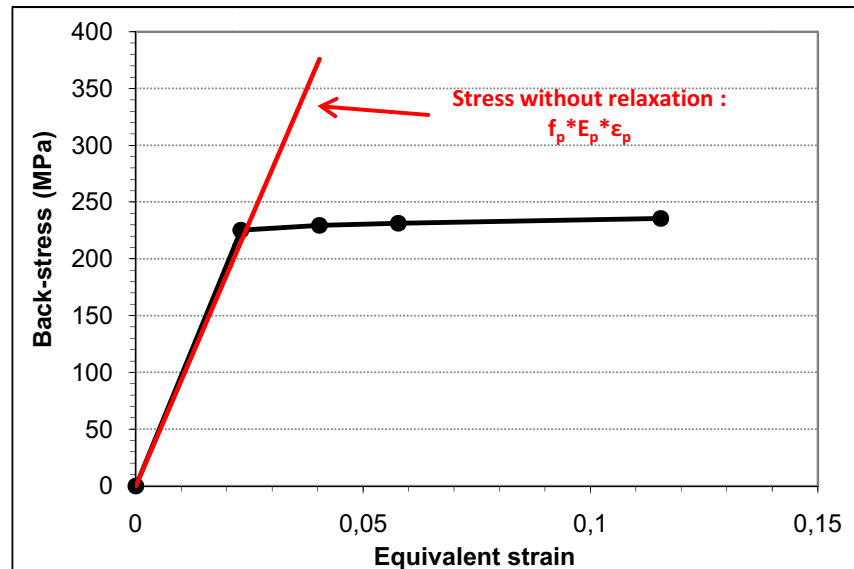


Figure V-8: evolution of backstress as a function of equivalent strain compared with the theoretical stress without relaxation

B. Modeling results

Now that the experimental data is available, it seems interesting to see whether the existing models are able to predict the behavior of the Fe-Si-Ti alloy in terms of Yield stress and Strain hardening.

1) Modeling of the Yield stress evolution

The values of Radius and Volume fraction of precipitates obtained by SANS enabled to compare models of Yield stress with the experimental results presented in Chapter III. Since the observation of dislocation structures in the Fe-Si-Ti alloy could not reveal clearly the deformation mechanism (shearing or by-passing of particles by dislocations) the modeling of yield stress evolution requires certain hypotheses, which are plausible but not unambiguously supported by experimental observations of the dislocation structures.

The three models used can be summarized as:

- Shearing model:

$$\sigma = \sigma_0 + 0.7 \frac{k^{3/2} M \mu}{\sqrt{b}} \sqrt{R f_p} \approx \sigma_0 + K \sqrt{R f_p} \quad (\text{V-18})$$

- Orowan by-passing :

$$\sigma = \sigma_0 + 0.8 \frac{M \mu b}{\lambda_p} \quad (\text{V-19})$$

- Orowan modified by Ashby:

$$\sigma = \sigma_0 + 0.84 \frac{1.2 M \mu b}{2\pi \lambda_p} \ln \left(\frac{R}{b} \right) \quad (\text{V-20})$$

with R and f_p the radius and volume fraction of particles, λ_p the interparticle distance and k the obstacle strength coefficient. k was evaluated experimentally so as to fit the experimental curve. Deschamps [DES1997] evaluated this coefficient as 0.1 in Aluminum alloys, which is too important in the present case. But since k depends on the nature of precipitates coupled with the crystallography of the matrix, there is no reason for which k should be identical in both cases.

The values of the different parameters are given Table V-1 below.

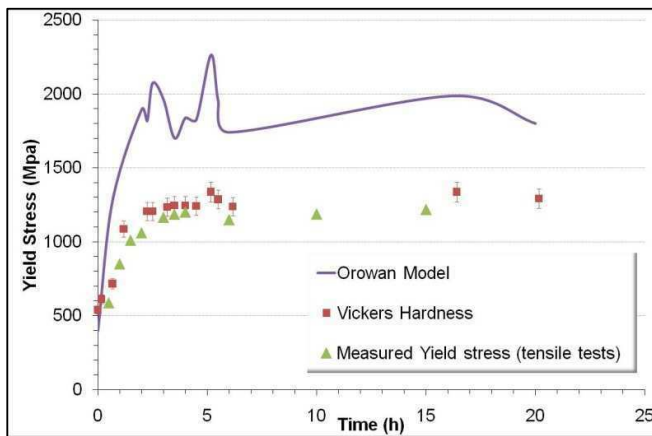
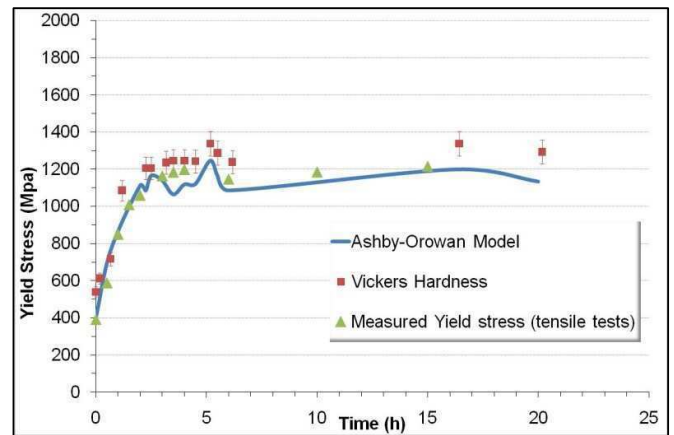
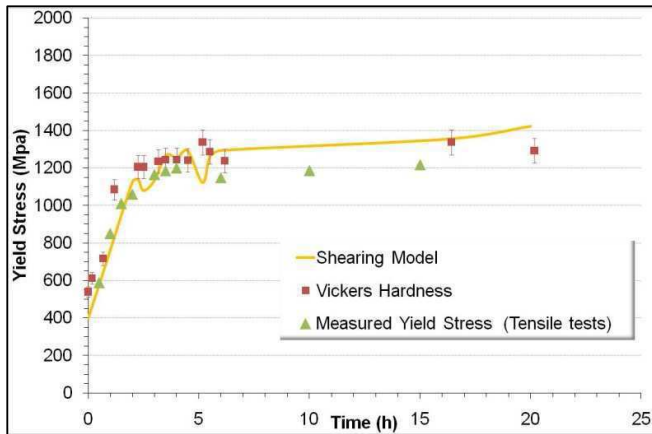
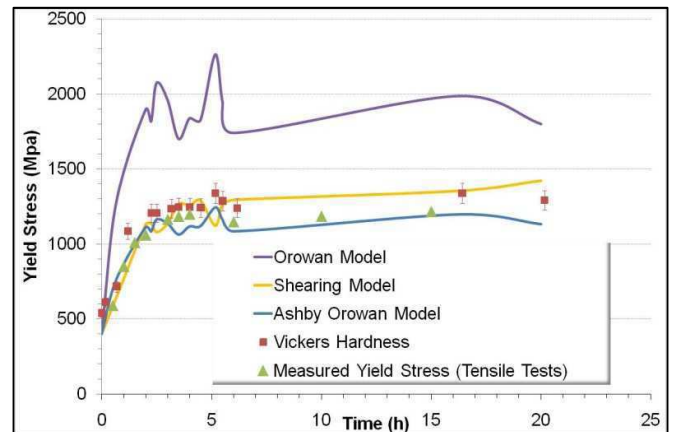
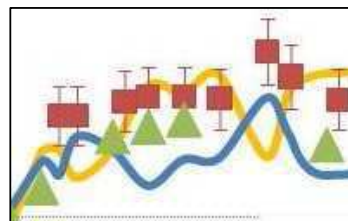
Parameter	Value
M	2.77
μ	80GPa
b	2.5e-10 m

σ_0	400MPa
k for the shearing model (fitted on experimental results)	0.04

Table V-1: Values of the different parameters used for modeling

The value of σ_0 was taken using the value of the Yield stress measured for the as-quenched sample, which is of 400MPa.

Values of volume fraction and radius provide from the experimental data of the SANS experiments (see Chapter IV). Figures 9, 10, and 11 show the modeling results obtained with the three different approaches, Figure V-12 being a summary of all three. (*)

**Figure V-9: Orowan model compared with experimental data****Figure V-10: Ashby-Orowan model compared with experimental data****Figure V-11: shearing model compared with experimental data****Figure V-12: summary of the different models****Figure V-13: magnified part of Yield stress evolution between 2 and 6 hours (see Figure V-12)**

(*) One can notice that hardness increases slightly for the sample aged at 550°C during 5 hours, as mentioned in previous chapters. This slight increase in hardness is also observed with the modeled values, since they use the values of radius which also increase (as seen with SANS results).

We notice on the Figures above that the value of yield stress varies slightly in the time interval from two to four hours ageing due to the fluctuation of the radius values obtained by SANS (see Chapter IV). This is particularly amplified by the Orowan model.

Regarding the comparison between the three models, two approaches could be considered: the Ashby-Orowan and shearing equations. But following the shape of the curves, one can notice on Figure V-10 the shape of the Ashby-Orowan modeling curve which follows exactly the fluctuations of the yield stress measured by hardness tests and radius measurements. The shearing model however predicts a decrease in hardness at 5 hours ageing, which is the contrary of what is experimentally observed (see Figure V-13). Thus, one can conclude on a probable by-passing of particles, since Ashby-Orowan follows the best the experimental observations.

2) Modeling strain hardening

Modeling of the plastic behavior of the material was done using the equations described previously taking into account the kinematic strain hardening as summarized in Table V-2. In this model the parameters which are dependent on the material and need to be determined are: α , μ , k_1 , k_2 and λ . These were based on modeling results on IF steels performed by A. Aouafi in [AOU2009]. Some other parameters are unknown such as, for example, the value of Young's modulus from the precipitates, E_p , which does not exist in the literature, or n_0 and n_{0p} . n_0 was proposed by A. Aouafi ($n_0 = 7.5$), the two other parameters have been adjusted in order to reproduce our experimental results. The values are summarized in Table V-3 below.

	Isotropic strain hardening	Kinematic strain hardening
Grain size effect	$\sigma_f = \alpha M \mu b \sqrt{\rho}$	$X_D = n \frac{M \mu b}{d}$
Precipitation effect	$\sigma_p = 0.84 \frac{1.2 M \mu b}{2 \pi \lambda_p} \ln \left(\frac{d_p}{2b} \right)$	$X_p = \frac{f_p E_p b}{M d_p} n_p$

Table V-2: Summary of the equations used for strain-hardening modeling

Parameters	Values
Solid solution strengthening: σ_0	300 MPa
Material constant: α	0.38 (ferrite)
Taylor factor: M	2.77
Shear modulus: μ	80 GPa
Efficiency of dislocation storage on the dislocation forest: k_1	0.01

Dynamic recovery term: k_2	1.3
Efficiency of solid solution hardening: λ	90 b
Young's modulus of precipitates: E_p	300 GPa
Maximum number of dislocations stored at grain boundaries: n_0	7.5
Maximum number of dislocations stored around precipitates: n_{0p}	2
m (power law for influence of isotropic strain hardening)	2

Table V-3: values of the parameters used for the model (based on [AOU2009])

The results show a relatively good agreement between experimental measurements and the model as shown Figure V-14. The value of k_1 was modified from the value found in [AOU2009] in order to fit the curve of as-quenched sample, which was taken as a reference. For the as-quenched sample, since no precipitates are present to contribute to hardening, the influence of the solid solution is more important than in the precipitate-hardened samples. Thus, the value of σ_0 was taken as 400MPa for the as-quenched sample and 300MPa for the other samples. This evolution of the influence of σ_0 takes into account the depletion of the solid solution with precipitation.

On Figure V-14 one can notice the good agreement between model and experiments for almost all samples except for the one aged during 30minutes. The underestimation of strain hardening in this case, as one can see on the slope Figure V-14, is probably due to the importance of solid solution effect in this sample. In fact, at this stage the precipitation is still in the nucleation-growth process, as is visible on the evolution of volume fraction measured by SANS in Chapter IV (Figure 14), since at 30 minutes the volume fraction is still increasing. Thus, the addition of precipitation and solid solution effect on strain hardening at that state is probably underestimated.

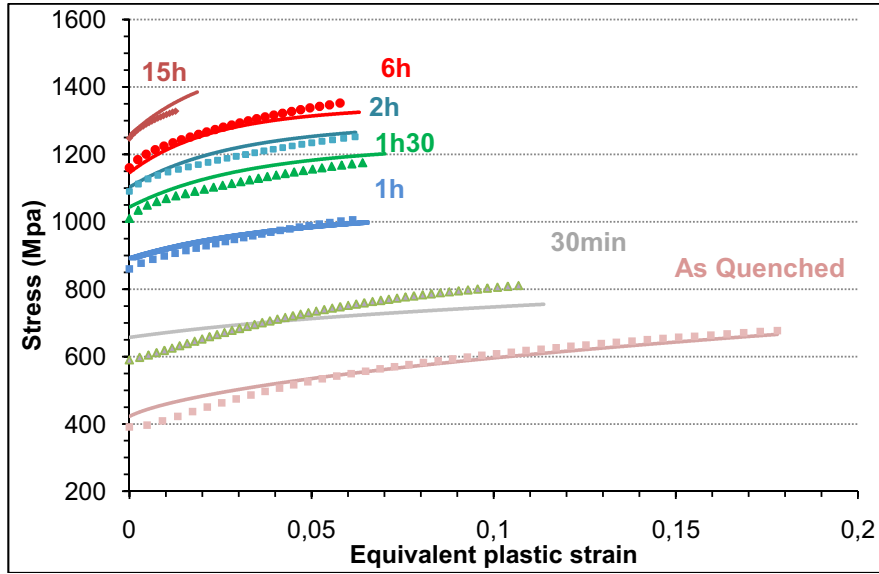


Figure V-14: Summary of the plastic part of tensile test curves compared with strain hardening modeling

One other way to confirm the model is by comparing the values of backstress measured experimentally and the ones calculated using the models of kinematic strain hardening. Figure V-15 shows the results obtained, revealing a relatively good description for pre-deformation states around 5%.

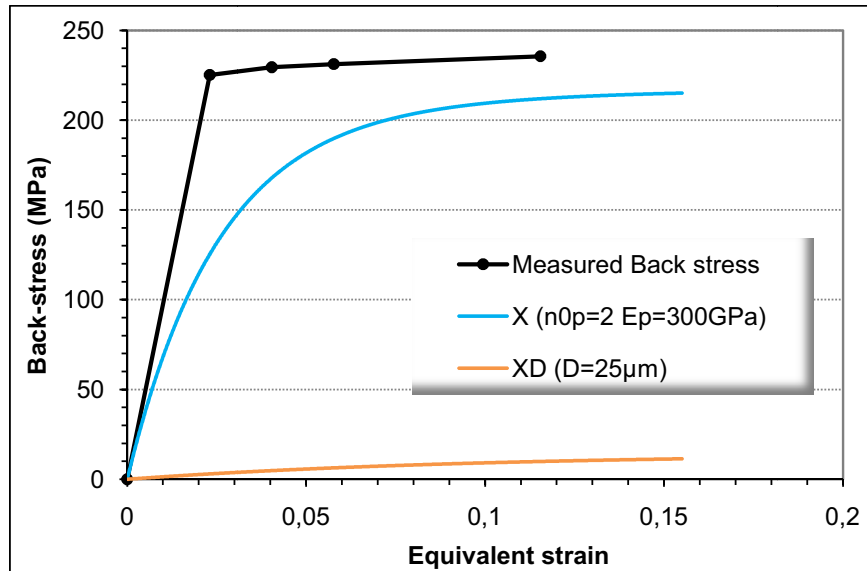


Figure V-15: comparison between calculated and measured backstress due to the precipitates

For smaller pre-deformation states the calculated backstress is slightly underestimated, meaning that the real value of Backstress is greater than half of difference between Forward stress and Reverse Stress: $X = \frac{\sigma_F - \sigma_R}{2}$. This phenomenon was observed in several studies ([FRI2009], [AOU2009], [BOU2010]) and is assumed to be due to the irreversibility of glide. In fact, this was explained in [FRI2009] by the fact that during the reverse loading a mobile dislocation passing by a non-shearable precipitate surrounded by dislocation loops, will annihilate the dislocation loops of inverse Burgers vector. Thus, the precipitate becomes “invisible” to this mobile dislocation (as illustrated Figure V-16). In other

words, the precipitate, in the first step of reverse loading, would not influence the total flow stress, thus reducing σ_p to 0. This would change the equation: $\sigma_R = \sigma_0 + \sqrt{\sigma_p^2 + \sigma_f^2} - X$ into: $\sigma_R = \sigma_0 + \sigma_f - X$ in the first steps of reverse loading. This could explain that $\Delta\sigma_B$ underestimates the backstress since σ_p would also have an effect on kinematic strain-hardening [BOU2010].

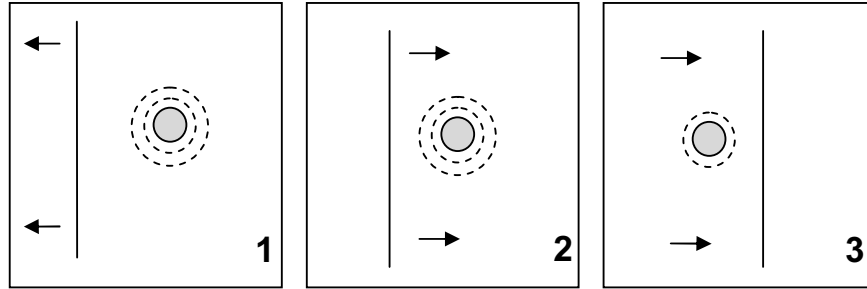


Figure V-16: scheme of annihilation of Orowan loops by mobile dislocations in reverse loading

Another important remark concerning Figure V-15 is the very small value of X_D , showing that the grain boundaries have a very small effect on kinematic strain hardening, due to the large grain size of 25 μm .

To conclude, the satisfying results obtained with modeling of tensile tests on samples aged at 550°C, enable to conclude that the particles are by-passed by the dislocations leaving Orowan loops.

III. Discussion

To summarize, we have been presenting in this part, the different microstructural parameters influencing strain hardening, and the models existing to describe the strain hardening of the material taking into account the isotropic and kinematic components. We have thus seen the complex contribution of precipitates in the reverse loading direction. Since in literature, no tensile test data are available, these have been done for the first time, as well as Bauschinger tests. The experimental results of both revealed an important backstress induced by the presence of non-shearable precipitates, while the backstress induced by the grain boundaries is negligible.

The experimental results also enabled to determine the parameters for modeling strain hardening, which were based on results obtained on IF Steels containing non-shearable precipitates [AOU2009] and slightly modified for the present study. These modeling attempts were relatively satisfying for the description of the global strain hardening evolution with strain, meaning that the use of a model predicting Orowan looping of precipitates seems correct. But the description of the backstress due to the precipitates X_p shows a difficulty to describe the Bauschinger effect for small pre-deformation states. This corresponds to observations found in similar studies ([FRI2009], [AOU2009]), showing the limits of the existing models which do not take into account the reversible character of glide.

Although the modeling results seem to indicate that the precipitates are bypassed by dislocations according to Orowan mechanism, this may seem surprising at such small precipitate sizes. In fact, the presence of coherent and ordered precipitates is usually a sufficient characteristic to induce shearing of precipitates when they are small enough. In our case, the presence of over 50% Iron inside the precipitates, which is the principal element contained in the matrix as well, also tends to indicate a rather smooth precipitate-matrix interface and thus a simplified shearing of the particles. However, a certain number of arguments encouraged us to consider a particle by-passing mechanism.

At first the very high Backstress observed during Bauschinger tests, reaching a value of 230Mpa, is usually the signature of internal stresses, which would be consistent with Orowan mechanism leading to loop accumulation around precipitates. During these reversed shear tests, the reverse stress never reaches the forward stress, meaning there is a small “permanent softening”, indicating a non-reversible dislocation glide. In fact, in the case of shearable particles, the reverse stress reaches the forward stress again after only a few percents of deformation, as shown for example in the study by Decreus [DEC2010]. This is not the case here thus indicating rather a bypassing mechanism. Furthermore, in the hypothesis of a weak obstacle, namely if the Friedel statistics could be applied, the obstacle strength is defined as $F_c = \left(\frac{2\pi b^4 \mu R^2}{3f_v M^2} \Delta\sigma^2 \right)^{1/3}$ and can be calculated. If the hardening results from chemical order, the corresponding energy of the chemical defect created $\gamma_s = \frac{F_c}{2b}$ can be calculated. The values found using the experimental values of Radius and Volume Fractions, are comprised between 2.5 and 3.5 J/m², which is very large compared to the ones found in other studies (which are often closer to a few 0.1J/m²) but no experimental data are available to confirm these values.

It is also interesting to notice that another deformation mechanism was suggested by Russell and Brown [RUS1972] in the case of the Fe-Cu alloy. The bcc Copper particles, which have a lower elastic modulus than the matrix, have an attractive effect on the matrix dislocations, thus pinning them and inducing a strengthening [HUT2007]. Furthermore, in [RUS1972] the authors show that given a difference in modulus $\frac{E_p}{E_M} = \frac{1}{2}$, with E_p and E_M the elastic moduli of the precipitate and the matrix respectively, the strengthening obtained is only 10% less than by Orowan mechanism. They also show that with this type of deformation mechanism it is possible to find large strengthening without having an important work-hardening in the over-aged state since no Orowan loop is left behind after deformation. In our case, the elastic modulus of the precipitates is believed to be larger than the one from the matrix, which is not compatible with this model, but this theory shows the numerous available theories concerning the deformation mechanisms in second-phase hardened materials.

In the present study, we have considered that the deformation mechanism is the Orowan by-passing of particles, since it seems the most plausible scenario. However, some more accurate experimental data, such as TEM observations, would be necessary to make a satisfactory conclusion.

Conclusions

The objective of this thesis was to contribute to the understanding of the relationship between precipitation evolution and mechanical properties in the Fe-2.5wt%Si-1wt%Ti alloy. Important studies have been performed in the past about this alloy, especially of its precipitation structure and characterization, but very few studies exist on the mechanical behavior of this alloy. There probably lies the greatest challenge of this domain.

As a reminder, one could list the different aspects motivating the detailed study of the Fe-Si-Ti system. We have seen in the literature such as in Henon et al [HEN1966], the important hardening capacities of the precipitation induced by the metastable Fe_2SiTi component with the addition of small quantities of Silicon and Titanium, namely from 2.5wt%Si and 1wt%Ti, at temperatures ranging from 450 and 800°C. This precipitation is dense, with a very high volume fraction (4%), which is rather unusual in Iron-based alloys. It contains spherical, coherent and ordered precipitates embedded in a ferritic matrix. The low carbon content makes this alloy a good candidate to avoid the welding problems sometimes observed in high strength steels during the steel to steel assembling in a car framework for example. More generally, the understanding of the precipitation evolution on mechanical properties of materials of any kind (Aluminum alloys, Steels, etc) is a subject of interest since it is a non-negligible source of increase in Yield stress and strain-hardening.

Precipitation characterization

In the present study the methods used to characterize this precipitation were Transmission Electron Microscopy (TEM), Small Angle Neutron Scattering (SANS) and Atom Probe Tomography (APT). TEM and APT permit to obtain local information about the microstructure at different scales, whereas the SANS gives an average microstructural evolution. The combination of these three methods enabled to confirm the presence of the metastable ternary phase Fe_2SiTi , which has been characterized in former studies on this alloy [JAC1972], having a face cubic centered structure, also called Heusler structure of L2_1 type.

In the present study TEM observations, confirmed the structure of the precipitates being Fe_2SiTi . The use of Small Angle Neutron Scattering (SANS) was found out to be very interesting, since it provides accurate quantitative data on the evolution of the radius and volume fraction of precipitates during ageing. This data was confirmed by analysis and 3D-images of Atom Probe Tomography (APT) experiments showing an important density of spherical ternary precipitates of Fe_2SiTi type.

Mechanical properties

In former studies found in literature, the mechanical properties were characterized on samples aged at high temperatures comprised between 800°C and 1000°C which contain Fe_2Ti particles. These particles have been shown to embrittle drastically the material, and only compression tests and hardness tests could be carried out so far. Thus, tensile tests on samples aged at low temperatures, containing Fe_2SiTi precipitates, have been performed for the first time in our work, and they were compared with microhardness tests. Results showed

a yield stress of 1200MPa, namely a gain of 800MPa when compared to the initial as-quenched sample, simply by the introduction of precipitated particles. For the characterization of the strain-hardening evolution induced by the presence of the precipitates, Bauschinger tests were done, using the method of reverse shear-test. These revealed an important Backstress, which is often the signature of dislocation pile-ups, indicating the probable mechanism of Orowan loops around the precipitates.

Relation between microstructure and mechanical properties

The mechanical tests performed on age-hardened samples containing precipitates were compared with modeling, both for the yield stress and for the flow stress. The yield stress evolution is described by Ashby-Orowan equation, and most likely the precipitates are by-passed by dislocations. The strain-hardening evolution is described by a model taking into account both the isotropic hardening resulting from random dislocation storage, and the kinematic strain-hardening induced by polarized dislocation storage. The kinematic component of strain-hardening takes into account separately the contribution of grain boundaries and precipitates. These confirmed the negligible role of the grains on the strain-hardening, as was expected by the relatively large grain size. The model used was developed by Aouafi [AOU2009], based on already existing models, among others by Proudhon et al. [PRO2008]. The proposed model shows a good correlation with experimental data, providing a hint, if not a proof, that the probable deformation mechanism is by Orowan mechanism.

About the fracture mechanism

Observation of fracture surface of samples after tensile tests has revealed strong variations across samples, making it difficult to characterize the fracture mechanism quantitatively. In fact, the fractography observations of Fe-Si-Ti samples showed essentially a mix between dimpled rupture and transgranular cleavage fracture. This mixed mode has also been observed in a study by Wittig et al. [WIT2008] concerning Fe-Si alloys containing 4.5 to 6.4wt% Silicon. The authors attributed this cleavage fracture to the effect of Silicon on deformation mechanisms, namely the enhancement of planar slip, since alloys with more Silicon are more likely to fracture by pure cleavage. Another point has been observed in the present study, namely the variability of the behavior across samples. As shown Figure V-17 below, which provides a comparison between the engineering curves of two tensile test bars of same heating treatment namely at 550°C during 4 hours, the elongation to fracture of the two curves are very different, 4 and 8%, and the tensile test bar nr. 1 does not undergo any necking, since the engineering stress does not decrease with elongation. Fractography observation with SEM also revealed a difference in fracture mechanisms as shown figure v-18 and 19 below. The tensile test bar nr. 1 reveals a pure cleavage fracture whereas the tensile test bar nr. 2 contains a mixed fracture with some ductile zones containing dimples.

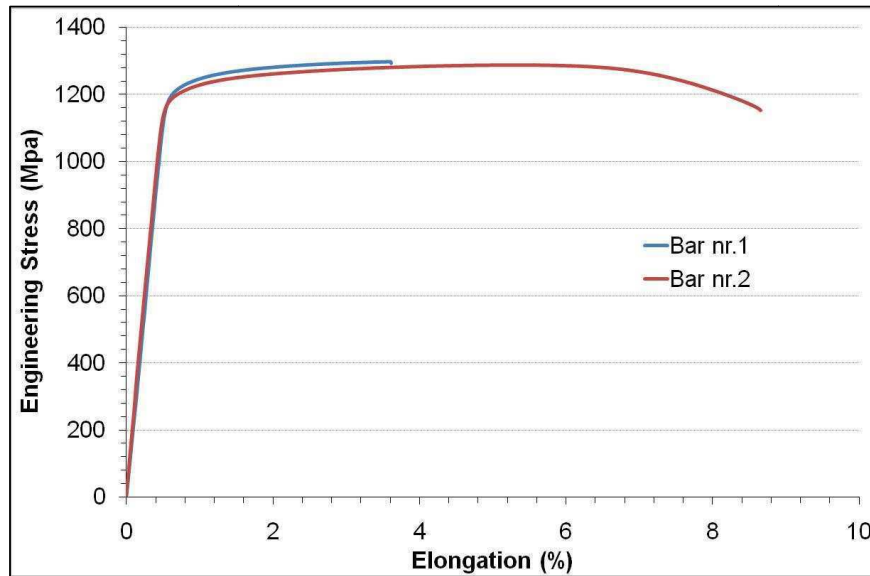


Figure V-17: Tensile tests performed on sample aged at 550°C during 4 hours. Comparison between two tensile test bars of same heating treatment

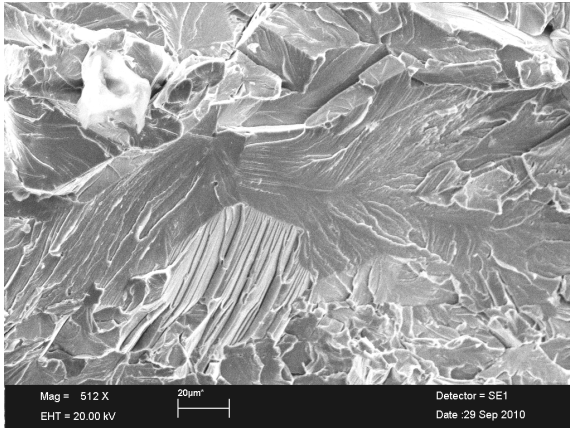


Figure V-18: Fractography observed at SEM of tensile bar after fracture, of a sample aged at 550°C during 4H, corresponding to the Engineering stress curve nr. 1

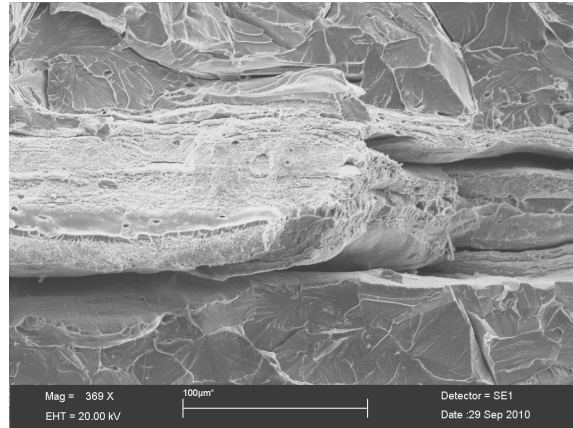


Figure V-19: Fractography observed at SEM of tensile bar after fracture, of a sample aged at 550°C during 4H, corresponding to the Engineering stress curve nr. 2

The difference in tensile behavior in this case was attributed to the presence of inclusions aligned as could be seen optically on the fractured tensile bars. In fact, as mentioned already in a study by McMahon et al. [MCM1965], and confirmed by several other studies concerning the fracture of ferritic steels (e.g. Fairchild et al. [FAI2000]), the presence of hard inclusions in a soft matrix can be cleavage initiating sites. This is due to the fact that when the material containing inclusions undergoes a certain deformation, the dislocations will tend to accumulate at the matrix-inclusion interface generating high stresses which can lead to the cracking of the particle, providing an incipient sharp crack. This cleavage crack initiated from the fracture of the brittle particle can propagate within the adjacent ferrite with a rapidly advancing microcrack, and if the arrest fracture toughness of the ferrite is too low, the crack will propagate into the neighboring ferrite grains [PIN2007].

The observation of as-quenched sample with SEM reproduced Figure V-20 and 21, shows the presence of randomly distributed inclusion lines in an as-quenched sample. These

inclusions were identified to be either TiN or TiC. A study by Fairchild et al. [FAI2000] mentions the important role of these inclusions on cleavage fracture initiation. X-ray analysis of cleavage fracture surfaces of an Fe-Si-Ti sample aged at 550°C during 2 hours, reveals the very important amount of Titanium contained in the center of cleavage surface, as shown figure v-22 and 23. This results would confirm the hypothesis of a cleavage fracture initiated by an inclusion.

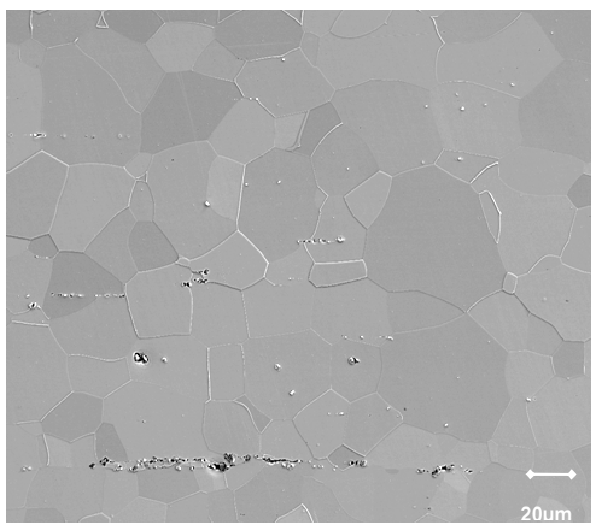


Figure V-20: SEM observation of as-quenched sample with visible line of inclusions in Fe-Si-Ti alloy

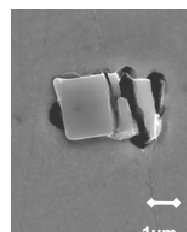


Figure V-21: magnified inclusion of as-quenched sample of Fe-Si-Ti

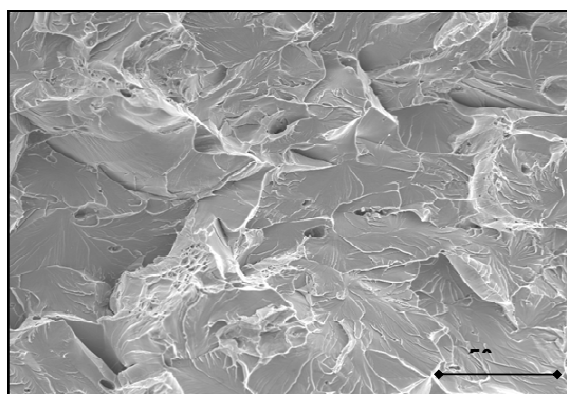


Figure V-22: fractography of sample aged at 550°C during 2 hours observed on SEM-FEG

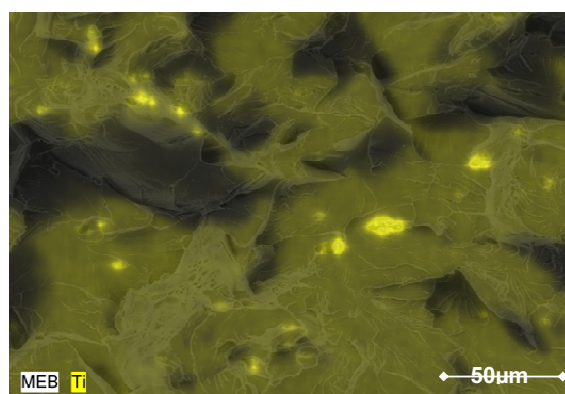


Figure V-23: X-ray analysis of Titanium on sample aged at 550°C during 2 hours

Thus, the fracture mechanisms involved in Fe-Si-Ti alloys have not been fully understood yet and further investigation would be necessary, and they will involve not only the competition between cleavage and ductile fracture, but also the seminal role of inclusions.

Perspectives

Although a variety of experiments have been performed in the present study, the perspectives in the understanding of the relation between microstructure and mechanical properties are numerous, and the system is far from being fully understood. In fact, the present study has enabled to show some interesting aspects in the mechanical properties and in the precipitation kinetics, but for a complete characterization, more accurate investigations still need to be done.

Precipitation characterization

The precipitation was characterized at temperatures ranging from 450°C to 580°C using SANS technique, Atom Probe Tomography and TEM. These showed the presence of the metastable phase Fe_2SiTi , but heating treatments were only done up to 20 hours. It could be interesting to characterize the complete precipitation kinetics with time, namely to go up to longer ageing times and see, using modern characterization techniques, the change from metastable to stable phase. In-situ experiments would be a great advantage in that sense.

Strain-hardening evolution

As already mentioned previously, the strain hardening model used here, has shown some limitations, for instance in the description of the reversibility of glide. The simple addition of the different contribution of the isotropic strain-hardening in the model could be too simplistic. In that sense, a model taking into account the difference in interaction between the dislocation at forward and reverse loading could be interesting, especially for a full understanding of the Bauschinger effect.

Fracture mechanism

Concerning the fracture mechanism involved in the Fe-Si-Ti, we have seen that it is probably influenced by a combination of factors, such as the presence of Silicon, which favors planar glide, the presence of non-metallic inclusions, which could be cleavage initiating sites, and the presence of an important volume fraction of small precipitates. The contribution of each of these elements is not fully understood yet and would require a complete investigation, both to study ductility and fracture toughness.

General understanding

Finally, in the present study we have seen the influence of a small, dense and spherical precipitation on the mechanical properties of ferritic Fe-Si-Ti matrix. It could thus be interesting to change the matrix phase, namely by introducing the same precipitates into a harder matrix, the same way it is done in the maraging steels, using a martensitic matrix to introduce precipitates. This is a possible route for alloy design: choosing an additional element changing the M_s Temperature without having too much interference with Ti and Si.

References

- [ABS1968] *Precipitation of intermetallic compounds in some ferritic ternary alloys*, D.J. Abson, G.G. Brown, J.A. Whiteman; The journal of the Australian institute of Metals, Vol.13, no.2 (May 1968)
- [ACE2007] *Evolution de l'état de précipitation au cours de l'austénitisation d'aciers microalliés au Vanadium et au Niobium*, D. Acevedo Reyes, PhD Thesis INSA Lyon, France (2007) (French)
- [AND1995] *Fracture mechanics: Fundamentals and Applications*, T.L. Anderson, 2nd ed. CRC Press (1995)
- [AOU2009] *Analyse et modélisation du comportement en chargement inverse d'aciers ferritiques et micro-alliés : Prise en compte de la taille de grains et des précipités dans des lois d'écrouissage mixte*, A. Aouafi, PhD Thesis LPMTM Paris XIII, France (2009) (French)
- [ARD1985] *Precipitation Hardening*, A.J. Ardell; Metallurgical Transactions A Vol. 16 pps.2131-2165 (Dec. 1985)
- [ARG1969] *Physics of Strength and Plasticity*, ed. A.S. Argon; MIT Press (1969)
- [ASH1966] *Work-hardening of dispersion-hardened crystals*, M.F. Ashby; Philosophical Magazine, Vol. 14, pp. 1157-1178 (1966)
- [ASH1968] *The theory of the critical shear stress and work hardening of dispersion-hardened crystals*, M.F. Ashby in Proceedings of the 2nd Bolton Landing Conference-Oxide Dispersion Strengthening (ed. Gordon and Breach), pp. 143-205 (1968)
- [ASH1970] *Deformation of plastically non-homogeneous materials*, M.F. Ashby; Philosophical Magazine, Vol. 21, pp. 399-424 (1970)
- [ASH1986] *Engineering Materials II*, M.F. Ashby & D.R.H. Jones, Pergamon Press (1986)
- [AVR1939] *Kinetics of phase change*, M. Avrami, Journal of Phys. Chem., Vol.7, p. 1103 (1939)
- [BAC1955] *Neutron Diffraction*, G.E. Bacon; Oxford Press (1955) (2nd edition 1962)
- [BAT1953] *Technical Notes – Diffusion of Silicon in Iron*, Batz, W., Mean H.W. & Birchenall C.E.; Transactions AIME, Vol.194, p.1170 (1953)
- [BOU2006] O. Bouaziz & G. Dirras, Proceedings of Conference MATERIAUX 2006, Dijon, France, 2006 (French)
- [BOU2010] *Study of the reversibility of dislocation glide*, O. Bouaziz, to be published
- [BOW1968] *The coarsening of Spherical Intermetallic Particles in a Ferritic Fe-Si-Ti Alloy*, E.N. Bower & J.A. Whiteman; Research Note, University of Sheffield (1968)
- [BRA1968] *Special Alloy Steels*, T. Bracewell in *Low Alloy Steels*; Conference proceeding of the Iron and Steel Institute in London pps.229-239 (2-4 April 1968)
- [BRA1997] *Modelling of precipitation reactions in industrial processing*, D.H. Bratland, O. Grong, H. Shercliff, O.R. Myhr & S.Tjøtta; Acta Materialia Vol. 45, No. 1, pp. 1-22 (1997)
- [BRO1971] *The work-hardening of Copper-Silica, II. The role of plastic relaxation*, L.M. Brown & W.M. Stobbs, Philosophical Magazine, Vol.23, p.1201 (1971)
- [BRO1977] *Orowan's explanation of the Bauschinger effect*, L.M. Brown, Scripta Metallurgica Vol.11, pp. 127-131 (1977)

- [CAH1996] *Physical Metallurgy* in 3 Volumes, R.W. Cahn, P. Haasen (1996)
- [CON1971] *Effect of Second-Phase Particles on the Mechanical Properties of Steel*, Conference Proceeding; organized by The British steel corporation and The Iron and Steel Institute, London (24-25 March 1971)
- [COT1954] *Interactions of Dislocations and Solute Atoms*, A.H. Cottrell in *Relation of Properties to Microstructure*, American Society of Metals, pp. 131-162 (1954)
- [DEC2010] *Etude de la précipitation dans les alliages Al-Li-Cu de troisième génération – Relations entre microstructures et propriétés mécaniques*, B. Decreus, PhD Thesis, Grenoble-INP, France (2010) (French)
- [DES1997] *Influence de la prédéformation et des traitements thermiques sur la microstructure et les propriétés mécaniques des alliages Al-Zn-Mg-Cu*, A. Deschamps, PhD Thesis INPGrenoble (1997)
- [DES1999] *Influence of pre-deformation and ageing of an Al-Zn-Mg alloy_II. Modeling of precipitation kinetics and yield stress*, A. Deschamps & Y. Bréchet; *Acta Materialia* Vol. 47, No. 1, pp. 293-305 (1999)
- [DES2003] *Précipitation durcissante dans les matériaux de structure*, A. Deschamps, Mémoire d'HDR, INPGrenoble, France (2003) (French)
- [DUN2005] *Approche par variable interne de fluage et recristallisation des alliages en zirconium*, J.Dunlop ; Phd Thesis, INP Grenoble, France (2005)
- [EDI1975] *Interpretation of transmission electron micrographs*. J.W. Edington in *Monographs in Practical Electron Microscopy in Materials Science*; No. 3, II2 p. Philips Technical Library-MacMillan, (1975) London
- [EMB1987] *Structural aspects of the Bauschinger effect*, J.D. Embury, *Material Science Forum*, Vol. 10 (1), pp.27-32 (1987)
- [EST1984] *A unified phenomenological description of work-hardening and creep based on one-parameter models*, Y. Estrin & H. Mecking, *Acta Metallurgica*, Vol. 32, No. 1, pp. 57-70 (1984)
- [EST1996] *Dislocation-Density-related constitutive modeling*, Y. Estrin; *Unified constitutive laws of plastic deformation*, Ed. Krausz (1996)
- [EST1999] *Deformation behavior of particle-strengthened alloys: a Voronoi mesh approach*, Y. Estrin, S. Arndt, M. Heilmaier & Y. Bréchet, *Acta Materialia*, Vol. 47, No. 2, pp. 585-606 (1999)
- [FAI2000] *The Mechanism of Brittle Fracture in a Microalloyed Steel: Part I. Inclusion-Induced Cleavage; Part 2. Mechanistic Modeling*; D.P. Fairchild, D.G. Howden and W.A.T. Clark; *Metallurgical and Materials Transactions A*, Vol. 31, pp. 641-652 and 653-667 (2000)
- [FEI1987] *Structure Analysis by Small-Angle X-Ray and Neutron Scattering*, L.A. Feigin & D.I. Svergun; ed. G.W. Taylor, Plenum Press New-York and London (1987)
- [FIS1953] *The hardening of Metal Crystals by Precipitate Particles*, J.C. Fisher, E.W. Hart & R.H. Pry; *Acta Metallurgica* Vol.1 (1953)
- [FIS1954] *On the Strength of Solid Solution Alloys*, J.C. Fisher; *Acta Metallurgica* Vol. 2 pgs.9-10 (Jan.1954)
- [FOR1966] *Dislocation movement through random arrays of obstacles*, A.J.E. Foreman & M.J. Makin; *Philosophical Magazine*, Vol. 14, pp. 911-924 (1966)
- [FRA2004] *Endommagements et rupture de matériaux*, D. François; EDP Sciences (2004) (French)

- [FRI1964] *Dislocations*, J. Friedel, Pergamon Press, Oxford (1964)
- [FRI2009] *Couplages entre précipitation et plasticité dans un alliage d'Aluminium 7xxx : application à des traitements thermomécaniques de réduction des distorsions dans des composants aéronautiques*, G. Fribourg, PhD Thesis, Grenoble-INP (2009)
- [GAL2008] *Precipitation microstructures in a AA6056 Aluminum alloy after Friction Stir Welding: characterisation and Modelling*, C. Gallais, A. Denquin, Y. Bréchet, G. Lapasset.; Materials Science and Engineering A, Vol. 496, pp. 77-89 (2008)
- [GEN2001] *Cinétique de précipitation du carbure de Niobium dans la ferrite*, D. Gendt ; PhD Thesis, Université Paris-Sud, France (2001) (French)
- [GER1979] *Precipitation Hardening*, V. Gerold in *Dislocations in Solids* ed. by F.R.N. Nabarro, North Holland Publishing Company (1979)
- [GLA1997] *The physical metallurgy of microalloyed steels*, T. Gladman, Ashgate Publishing, 240 pages (1997)
- [GOU2004] *Precipitation of copper in ferrite: Prediction of the strengthening kinetics*, M. Gouné, P. Maugis, E. Pinto Da Costa and D. Bouleau; Revue de Metallurgie, N°1, pp. 71-78 (January 2004)
- [GRI1966] *Dislocation arrangements in deformed polycrystalline 3% Silicon-Iron*, D. Griffiths & J.N. Riley, Acta Metallurgica, Vol. 14 (1966) p.755
- [HAA1979] *Strength of Metals and Alloys*, Conference Proceedings, P. Haasen, V. Gerold & G. Kostorz, Pergamon Press (27-31 August 1979)
- [HAN1952] *The Titanium-Silicon System*, M. Hansen et al.; Transaction of American Society of Metals Vol.44, pp. 518-538 (1952)
- [HEN1963] *Quelques résultats concernant la précipitation dans les alliages Fe-Ti, Fe-Si-Ti et Fe-Ti-Ni*, J.P. Hénon, J. Manenc & C. Crussard ; Compte Rendus de l'Académie des Sciences (French), 257, p. 671, (Séance du 17 juillet 1963) (French)
- [HEN1966] *Etude de la précipitation dans les alliages Fe-Ti, Fe-Si-Ti, Fe-Ti-Ni*, J-P. Hénon, C. Waché, J. Manenc ; Mémoires scientifiques revues métallurgiques, LXIII, n°2 (1966) (French)
- [HOB1968] *Precipitation of Intermetallic Compounds in Iron*; R.M. Hobbs, I.S. Brammar and A.R.; Transactions of the Japan Institute of Metals, Vol.9 (1968)
- [HUT2007] *Selecting non-isothermal heat treatment schedules for precipitation hardening systems: An example of coupled process-property optimization*, C.R. Hutchinson, M. Gouné and A. Redjaïmia; Acta Materialia, Vol. 55, pp.213-223 (2007)
- [JAC1970] *Intermetallic precipitates in an Fe-Si-Ti alloy*, D.H. Jack; Metal science Journal, Vol.4 (1970)
- [JAC1972] *Age hardening of an Fe-Ti-Si Alloy*; D. H. Jack, R. W. K. Honeycombe; Acta Metallurgica, Vol.20 Issue 6, pp. 787-796 (June 1972)
- [JAC1975] *Low temperature deformation mechanisms in an Fe-Si-Ti alloy*, D.H. Jack, F. Guiu; Journal of Materials Science, Vol.10, pp. 1161-1168 (1975)
- [JOH1939] *Reaction kinetics in processes of nucleation and growth*, W.A. Johnson & R.F. Mehl, Transactions AIME, Vol.135, p. 416 (1939)
- [KAU1979] *Coupled Phase Diagrams and Thermochemical Data for Transition Metal Binary Systems*, L. Kaufmann; Calphad VI, pp. 45-76 (1979)

- [KEO1966] *Observation and orientation relationship of an epitaxial oxide of R3O4 type with ferrite*, S.R. Keown & D.J. Dyson, Journal of the Iron and Steel Institute, Vol. 204, pp. 832-836 (Aug 1966)
- [KOC1966] *A statistical theory of flow stress and work-hardening*, U.F. Kocks; Philosophical Magazine, Vol. 13, pp. 541-566 (1966)
- [KOC1976] *Laws for work-hardening and low-temperature creep*, U. Kocks; Journal of Engineering Materials and Technology Vol. 98, pp. 76-85 (1976)
- [LAN1990] *Kinetics of nucleation in near-critical fluids*, J.S. Langer & A.J. Schwartz; Physical Review A, Vol.21, No.3, pp. 948-958 (1980)
- [LEN1957] *Precipitation Reactions in Iron-Base Alloys*, A.J. Lena in *Precipitation from solid solution*, R.F. Mehl et al. American Society of Metals, pgs. 244-327 (1957)
- [LIF1961] *The kinetics of precipitation from supersaturated solid solutions*, I.M. Lifshitz & V.V. Slyozov; Journal of Phys. Chem. Solids, Vol. 19, pp. 35-50 (1961)
- [LOE2003] *Untersuchung der ternären Systeme Fe-Si-Mg und Fe-Si-Ti: Phasengleichgewichte und mechanisches Verhalten ausgewählter Legierungen*, F.Löffler; PhD Thesis, Fortschritt-Berichte VDI Düsseldorf (2003) (German)
- [LOE2004] *Iron-Rich Iron-Silicon-Titanium Alloys with Strengthening Intermetallic Laves Phase Precipitates*, F.Löffler, M. Palm, G. Sauthoff; Steel Research International Vol. 75 nr.11, pp. 768-772 (2004)
- [LOU1979] *Plasticité des métaux de structure cubique centrée*, F. Louchet, « Dislocations et déformation plastique », école d'été Yrvals 1979 p.149 (French)
- [LUE1973] *The Inhomogeneity of plastic deformation*, Lücke K. and Mecking H., ASM, Ohio, ed. R.E. Reed-Hill, p.223 (1973)
- [MAG1994] *Influence of the hot rolling conditions on texture formation of Fe-Si sheets*, S.Mager & J. Wieting; Journal of Magnetism and Magnetic Materials, Vol. 133, pp. 170-173 (1994)
- [MAR1980] *Micromechanisms in particle-hardened alloys*, J.W. Martin, Cambridge Solid State Science Series, Cambridge University Press (1980)
- [MAS1990] *Binary alloy phase diagrams*, T.B. Massalski; American Society of Metals, Metals Park (OH) (1990)
- [MAU2003] *A model for carbonitride precipitation in ferrite*, P. Maugis, M. Gouné, P. Barges, D. Dougnac, D. Ravaine, M. Lamberigts, T. Siwecki & Y. Bi; Materials Science Forum, Vol. 426-432, Part 2, pp. 1313-1318 (2003)
- [MAU2005] *Kinetics of Vanadium Carbonitride Precipitation in steels: a computer model*, P. Maugis & M. Gouné, Acta Materialia, Vol. 53, pp. 3359-3367 (2005)
- [MCM1965] *Initiation of Cleavage in Polycrystalline Iron*, C.J. McMahon & M. Cohen; Acta Metallurgica, Vol. 13, pp. 591-604 (1965)
- [MEC1981] *Kinetics of flow and strain-hardening*, H. Mecking, and U. Kocks; Acta Metallurgica Vol. 29, pp. 1865-1875 (1981)
- [MEY1999] *Mechanical Behavior of Materials*, M.A. Meyers & K.K. Chawla; Prentice Hall ed. (1999)
- [MIL1986] *Atom Probe Tomography: Analysis at the Atomic Level*, M. Miller, Kluwer Academic / Plenum Publishers (2000)
- [MIS1984] *On the development of the Goss texture in Iron-3%Silicon*, S. Mishra, C. Därmann & K. Lücke; Acta Metallurgica Vol. 32, No.12, pp. 2185-2201 (1984)

- [MUE1968] *The Atom-Probe Field Ion Microscope*; Erwin Müller, J. A. Panitz, and S. Brooks McLane; Review of Scientific Instruments Vol. 39 (1) pps.83-86 (1968)
- [NEW1957] *General Theory, Mechanism and Kinetics*, J.B. Newkirk in *Precipitation from solid solution*, R.F. Mehl et al. American Society of Metals, pgs. 6-149 (1957)
- [NIC2002] *Evolution de l'état de précipitation dans un alliage Al-Zn-Mg lors de traitements thermiques anisothermes et dans la zone affectée thermiquement de joints soudés*, M.Nicolas, PhD Thesis; INP Grenoble, France (2002)
- [ORO1948] *Discussion on Internal Stresses*, E. Orowan in *Internal Stresses in Metals and Alloys*, The Institute of Metals, London p. 451 (1948)
- [ORO1959] *Internal Stresses and Fatigue in Metals*, E. Orowan; Elsevier, p.59 (1959)
- [PAP1970] *The deformation mechanism in ferritic Fe-Si-Ti alloys containing intermetallic precipitates*, R. Papaleo, J.A. Whiteman; Micron, 2, pp. 63-70 (1970)
- [PAP1971] *Deformation mechanism in ferritic Fe-Si-Ti alloys containing ordered misfit-free intermetallic particles*, R.Papaleo & J.A. Whiteman, in *Effect of Second-Phase Particles on the Mechanical Properties of Steel*, Conference Proceeding; The Iron and Steel Institute, London (24-25 March 1971)
- [PER2004] *Caractérisation et modélisation de la précipitation du carbure de niobium et du cuivre dans les aciers bas carbone*, F. Perrard, PhD Thesis; INP Grenoble, France (2004) (French)
- [PIN1982a] *The precipitation of the Intermetallic Compound NiAl in Fe-19wt.%Cr Alloys*, R. Taillard & A. Pineau; Materials Science and Engineering, Vol.54 p.209 (1982)
- [PIN1982b] *Room Temperature Tensile Properties of Fe-19wt.% Cr Alloys Precipitation Hardened by Intermetallic Compound NiAl*, R. Taillard, A. Pineau and B.J. Thomas, Vol. 56 p.219 (1982)
- [PIN2007] *Failure mechanisms of Metals*, A. Pineau, T. Pardoen in *Comprehensive Structural Integrity Encyclopedia vol. 2*, Elsevier (Chapter 6) (2007)
- [PRO2008] *The role of internal stresses on the plasticity of the Al-Mg-Si-Cu alloy AA 6111*, H. Proudhon, W.J. Poole, X. Wang, Y. Bréchet; Philosophical Magazine Vol. 88 No. 5, pp.621-640 (11 February 2008)
- [RAG1987] *The Fe-Si-Ti (Iron-Silicon-Titanium) system*, V. Raghavan; Phase Diagrams of Ternary Iron Alloys, Part 1, ASM International, pp. 65-72 (1987)
- [RAG2009] *Fe-Si-Ti (Iron-Silicon-Titanium)*, V. Raghavan ; Journal of phase Equilibria and Diffusion, Vol.30 No. 4, pp. 393-396 (2009)
- [RAU2007] *Work-hardening model for polycrystalline metals under strain reversal at large strains*, E.F. Rauch, J.J. Gracio, F. Barlat, Acta Materialia, Vol. 55 (9), pp. 2939-2948 (2007)
- [REP1993] *Particle strengthening*, B. Reppich; in: R.W. Cahn, P. Haasen, E.J. Kramer, (Eds.), Materials Science and Technology, vol. 6, in: H. Mughrabi, (Ed.), *Plastic Deformation and Fracture of Materials*, Wiley-VCH, Weinheim, Germany, pp. 311–357 (1993)
- [RUS1972] *A dispersion strengthening model based on differing elastic moduli applied to the Iron-Copper System*, K.C. Russell & L.M. Brown; Acta Metallurgica, Vol. 20, pp. 969-974 (1972)
- [SAE2010] Society of Automotive Engineering, <http://www.sae.com>
- [SCH1969] *The early stages of growth of second phase particles in an Fe-Si-Ti alloy*, D.M. Schwartz, B. Ralph; Metal science Journal, Vol.3 Nr.1 pp.216-219 (1969)

- [SES1979] *Plasticity and crystal structure*; B. Sestak, in *Strength of metals and alloys*, Ed. P. Haasen, P. Gerold & G. Kosterz, vol.3 p.1461 (1979)
- [SIM2007] *Sequential modelling of local precipitation, strength and strain hardening in friction stir welds of an aluminium alloy 6005 A-T6*, A. Simar, Y. Bréchet, B. De Meester, A. Danquin & T. Pardoen ; *Acta Materialia* Vol.55 Issue 18, pp. 6133-6143 (2007)
- [SIN2006] *A model for the grain size dependent work hardening of copper*, C.W. Sinclair, W.J Poole & Y. Brechet, *Scripta Materialia*, Vol.55, p. 739 (2006)
- [URI2006] *Preliminary internal results and technical survey on hardening by precipitation of ordered phases*, J-L. Uriarte and P. Barges; Internal note Arcelor research (2006)
- [VAN1979] *Glissement dévié des dislocations*, G. Vanderschaeve & B. Escaig in *Dislocations et déformation plastique*, école d'été d'Yrivals, p.141(1979) (French)
- [VER1975] *Fundamentals of Physical Metallurgy*, J.D. Verhoeven, ed. Jon Wiley & Sons Inc. (1975)
- [VOG1909] *Über Magnesium-Siliciumlegierungen*, R. Vogel; *Zeitschrift Anorganischer Chemie*, Vol. 61 pp. 46-53 (1909) (German)
- [VOG1938] *The Iron corner of the Iron-Silicon-Titanium System*, R. Vogel, *Archiv für das Eisenhüttenwesen*, Vol.12 No. 4, pp. 207-212, (1938) (German)
- [WAG1961] *Z. Elektrochem.*, Vol. 65, p. 581 (1961) (German)
- [WAG1991] *Homogeneous second phase*, R. Wagner, R. Kampmann; In: R. Cahn, P. Haasen and E. Kramer, Editors, *Phase Transformation in Materials of Material Science and Technology* vol. 5, VCH, Weinheim, Germany, pp. 213–303 (Chapter 4) (1991)
- [WAS1931] R. Wasmuth, *Archiv für das Eisenhüttenwesen*, Vol. 5 p.45 (1931) (German)
- [WEE1964] *Elementary dislocation theory*, J. & J. Weertman; Oxford University Press, (1964)
- [WIL1965] *Reversible Work hardening in alloys of cubic metals*, D.V. Wilson, *Acta Metallurgica*, Vol. 13, pp. 807-815 (July 1965)
- [WIL1996] *Transmission Electron Microscopy*, D. Williams & B. Carter; Plenum Press, in 5 volumes (1996)
- [WIT2008] *Deformation and Fracture behavior of Rapidly Solidified and Annealed Iron-Silicon Alloys*, J.E. Wittig & G. Frommeyer; *Metallurgical and Materials Transactions A*, Vol. 39A, pp. 252-265 (Feb. 2008)
- [WOR2010] *Worldautosteel*, Automotive group of Worldsteel Association, <http://www.worldautosteel.com>
- [XIO2009] *Iron-Silicon-Titanium*, W. Xiong, Y. Du & C. Zhang; *Iron Systems: Phase Diagrams, Crystallographic and Thermodynamic Data*, Landolt-Börnstein New Series IV/11 D5 (2009)